

# **Inference, Estimation, and Prediction for Stable Operation of Modern Electric Power Systems**

by

Samuel Chapman Chevalier

B.S. in Electrical Engineering, University of Vermont (2015)  
M.S. in Electrical Engineering, University of Vermont (2016)

Submitted to the Department of Mechanical Engineering  
in partial fulfillment of the requirements for the degree of

Doctor of Philosophy in Mechanical Engineering

at the

MASSACHUSETTS INSTITUTE OF TECHNOLOGY

February 2021

© Massachusetts Institute of Technology 2021. All rights reserved.

Author .....  
Department of Mechanical Engineering  
January 15, 2021

Certified by .....  
Luca Daniel  
Professor of Electrical Engineering and Computer Science  
Thesis Supervisor

Accepted by .....  
Nicolas Hadjiconstantinou  
Professor of Mechanical Engineering  
Chairman, Committee for Graduate Students



# Inference, Estimation, and Prediction for Stable Operation of Modern Electric Power Systems

by

Samuel Chapman Chevalier

Submitted to the Department of Mechanical Engineering  
on January 15, 2021, in partial fulfillment of the  
requirements for the degree of  
Doctor of Philosophy in Mechanical Engineering

## Abstract

To keep pace with social-ecological disruptions and technological progressions, electrical power systems must continually adapt. In order to address the stability-related challenges associated with these adaptations, this thesis develops a set of analytically rigorous yet practically oriented methods for ensuring the continued stability of modern power systems. By leveraging inference, estimation, and predictive modeling techniques, the proposed methods capitalize on the unprecedented amount of real time data emerging from modernizing smart grids. For each method, we provide simulated test results from IEEE benchmark systems.

Newly deployed Phasor Measurement Units (PMUs) are observing the presence of detrimental low frequency forced oscillations (FOs) in transmission grid networks. To begin this thesis, we address the problem of locating the unknown sources of these FOs. To perform source identification, we develop an equivalent circuit transformation which leverages suitably constructed transfer functions of grid elements. Since FO sources appear in this equivalent circuit as independent current injections, a Bayesian framework is applied to locate the most probable source of these injections. Subsequently, we use our equivalent circuit to perform a systematic investigation of energy-based source identification methods.

We further leverage this equivalent circuit transformation by developing “plug-and-play” stability standards for microgrid networks that contain uncertain loading configurations. As converter-based technology declines in cost, microgrids are becoming an increasingly feasible option for expanding grid access. Via homotopic parameterization of the instability drivers in these tightly regulated systems, we identify a family of rotational functions which ensure that no eigenmodes can be driven unstable. Any component which satisfies the resulting standards can be safely added to the network, thus allowing for plug-and-play operability.

High-fidelity linearized models are needed to perform both FO source identification and microgrid stability certification. Furthermore, as loss of inertia and real-time observability of grid assets accelerate in tandem, real-time linearized modeling is becoming an increasingly useful tool for grid operators. Accordingly, we develop tools for performing real-time predictive modeling of low frequency power system

dynamics in the presence of ambient perturbations. Using PMU data, we develop a black-box modeling procedure, known as Real-Time Vector Fitting (RTVF), that takes explicit account for initial state decay and concurrently active input signals. We then outline a proposed extension, known as stochastic-RTVF, that accounts for the corrupting effects of unobservable stochastic inputs.

The surrogate modeling utilized by vector fitting can also be applied to the steady state power flow problem. Due to an unprecedented deployment of distributed energy resources, operational uncertainty in electrical distribution networks is increasing dramatically. To address this challenge, we develop methodology for speeding up probabilistic power flow and state estimation routines in distribution networks. We do so by exploiting the inherently low-rank nature of the voltage profile in these systems. The associated algorithms dynamically generate a low-dimensional subspace which is used to construct a projection-based reduced order model (ROM) of the full nonlinear system. Future system solves using this ROM are highly efficient.

Thesis Supervisor: Luca Daniel

Title: Professor of Electrical Engineering and Computer Science

## Acknowledgments

While laying out the foundations of calculus, Sir Isaac Newton sought to help his readers overcome the ancient paradox posed by the taking of *limits*:

It may be objected that there is no such thing as an ultimate proportion of vanishing quantities, inasmuch as before vanishing the proportion is not ultimate, and after vanishing it does not exist at all... But the answer is easy...the ultimate ratio of vanishing quantities is to be understood not as the ratio of quantities *before* they vanish or *after* they have vanished, but the ratio *with which* they vanish. [132]

So, too, can the contributions of this thesis only be properly understood “in the limit”-ing relationship to the amazing people who have supported me along the way. In comparison to their efforts, which cannot be overstated, my personal contributions can sometimes feel vanishingly small. In those moments, I take comfort in remembering that I have had the unique privilege of standing “on the shoulders” of the “giants” [68] whose names follow. Accordingly, I would like to thank...

- My advisor, Prof. Luca Daniel, to whom I owe deep appreciation and gratitude. I have found Luca to be a *limitless* wellspring of new ideas, insightful commentary, and advisorly wisdom. Our work together represents the fruitful collaboration of two people with vastly different academic backgrounds (i.e. power system dynamics in my case, and all things numerical methods in his), and I will forever be thankful for the numerous ways in which he has challenged and shaped my approach to academic problem solving.
- Dr. Kostya Turitsyn. To me, Kostya represents a consummate academic, embodying everything I should aspire to be: analytically brilliant, thoughtfully diverse, and principally humble. Thank you, Kostya, for your endless support.
- Prof. Petr Vorobej. Petr is the primary exception to the general rule: “Physicists do not make good engineers, and vice versa.” Accomplished in both fields, Petr has taught me so much about exploiting the beautiful synergies between math and physics. He has instilled in me the importance of building up intuition in the context of a simplified system, and only then searching for analytical elegance in a corresponding complexified system.
- The remaining members of my thesis committee: Profs. Themsis Sapsis and Steve Leeb. While their feedback and insights from our committee meetings have been invaluable to the progression of my research, even more so has been the simple knowledge that *they* would be the ones evaluating my work. Such knowledge helped ensure that the quality and integrity of my research methods would live up to their own standards. I thank them both for lending me their time, and for lending this thesis project their esteemed credibility.

- My other collaborators and co-authors, including Prof. Luca Schenato, Prof. Stefano Grivet-Talocia, Tommaso Bradde, Marco De Stefano, Dr. Dan Wu, Dr. Bin Wang, & Dr. Slava Maslennikov. I have learned so much from each of these persons, and many of their ideas and words echo throughout this corpus.
- The structures at MIT which have supported me and funded my research activities, including the MIT Energy Initiative, the Skoltech-MIT Next Generation Program, and the Graduate Association of Mechanical Engineers (GAME).
- My academic mentors and advisors at the University of Vermont (UVM), especially Profs. Paul Hines and Mads Almassalkhi. Both have encouraged my academic studies, inspired my curiosity, and supported me from afar. During fits of premature intractability, I have found comfort in a word of advice Paul often gave when advising me as an MS student: “*You cannot* solve a hard problem unless you can *first* solve a simple problem.”
- My friends, lab-mates and co-workers at (and around) MIT. This includes, but is certainly not limited to, Georgy Guryev, Donchan Lee, Essie Yu, Prof. Hung Nguyen, Katie Cavanagh, Dr. Ashkan Hosseinloo, Dr. Thanh Long Vu, Prof. Jerry Wang, Andrew Bouma, Colin Kelsall, Tom Cervantes and Sarah Southerland, Reed and Michelle Kopp, Dr. Mahraz and Shima Amini, and the GRTs and House Team members of East Campus, with a special thanks to Prof. Sandy Alexandre, whose leadership prowess is only surpassed by her relentless care for every single individual person in her flock (and, maybe, her unmatchable wordsmithing).
- My loving and extended Chevalier, Busch, Pinckney, McClintock, Dubie, Fyfe, Batchelder and McKenzie family. Most especially, my mom, Martha, whose Leonardo da Vinci-like curiosities and passions fuel her never-ending sense of wonder, and my Dad, Denis, whose hard work and vigor for life always inspire me to try harder and reach higher. Together, they have taught me to give glory to the Lord in all I do, and lean not on my own understanding. “But knowledge puffs up, while love builds up.” Also, my Uncle Mike Dubie, and a bit of often-considered advice he once gave me, which has helped anchor my confidence during times of seeming inadequacy: “Run *your* race.”
- Finally, and most importantly, my wife, Kay, whose endless love and care have been the ultimate container for my growth throughout my doctorate. Her faith, creativity, and selflessness inspire me daily, and I could never thank her enough for the support and friendship she provides.

# Contents

<b>1</b>	<b>Introduction and Motivation</b>	<b>29</b>
1.1	An Inverse Problem Framework for Data-Driven Control of MEPS . . . . .	31
1.2	Forced Oscillation Source Location . . . . .	33
1.3	Small-Signal Stability Standards for Microgrid Networks . . . . .	37
1.3.1	DC Microgrids . . . . .	37
1.3.2	AC Microgrids . . . . .	39
1.4	Real-Time Predictive Modeling of Low Frequency Power System Dynamics . . . . .	41
1.4.1	Generator Modeling . . . . .	42
1.4.2	Wide Area Monitoring . . . . .	43
1.4.3	Inadequacy of Existing Methods . . . . .	44
1.5	Probabilistic Power Flow and State Estimation in Electrical Distribution Networks . . . . .	46
1.5.1	Probabilistic Power Flow in Electrical Distribution Networks .	46
1.5.2	Probabilistic State Estimation in Electrical Distribution Networks	48
1.6	Thesis Contributions and Outline . . . . .	50
1.6.1	Contributions of this Thesis . . . . .	50
1.6.2	Thesis Outline . . . . .	54
<b>2</b>	<b>Locating the Sources of Low Frequency Forced Oscillations</b>	<b>55</b>
2.1	Mathematical Background . . . . .	55
2.1.1	Modeling the Forced Periodic Steady-State Response of LTI Systems . . . . .	55
2.1.2	Likelihood Function Modeling and Maximum A Posteriori (MAP) Estimation . . . . .	57
2.1.3	Dissipative and Positive Real Systems . . . . .	58
2.2	Using Effective Generator Impedance for FO Source Location . . . . .	60

2.2.1	Representing Generators as Admittance Functions . . . . .	60
2.2.2	Leveraging $\mathcal{Y}$ For Source Detection . . . . .	71
2.2.3	Defining a Practical Source Location Technique . . . . .	74
2.2.4	Test Results . . . . .	75
2.3	A Bayesian Approach to FO Source Location Given Uncertain Generator Parameters . . . . .	90
2.3.1	Problem Formulation . . . . .	91
2.3.2	Defining a Forced Oscillation Source Location Algorithm . . .	100
2.3.3	Test Results . . . . .	101
2.4	A Dissipativity Interpretation of Energy-Based FO Source Location Methods . . . . .	107
2.4.1	A DQR Interpretation of the DEF Method . . . . .	108
2.4.2	Deriving a “Perturbative” Network Model . . . . .	115
2.4.3	Practical Applications of the DQR Analysis . . . . .	127
2.4.4	Test Results . . . . .	133
<b>3</b>	<b>Decentralized Small-Signal Stability Certification Standards for Microgrid Networks</b>	<b>141</b>
3.1	Mathematical Background . . . . .	141
3.1.1	Constant Power DC Load Model . . . . .	142
3.1.2	Network Modeling for Small-Signal Stability Analysis . . .	143
3.1.3	Modeling Droop-Controlled Inverter-Based Components in AC Microgrids . . . . .	145
3.2	Stability Certificates for DC Microgrids . . . . .	148
3.2.1	From Centralized to Decentralized Stability Certificates . . .	148
3.2.2	Numerical Test Results . . . . .	154
3.2.3	Practical Applications to the Design and Operation of DC Microgrids . . . . .	160
3.3	Decentralized Small-Signal Stability Certificates for AC Microgrids .	161
3.3.1	Decentralized Stability of AC Microgrids . . . . .	161
3.3.2	Test Results: Droop-Controlled Microgrid . . . . .	164
3.3.3	Connecting AC Microgrid Decentralized Stability Certificates to Forced Oscillation Source Location . . . . .	166
<b>4</b>	<b>Vector Fitting Approaches for Real-Time Predictive Modeling of Low Frequency Power System Dynamics</b>	<b>169</b>

4.1	Mathematical Background . . . . .	169
4.1.1	Overview of the Time Domain Vector Fitting Algorithm . . . . .	169
4.1.2	The Overdetermined Modified Yule–Walker Method . . . . .	173
4.2	Handling Initial Conditions in Vector Fitting for Real Time Modeling of Power System Dynamics . . . . .	174
4.2.1	A New Problem Setting for TDVF . . . . .	174
4.2.2	Handling Initial Conditions . . . . .	175
4.2.3	The Real-Time Vector Fitting scheme . . . . .	178
4.2.4	Implementation . . . . .	179
4.2.5	Numerical Results . . . . .	181
4.3	The stochastic-RTVF Scheme . . . . .	188
4.3.1	Stochastic Process Characterization . . . . .	190
4.3.2	Formulating the sRTVF Procedure . . . . .	191
4.3.3	Illustrative Test Results . . . . .	199
<b>5</b>	<b>Accelerating Probabilistic Steady State Operational Analysis of Elec- trical Distribution Networks</b>	<b>201</b>
5.1	Mathematical Background . . . . .	201
5.1.1	Standard Network Model Statement . . . . .	201
5.1.2	The Power Flow Problem . . . . .	202
5.1.3	Standard Numerical Solution Technique for Power Flow . . . . .	203
5.1.4	Additional State Estimation Equations . . . . .	204
5.1.5	Power System State Estimation . . . . .	205
5.1.6	Numerical State Estimation Solution Techniques . . . . .	207
5.1.7	Neumann Series Expansion of a Perturbed Matrix . . . . .	208
5.1.8	Projection Based Model Order Reduction . . . . .	208
5.2	Accelerated Probabilistic Power Flow via Model Order Reduction and Neumann Expansion . . . . .	209
5.2.1	Computationally Efficient Power Flow Solution via Neumann Series Expansion . . . . .	209
5.2.2	Reduced Order Modeling of the Nonlinear Power Flow for Prob- abilistic Power Flow . . . . .	213
5.2.3	Test Results . . . . .	217
5.3	Accelerated Probabilistic State Estimation in Distribution Grids via Model Order Reduction . . . . .	223
5.3.1	Model Order Reduction of the State Estimation Problem . . . . .	223

5.3.2	Numerical Test Results . . . . .	228
<b>6</b>	<b>Conclusions and Future Work</b>	<b>231</b>
6.1	Concluding Remarks . . . . .	231
6.1.1	Forced Oscillations . . . . .	232
6.1.2	Microgrid Stability Certificates . . . . .	234
6.1.3	Predictive Modeling via Vector Fitting . . . . .	234
6.1.4	Distribution System Power Flow and State Estimation . . . . .	235
6.2	Future Work Extensions . . . . .	236
6.2.1	Identifying Effective Energy Functions: From Semidefinite Programming to Neural Networks . . . . .	236
6.2.2	Predictive Modeling of Weakly Nonlinear Systems: Embedding a Volterra Series inside Vector Fitting . . . . .	238
6.2.3	Representing the Estimation, Control and Performance of Distribution Grids as a Cascade of Nonlinear Maps . . . . .	240
<b>A</b>	<b>Forced Oscillation Modeling Tools</b>	<b>243</b>
A.1	Modeling Phase Shifting Transformers . . . . .	243
A.2	Polar to Cartesian Transformation Matrices . . . . .	244
A.3	Positive Realness: Admittance and Impedance . . . . .	244
A.4	DEF: A Power-Voltage Formulation . . . . .	245
A.5	Basis Matrices of the Classical Generator . . . . .	246
A.6	The Effects of Resistive Energy Injections from Transmission Networks	247
<b>B</b>	<b>Simulation Modeling Notes</b>	<b>249</b>
B.1	Modeling AC Power System Dynamics . . . . .	249
B.2	Initialization and Modeling of DC Microgrid Dynamics in the Time Domain . . . . .	255
<b>C</b>	<b>Dynamic Phasor Modeling</b>	<b>257</b>

# List of Figures

1-1	Contextualization of the inverse problems which are posed and solved in this thesis. As portrayed, the inverse problems are informed by a set of measured data and potentially some prior modeling information. The solver outputs a model characterization which is eventually used to create actionable information for a controller (human or automated). This controller then acts on the physical power system. The overall operational paradigm is an example of data-driven control. . . . .	32
1-2	Predictive modeling opportunities for system operators: closed loop generator systems (panel <b>(a)</b> on the right) and wide-area interconnections (panel <b>(b)</b> on the left). . . . .	42
1-3	Typical sampling-based methodology for solving PPF: load profile distributions are sampled, the corresponding sample is solved, and the results are passed to an uncertainty quantification tool. Random variable $\xi$ parameterizes the uncertainty. . . . .	48
2-1	$2^{\text{nd}}$ order generator tied to a network. Internal generator voltage $E'e^{j\delta}$ , terminal voltage $V_t e^{j\theta_t}$ , and swing bus voltage $V_s e^{j\theta_s}$ with $\theta_s = 0$ are all shown. . . . .	61
2-2	Panel <b>(a)</b> shows the steady state phasor $V_t e^{j\theta_t}$ and phasor deviation $\Delta \tilde{V}_t$ . Panel <b>(b)</b> expands deviation $\Delta \tilde{V}_t$ from panel <b>(a)</b> and decomposes the relationship between the rectangular deviations ( $\text{Re}(\Delta \tilde{V}_t)$ , $\text{Im}(\Delta \tilde{V}_t)$ ) and the corresponding polar deviations ( $\Delta V_t$ , $V_t \Delta \theta_t$ ). . . . .	63
2-3	A FO in the time domain shows up as a current injection source at the forcing frequency $\Omega_d$ (panel <b>(b)</b> ) when the system is transformed into the frequency domain ( $\mathcal{F}$ ). When $\Omega \neq \Omega_d$ , this current injection is absent (panel <b>(a)</b> ). . . . .	66
2-4	Orientation of the direct ( $d$ ) and quadrature ( $q$ ) axes. . . . .	67

2-5	Circuit diagram interpretation of equation (2.53), where $\mathcal{I}_\tau^d = -\gamma \frac{X'_d}{E'} \tilde{\tau}_m$ , $\mathcal{I}_E^d = \gamma \frac{V_t \sin(\varphi)}{E'} \tilde{E}'$ , and $\mathcal{I}_E^q = \frac{1}{X'_d} \tilde{E}'$ as taken from (2.55) and (2.56). At non-source buses, $\mathcal{I}_\tau^d = \mathcal{I}_E^d = \mathcal{I}_E^q = 0$ and all current flows are caused by terminal voltage deviations. . . . .	67
2-6	DAE modeled component tied to a larger power system. . . . .	68
2-7	Voltage excitation system associated with source bus #1 in subsection 2.2.4. The forced oscillation source is given by $G \sin(\Omega_d t)$ . . . . .	70
2-8	3 Bus Diagram with Infinite Bus. Both generators are 2 <sup>nd</sup> order, and a mechanically forced oscillation $\tau_m = \tau_0 + \tilde{\tau}$ is placed on generator 1. White noise is applied to the phase and magnitude of the infinite bus voltage. . . . .	76
2-9	Active power injection deviations for generators 1 and 2. . . . .	76
2-10	Spectral magnitude of current magnitude (panels (a) & (b)) and current phase (panels (c) & (d)) perturbations are given for each generator. The forcing frequency is located at $f_d = 0.32$ . The $\Delta$ symbol in panels (a) and (c) highlight the locations of significant deviations between the predicted and expected spectrums. . . . .	77
2-11	Actual and measured voltage magnitude at bus 70 (generator). . . . .	79
2-12	The spectral magnitude of the measured current magnitude (panel (a)) and the measured current phase (panel (b)) perturbations at generator bus 9 are given by the blue traces. The associated predicted spectral magnitudes are given by the black traces. Finally, the orange traces give the estimated maximum PMU measurement noise errors. . . . .	80
2-13	The prediction error $\ \tilde{\mathbf{I}}_p - \mathcal{Y}\tilde{\mathbf{V}}_p\ _2$ and the maximum measurement noise error $\Sigma_2$ associated with the non-source generator at bus 9 are plotted. Since there is no internal forced oscillation, prediction error is mostly caused by measurement error. Accordingly, the prediction error is bounded by the conservative maximum measurement noise error estimate $\Sigma_2$ . . . . .	80
2-14	The spectral magnitude of the measured current magnitude (panel (a)) and the measured current phase (panel (b)) perturbations at generator bus 4 are given by the blue traces. The associated predicted spectral magnitudes are given by the black traces. Finally, the orange traces give the estimated maximum PMU measurement noise errors. . . . .	81

2-15 The prediction error $\ \tilde{\mathbf{I}}_p - \mathcal{Y}\tilde{\mathbf{V}}_p\ _2$ and the maximum measurement noise error $\Sigma_2$ associated with the source generator at bus 4 are plotted. Since there is an internal forced oscillation at $f_d = 0.86$ Hz, the prediction error greatly exceeds the measurement noise error bound at this frequency. . . . .	81
2-16 The prediction error $\ \tilde{\mathbf{I}}_p - \mathcal{Y}\tilde{\mathbf{V}}_p\ _2$ and the maximum measurement noise error $\Sigma_2$ associated with the source generator at bus 13 are plotted. Since there is an internal forced oscillation at $f_d = 0.5$ Hz, the prediction error greatly exceeds the measurement noise error bound at this frequency. . . . .	82
2-17 The prediction error $\ \tilde{\mathbf{I}}_p - \mathcal{Y}\tilde{\mathbf{V}}_p\ _2$ and the maximum measurement noise error $\Sigma_2$ associated with the source generator at bus 65 are plotted. Since there is an internal forced oscillation at $f_d = 2.0$ Hz, the prediction error greatly exceeds the measurement noise error bound at this frequency. . . . .	82
2-18 The LSD is computed at each generator for $f_d = 0.5$ Hz (panel (a)), $f_d = 0.86$ Hz (panel (b)), and $f_d = 2.0$ Hz (panel (c)). At each frequency, the correct generator is located, despite strong PMU measurement noise. Generator index 1 corresponds to the generator at bus 4, generator index 5 corresponds to the generator at bus 13, and generator index 15 corresponds to the generator at bus 65. . . . .	83
2-19 The LSD is computed at each generator for $f_d = 0.5$ Hz (panel (a)), $f_d = 0.86$ Hz (panel (b)), and $f_d = 2.0$ Hz (panel (c)) over 100 trials to consider the impact of generator parameter uncertainty. . . . .	84
2-20 The voltage magnitude at buses 45 and 159 are plotted before, while, and briefly after the system experiences a fault. Measurement noise is not shown. . . . .	85
2-21 The prediction error $\ \tilde{\mathbf{I}}_p - \mathcal{Y}\tilde{\mathbf{V}}_p\ _2$ and the noise error bound $\Sigma_2$ associated with generator 45 are plotted for test case ND1. The prediction error slightly exceeds the noise error bound at $f = 1.41$ Hz. . . . .	85
2-22 The prediction error $\ \tilde{\mathbf{I}}_p - \mathcal{Y}\tilde{\mathbf{V}}_p\ _2$ and the noise error bound $\Sigma_2$ associated with generator 159 are plotted for test case ND1. The prediction error slightly exceeds the noise error bound at $f = 1.41$ Hz. . . . .	86
2-23 The maximum LSD, from $f = 1.38$ to $f = 1.42$ , is plotted for each generator. The maximum LSDs at generators 13 (bus 45) and 28 (bus 159) are slightly positive, but are still sufficiently small. . . . .	86

2-24 The voltage magnitude at buses 65 and 79 are plotted over 35 seconds. The natural mode frequency of 0.37 Hz, the forcing frequency of 0.40 Hz, and the resulting beat frequency can all be seen clearly. Measurement noise is not shown. . . . .	87
2-25 The prediction error $\ \tilde{\mathbf{I}}_p - \mathcal{Y}\tilde{\mathbf{V}}_p\ _2$ and the noise error bound $\Sigma_2$ associated with generator 65 are plotted for the test case where an underdamped natural mode is excited by a forced oscillation. Despite a strong oscillatory response from generator 65 at 0.37 Hz, the prediction error is entirely contained by the measurement noise error bound for all frequencies. . . . .	88
2-26 The prediction error $\ \tilde{\mathbf{I}}_p - \mathcal{Y}\tilde{\mathbf{V}}_p\ _2$ and the noise error bound $\Sigma_2$ associated with generator 79, the source bus, are plotted for the test case where an underdamped natural mode is excited by a forced oscillation. The prediction error violates the measurement noise error at $f = 0.4, 1.2, 2.0$ and $2.8$ Hz. . . . .	88
2-27 The LSD is computed at each generator across the full range of measured frequencies for the natural + forced oscillation test case. Only the largest LSD for each generator is plotted here, though. Generator index 18, which corresponds to the generator at bus 79, is correctly identified as the source generator. . . . .	88
2-28 3 bus system with two 2 <sup>nd</sup> order generators and a resistive load. Resistive Ornstein-Uhlenbeck noise is added to mimic system fluctuations.	89
2-29 The DEF is computed for lines {12}, {13}, and {32}. . . . .	89
2-30 The prediction error $\ \tilde{\mathbf{I}}_p - \mathcal{Y}\tilde{\mathbf{V}}_p\ _2$ (given as the Squared Spectral Magnitude (SSM)) and the noise error bound $\Sigma_2$ associated with generator 1 (panel (a)) and generator 2 (panel (b)) are given. . . . .	90
2-31 The modulus of the measured and predicted current magnitude $\tilde{\mathbf{I}}$ and current phase $\tilde{\phi}$ spectrums at a source generator are plotted in panels (a) and (b), respectively. At the forcing frequency of $f_d = 0.5$ Hz, the current injection magnitudes $ \mathcal{I}_I $ and $ \mathcal{I}_\phi $ can be seen as deviations from the predicted terminal current spectrum. . . . .	92
2-32 The frequencies between $\Omega_p = \Omega_d - \Omega_r$ and $\Omega_q = \Omega_d + \Omega_r$ represent the frequency range over which the FO has significant effect on the system. $\Omega_r$ is half the range over which the forcing frequency has effect. . . . .	96
2-33 Three 3 <sup>rd</sup> order generators (with AVR) are radially tied to an infinite bus with white noise. An FO is applied to generator 2's torque. . . . .	102

2-34 Shown are the measured ( $\tilde{\mathbf{I}}_p$ ) and predicted ( $\mathcal{Y}\tilde{\mathbf{V}}_p$ ) current magnitude ( $\tilde{\mathbf{I}}$ ) and current phase ( $\tilde{\phi}$ ) power spectral density (PSD) across a range of frequencies around the forcing frequency (0.5 Hz) before optimization has occurred. Panels (a) and (b) correspond to generator 1, panels (c) and (d) correspond to generator 2, and panels (e) and (f) correspond to generator 3. . . . .	103
2-35 Shown are the measured ( $\tilde{\mathbf{I}}_p$ ) and predicted ( $\mathcal{Y}\tilde{\mathbf{V}}_p$ ) current magnitude ( $\tilde{\mathbf{I}}$ ) and current phase ( $\tilde{\phi}$ ) power spectral density (PSD) around the forcing frequency (0.5 Hz) after stage 1 of the optimizer has been run. . . . .	104
2-36 Shown are the stage 2 current injection results, as quantified by (2.124). . . . .	104
2-37 The prediction error, as quantified by the percent difference in the measured and predicted currents in (2.125), are shown for the system forcing frequencies of 0.70 Hz in panel (a) and 0.86 Hz in panel (b). . . . .	105
2-38 The predicted current magnitude spectrum is plotted in panel (a) for generator 3 (located at bus 9) before stage 1 of the optimization procedure. The predicted current magnitude spectrum is replotted in panel (b) after stage 1 is completed. Generator 3 is not a FO source. . . . .	106
2-39 The predicted current magnitude spectrum is plotted in panel (a) for generator 15 (located at bus 65) before stage 1 of the optimization procedure. The predicted current magnitude spectrum is replotted in panel (b) after stage 1 is completed. Generator 65 is a FO source at 0.70 Hz. . . . .	107
2-40 Current injection magnitudes of (2.124) found by the optimizer in stage 2 at both forcing frequencies. . . . .	107
2-41 A generator (element 1), a constant impedance load (element 2), and a constant power load (element 3) are tied to an oscillating infinite bus. . . . .	114
2-42 Simulated DEFs associated with the generator, impedance, and constant power load from Fig. 2-41. Real voltage perturbations lead the phase of imaginary voltage perturbations at the infinite bus, and generator damping is positive. . . . .	114
2-43 Simulated DEFs associated with the generator, impedance, and constant power load from Fig. 2-41. Real voltage perturbations lag the phase of imaginary voltage perturbations at the infinite bus, and generator damping is slightly negative. . . . .	115

2-44 Panel <b>(a)</b> shows a model of the IEEE 39-bus power system in the time domain, where blue circles are generators, green arrows are loads, and an oscillation source is located in the upper left corner. Panel <b>(b)</b> shows the same system in the frequency domain, at $\Omega = \Omega_d$ , where loads, generators and sources have become admittances, and the oscillation source has been transformed into a current injection $\mathcal{I}$ , which excites the entire circuit. Accordingly, panel <b>(b)</b> is entirely <i>analogous</i> to an AC circuit in oscillatory steady-state excited by a single current injection source. . . . .	119
2-45 Plot of the eigenvalues of $\mathbf{M}\mathcal{Y} + (\mathbf{M}\mathcal{Y})^\dagger$ , where $\mathcal{Y}$ is associated with the dynamics of a droop-controlled inverter. For $\alpha = 0$ , the system is fully DQR since both eigenvalues are positive. . . . .	132
2-46 Dissipating power flow $P^*$ in the IEEE 39-bus power system for an applied FO of 2 Hz. All line resistance has been removed. Circles represent generators while rounded rectangles represent loads. Line thickness and arrow size represent dissipating power flow magnitude. . . . .	134
2-47 Dissipating power flow $P^*$ in the lossy IEEE 39-bus power system. The source of the FO cannot be located using the energy-based DEF method in this situation. . . . .	136
2-48 Shown are the generator frequency oscillations for all 29 system generators. Panel <b>(a)</b> shows 10s of time series data for when the FO is the only source of system excitation, and panel <b>(b)</b> shows 35s of time series data for when the FO and random load perturbations are both exciting the system. . . . .	138
2-49 Plotted are the current injection magnitudes of (2.218). The perturbative model (2.168) predicts nodal current balances with a high degree of accuracy. Non-source current injections are due to extraneous load perturbations. . . . .	138
2-50 Plotted are the dissipating power injections across all 29 generators. All injections are positive, indicating the positive dissipation of $P^*$ . Generators are listed in ascending order of corresponding bus number. Some magnitudes are too small to appear on the plot. . . . .	139
3-1 Definition of Small-Signal Load Model . . . . .	143

3-2	Shown are the real parts of the input admittance for a buck converter (blue), constant resistance load (green), and constant power load (orange). . . . .	143
3-3	Simple 2 bus DC microgrid network. The source, load, and line dynamics are represented by $Y_s(s)$ , $Y_l(s)$ , and $Y_t(s)$ , respectively. . . . .	144
3-4	Inverter connected to a grid node: $v_d$ and $v_q$ are small-signal variations of grid node voltage while $e_d$ and $e_q$ are variations of inverter terminal voltage. The combined coupling and virtual inductance and resistance are $L_c$ and $R_c$ respectively. . . . .	146
3-5	The shaded regions are the values that function $\phi(\omega, \alpha)$ can take, according to inequality (3.27), for a continuum of frequency and controller gain values. The grey sector corresponds to the line phase function (3.35), while the red sector corresponds to the load phase function (3.36). Loss of overlap between these shaded regions indicates the non-existence of function $\phi(\omega, \alpha)$ . . . . .	154
3-6	Meshed 8-bus microgrid with two stiff voltage sources and six loads. .	156
3-7	Plotted are the values that $\phi(\omega, \alpha)$ can take, according to (3.27), for a continuum of frequency and gain values. The grey sector corresponds to the line phase function (3.41), while the red sector corresponds to the load phase function (3.42), where $G_c(s)$ is a lead-lag controller. .	158
3-8	Eigenmode locus of the Fig. 3-6 microgrid via (3.43). All buck converters are outfitted with lead-lag controllers. Stability is never lost for $\alpha \leq 10$ . . . . .	158
3-9	Shown are the nodal voltage (panel (a)) and line current (panel (b)) dynamic responses for a 0.5V step change in supply voltage at source bus 5. Despite the large controller gain values associated with $\alpha = 10$ , system settling time is on the order of 10ms. . . . .	158
3-10	Plotted are the values that $\phi(\omega, \alpha)$ can take, according to (3.27), for a continuum of frequency and gain values. The grey sector corresponds to the line phase function (3.41), while the red sector corresponds to the load phase function (3.42), where $G_c(s)$ is a PI controller. . . . .	159
3-11	Eigenmode locus of the Fig. 3-6 microgrid via (3.43). All buck converters are outfitted with PI controllers. System stability is lost when $\alpha > 4.5$ . . . . .	159

3-12	Plotted are the eigenvalues associated with the matrix $(\mathbf{M}\mathcal{Y}_k\Gamma) + (\mathbf{M}\mathcal{Y}_k\Gamma)^\dagger$ , for both inverter and line admittances, across a continuum of frequency and gain values. In this trivial case, $\mathbf{M} = \Gamma = \mathbb{1}$ . Since inverter eigenvalues dip into the negative (i.e. lower red shaded) region, (3.50) cannot be satisfied. . . . .	166
3-13	Plotted are the eigenvalues associated with the matrix $(\mathbf{M}\mathcal{Y}_k\Gamma) + (\mathbf{M}\mathcal{Y}_k\Gamma)^\dagger$ , for both inverter and line admittances, across a continuum of frequency and gain values. In this non-trivial case, $\Gamma = \mathbb{1}$ , but $\mathbf{M}$ is set to (3.55). Since no eigenvalues dip into the negative (i.e. lower red shaded) region, (3.50) is satisfied. . . . .	167
4-1	Shown is the pole convergence procedure associated with TDVF. In this figure, $\mathbf{q} = [q_1, \dots, q_N]^T$ is the vector of poles from (4.8), $\mathbf{d} = [d_1, \dots, d_N]^T$ is the vector of denominator coefficients from the numerator of (4.8), $\mathbf{e} = [1, \dots, 1]^T$ is a vector of 1's, and $\lambda\{\cdot\}$ is the eigenvalue operator. . . . .	172
4-2	Shown is the pole convergence procedure associated with RTVF. In this figure, $\mathbf{q} = [q_1, \dots, q_N]^T$ is the vector of poles which become increasingly refined as the procedure iterates. . . . .	181
4-3	Time domain modeling results for a synthetic test case with $P = 2$ . The modeling window starts after 24 s, the validation window starts at 372 s. . . . .	182
4-4	Top panel: the trend of TD – SER and FD – SER against the SNR. Middle panel: corrupting one training input signal (solid line) with SNR=16 (a cloud of $R = 50$ different realizations are depicted in a grey shade). Bottom panel: response of a time domain model extracted from one noisy data realization (SNR=16) compared to the reference noise-free signal. . . . .	185
4-5	Shown is the interaction between the generator, its three controllers, and the network. The PMU collects data at the generator's point of connection. . . . .	186
4-6	Noise-free generator model extraction. Top panel: frequency domain validation of the generator model (order $N = 9$ ) against exact machine equations. Bottom panel: the time domain validation of the model against the current magnitude reference output. . . . .	187

4-7	Generator model training from noisy data (SNR = 32). Top panel: frequency responses. Middle panel: small signal current magnitude. Bottom panel: noise-corrupted input training signals (samples from a cloud of $R = 100$ different realizations depicted with a shade of grey).	189
4-8	Generator System with Observable Stochastic Input . . . . .	190
4-9	Shown is the pole convergence procedure associated with sRTVF. In this figure, $\mathbf{q} = [q_1, \dots, q_N]^T$ is the vector of poles which becomes increasingly refined as the procedure iterates. The green box performs the cross- and auto-correlation calculations from (4.87)-(4.88). . . . .	198
4-10	Shown are the true poles $p$ of the 10 <sup>th</sup> order synthetic system. Also shown are the surrogate poles identified by the sRTVF procedure. . . . .	199
4-11	Shown are both of the inputs concurrently applied to the synthetic system. Only the observable blue curve is used by the vector fitting algorithm. . . . .	199
4-12	The blue curve represents the data measured at the output terminal of the system. The dashed red curve was generated by feeding the measured input data into the identified sRTVF model and simulating forward in time. Clearly, there is a high degree of agreement between the measured output and the predicted output data. . . . .	200
4-13	Shown is a comparison between the true 10 <sup>th</sup> order FRF and the surrogate 5 <sup>th</sup> order FRF, as identified by the sRTVF procedure. . . . .	200
5-1	Contrasted are the traditional sampling-based Probabilistic Power Flow (PPF) (top panel), and the Accelerated Probabilistic Power Flow (APPF). In the APPF, a reduced modeler first attempts to solve power flow. If it fails, the full-order Neumann series solver is used. If the resulting solution isn't in the basis $\mathbb{V}$ , it is dynamically added, and the reduced model is updated. . . . .	217
5-2	Sampled active and reactive power input distributions (panels (a) and (b), respectively) for the 25 largest loads in the 8500-node network. .	220

5-3 PPF results from the 8500-node network. Panel <b>(a)</b> shows the range of output voltages across 1000 trials for each node (sorted for clarity.) Panel <b>(b)</b> shows a histogram of all $1000 \times 8531$ voltage magnitude points across all nodes, with an approximated black PDF curve plotted on top. Panel <b>(c)</b> shows a histogram of the current magnitudes flowing on the line connecting nodes 5724 and 8410; an approximated black PDF curve is plotted on top. . . . .	221
5-4 Shown is timing analysis for the traditional Newton-based PPF solver versus the APPF solver over the first 175 load profiles. Notably, the traditional PPF solver has a fairly constant solve speed, usually requiring two Newton iterations (although the locations of three iterations are marked in the upper right). At load profile $n_q = 37$ , the APPF stopped building $\mathbf{H}_c$ , which was becoming very time intensive. Between load profiles 38 and 60, the NSBPF and RMS worked together to continue building out the basis $\mathbb{V}$ and solving the system. After load profile 60, the RMS quickly solved the system on its own without the NSBPF, and no more basis expansion was needed. . . . .	221
5-5 Panel <b>(a)</b> shows the number of Newton iterations performed by traditional PPF for each new load profile vs. the number of Newton iterations taken by the NSBPF solver in the APPF. Panel <b>(b)</b> shows the number of iterations taken by the RMS inside the APPF. . . . .	222
5-6 Residual active and reactive power (panels <b>(a)</b> and <b>(b)</b> , respectively) at the 25 perturbed load buses in the 8500-node network <i>after</i> the RMS has converged. As $\mathbb{V}$ expands, the RMS is able to consistently drive the residual at each of these buses below the stopping criteria $\epsilon_N$ . . . . .	223
5-7 Plot of the singular values $\sigma$ of matrix $\mathbf{W} = [\mathbf{x}_1, \mathbf{x}_2, \dots, \mathbf{x}_{1000}]$ . . . . .	223
5-8 In the APSE algorithm, sampled measurement profiles are passed to the RMSE. If the results are of sufficient accuracy, the solver moves on to the next measurement profile. Otherwise, GNvQR solves the system. The resulting solution is then conditionally used to update basis $\mathbb{V}$ . . . . .	228
5-9 Map of the 8500-node network (LV distribution load buses not shown). The two measurement Uncertainty Regions (URs) are identified. In each of these URs, we identify 30 loads whose measurements are highly uncertain. . . . .	230

5-10 Shown are voltage magnitude (panel <b>(a)</b> ) and current magnitude (panel <b>(b)</b> ) histograms resulting from the 1000 solves of the 8500-node network.	230
5-11 Timing analysis of the full order solver (GNvQR), the APSE, and the RMSE. After measurement profile 186, the APSE is 4.5 times faster than the GNvQR procedure. The amount of time spent testing the RMSE solution via (5.70) dominates the APSE and is shown by the double-arrow. The expansion of $\hat{\mathbf{H}}$ concludes after measurement profile 50.	230
6-1 A depiction of a vector fitting procedure which has been embedded with a Volterra series representation of the underlying dynamical system. . . . .	239
6-2 Interaction between estimation, control, and performance processes in a distribution network. . . . .	241
6-3 Overlap between what can be observed through state estimation, what is needed for control, and what affects system performance. This diagram is overlaid on a “generalized” state space, since the state space region might refer to more than just the canonical nodal voltage “state” vector $\mathbf{x} = [\mathbf{V}^T, \boldsymbol{\theta}^T]^T$ . We note that in a practical system, some regions of overlap between these circles may be null. . . . .	241
B-1 Generator interacting with its controllers and the network. The (6 <sup>th</sup> order) generator + controller system has a total of 15 differential states, with time constants varying from 0.01s to 50s. . . . .	252
B-2 Automatic Voltage Regulator . . . . .	252
B-3 Power System Stabilizer . . . . .	253
B-4 Turbine Governor . . . . .	253



# List of Tables

1	Commonly Used Notation . . . . .	26
2	Commonly Used Acronyms . . . . .	28
2.1	Definition of LSD Terms from (2.83) . . . . .	74
2.2	Generator Parameters . . . . .	77
2.3	Eigenvalues of System with Droop-Controlled Inverters . . . . .	136
3.1	Converter, Controller, and Network Parameters . . . . .	156
3.2	Equilibrium DC Voltages of the Circuit in Fig. 3-6 . . . . .	156



# Mathematical Notation & Acronyms

In Table 1, we summarize the function and variable notation most commonly used in this thesis document. In order to engender consistency between chapters, the notation utilized in this document may at times slightly disagree with the notation used in associated academic publications.

In this thesis, column vectors  $\mathbf{a}, \mathbf{b}, \mathbf{c}, \dots, \mathbf{x}, \mathbf{y}$  are generally written using bold symbol notation, and matrices  $\mathbf{A}, \mathbf{B}, \mathbf{C}, \dots, \mathbf{X}, \mathbf{Y}, \mathbf{Z}$  are generally written using bold faced notation, although certain special matrices are not bold. Column vector functions ... $\mathbf{f}(\cdot), \mathbf{g}(\cdot), \mathbf{h}(\cdot)$ ... are generally written with bold faced notation.

Depending on the context,  $\tilde{x}$  may have refer to

1. a standard phasor (e.g.  $\tilde{V} = V e^{j\theta}$ ), commonly used in power system engineering, resulting from a quasi-stationary solution of the telegrapher equations;
2. a *dynamic* phasor (e.g.  $\tilde{V}(t) = \tilde{V}_{dq} e^{j\omega_0 t}$ ), commonly used in microgrid modeling;
3. a Laplace domain variable:  $\tilde{x}(s) = \mathcal{L}\{x(t)\}$ ;
4. a Fourier domain variable:  $\tilde{x}(\omega) = \mathcal{F}\{x(t)\}$ .

Furthermore, in the context of vector fitting, wide-tilde notation (e.g.  $\widetilde{\mathbf{X}}$ ) will be used to indicate deviation from some initial condition:  $\mathbf{X}(t) = \mathbf{X}(t_0) + \widetilde{\mathbf{X}}(t)$ .

Symbol(s)	Description
$\mathbf{A}, \mathbf{B}, \mathbf{C}, \dots, \mathbf{X}, \mathbf{Y}, \mathbf{Z}$	Matrices, generally (certain special matrices are not bold)
$\mathbf{a}, \mathbf{b}, \mathbf{c}, \dots, \mathbf{x}, \mathbf{y}, \mathbf{z}$	Column vectors of values, generally
$\dots \mathbf{f}(\cdot), \mathbf{g}(\cdot), \mathbf{h}(\cdot) \dots$	Column vectors of functions, generally
$\text{diag}\{\cdot\}$	Diagonalization operator, mapping a vector to a matrix
$\det\{\cdot\}$	Determinant operator
$E\{\cdot\}$	Expected value operator
$E$	Signed nodal incidence matrix
$\mathcal{F}\{\cdot\}$	Fourier transform operator
$\text{fft}\{\cdot\}$	Fast Fourier Transform operator
$\Gamma, \mathbf{M}$	Transformation matrices: $\Gamma, \mathbf{M} \in \mathbb{R}^{2 \times 2}$

$\odot$	Hadamard product
$\mathbf{I}$	Vector of current magnitudes (AC) or currents (DC)
$\phi$	Vector of nodal current injection phase angles
$\tilde{\mathbf{I}}$	Vector of complex nodal currents: $\tilde{\mathbf{I}} = \mathbf{I}e^{j\phi}$
$\tilde{\mathbf{I}}(s)$	Vector of frequency domain current perturbations
$i, j, k$	Used for indices
$j$	Imaginary unit, where $j = \sqrt{-1}$
$\otimes$	Kronecker product
$\mathcal{L}\{\cdot\}$	Laplace transform operator
$\lambda\{\cdot\}$	Eigenvalue operator
$\Omega, \omega$	Angular frequency variables
$R_{x,y}(\delta t)$	Cross-correlation of signals $x$ and $y$ with $\delta t$ time shift
$\text{Re}\{\cdot\} = \{\cdot\}_r$	Real part operator
$\text{Im}\{\cdot\} = \{\cdot\}_i$	Imaginary part operator
$\sum$	Summation
$\Sigma$	Covariance matrix
$s$	Laplace domain complex frequency variable: $s = \sigma + j\omega$
$\text{svd}\{\cdot\}$	Singular Value Decomposition operator
$\{\cdot\}^T$	Transposition operator
$\{\cdot\}^\dagger$	Hermitian transposition operator
$\{\cdot\}^*$	Complex conjugation operator
$\mathbb{V}$	Projection subspace for model order reduction
$\mathbf{V}$	Vector of voltage magnitudes (AC) or voltages (DC)
$\theta$	Vector of nodal voltage phase angles
$\tilde{\mathbf{V}}$	Vector of complex nodal voltages: $\tilde{\mathbf{V}} = \mathbf{V}e^{j\theta}$
$\tilde{\mathbf{V}}(s)$	Vector of frequency domain voltage perturbations
$Y_b$	Nodal admittance (“Y-bus”) matrix: $Y_b = E^T Y_l E + Y_s$
$Y_l$	Diagonal line admittance matrix
$Y_s$	Diagonal shunt admittance matrix
$\mathcal{Y}(s), \mathcal{Y}(\omega)$	Admittance of AC grid components, in $s$ and $\omega$ domains
$\mathbb{1}$	Identity matrix of appropriate size

Table 1: Commonly Used Notation

In Table 2, we summarize the acronyms most commonly used in this thesis document. The bolded acronyms are used especially often.

<b>Acronym</b>	<b>Description</b>
<b>AC/DC</b>	<b>Alternating Current/Direct Current</b>
APPF	Accelerated Probabilistic Power Flow
APSE	Accelerated Probabilistic State Estimation
AVR	Automatic Voltage Regulator
AWG	Additive White Gaussian
<b>DEF</b>	<b>Dissipating Energy Flow</b>
<b>DQR</b>	<b>Dissipative with respect to Quadratic supply Rate</b>
DSE	Dynamic Subspace Expansion
DWE	Dynamic Ward Equivalent
GNvQR	Gauss-Newton via QR-factorization
<b>FO</b>	<b>Forced Oscillation</b>
<b>FRF</b>	<b>Frequency Response Function</b>
FDVF	Frequency Domain Vector Fitting
ISONE	Independent System Operator of New England
L(R)HS	Left (Right) Hand Side
LSD	Local Spectral Deviation
LTI	Linear Time Invariant
MAP	Maximum A Posteriori
MEPS	Modern Electric Power Systems
<b>M(S)IM(S)O</b>	<b>Multi (Single) Input - Multi (Single) Output</b>
M(k)W	Mega (kilo) Watt
MOR	Model Order Reduction
NSBPF	Neumann Series Based Power Flow
OU	Ornstein-Uhlenbeck
<b>PMU</b>	<b>Phasor Measurement Unit</b>
<b>PPF</b>	<b>Probabilistic Power Flow</b>
PSS	Power System Stabilizer
RMS	Reduced Model Solver or Root Mean Square
<b>ROM</b>	<b>Reduced Order Model</b>
RMSE	Reduced Model State Estimator
<b>RTVF</b>	<b>Real-Time Vector Fitting</b>
RWNP	Relaxed White Noise Process

SER	Signal to Error Ratio
SNR	Signal to Noise Ratio
sRTVF	stochastic-Real-Time Vector Fitting
<b>TDVF</b>	<b>Time Domain Vector Fitting</b>
TVE	Total Vectro Error
VF	Vector Fitting
WECC	Western Electricity Coordinating Council
ZIP	Constant Impedance(Z)-Current(I)-Power(P) Load Model

Table 2: Commonly Used Acronyms

# Chapter 1

## Introduction and Motivation

Modern electric power systems (MEPS) are an engineering marvel, representing over 140 years of incremental advancement in design, construction, and operation. In order to keep pace with the technological advances and social-ecological challenges of each new generation, these systems require continual updating and modernization. This task is made all the more challenging due to the fact that MEPS operate on highly disparate timescales; such timescales range from the microsecond effects of electromagnetic transients and power electronic switching to the decade-scale timelines associated with expansion planning and generation capacity procurement [105].

Over the last two decades, a variety of factors have lead to the severe disruption of MEPS' conventional operating paradigm. The primary factors contributing to this disruption include the following:

- a dramatic increase in grid-scale renewable energy penetration and a corresponding decrease in traditional fossil-fuel based generation [103, 127];
- the advent of new Smart Grid technologies [173];
- the increased popularity and reliance on microgrid systems [172, 83];
- the increasing electrification of the transportation sector [20, 97];
- and the distributed energy resources (DERs) which allow traditional consumers to act as “pro-sumers” [70, 173].

Although each of these factors represents an opportunity for enhancing the efficacy and sustainability of MEPS, they also represent new challenges associated with maintaining system *stability*. The term stability is often used loosely in the literature, but the IEEE/CIGRE Joint Task Force on Stability Terms and Definitions indicates that

power system stability refers to “the continuance of intact operation following a disturbance” [104]. The disturbance type may range anywhere from typical ambient load switching to a severe line fault.

Despite the new stability-related challenges, the roll-out of new Smart Grid technologies is accompanied by new opportunities for system operators to significantly enhance system stability. In particular, the deployment of Phasor Measurement Units (PMUs) [141], micro-PMUs ( $\mu$ -PMUs) [181] and Advanced Metering Infrastructure (AMI) [136] are increasing system observability in considerable ways. PMUs are devices which can provide time synchronized measurements of a variety of grid signals at high sample rates (30 to 60 Hz); these measurements are aggregated at Phasor Data Concentrators (PDCs) [45] and then relayed back to the system operators in near real-time. Typically, PMUs are capable of measuring voltage and current phasors (magnitude and phase), frequency and rate of change of frequency. Active and reactive power flows and injections are computed directly from the voltage and current data. While PMUs have seen widespread deployment in power systems for almost a decade now, actual real-time uses of these data stream are only now emerging. One newly celebrated example is the real-time control of the so-called Pacific DC Intertie (PDCI) line in the Western United States. As described in [142], the project uses real-time PMU data to perform active power modulation (up to  $\pm 125$  MW) on the intertie line in order to increase the damping ratio associated with a poorly damped system mode. On average, only 82ms lapse between the time when the PMU time-stamps the data and when the closed loop feedback controller (which is located hundreds of miles away) performs modulation of active power. Such control would never be possible without synchrophasors.

While PMUs are typically located at high voltage transmission substations,  $\mu$ -PMUs are placed at distribution feeders and, potentially, throughout the distribution network. Due to smaller phase angle differences between nodes and the higher degree of process noise (load switching),  $\mu$ -PMUs are engineered to have a higher accuracy than transmission grade PMUs [181]. AMI is defined as the “integrated system of smart meters, communications networks, and data management systems that enables two-way communication between utilities and customers” by the DOE [136]. The smart meter devices measure load usage at the customer interface. They are typically capable of relaying active and reactive power usage along with voltage magnitude, current magnitude and basic power quality data back to utilities in 5, 15, 30, or 60 minute intervals. As of 2018, approximately 86.8 million smart meters had been installed across the US [6].

## 1.1 An Inverse Problem Framework for Data-Driven Control of MEPS

The massive amounts of real-time data being generated by PMUs,  $\mu$ -PMUs and smart meters not only provide direct observability of previously unobservable system facets, but they also allow for the formulation of previously unimagined *inverse problems*. In formulating an inverse problem, the inherent objective is to reconstruct some aspects of the particular “model”<sup>1</sup> which generated some set of observed measurements [86, 88]. Much of this thesis focuses on formulating inverse problems which exploit these newly available measurement data sets in new ways. The ultimate purpose of posing and solving these inverse problems is to transform potentially unused data streams into, so-called, *actionable information*. Such information can allow system operators to make dispatch and control decisions which enhance the stability of the network. The relationship between the contributions of this thesis and the eventual derivation of this actionable information (as used by a controller) are graphically portrayed in Fig. 1-1. At a high level, this operational paradigm can be considered a sort of data-driven control [28] procedure, since control decisions are based on the continual identification or characterization of the plant model. If deployed properly, this control can have a stabilizing effect on the system. Such control strategies, though, ultimately hinge on the ability of an inverse problem solver to identify useful<sup>2</sup> system models.

The central premise of this thesis is that *inference*, *estimation*, and *prediction* strategies can be applied to characterize useful power system models.

The resulting models can be used, as in Fig. 1-1, to potentially enhance the stability of MEPS. As shown in this figure, though, this thesis focuses exclusively on model characterization; accordingly, performing analysis on the derived models to extract actionable information or develop control strategies is beyond the scope of this thesis.

While a useful construct in general, the data-driven control of Fig. 1-1 faces a number of practical challenges, many of which will be reviewed as specific problems are introduced later in this chapter. Motivated by the overarching application of data-driven control, though, the following sections of this chapter introduce four fundamental problems emerging in MEPS. The first, third, and fourth problems can

---

<sup>1</sup>While inverse problems are often concerned with physical (i.e. physics-based) model reconstruction, parts of this thesis will also consider surrogate, or “black-box”, models as well.

<sup>2</sup>The term “useful” is defined relative to the application (i.e. data-driven control from Fig. 1-1) and the ultimate goal of the application (i.e. power system stability).

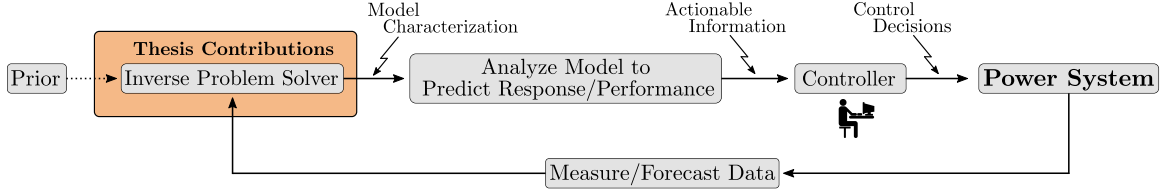


Figure 1-1: Contextualization of the inverse problems which are posed and solved in this thesis. As portrayed, the inverse problems are informed by a set of measured data and potentially some prior modeling information. The solver outputs a model characterization which is eventually used to create actionable information for a controller (human or automated). This controller then acts on the physical power system. The overall operational paradigm is an example of data-driven control.

be classified as inverse problems which fit neatly into the framework presented by Fig. 1-1, while the second problem is more suitable for operational planning rather than real-time operation.

- In Section 1.2, we introduce the problem of **locating** the sources of low frequency forced oscillations in transmission systems, given measured PMU data from throughout the network.
- In Section 1.3, we introduce the problem of **identifying** a family of rotational functions which guarantee small-signal stability for microgrid networks. The resulting contributions of this chapter are theoretical in nature, rather than algorithmic (as they are in the other chapters).
- In Section 1.4, we introduce the problem of **inferring** a non-unique set of surrogate model parameters for real-time predictive modeling of power system dynamics, given measured PMU data from the terminals of a system element.
- In Section 1.5, we introduce the problem of **estimating** the probabilistic operational state of an electrical distribution system network, given measured (in the case of probabilistic state estimation) or forecasted (in the case of probabilistic power flow) data about the loads in the network.

For each of the posed problems, a corresponding literature review is provided, and the potential impacts of the problem are outlined. Finally, in Section 1.6, we provide a brief outline of the remainder of this thesis document.

## 1.2 Forced Oscillation Source Location

With the recent widespread deployment of PMUs across the US transmission grid [5], system operators are becoming keenly aware of the pervasive presence of low frequency oscillations. Generally, low frequency oscillations are either due to natural modes, attributed to poorly tuned control settings and large power flows across weak tie lines, or forced oscillations (FOs), which are caused by extraneous disturbances. FOs generally refer to a system’s response to an external periodic disturbance [67]. Such external inputs may be related to a broad range of causes [3, 67], such as faulty controllers, turbine vibrations, or cyclical loads [180, 155, 199]. A new report [116] published by the Independent System Operator of New England (ISONE) highlights several recent causes of FOs observed in their 345kV transmission network:

- On January 11<sup>th</sup> of 2019, a 0.25 Hz oscillation of up to 50 MW (peak-to-peak) was observed in the ISONE network for 17 minutes. The cause was a faulty power-imbalance controller in a combined cycle power plant in Florida (more than 1000 miles away). Since the oscillation frequency was close to a resonant mode, oscillations of up to 200 MW were observed across the entire Eastern Interconnect.
- On April 7<sup>th</sup> of 2019, a 0.1 Hz oscillation, 5 MW in magnitude, was observed in the ISONE network for 10 minutes. A large combined cycle generator in the ISONE system was eventually identified as the source, and the FO was deemed to be caused by a “pin hole in the primary gas inlet pressure regulator boot of the upstream gas pressure regulator.”
- From January 11<sup>th</sup> through the 20<sup>th</sup> of 2020, a 0.2 Hz oscillation appeared numerous times in the ISONE network, having a magnitude of around 10 MW. The source of the FO was a large generator in the New Brunswick region. Remarkably, subsequent investigations determined that the oscillations in the generator were caused by a change in the quality of the natural gas that was used to fuel the generator. Prior to January 11<sup>th</sup>, the supply source had switched to an offshore gas field. In the end, turbine governor control was to blame: “Governor control was optimized for regular gas quality but became suboptimal for the new gas causing oscillations when the generator was operating in the 135-140 MW output range.”

The existence of FOs reduces the quality of electric power and has potential detrimental effects on various equipment [157, 180]. One of the most severe examples in

modern times of the potential devastating effects of oscillations in MEPS was an incident at the Sayano-Shushenskaya hydro power in 2009 [106]. This incident was ultimately caused by fatigue failure of the turbine cover of one of the generators, and the ensuing disaster lead to the death of 75 people and a massive blackout. Before the mechanical vibrations of the rotor caused the generator to effectively explode, there were long periods of low frequency vibrations ( $\leq 1.5$  Hz), as recorded by local seismic station sensors. If such low frequency oscillations could be sensed by power grid operators and responded to in real time, future incidents similar to Sayano-Shushenskaya could, at least potentially, be avoided.

Whenever a disturbance occurs at the frequencies close to one of the natural system modes, a resonance condition may lead to significant amplification of the oscillation source amplitude; thus, a relatively small perturbation on one bus can cause rather large power swings in different locations around the system. A classical example of this effect is the 2005 WECC disturbance, where a reasonably small 20 MW oscillation at the Nova Joffre co-generation power plant in Canada resonated with one of the WECC's main inter-area modes. This resulted in a 200 MW power oscillation on the Oregon-California intertie [157].

Accordingly, there is a need in the MEPS community for the development of methods which are capable of using on-line PMU data to trace the source of a FO. Locating the sources of FOs remains a challenging task due to their sporadic nature, speed of propagation, and inability to be predicted by the system operators' dynamical models (i.e. FOs are extraneous in nature, so they cannot be predicted *a priori*). Across academia and industry, it is an accepted fact that designing control methods for the specific purpose of damping forced oscillations is impractical [122], since FOs are inherently problematic and should be dealt with at their sources<sup>3</sup>. Instead of closed loop control, disconnection of the identified source with subsequent investigation of the cause of the disturbance is the universally accepted solution to the problem. Before applying any source location procedure, though, the type of observed disturbance has to first be classified. To differentiate between FOs and other types of disturbances, a method based on statistical signatures of different types of oscillations was proposed in [188]. Similarly, [135] uses spectral analysis of PMU data to “trigger” a FO warning. The authors then suggest using statistical tools (pattern mining and maximal variance ratios) from on-line generator SCADA data to determine the oscillation source. If oscillation magnitudes are low and signal noise is high,

---

<sup>3</sup>The previously mentioned PDCI controller has actually been found to somewhat effectively damp FOs, as reported in [190], although this is not the intended purpose of the controller.

[209] proposes using the self-coherence spectrum of a PMU signal and its time shifted version to perform FO detection/classification.

A variety of source identification techniques have been developed with varying levels of success [29, 7, 135, 10, 123, 39, 38]; many are outlined in a recent literature survey [185], where the main requirements for such methods are also stated. A set of test cases for validating different source location methods is presented in [117]. These cases were developed in coordination with IEEE Task Force on Forced Oscillations, and they allow for a standardized examination of all source detection algorithms. In [10], phase coherency is used to identify groups of generators which swing together. The source is identified as the generator in the source group which is providing the smallest contribution to the overall damping. This will correspond to the generator whose rotor oscillation phase is leading all other source group rotor oscillation phases. In [29], eigenvalue decomposition of the linearized system's state matrix is used in conjunction with the FO's measured characteristics to perform source location identification. The authors of [125] employ machine learning techniques, via multivariate time series analysis, to perform source identification; all off-line classifier training is based on simulated data. A fully data driven method, which employs convex relaxation to optimally locate sparse FO sources, is introduced in [92]. Due to the characteristically narrow bandwidth of FOs, other authors have embraced frequency domain techniques. In [7], the pseudo-inverse of a set of system transfer functions are multiplied by a vector of PMU measurements to yield a FO solution vector.

An important class of source location methods, which are termed the hybrid methods in [185], leverage both a known system model and measured PMU data. Demonstrated in [194] and [114], these methods use measured PMU signals as inputs for a power system model. After simulating this model, the time domain model outputs are compared with their corresponding measured PMU signals. Significant deviation between the model predictions and the PMU measurements may indicate the presence of a FO. These types of “playback” methods are also used for model validation. Model based source location algorithms incorporate the unfortunate drawback of solution accuracy being constrained by the accuracy of the model parameters used in the analysis. Purely data driven approaches, on the other hand, do not leverage known system structure and dynamics. Others have applied Bayesian analysis to MEPS in past. For example, [22] used a Bayesian particle filter for power plant parameter estimation, and [140] solved a maximum a posteriori (MAP) optimization problem in the time domain to perform system parameter identification.

Of the many source location techniques currently available in the academic marketplace, the so-called Dissipating Energy Flow (DEF) method has enjoyed some of the most successful testing results, both in simulation environments [122] and in real-time applications [121] in the ISONE and WECC networks. The method was originally developed by Chen et al. [35] as the Transient Energy Flow method, but its underlying mathematics leverage the Lyapunov functions from [177]. The DEF method, which was developed under the assumptions of a lossless network and constant power loads, tracks the system-wide flow of so-called “dissipating energy” in order to locate the FO source. One of the main advantages of this method is that it tracks the dissipating energy flow in all lines where PMU data is available, thus being naturally model independent.

The primary challenge to reliable DEF performance is the contribution of dissipating energy from non-FO sources, such as lossy transmission lines, lossy or negatively damped loads, and generator dynamics dominated by non-passive controllers. This phenomena has been evidenced in simulation [38] and in real application at ISONE. An actual example of this contribution may be found in Fig. 1 of [40]. If these contributions are large enough, the FO source can appear to be a dissipating energy sink and the DEF method can fail. Despite its inadequacies, the DEF’s excellent performance in real-time application at ISO New England strongly implies that further research should be performed in order to more systematically characterize the method. Shortcomings of the DEF method have been analyzed in [36], and [40] has recommended using passivity theory to interpret the method from a new mathematical perspective, but no theoretical methods have been devised for testing how the DEF method will perform in an arbitrary network. Such testing is essential in order to ensure that the DEF can perform adequately in new environments, such as in microgrids where “R/X” line ratios are high and voltage control is fast, or in networks that have particularly resistive load pockets. To make such predictions, a systematic framework is needed in order to thoroughly study the DEF.

Due to the plethora of challenges associated with locating the sources of FOs in real-time, and in the context of the provided literature review, we offer the following conclusions which guide the FO-related research in this thesis

- The MEPS community needs a more systematic approach to analyzing, properly characterizing, and reliably locating the sources of FOs.
- Due to the quickly emerging changes of MEPS, methods which perform these tasks and do not heavily rely on strong modeling assumptions (especially ones

which were more justifiable in the context of classical grid architecture), but do leverage known physics-based modeling priors, are of particular value.

- Furthermore, due to the ubiquity of energy-based FO source location methods which are currently being used by ISOs, methodologies which can predict the conditions under which energy-based source location methods will succeed or fail are needed.

## 1.3 Small-Signal Stability Standards for Microgrid Networks

In academia, industry, and defense, microgrids are becoming an increasingly popular topic [107]. According to the DOE, a Microgrid may be defined as [172]

a group of interconnected loads and distributed energy resources within clearly defined electrical boundaries that acts as a single controllable entity with respect to the grid. A microgrid can connect and disconnect from the grid to enable it to operate in both grid-connected or islandmode.

Advances in power electronic technologies have lead to a significant decrease in renewable energy generation costs: this has inspired discussions about splitting certain existing distribution grids into autonomous systems. Subsequently, there has been significant progress in the development of control architectures for power electronics-interfaced generation, further allowing for flexible microgrid operation [146, 208]. In the following two subsections, both DC and AC microgrid stability-related research is reviewed.

### 1.3.1 DC Microgrids

Recent advances in power electronics technologies and the general trend towards renewable energy sources have lead to increased interest in DC grids [145, 98]. Small-scale DC microgirds have been in use for several decades already, mainly as autonomous electric systems on board of vehicles [56]. As such, the configuration of these microgrids was fixed and well planned for the exact operating conditions which were known in advance. On the other hand, DC microgrids with an “open” structure, capable of being expanded and reconfigured while remaining stable for a broad range of loading conditions, have mostly been out of the scope of academic research. In

part, this is justified by the fact that, currently, the majority of microgrids are using an AC interface for power distribution, even if all the sources and loads are naturally DC. However, fully DC microgrids can become an economically feasible solution for supplying power in remote communities.

Unlike in AC grids where a substantial part of the load is of the electro-mechanical type, loads in DC grids are mostly represented by power electronics converters with tight controls to achieve flat voltage at their outputs [58]. This leads to a constant power load (CPL) behavior on the input within the control loop bandwidth, which is regarded to be one of the main sources of instabilities in DC grids. The origin of the instability is often related to the, so-called, negative incremental resistance introduced by CPL; a number of methods for stability assessment are based on such representation. Recent reviews [170, 153] present a comprehensive classification of the existing stability criteria and stabilization methods for DC grids.

Recently, the problem of stability assessment for CPL-based microgrids has attracted substantial attention from the controls community [156, 168, 207, 16, 43]. Previous works on the subject [18, 94, 32] have demonstrated that the problem of linear and transient stability of DC microgrids with CPL can be addressed using Brayton-Moser mixed potential approach [26, 96]. However, stability conditions derived under the conservative CPL modeling assumption may lead to excessive constraints on network configuration and installed equipment, and they neglect the complex dynamical behaviour of the controllers which regulate these loads. In reality, regulated power converters act similar to CPL only within their control loop bandwidth [151]. Accordingly, methods which explicitly account for the finite bandwidth of load controllers can potentially provide less restrictive stability conditions. However, dealing with load models that are more complex than a simple CPL requires development of rather specific techniques.

Traditionally, the power electronics community has relied on a number of different impedance based stability conditions. Most of them consider the minor loop gain, which is the ratio of the source output impedance to the load input impedance. The celebrated Middlebrook criterion [126], originally proposed for input filter design, is based on a small-gain condition for minor loop gain, demanding its absolute value to be less than unity for all frequencies. While a rather conservative method, it only requires knowledge of the absolute values of impedances over the whole frequency range. A less conservative Gain-Margin Phase-Margin criterion [191] allows the Nyquist plot of the minor loop gain to leave the unit circle provided there is a sufficient phase margin. Another method - the opposing argument criterion - is based on conditions

imposed on the real part of the minor loop gain [62]. The main advantage of this method is that it can be applied to multi-load systems, since the contributions from each individual load can now be simply added together. Finally, the least conservative methods are based on the so-called energy source consortium analysis (ESCA) [176] and the similar root exponential stability criterion (RESC) [175]. Both offer the smallest forbidden region for the minor loop gain of all the existing methods.

Most of the described stability assessment methods are primarily concerned with single-source single-load systems and a possible destabilizing interaction between the impedances of corresponding components. Under certain conditions, it could be possible to generalize some of these methods by attributing network components to either loads or sources and changing the corresponding effective impedance. In all the cases, the explicit knowledge of both the models of all the system components and the network configuration are required to perform the stability assessment. However, in the case of the aforementioned “open structure” DC grids, not all of the parameters can be exactly known. Moreover, running a separate stability test upon every grid reconfiguration can be practically infeasible. Thus, there is the need for stability assessment methods that can be realized under limited knowledge about the system parameters and/or configuration. In this thesis, we have made a step towards offering a “plug-and-play” approach for DC grids, where certain general criteria can be issued for both loads and network elements that can guarantee stable operation of the full system under arbitrary grid configurations. To achieve this end, we develop a specialized procedure that allows for the overall system stability assessment to be reduced to a separate consideration for individual load and line impedances, thus resulting in completely decentralized stability criteria.

### 1.3.2 AC Microgrids

It was quickly realized that control methods which were standard for large scale AC MEPS have rather limited applications in microgrids due to differing stability constraints [17]. Moreover, modelling approaches (e.g. modelling based on time-scale separation) routinely used for conventional MEPS appeared to be inadequate for microgrids, which demand new modeling techniques [134]. Due to the characteristic differences between large scale conventional power grids and microgrids, new approaches and methodologies are necessary for certifying microgrid stability. Relevant stability definitions and state of the art methodologies for AC microgrids are reviewed in [60] by the IEEE Task Force on Microgrid Stability Definitions, Analysis, and Modeling.

It is generally possible to employ full-scale dynamic modeling for stability analysis of microgrids, directly calculating the eigenvalues of the state matrix for any specific operating point. This is done in [17], where the stability of a droop control dominated microgrid is analyzed via root locus. However, such an approach assumes the full knowledge of system configuration which is much less likely for a microgrid than for a conventional MEPS. Certifying the stability of microgrid systems can be challenging due to the lack of information on exact values of system parameters. Moreover, performing full-scale stability analysis for every possible microgrid configuration is most likely economically, technically, and numerically inconvenient. Authors in [184] developed a low-dimensional model for inverter-based microgrids which allowed for the pinpointing of the main sources of instabilities and paved the way towards development of completely decentralized interconnection rules for such systems. However, the methods still rely on rather specific dynamic models of system components (namely, droop-controlled inverters) and assumed at least partial knowledge about the system configuration. Moreover, stability certificates formulated in [183], while being decentralized, depend not only on the settings of the system components, but also on their interconnection.

The celebrated concept of *dissipative* dynamic systems [192, 193] allows for formulation of stability certificates for an entire system through the separate consideration of its components: if every component of the system is dissipative, then the whole system is also dissipative, and therefore stable, irrespective of the way components are interconnected. Specific forms of dissipativity [1] have allowed the formulation of rather simple, although not always easily realisable, constraints on input admittances of power system components [154, 81, 82]. The advantage of such an approach is that input admittances of individual components do not have to be known from a model, but can simply be measured. However, it is not straightforward to apply the method to components that are not dissipative and cannot be made so by simple adjustments of their control settings. Researchers have advocated for a passivity-based approach for microgrid stability certification. In [202], an active stabilization (control) strategy was proposed which would enforce passive terminal behaviour of all interface controllers. Once engineered to behave passively, the system was guaranteed to be stable for an arbitrary interconnection of converters. The robustness of such passivity-based control laws was analyzed in [14].

There is, therefore, the need for simple but reliable stability certificates that can be routinely used for a wide class of AC microgrid configurations. In an ideal operating paradigm, standards could be developed for typical microgrid components that

will allow stable operation under arbitrary interconnections. Such a system would provide a significant step towards realizing the so-called “plug-and-play” operation of a microgrid [53].

## 1.4 Real-Time Predictive Modeling of Low Frequency Power System Dynamics

Due to the aggressive deployment of Wide Area Monitoring Systems (WAMS), a deluge of time series data streams are emerging from modernizing smart grids. For instance, as of 2017, Operating Procedure No. 22 specifies that all generation above 100MW in the ISO New England system must provide Phase Measuring Unit (PMU) observability at the point of interconnection [178]. Similarly, the 2018 Nodal Operating Guide specifies that all new generators above 20MVA in the ERCOT (Texas) system must provide PMU observability [57]. In order to both capitalize on these data streams and enforce effective dynamic security assessment (DSA) in the face of a rapidly modernizing energy landscape, the North American Electric Reliability Corporation (NERC) recently implemented the so-called MOD-033-1 directive in July of 2017 [150]. Not only does “MOD33” mandate the continual development of static and dynamic network planning models, but it also requires that the simulated response of these models be compared to actual time series data collected in the network to validate their accuracy [9]. Associated procedures must also resolve model prediction aberrations. Traditional “staged” testing of generator models can be costly and inconvenient, because the generator must go offline [109]. Thus, performing model tuning and validation online is particularly valuable.

In this thesis, we use the phrase “predictive modeling” to generally refer to the procedure of using PMU data to construct an input/output model of some underlying dynamics; this model can then be used to predict future input/output behavior of the system. Naturally, “real-time predictive modeling” refers to performing the modeling online, i.e. in real time. In the MEPS literature, there exist two salient applications of real-time predictive modeling: (i) individual generator<sup>4</sup> monitoring, and (ii) wide-area modeling. Both of these situations, for example, are showcased in Fig. 1-2. In this figure, we present the hypothetical perspective of a system operator, ISONE. Panel (a) on the right shows a connection to an individual generator inside the ISONE

---

<sup>4</sup>Predictive monitoring of loads is also a potentially useful application, as exemplified by the load modeling failures which contributed to the August 10, 1996 blackout in the Western US [102]. This application, though, presents additional challenges which are beyond the scope of this thesis.

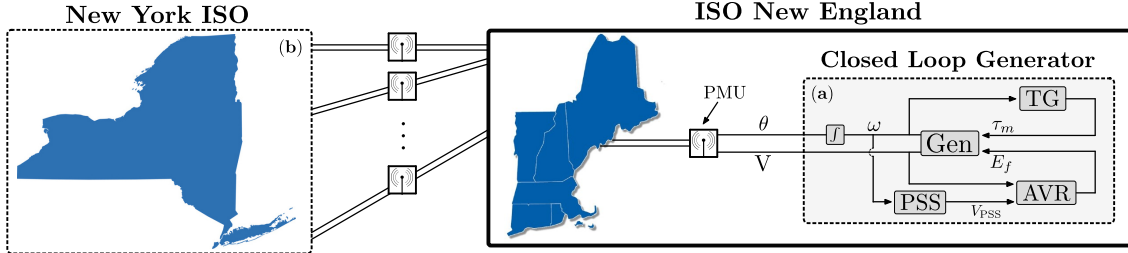


Figure 1-2: Predictive modeling opportunities for system operators: closed loop generator systems (panel **(a)** on the right) and wide-area interconnections (panel **(b)** on the left).

system. Since the generator is observable via PMU, ISONE may want to use predictive modeling techniques to build or update real-time models of this generator system. Panel **(b)** on the left, however, shows a series of connections to the neighboring NYISO system. Assuming these “tie lines” are all observable via PMUs, ISONE may want to use the data to build a dynamic equivalent of the NYISO network. Indeed, wide-area modeling was the original problem which motivated the predictive modeling techniques developed in this thesis. The following subsections briefly introduce both generator and wide-area predictive modeling approaches in the literature.

### 1.4.1 Generator Modeling

In the electromechanical frequency range, power system dynamics are still dominated by synchronous generators [127]. A wealth of literature exists on the non-linear physical modeling of these generators and their associated high-order controllers [105, 158, 115]. MOD33-flavored tuning and validation of these models, though, still faces a variety of practical obstacles; these include the exclusion of unmodeled dynamics, measurement noise, uncertain physical parameter values, unknown controller changes, and, in the limiting case of linearized modeling, residual nonlinearities and drifting equilibrium points. In recent years, a variety of “grid-scale” methods have been proposed for the purpose of validating these generator + controller models in the presence of strong network perturbations [150, 64, 92, 109, 93, 195]. Most of these perform some variation of Kalman filter-based parameter tuning via “play-back” simulation.

### 1.4.2 Wide Area Monitoring

With the increased observability provided by WAMS, system operators are beginning to have complete real-time observability of the connections (i.e. tie lines) between their respective “internal” regions and the “external” regions to which they are tied. With this complete observability comes the opportunity to infer the underlying input/output dynamics of these neighboring systems. Thus, creating a dynamical equivalent of these external systems is appearing increasingly realistic. Using advanced system identification (SysID) techniques, high sample rate PMU data can be used to construct an equivalent black-box dynamical model. While most commercial MEPS simulators, such as PSS/E and the DSATools suite, have external system reduction techniques built directly into the software package, the resulting analytical models can often provide poor predictive capabilities due to real-time changes in the system which the system operators are not aware of [204, 120].

Since PMU data can only reconstruct dynamics of up to  $\sim 8$  Hz, the dynamics of interest are primarily electromechanical in nature. There is a fairly vast literature devoted to (i) the estimation of electromechanical modes in MEPS and (ii) the creation of linear dynamical black-box models from wide-area time series data [34, 61, 46, 186, 210, 78, 79, 143, 8]. Excellent reviews on the topic are provided in [144, 50]. One of the most popular “modal identification” methods, known as Prony analysis, was first applied to power systems in the Pacific Northwest in 1990 [84]. The method uses so-called transient “ring-down” data in order to linearly approximate the frequency, phase, amplitude, and damping of the different system modes. Prony-type methods are primarily applicable when the system transient response is strong. Authors in [143] collect 50 minutes of ambient data followed by transient data associated with the controlled application of a 1400 MW brake resistor. They show that Prony analysis of the transient data and Wiener-Hopf linear prediction applied to the ambient data were both able to predict the four dominant system modes and their respective damping ratios. Subsequent publications further refined these methods [189, 49], but most of them were focused on identification of system modes (i.e. poles), rather than the full transfer functions.

More recent work has focused on building actual, but model reduced, input/output transfer functions from measured terminal data, since these methods are generally less developed. Authors in [34] propose aggregation techniques based on coherency methods in order to construct simple dynamic equivalents of wide areas; parameters of these equivalent reductions are then inferred. Using a simple autoregressive

with exogenous input (ARX) model, [33] develops a process for computing a dynamic equivalent transfer function with simulated or measured data. Voltage magnitude and frequency are chosen as inputs, while active and reactive power flows across lines are chosen as outputs. Each tie line, though, is considered and modeled independently. Simple MIMO transfer function approaches are developed in [205, 204], where poles, zeros, and model order are iteratively perturbed based on a least-squares numerical procedure inside a standard MATLAB toolbox. In each of these papers [204, 205, 33], measurement noise and process noise (i.e. load noise) are not considered, and dynamics are inferred after a transient switching event rather than from ambient data. For online oscillation damping control tuning, [111] uses a lower order autoregressive moving average exogenous (ARMAX) model for MIMO system identification. In [210], transfer function identification is performed on PMU data, but the modes of the system are assumed known apriori, and “`arx.m`” from MATLAB is used to perform the system identification.

### 1.4.3 Inadequacy of Existing Methods

The vast majority of the proposed modeling and validation algorithms are characterized by (at least one of) two salient features. First, they are parameterized by a physical prior; that is, they leverage the structure of a given physical generator of system model which can assumably be tuned to explain the full set observed dynamics. Second, these algorithms are typically designed to be deployed in the presence of a sufficiently strong network perturbation (e.g. ground fault). Together, these assumptions allow for a variety of helpful assumptions, such as the neglecting of initial state decay and the availability of a high-fidelity prior. Such algorithmic features, although widespread, can be burdensome if the prior model is incomplete, or if real-time model updates are desired<sup>5</sup> and no sufficiently recent perturbation events have occurred.

Predictive modeling algorithms which are free from both of these limitations can provide a variety of advantages. If the modeling of generator systems can be performed by a parameterized “black box” approximation, then the associated algorithm will be freed from the constraints of a potentially erroneous, or completely unknown, prior model. Additionally, if this algorithm can be implemented in the face of ambient, rather than severe, operating conditions, then updates can be performed on the fly, and otherwise unused PMU data can be transformed into actionable information

---

<sup>5</sup>Real-time updates can be desirable for a variety of reasons, such as in situ controller tuning or operational decision making. As portrayed in Fig. 1-1, this thesis will not explore these applications, but assumes they are potentially valuable for operators.

(see Fig. 1-1). Of course, since ambient excitation typically under-excites the non-linear dynamics of the true physical model, linearized modeling is the most tenable choice for performing dynamical inference in the presence of ambient fluctuations.

Recently, vector fitting approaches have been leveraged to construct power system models from measured field data. In [15], authors use the numerical Laplace transform to push the problem into the frequency domain. Next, vector fitting and relative dominant-pole measurements (RDPMs) are iteratively leveraged to build estimations of the system modes. Similarly, [162] combines Time Domain Vector Fitting (TDVF) and the popular ring down analysis to develop a novel modal estimation routine. In a more generic application, [95] uses out-of-the-box TDVF to construct a SISO linear model of a turbine governor system from measured PMU; droop gain values are then captured from the derived model.

Of course, the black-box identification of dynamic models from time series data goes far beyond power system applications and is regarded as a well established field [73, 31]. As noted, one prominent approach is the TDVF scheme [71, 72, 73]. This approach is applicable for estimating rational models of linear systems, starting from the time domain samples of input and output data. Unfortunately, canonical TDVF has the following restrictions:

- The system must be at rest when the data acquisition begins. This guarantees that the input and output data are related by a linear transfer function with no contribution from the zero-input (i.e. initial state decay) response.
- For a MIMO system with  $P$  ports, only separate modeling of each column of the transfer matrix is possible. This limitation requires that only one of the  $P$  input components is acting on the system during the separate modeling periods for each transfer matrix column.

Since online modeling requires the unknown system to be characterized (i) during its dynamic evolution and (ii) in the presence of concurrently acting inputs, the above limitations often make TDVF unsuitable for real-time MIMO applications. Accordingly, there exists a need in the MEPS community for the further development of methods which are capable of performing black-box, online, input/output predictive modeling of both generator and external wide area systems from ambient data in numerically expedient ways; such methods are generally lacking.

## 1.5 Probabilistic Power Flow and State Estimation in Electrical Distribution Networks

While the transmission grid is vitally important for transporting electrical power long distances, the distribution networks facilitate the final step of power delivery to homes and businesses. The ongoing democratization of energy is causing a series of fundamental changes to electrical distribution grids. Distributed energy resources (DERs), such as Tesla powerwalls and rooftop photovoltaic systems, automated sensing devices equipped with telemetry capabilities, such as  $\mu$ -PMUs and smart meters, and active loads, which are capable of reactively responding to real-time pricing signals, are all majorly disrupting the standard operating procedures of distribution networks [21, 101]. Accordingly, distribution system operation and control are receiving much more attention in the MEPS research community than they have in the past.

All of the aforementioned changes are contributing to an increasing amount of *uncertainty* in distribution networks. Due to this increase in uncertainty, so-called probabilistic methods are becoming increasingly popular tools for system planning and, in the future, system operation. In this thesis, we consider two problems which both seek to ease the computational burden associated with the deployment of probabilistic methods.

- First, we consider the probabilistic power flow problem, where *forecasted* load profiles are the source of uncertainty.
- Second, we consider the probabilistic state estimation problem, where *measured* load profiles, lines flows, and voltage magnitudes are the source of uncertainty.

Both of these problems are introduced and motivated in the following subsections.

### 1.5.1 Probabilistic Power Flow in Electrical Distribution Networks

In order to properly operate and control distribution grids, probabilistic forecasting of the network “state” (i.e. complex nodal voltages) is vitally important information, both for system operators and for the automated controllers embedded in the network. Performing such probabilistic forecasting in real-time can be computationally challenging but can also provide numerous operational benefits. The so-called

probabilistic power flow (PPF) [149] maps uncertainties in the power injection and parameter space to corresponding performance uncertainties in the operational state. This tool has become increasingly useful for system operators since its academic inception in 1974 [24, 11]. An excellent review on the topic is provided in [149], although the state of the art has advanced considerably in recent years, due to the rapid improvement of advanced Uncertainty Quantification (UQ) techniques.

Most PPF solvers fall into two general categories: analytical methods and simulation methods. The analytical methods typically use mathematical simplifications and expansions in order to alleviate the computational burden associated with the simulation methods. For example, [11] uses a convolution of random variables in order to infer the output probability density function (PDF) of power flow solutions. The stochastic response surface method (SRSM) was first applied to the PPF in [152], where polynomial chaos expansion (PCE) is used to construct statistically equivalent output voltage distributions. Since then, the application of PCE to the PPF problem has seen a variety of improvements. In [133], optimal truncation and degree selection of the PC series is considered, and nonlinear correlation of RVs is dealt with; in [74], so-called Stochastic Testing from [206] is applied to the generalized PCE in the context of time varying loads. Since PCE can suffer from the curse of dimensionality, [167] proposed the use of the low rank approximation (LRA), where the polynomial basis coefficient count grows linearly rather than exponentially. The cumulant [203, 59] and point estimate [41, 44] methods are other relatively older, but still popular, analytical PPF methods. Both, though, must be augmented with series expansions in order for surrogate output PDFs to be constructed [152].

Direct simulation approaches are typically referred to as Monte Carlo Simulations (MCS) or, more generally, as sampling-based methods (also sometimes called *non-intrusive*). These approaches attempt to directly build either the output distribution or quantities related to such distribution (i.e. statistical moments) through copious sampling and simulation of the underlying black box power flow solver. There are two key aspects that determine the overall speed and efficiency of such sampling-based methods: the way they choose the samples where the system is to be solved; and the time it takes to solve each chosen sample.

There are many contributions in the literature on improving the choice of the samples. For instance, in [90] importance sampling is applied to probabilistic optimal power flow problem. Latin hypercube and Latin supercube sampling are employed in [201] and [77], respectively. These advanced sampling approaches attempt to limit the number of simulations needed to produce output PDFs of sufficiently high-fidelity.

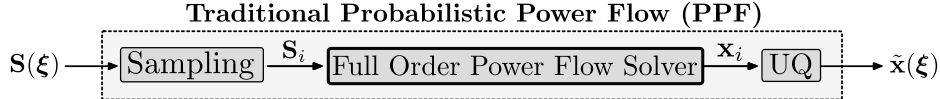


Figure 1-3: Typical sampling-based methodology for solving PPF: load profile distributions are sampled, the corresponding sample is solved, and the results are passed to an uncertainty quantification tool. Random variable  $\xi$  parameterizes the uncertainty.

While they present some distinct advantages and are typically chosen as the benchmark against which alternative techniques are tested [152], MCS-based and in general sampling-based approaches tend to still be quite computationally heavy.

On the contrary, contributions which seek to speed up the individual “black box” power flow solutions for a sampling-based PPF solver, especially in the context of distribution networks, have seldom been published, despite the fact that the power flow problem itself has been studied for many years. Ostensibly, solving power flow is not nearly as computationally burdensome as modern neural network training type problems. In a massive network, though, with three unbalanced phases, the problem can grow quite large, with tens of thousand of variables, and the numerics can become poorly conditioned. When it is desirable to solve power flow thousands of times in a short time period, using only local computational resources, rapid system solves can be highly attractive.

An essential tool for speeding up numerical solutions of physical systems is Model Order Reduction (MOR); see [19] for an excellent review of projection-based MOR techniques. More specifically, [54] proposes a procedure which *dynamically* constructs the projection subspace as an external solver runs. This procedure is highly applicable to the PPF problem. Intuitively, PPF subspace construction can be achieved by exploiting the practical observation that the vast majority of power flow solutions for the millions of different samples actually live within a small subspace (i.e. 10-50 dimensions). From an implementation perspective, this subspace is progressively uncovered from sequentially obtained solutions. In this thesis, the subspace is concurrently used in a projection framework to construct and update a ROM which results in orders of magnitude faster solutions for the majority of the remaining samples.

### 1.5.2 Probabilistic State Estimation in Electrical Distribution Networks

Active management of distribution grids and their embedded resources is becoming a critically important task for network operators [21, 101]. In order to prop-

erly operate and control these distribution grids, knowledge of the network “state” is vitally important information. In the seminal state estimation works by Fred Schweppe [165, 164, 163], the state of an electric power system is defined as “the vector of the voltage magnitudes and angles at all network buses.” Furthermore, state estimation is defined as “a data processing algorithm for converting redundant meter readings and other available information into an estimate of the static-state vector.” Being a well established technology at the transmission level [4], state estimation is performed every few seconds, and its output allows system operators to make important decisions regarding power dispatch, voltage regulation, and stability assessment. The many potential similar advantages associated with distribution system state estimation (DSSE) are discussed in [85]. Despite these advantages, very few utilities have implemented real time DSSE in their systems [21, 148], suggesting that more research must be completed before utilities choose to invest in and adopt DSSE as a tool for system management.

The challenges associated with DSSE are well documented in the literature; they most saliently include unbalanced operation, highly time varying loads, disparate measurements ( $\mu$ -PMU, SCADA, other AMI), and a high degree of load uncertainty. Research survey [148] highlights an overall lack of “data synergy”, due to heterogeneous data types, measurement collection protocols, and timing coordinations, as a primary roadblock for DSSE implementation.

A variety of DSSE solvers have been proposed across the academic literature [169, 139, 112, 147, 159, 47, 124, 130, 187]. Many of these approaches leverage Bayesian estimation, Kalman filtering, SDP relaxation, or the inclusion of regularizing pseudo-measurements. A famous solution to the three-phase load flow problem on distribution circuits, known as forward-backward sweep method, was first proposed in [37], and a recent review of state-of-the-art DSSE techniques is given in [148]. Authors in [169] provided side-by-side comparisons of primary DSSE frameworks: weighted least squares (WLS), weighted least absolute value (WLAV), and the Schweppe Huber Generalised M (SHGM) estimator.

One of the more famous DSSE methods, formulated with rectangular branch current flows in a system with few measurements and many pseudo-measurements, is given in [113]. The effect of including PMUs is considered in [139]. A similar (but linearized) formulation, developed for “smart distribution systems”, is proposed in [85]. In this paper, measurement variances are carefully constructed using the so-called delta method. Stochastic optimization methods are leveraged in [112] in order to minimize meter investment costs while taking DSSE uncertainty into consideration.

Meter placement is also considered in [166], where the authors seek to minimize the bus voltage estimation variance at buses without measurement equipment. The effects of direct smart meter measurement integration are characterized in [147]. A linear Bayesian state estimator is compared to the typical weighted least squares formulation in [159]. By leveraging load forecasting, [47] also incorporates a Bayesian state estimator in a linearized network with limited sensing. State estimation via Kalman filtering, combined with load control, is proposed in [124].

To overcome the inherent uncertainty highlighted in [148], though, advanced uncertainty quantification (UQ) approaches should be applied to DSSE, just as they have been successfully applied to the probabilistic power flow (PPF) problem [149]. In PPF, UQ methods, such as Polynomial Chaos Expansion [152], efficiently map uncertainty in the load forecast space to uncertainty in the voltage profile space. Analogously, in DSSE, UQ maps uncertainty in the “measurement profile” space to uncertainty in the voltage profile space, as first proposed in [110]. In massive distribution networks, with tens of thousands of state variables, sampling-based UQ approaches can require many minutes to converge if traditional DSSE solvers are employed. For real-time operation and control, this can be too slow.

## 1.6 Thesis Contributions and Outline

### 1.6.1 Contributions of this Thesis

In light of the four problems which were introduced, reviewed and motivated in the previous subsection, we now state the specific contributions associated with each.

#### Locating the Source of Forced Oscillations

In this thesis, we develop a systematic procedure to locate the sources of FOs. We start by deriving a relation between generator terminal voltage and current fluctuations in the presence of persistent oscillation. This relation, which is characterized by a frequency response function (FRF), can be considered the effective admittance of the machine, and it will be used to build an equivalent circuit representation of the grid. Based on this relation, it is possible to effectively distinguish between source and non-source generators at the forcing frequency. The specific contributions follow:

- A systematic method for calculating a generator’s frequency response function, with respect to terminal voltage and current perturbations, is given.

- An *equivalent circuit transformation* is introduced which treats a generator's frequency response function as an effective admittance matrix  $\mathcal{Y}$  and any internal forced oscillations as a current injection  $\mathcal{I}$ .
- An explicit forced oscillation source location algorithm, which compares predicted and measured current spectrums while making unique measurement noise considerations, is presented.

Since model parameters inside of the equivalent circuit model are often uncertain, we then apply a Bayesian optimization framework to the source identification problem:

- A likelihood function and its physically meaningful covariance matrix are derived with respect to a generator's terminal perturbations in the frequency domain.
- A Bayesian source location algorithm, via two-stage MAP optimization, is formulated to find the most likely set of dynamic model parameters and FO injection terms.
- A numerical procedure is given which engenders computational tractability in the context of large scale systems.

Finally, we use the proposed framework to analyze so-called “energy based” source location methods, such as the DEF method, via dissipativity theory and positive realness, in the context of a full-scale system. Initially, this framework is used to analyze a lossy classical power system, but the methods are then generalized to include arbitrary system models; these generalized methods are thus capable of investigating all of the problematic effects presented by lines, loads and generator controllers. In this regard, the primary contributions follow:

- Using the proposed equivalent circuit transformation, we leverage a variety of tools from AC circuit theory in order to develop a linearized framework for analyzing oscillation propagation at the system level.
- We subsequently use the proposed framework to theoretically justify the DEF method and show that there exists no other frequency domain transformation which will render all components of a classical power system simultaneously dissipative.

- A simulation-free algorithm is developed which predicts the performance of the DEF method in a generalized power system.
- The proposed DQR-transformation is used to analytically investigate the dissipating energy flow properties of three common, yet non-classical, grid components.

## **Decentralized Stability Standard for Microgrids**

In this thesis, we develop a certification procedure to allow for plug-and-play operability of microgrid networks. The specific contributions of this thesis follow:

- In order to parameterize the drives of microgrid stability, we propose a novel homotopic parameterization of the closed loop controller gains.
- Based on the above parametrization, we develop a fully decentralized stability criteria, based on rigorous dissipativity concepts applied in the frequency domain, which can be applied to DC grids with different components (i.e. sources, lines, and loads) and can certify stability for an arbitrary network configuration of these components.
- We prove that any component which satisfies this criteria can be safely added to a network without a system eigenmode crossing into the unstable right half plane, thus allowing for “plug-and-play” operability of DC microgrids. A practical design algorithm is then offered.
- Finally, we extend this methodology to AC microgrid systems, where the rotational energy functions are replaced by nonsingular transformation matrices and applied to droop-controlled inverter-based AC microgrids.

## **Real-Time Predictive Modeling of Power System Dynamics**

This paper introduces a generalized extension of TDVF, known as Real-Time Vector Fitting (RTVF), in order to address the limitations associated with TDVF’s canonical formulation. The corresponding contributions of this thesis follow:

- We develop a first generalization of the basic TDVF scheme by removing the requirement of pure zero-state conditions, hence allowing for the presence of non-vanishing initial conditions.

- We develop a second generalization by allowing all input components to act concurrently in the time series data sets used to train the RTVF model.
- Finally, in order to account for unobservable stochastic inputs which can corrupt the identification procedure, we formulate a stochastic-RTVF (sRTVF) scheme, in which filtered data streams are replaced by the output of numerical correlation (both auto- and cross-) functions.

## Probabilistic Power Flow and State Estimation

For any sampling-based method performing PPF, we present a series of methods which effectively speed up each sample solve. Our work is otherwise completely agnostic to both the type of UQ methodology used to characterize the output distributions (i.e. PCE, Stochastic Collocation, etc.), and to the way samples are chosen (i.e. Monte Carlo, Important Sampling, etc.). We therefore refer to our routine as the *Accelerated-PPF* (APPF) routine, since it can be used to speed up *any* sampling-based PPF solver. Accordingly, the primary PPF related contributions of this thesis follow:

- We develop a fast power flow Jacobian solution technique which leverages a Neumann series approximation.
- We use a dynamically expanding subspace to construct a ROM of the system which solves rapidly.
- We combine the Jacobian solution and the reduced model solver to construct a routine which can rapidly solve many sequential power flow problems.

We then apply a similar projection-based model order reduction (MOR) technique to a standard set of overdetermined state estimation equations. For a given measurement sample (i.e. input), the resulting ROM is able to solve the underlying state estimation problem orders of magnitude faster than a full order solver. The associated algorithm, termed the Accelerated Probabilistic State Estimator (APSE), can then pass these solutions to any sampling-based UQ technique. The specific probabilistic state estimation related contributions of this thesis follow:

- We derive exact, second order expansions of the relevant distribution grid state estimation equations.

- Leveraging an orthonormalized subspace, we compress the derived expansions into a low-dimension system of equations (i.e. ROM) which can be solved rapidly.
- To dynamically construct this subspace and initialize the reduced order model, we implement an outer-loop QR factorization-based Gauss-Newton solver.

### 1.6.2 Thesis Outline

The remainder of this thesis document is structured as follows.

- \* In Chapter 2, we attack the problem of locating the sources of FOs. In doing so, we first introduce our equivalent circuit transformation technique, and then we use a Bayesian approach to locate the sources of oscillations in this circuit. Finally, we use the equivalent circuit to provide rigorous analysis of and practical implementation suggestions for the DEF method.
- \* In Chapter 3, we attack the problem of developing decentralized small-signal stability certification standards for microgrids. The majority of the chapter will be devoted to DC microgrids, but we will offer (published) extensions to AC microgrids as well.
- \* In Chapter 4, we attack the problem of performing real-time predictive modeling of power system components. We do so by leveraging the canonical TDVF procedure and adding a series of novel alterations, each rigorously rooted in system theory. The resulting procedure is thus suitable for real-time use by power system operators.
- \* In Chapter 5, we attack the problem of solving probabilistic power flow in electrical distribution networks. We then extend the developed methodology to the probabilistic state estimation problem.
- \* Finally, in Chapter 6, we offer concluding remarks on the research presented in this thesis, and we consider a variety of ways in which the work can be extended in the future.

# Chapter 2

## Locating the Sources of Low Frequency Forced Oscillations

This chapter includes four sections. In the first section, we provide the mathematical background which will be necessary for solving the problems considered in this chapter. In the second section, we outline a procedure for constructing the effective input admittance associated with a generator, as seen by the grid, and we explain how this admittance can be used for performing source location. In the third section, we utilize a Bayesian framework for locating the sources of FOs by incorporating inherent modeling uncertainties in the construction of these admittance functions. Finally, in the fourth section, we utilize the equivalent circuit transformation proposed in the second section to perform a systematic analysis of energy-based FO source location methods.

### 2.1 Mathematical Background

#### 2.1.1 Modeling the Forced Periodic Steady-State Response of LTI Systems

We consider a Hurwitz stable [100] Mingle-Input Multi-Output (MIMO) Linear Time-Invariant (LTI) system  $\mathcal{S}_l$  characterized by the state space formulation [65]

$$\left. \begin{aligned} \dot{\mathbf{x}}(t) &= \mathbf{A}\mathbf{x}(t) + \mathbf{B}\mathbf{u}(t) \\ \mathbf{y}(t) &= \mathbf{C}\mathbf{x}(t) + \mathbf{D}\mathbf{u}(t) \end{aligned} \right\} \mathcal{S}_l, \quad (2.1)$$

which is assumed to be expressed with a minimal realization. We further consider the limiting situation where there is only one input, and it is a pure sinusoid characterized by frequency  $\omega_0$ , magnitude  $u_0$ , and phase  $\theta_0$ :

$$u(t) = u_0 \cos(\omega_0 t + \theta_0) \quad (2.2a)$$

$$= \operatorname{Re} \{ u_0 e^{j\theta_0} e^{j\omega_0 t} \} \quad (2.2b)$$

$$= \operatorname{Re} \{ \tilde{u} e^{j\omega_0 t} \}. \quad (2.2c)$$

Signal  $\tilde{u}$  is referred to as a phasor<sup>1</sup>. If input (2.2a) has been applied to (2.1) and all transients have died out, then the system is said to be operating in so-called periodic steady state. In this case, by the properties of linearity, all system states and outputs will be pure sinusoids which can also be characterized by phasors:

$$\mathbf{x}(t) = \operatorname{Re} \{ \tilde{\mathbf{x}} e^{j\omega_0 t} \} \quad (2.3)$$

$$\mathbf{y}(t) = \operatorname{Re} \{ \tilde{\mathbf{y}} e^{j\omega_0 t} \}. \quad (2.4)$$

Plugging (2.2)-(2.4) into (2.1) yields

$$\operatorname{Re} \{ j\omega_0 \tilde{\mathbf{x}} e^{j\omega_0 t} \} = \mathbf{A} \operatorname{Re} \{ \tilde{\mathbf{x}} e^{j\omega_0 t} \} + \mathbf{B} \operatorname{Re} \{ \tilde{u} e^{j\omega_0 t} \} \quad (2.5)$$

$$\operatorname{Re} \{ \tilde{\mathbf{y}} e^{j\omega_0 t} \} = \mathbf{C} \operatorname{Re} \{ \tilde{\mathbf{x}} e^{j\omega_0 t} \} + \mathbf{D} \operatorname{Re} \{ \tilde{u} e^{j\omega_0 t} \}. \quad (2.6)$$

Since (2.5)-(2.6) are true  $\forall t$ , it is directly implied that the imaginary parts of these equations also satisfy the equality. Then, multiplying through by  $e^{-j\omega_0 t}$  yields

$$j\omega_0 \tilde{\mathbf{x}} = \mathbf{A} \tilde{\mathbf{x}} + \mathbf{B} \tilde{u} \quad (2.7)$$

$$\tilde{\mathbf{y}} = \mathbf{C} \tilde{\mathbf{x}} + \mathbf{D} \tilde{u}. \quad (2.8)$$

This is the canonical representation which we will use when analyzing the periodic steady state response of power systems which are driven by sinusoidal FO inputs. The frequency response function (FRF) associated with (2.7)-(2.8) can be constructed by eliminating the state vector  $\tilde{\mathbf{x}}$  and solving for the output:

$$\tilde{\mathbf{y}} = \underbrace{[\mathbf{C} (\mathbb{1} j\omega_0 - \mathbf{A}) \mathbf{B} + \mathbf{D}]}_{\mathbf{H}(\omega_0)} \tilde{u}. \quad (2.9)$$

---

<sup>1</sup>In power system engineering [69], phasor magnitude is typically defined as a sinusoidal peak amplitude divided by  $\sqrt{2}$ , yielding a Root Mean Square (RMS) value. This convention is typically not followed in the dynamical systems literature.

When evaluated at a singular frequency  $\omega_0$ , which in this thesis will typically represent the forcing frequency associated with a FO,  $\mathbf{H}(\omega_0)$  quantifies the degree of magnitude amplification and phase shift between input and output sinusoids.

### 2.1.2 Likelihood Function Modeling and Maximum A Posteriori (MAP) Estimation

We seek to construct the canonical likelihood function associated with a linear system  $\mathbf{y} = \mathbf{T}(\mathbf{p})\mathbf{u}$ , where  $\mathbf{u}$  is some observable input,  $\mathbf{y}$  is some observable output, and  $\mathbf{T}(\mathbf{p})$  is some linear transformation matrix which relates the input and output observations; the transformation  $\mathbf{T}(\mathbf{p})$  is assumed to be parameterized by some set of parameters  $\mathbf{p}$  [99]. We assume both the input and output observations are corrupted by independent identically distributed (IID) additive white Gaussian noise (AWGN) vectors  $\boldsymbol{\eta}_u$  and  $\boldsymbol{\eta}_y$ , with  $\eta \sim \mathcal{N}(0, \sigma^2)$  in each case. Thus, the observable input/output relationship is given by

$$(\mathbf{y} + \boldsymbol{\eta}_y) = \mathbf{T}(\mathbf{p}) (\mathbf{u} + \boldsymbol{\eta}_u). \quad (2.10)$$

The likelihood function, which characterizes the likelihood of the observed data *given* the model parameters  $\mathbf{p}$ , has an associated covariance matrix  $\Sigma_\eta$ . Since the parameters are assumed given (i.e. deterministic), the covariance matrix is given by

$$\Sigma_\eta = E \{ (\mathbf{y} - \mathbf{T}(\mathbf{p})\mathbf{u})(\mathbf{y} - \mathbf{T}(\mathbf{p})\mathbf{u})^T \} \quad (2.11a)$$

$$= E \{ (\mathbf{T}(\mathbf{p})\boldsymbol{\eta}_u - \boldsymbol{\eta}_y)(\mathbf{T}(\mathbf{p})\boldsymbol{\eta}_u - \boldsymbol{\eta}_y)^T \} \quad (2.11b)$$

$$= \mathbf{T}(\mathbf{p})E \{ \boldsymbol{\eta}_u \boldsymbol{\eta}_u^T \} \mathbf{T}(\mathbf{p})^T - E \{ \boldsymbol{\eta}_y \boldsymbol{\eta}_u^T \} \mathbf{T}(\mathbf{p})^T + \mathbf{T}(\mathbf{p})E \{ \boldsymbol{\eta}_u \boldsymbol{\eta}_y^T \} - E \{ \boldsymbol{\eta}_y \boldsymbol{\eta}_y^T \}. \quad (2.11c)$$

The covariance matrix is itself, therefore, a function of the parameters. The overall likelihood function (i.e. multivariate normal distribution) is given by [99]

$$p_{\text{likely}}(\mathbf{d}|\mathbf{p}) = \frac{e^{-\frac{1}{2}(\mathbf{y}-\mathbf{T}(\mathbf{p})\mathbf{u})^T \Sigma_\eta^{-1} (\mathbf{y}-\mathbf{T}(\mathbf{p})\mathbf{u})}}{\sqrt{(2\pi)^n \det \{\Sigma_\eta\}}} \quad (2.12)$$

where  $\mathbf{d} = [\mathbf{u}^T, \mathbf{y}^T]^T \in \mathbb{R}^{2n}$  is a data vector. This formulation will be utilized when building the likelihood functions associated with physical generator models.

A typical Bayesian model will utilize the derived likelihood function along with some statistical model of the parameters, known as a prior. If the prior model is

Gaussian, with covariance matrix  $\Sigma_p$  and mean  $\mu_p$ , then the prior can be stated as

$$p_{\text{prior}}(\mathbf{p}) = \frac{e^{-\frac{1}{2}(\mathbf{p}-\mu_p)^T \Sigma_p^{-1} (\mathbf{p}-\mu_p)}}{\sqrt{(2\pi)^m \det \{\Sigma_p\}}}.$$
 (2.13)

Finally, the posterior distribution, which quantifies and probability of the model, give the data, is given as the product of the likelihood and the prior, and then divided by the so-called marginal likelihood function  $p_{\text{marg}}(\mathbf{p})$ :

$$p_{\text{post}}(\mathbf{p}|\mathbf{d}) = \frac{p_{\text{likely}}(\mathbf{d}|\mathbf{p})p_{\text{prior}}(\mathbf{p})}{p_{\text{marg}}(\mathbf{d})}$$
 (2.14a)

$$\propto p_{\text{likely}}(\mathbf{d}|\mathbf{p})p_{\text{prior}}(\mathbf{p})$$
 (2.14b)

The so-called Maximum A Posteriori (MAP) formulation seeks to determine an optimal point estimate<sup>2</sup> of the posterior distribution [140]. This is accomplished by maximizing the probability of the model, given the observed data set, i.e.

$$\mathbf{p}_{\text{MAP}} = \underset{\mathbf{p} \in \mathbb{R}^m}{\text{argmax}} \{p_{\text{post}}(\mathbf{p}|\mathbf{d})\}.$$
 (2.15)

Due to the Gaussian nature of the prescribed likelihood function and prior, (2.15) is typically solved by minimizing the negative log of the posterior [140]:

$$\mathbf{p}_{\text{MAP}} = \underset{\mathbf{p} \in \mathbb{R}^m}{\text{argmin}} \{-\log \{p_{\text{post}}(\mathbf{p}|\mathbf{d})\}\}$$
 (2.16a)

$$= \underset{\mathbf{p} \in \mathbb{R}^m}{\text{argmin}} \left\{ (\mathbf{y} - \mathbf{T}(\mathbf{p})\mathbf{u})^T \Sigma_\eta^{-1} (\mathbf{y} - \mathbf{T}(\mathbf{p})\mathbf{u}) + (\mathbf{p} - \mu_p)^T \Sigma_p^{-1} (\mathbf{p} - \mu_p) \right\}.$$
 (2.16b)

If the prior term is neglected, the solution to (2.16b) exactly coincides with the Maximum Likelihood Estimate (MLE). One may also interpret (2.16b) as an MLE formulation with additional Tikhonov regularization (i.e.  $l_2$ -norm regularization).

### 2.1.3 Dissipative and Positive Real Systems

We define a dynamical system  $\mathcal{S}$  with input  $\mathbf{u}(t)$ , output  $\mathbf{y}(t)$ , and supply rate  $w(t) = w(\mathbf{u}(t), \mathbf{y}(t))$ . In [192],  $\mathcal{S}$  is defined to be dissipative if there exists a nonnegative and

---

<sup>2</sup>Traditionally, the MAP solution is associated with a single point estimate, rather than a full distribution. This point estimate is referred to as the solution.

continuously differentiable storage function  $S(\mathbf{x})$  such that

$$S(\mathbf{x}_0) + \int_{t_0}^{t_1} w(t)dt \geq S(\mathbf{x}_1), \quad (2.17)$$

where  $\mathbf{x}_0$ ,  $\mathbf{x}_1$  are the system states at times  $t_0$ ,  $t_1$  respectively. This dissipation inequality may be alternatively stated as

$$w(t) \geq \dot{S}(\mathbf{x}), \quad \forall t \quad (2.18)$$

which indicates that the energy supplied to the system must always be at least as large as the instantaneous change in the system's energy storage. If  $w(t) = \dot{S}(\mathbf{x})$ ,  $\forall t$ , then the system  $\mathcal{S}$  is said to be *lossless* and no dissipation occurs. Furthermore,  $\mathcal{S}$  is said to be *passive* [1, 100] if it is dissipative with respect to the quadratic supply rate

$$w(\mathbf{u}(t), \mathbf{y}(t)) = \mathbf{u}^T(t)\mathbf{y}(t). \quad (2.19)$$

Generally, a passive component is one which can only dissipate and store, but not produce, physical power. Notably though, the term *passivity* has engendered much confusion in the academic literature, as rigorously highlighted in [196, 197]. In this thesis, instead of using the word passivity, we alternatively use a definition offered by Willems [192, 193], which is often used when defining “passivity”.

**Definition 1.** A dynamical system  $\mathcal{S}$  is said to be **Dissipative with respect to a Quadratic supply Rate (DQR)** if there exists a nonnegative and continuously differentiable storage function  $S(\mathbf{x})$  such that

$$S(\mathbf{x}_0) + \int_{t_0}^{t_1} \mathbf{u}(t)^T \mathbf{y}(t) dt \geq S(\mathbf{x}_1). \quad (2.20)$$

For example, if  $\mathcal{S}$  is DQR with  $S(\mathbf{x}_0) = \mathbf{0}$  and  $S(\mathbf{x}) \geq 0$ , then from (2.20),

$$\int_0^t \mathbf{u}(\tau)^T \mathbf{y}(\tau) d\tau \geq 0. \quad (2.21)$$

Most often, in the analysis of “linear” (i.e. linearized) systems, the input and output vectors  $\mathbf{u}(t)$ ,  $\mathbf{y}(t)$  represent perturbations away from some equilibrium operating points. When dealing with such perturbations, standard dissipativity is replaced by so-called *incremental dissipativity*, which refers to the dissipative nature of a system's incremental change from its equilibrium, as defined by [179, eq. (4.159)]. This is

also known as “shifted dissipativity” in the literature. Unless otherwise noted, in the remainder of this thesis, the term DQR from Definition 1 will always be meant in an incremental sense.

### Positive Realness

The condition in (2.21) is known as positive realness, and its connections to linear systems are quite useful. To further specify this property, we consider linear system  $\mathcal{S}_l$  from (2.1), which is now assumed to have  $P$  inputs and  $P$  outputs. The system’s  $P \times P$  transfer function, given by  $\mathbf{H}(s) = C(s\mathbf{1} - \mathbf{A})^{-1}\mathbf{B} + \mathbf{D}$ , can be assessed in the  $s$  domain or the  $j\omega$  domain.

**Definition 2** (Willems [193]). *Assuming  $\mathcal{S}_l$  of (2.1) simultaneously satisfies*

1.  $\text{Re}\{\lambda(\mathbf{A})\} \leq 0$ , and
2. *the eigenvalues of  $\mathbf{A}$  on the  $j\omega$  axis are non-repeated, and the residue matrix at the simple poles on the  $j\omega$  axis is Hermitian and non-negative definite,*

*then the associated transfer function  $\mathbf{H}(s)$  is positive real if*

$$\mathbf{H}(j\omega) + \mathbf{H}(j\omega)^\dagger \succ 0, \forall \omega, j\omega \neq \lambda(\mathbf{A}). \quad (2.22)$$

The well known [193, 171, 100] connection between positive realness and (quadratic) dissipativity can finally be stated:

$$\mathcal{S}_l \text{ is DQR via (2.20)} \Leftrightarrow \mathbf{H}(s) \text{ is Positive Real via (2.22)}. \quad (2.23)$$

Furthermore, if  $\mathbf{H}(j\omega) + \mathbf{H}(j\omega)^\dagger \equiv \mathbf{0}, j\omega \neq \lambda(\mathbf{A})$ , then  $\mathbf{H}(s)$  is said to be lossless.

## 2.2 Using Effective Generator Impedance for FO Source Location

### 2.2.1 Representing Generators as Admittance Functions

This section introduces the concept of a generator’s effective admittance matrix  $\mathcal{Y} \equiv \mathcal{Y}(s)$  which, in the frequency domain, also characterizes its frequency response. If the generator is an oscillation source, then in addition to matrix  $\mathcal{Y}$ , we show that an effective current source  $\mathcal{I} \equiv \mathcal{I}(s)$  will appear in parallel with admittance  $\mathcal{Y}$ . We

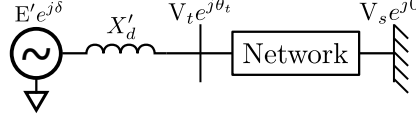


Figure 2-1: 2<sup>nd</sup> order generator tied to a network. Internal generator voltage  $E'e^{j\delta}$ , terminal voltage  $V_t e^{j\theta_t}$ , and swing bus voltage  $V_s e^{j\theta_s}$  with  $\theta_s = 0$  are all shown.

analytically derive these expressions for a classical generator model and then show how the methods extend to higher order models.

### State Space Formulation for a Classical Generator

In this section, the admittance matrix which relates a classical generator's rectangular voltage and rectangular current perturbations is derived. Effective current sources relating to torque and EMF oscillations are also derived. We start by considering a 2<sup>nd</sup> order generator with its internal EMF magnitude fixed. This generator is connected to some terminal bus with positive sequence phasor voltage  $V_t e^{j\theta_t}$  at frequency  $\omega_0$ . This configuration is shown by Fig. 2-1. The swing equation for the 2<sup>nd</sup> order generator [158] is formulated with polar variables using a quasi-stationary power flow approximation. We neglect armature resistance  $R_a$  since it is typically  $\sim 1\%$  of transient reactance  $X'_d$ :

$$\dot{\delta} = \Delta\omega \quad (2.24)$$

$$M\Delta\dot{\omega} = \tau_m - \frac{V_t E'}{X'_d} \sin(\delta - \theta_t) - D\Delta\omega, \quad (2.25)$$

where  $M = \frac{2H}{\omega_0}$ ,  $\omega = \omega_0 + \Delta\omega$ , and we have also assumed  $P_m = \omega\tau_m \approx \tau_m$  since the speed deviations are small. In order to quantify the admittance matrix ( $\mathcal{Y}$ ) and current injection ( $\mathcal{I}$ ) associated with this generator model, the expression may be linearized and expressed in state space formulation:

$$\Delta\dot{x} = \mathbf{A}\Delta x + \mathbf{B}\Delta u \quad (2.26)$$

$$\Delta y = \mathbf{C}\Delta x + \mathbf{D}\Delta u, \quad (2.27)$$

where the state variable vector  $x$  contains the torque angle ( $\delta$ ) and speed deviation ( $\Delta\omega$ ) of the generator, and the input vector  $u$  contains the mechanical torque

variations, two orthogonal terminal bus voltages, and the generator EMF:

$$\boldsymbol{x} = [\delta \ \Delta\omega]^T \quad (2.28)$$

$$\boldsymbol{u} = \left[ \tau_m \ \text{Re}(\tilde{V}_t) \ \text{Im}(\tilde{V}_t) \ E' \right]^T. \quad (2.29)$$

In linearizing the swing equation,  $\Delta\boldsymbol{u}_{V_p}$  is the input vector of polar voltage perturbations,  $\Delta u_\tau$  is the input torque perturbation,  $\Delta u_E$  is the input EMF variation, and power angle is defined as  $\varphi = \delta - \theta_t$ :

$$\Delta\dot{\boldsymbol{x}} = \mathbf{A}\Delta\boldsymbol{x} + \mathbf{B}_{V_p}\Delta\boldsymbol{u}_{V_p} + \mathbf{B}_\tau\Delta u_\tau + \mathbf{B}_E\Delta u_E \quad (2.30)$$

$$\begin{bmatrix} \Delta\dot{\delta} \\ \Delta\dot{\omega} \end{bmatrix} = \begin{bmatrix} 0 & 1 \\ -\frac{V_t E'}{MX'_d} \cos(\varphi) & -\frac{D}{M} \end{bmatrix} \begin{bmatrix} \Delta\delta \\ \Delta\omega \end{bmatrix} + \begin{bmatrix} 0 & 0 \\ -\frac{E'}{MX'_d} \sin(\varphi) & \frac{V_t E'}{MX'_d} \cos(\varphi) \end{bmatrix} \begin{bmatrix} \Delta V_t \\ \Delta\theta_t \end{bmatrix} + \begin{bmatrix} 0 \\ \frac{1}{M} \end{bmatrix} \begin{bmatrix} \Delta\tau_m \end{bmatrix} + \begin{bmatrix} 0 \\ \frac{-V_t}{MX'_d} \sin(\varphi) \end{bmatrix} \begin{bmatrix} \Delta E' \end{bmatrix}. \quad (2.31)$$

In deriving the admittance, we seek to relate terminal voltage and current perturbations in rectangular coordinates. To do so, small perturbations of the voltage magnitude  $\Delta V_t$  and phase  $\Delta\theta_t$  on the terminal bus voltage  $\tilde{V}_t$  are considered:

$$\tilde{V}_t + \Delta\tilde{V}_t = (V_t + \Delta V_t)e^{j(\theta_t + \Delta\theta_t)}. \quad (2.32)$$

After linearizing, the  $\Delta\tilde{V}_t$  components may be separated into their real and imaginary parts, and the polar rectangular relationships may be expressed by employing transformation matrix  $T_1$ . Fig. 2-2 graphically portrays the following relationships:

$$\underbrace{\begin{bmatrix} \text{Re}(\Delta\tilde{V}_t) \\ \text{Im}(\Delta\tilde{V}_t) \end{bmatrix}}_{\Delta\boldsymbol{u}_{V_r}} = \underbrace{\begin{bmatrix} \cos(\theta_t) & -V_t \sin(\theta_t) \\ \sin(\theta_t) & V_t \cos(\theta_t) \end{bmatrix}}_{T_1} \underbrace{\begin{bmatrix} \Delta V_t \\ \Delta\theta_t \end{bmatrix}}_{\Delta\boldsymbol{u}_{V_p}} \quad (2.33)$$

Accordingly, the inverse transformation matrix  $T_1^{-1}$  from (2.33) is employed to transform the vector of polar voltage perturbation variables ( $\Delta\boldsymbol{u}_{V_p}$ ) into the vector of rectangular voltage perturbation variables ( $\Delta\boldsymbol{u}_{V_r}$ ). The corresponding state space matrix

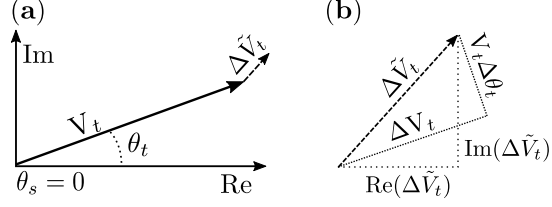


Figure 2-2: Panel (a) shows the steady state phasor  $V_t e^{j\theta_t}$  and phasor deviation  $\Delta \tilde{V}_t$ . Panel (b) expands deviation  $\Delta \tilde{V}_t$  from panel (a) and decomposes the relationship between the rectangular deviations ( $\text{Re}(\Delta \tilde{V}_t)$ ,  $\text{Im}(\Delta \tilde{V}_t)$ ) and the corresponding polar deviations ( $\Delta V_t$ ,  $V_t \Delta \theta_t$ ).

is  $\mathbf{B}_{V_r}$ , where  $\mathbf{B}_{V_r} = \mathbf{B}_{V_p} T_1^{-1}$ . Reformulating the state space representation yields

$$\Delta \dot{\mathbf{x}} = \mathbf{A} \Delta \mathbf{x} + \mathbf{B}_{V_r} \Delta \mathbf{u}_{V_r} + \mathbf{B}_\tau \Delta u_\tau + \mathbf{B}_E \Delta u_E, \quad (2.34)$$

where  $\mathbf{B}_{V_r}$  has the following analytical structure:

$$\mathbf{B}_{V_r} = \frac{E'}{MX'_d} \begin{bmatrix} 0 & 0 \\ -\sin(\delta) & \cos(\delta) \end{bmatrix}. \quad (2.35)$$

The state space model's output  $\mathbf{y}$  is defined as the orthogonal real and imaginary current flows into the generator (we call these the *negative current injections*):

$$\tilde{I} = \frac{( \text{Re}(\tilde{V}_t) + j \text{Im}(\tilde{V}_t) ) - E' e^{j\delta}}{jX'_d}. \quad (2.36)$$

Complex current  $\tilde{I}$  is linearized and split into real and imaginary currents.

$$\Delta \mathbf{y} = \mathbf{C} \Delta \mathbf{x} + \mathbf{D}_{V_r} \Delta \mathbf{u}_{V_r} + \mathbf{D}_E \Delta u_E \quad (2.37)$$

$$\begin{bmatrix} \Delta \text{Re}(\tilde{I}) \\ \Delta \text{Im}(\tilde{I}) \end{bmatrix} = \begin{bmatrix} -\frac{E' \cos(\delta_0)}{X'_d} & 0 \\ -\frac{E' \sin(\delta_0)}{X'_d} & 0 \end{bmatrix} \begin{bmatrix} \Delta \delta \\ \Delta \omega \end{bmatrix} + \quad (2.38)$$

$$\begin{bmatrix} 0 & \frac{1}{X'_d} \\ -\frac{1}{X'_d} & 0 \end{bmatrix} \begin{bmatrix} \Delta \text{Re}(\tilde{V}_t) \\ \Delta \text{Im}(\tilde{V}_t) \end{bmatrix} + \frac{1}{X'_d} \begin{bmatrix} -\sin(\delta) \\ \cos(\delta) \end{bmatrix} [\Delta E']$$

## Construction of Transfer Functions

With the state space model formulated, the Laplace transform of the system may be taken, such that  $s\tilde{\mathbf{x}}(s) = \mathcal{L}\{\dot{\mathbf{x}}\}$ ,  $\tilde{\mathbf{y}}(s) = \mathcal{L}\{\mathbf{y}\}$ , etc. Dropping the “of  $s$ ” notation,

$$s\tilde{\mathbf{x}} = \mathbf{A}\tilde{\mathbf{x}} + \mathbf{B}_{V_r}\tilde{\mathbf{u}}_{V_r} + \mathbf{B}_\tau\tilde{\mathbf{u}}_\tau + \mathbf{B}_E\tilde{\mathbf{u}}_E \quad (2.39)$$

$$\tilde{\mathbf{y}} = \mathbf{C}\tilde{\mathbf{x}} + \mathbf{D}_{V_r}\tilde{\mathbf{u}}_{V_r} + \mathbf{D}_E\tilde{\mathbf{u}}_E. \quad (2.40)$$

The transfer functions, which directly relate inputs and outputs, can be solved for:

$$\tilde{\mathbf{x}} = \Theta(B_{V_r}\tilde{\mathbf{u}}_{V_r} + B_\tau\tilde{\mathbf{u}}_\tau + B_E\tilde{\mathbf{u}}_E) \quad (2.41)$$

$$\tilde{\mathbf{y}} = \underbrace{[C\Theta B_{V_r} + D_{V_r}]}_{\text{admittance}} \tilde{\mathbf{u}}_{V_r} + \underbrace{[C\Theta B_\tau] \tilde{\mathbf{u}}_\tau}_{\text{current injection}} + \underbrace{[C\Theta B_E + D_E] \tilde{\mathbf{u}}_E}_{\text{current injection}}. \quad (2.42)$$

where  $\Theta = (s\mathbb{1} - A)^{-1}$ . In this formulation, the following observations may be made. The term which relates terminal bus voltage differentials to the current flows acts as an admittance matrix. Similarly, the term relating the torque perturbation to the current flows, in conjunction with the torque perturbation term itself, acts as one *potential* current source, and the terms relating the generator EMF perturbation to the currents flows, in conjunction with the EMF perturbation term itself, acts as a second *potential* current source. These are explicitly defined as

$$\mathcal{Y}(s) = C(s\mathbb{1} - A)^{-1}B_{V_r} + D_{V_r} \quad (2.43)$$

$$\mathcal{I}_\tau(s) = [C(s\mathbb{1} - A)^{-1}B_\tau] \tilde{\tau}_m \quad (2.44)$$

$$\mathcal{I}_E(s) = [C(s\mathbb{1} - A)^{-1}B_E + D_E] \tilde{E}' \quad (2.45)$$

With this observation, the following intuitive model formulation emerges:

$$\underbrace{\begin{bmatrix} \tilde{I}_R(s) \\ \tilde{I}_I(s) \end{bmatrix}}_{\tilde{\mathbf{I}}(s)} = \mathcal{Y}(s) \underbrace{\begin{bmatrix} \tilde{V}_r(s) \\ \tilde{V}_I(s) \end{bmatrix}}_{\tilde{\mathbf{V}}(s)} + \mathcal{I}_\tau(s) + \mathcal{I}_E(s), \quad (2.46)$$

where  $\mathcal{Y}$  is a  $2 \times 2$  matrix, and  $\tilde{I}_r(s) = \mathcal{L}\{\Delta \operatorname{Re}(\tilde{I})\}$ ,  $\tilde{I}_I(s) = \mathcal{L}\{\Delta \operatorname{Im}(\tilde{I})\}$  etc.

**Definition 3.** We refer to the framework presented by (2.46) as an **equivalent circuit transformation**.

This equivalent circuit transformation will be used in later sections to perform

quadratic energy function analysis.

## From Transfer Function to Frequency Response Function

The primary usefulness of (2.46) comes when evaluating the expression in the frequency domain by setting  $s = j\Omega$ . In this case,  $\mathcal{Y}(s = j\Omega)$  becomes a Frequency Response Function (FRF) which relates voltage and current spectrums.

**Remark 1.** *In this thesis, both  $\omega$  and  $\Omega$  represent radial frequency. For the remainder of this chapter,  $\omega$  will represent the frequency associated with a generator's rotor (i.e. grid frequency), while  $\Omega$  will represent the frequency domain variable from  $s = \sigma + j\Omega$ .*

Particularly, we are interested in the frequency  $\Omega = \Omega_d$ , where  $\Omega_d$  is the forcing frequency associated with an observed FO. The structure of the FRF  $\mathcal{Y}(s = j\Omega)$  evaluated at forcing frequency  $\Omega_d$  may be written explicitly as

$$\mathcal{Y}(s = j\Omega_d) = \gamma \begin{bmatrix} \sin \delta \cos \delta & -\cos^2 \delta \\ \sin^2 \delta & -\sin \delta \cos \delta \end{bmatrix} + \begin{bmatrix} 0 & \frac{1}{X'_d} \\ \frac{-1}{X'_d} & 0 \end{bmatrix} \quad (2.47)$$

$$\gamma = \frac{\frac{E'^2}{X'^2}}{\left( \frac{V_t E'}{X'_d} \cos(\varphi) - M\Omega_d^2 \right) + j(\Omega_d D)} \quad (2.48)$$

and the voltage and current signals may also be evaluated at the forcing frequency  $s = j\Omega_d$ . Of course, this is equivalent to evaluating an associated Fourier transform at the forcing frequency:

$$\tilde{X}(\Omega_d) = \int_{-\infty}^{+\infty} X(t) e^{j\Omega_d t} dt, \quad X \in \{\Delta \text{Re}(\tilde{V}_t), \Delta \text{Im}(\tilde{V}_t), \Delta \text{Re}(\tilde{I}), \Delta \text{Im}(\tilde{I})\}. \quad (2.49)$$

Additionally, the negative current injections  $\mathcal{I}_\tau$  and  $\mathcal{I}_E$  are given as

$$\mathcal{I}_\tau(s = j\Omega_d) = -\gamma \frac{X'_d}{E'} \begin{bmatrix} \cos(\delta) \\ \sin(\delta) \end{bmatrix} \tilde{\tau}_m \quad (2.50)$$

$$\mathcal{I}_E(s = j\Omega_d) = \left( \gamma \frac{V_t \sin(\varphi)}{E'} \begin{bmatrix} \cos(\delta) \\ \sin(\delta) \end{bmatrix} + \begin{bmatrix} -\frac{\sin(\delta)}{X'_d} \\ \frac{\cos(\delta)}{X'_d} \end{bmatrix} \right) \tilde{E}' \quad (2.51)$$

In (2.50)-(2.51), we note that  $\tilde{\tau}_m$  and  $\tilde{E}'$  represent are the Fourier transforms of torque and EMF perturbations (i.e.  $\tilde{\tau}_m = \mathcal{F}\{\Delta\tau_m\}$  and  $\tilde{E}' = \mathcal{F}\{\Delta E'\}$ ) evaluated at the frequency  $\Omega_d$ , as in (2.49). For this reason, we can refer to them as “phasors”, since they are complex values with an associated magnitude and phase.

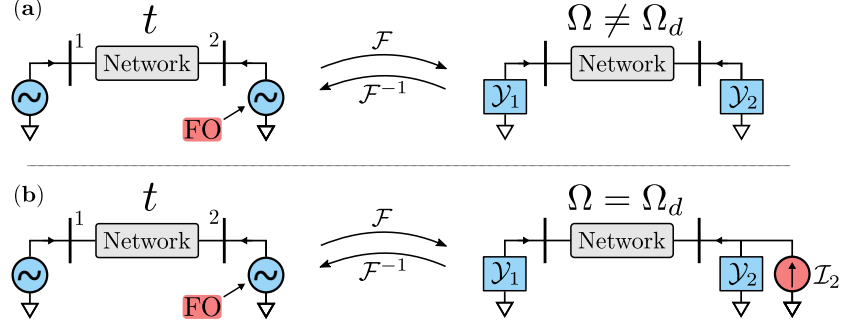


Figure 2-3: A FO in the time domain shows up as a current injection source at the forcing frequency  $\Omega_d$  (panel (b)) when the system is transformed into the frequency domain ( $\mathcal{F}$ ). When  $\Omega \neq \Omega_d$ , this current injection is absent (panel (a)).

**Remark 2.** To avoid confusion, we note that the frequencies  $\Omega$  and  $\Omega_d$  have nothing to do with the fundamental AC frequency of 50 or 60 Hz; the transformation in (2.49) is performed on phasors with AC frequencies already excluded.

Most usefully, when a FO does exist at some generator, due to an oscillatory torque perturbation  $\tilde{\tau}_m$  or an exciter oscillation  $\tilde{E}'$ , for example, then the associated current injection will only show up in the equivalent circuit representation at the forcing frequency  $\Omega_d$ ; this is shown in panel (b) of Fig. 2-3. At all other non-forcing frequencies (i.e.  $\Omega \neq \Omega_d$ ), the current injection is absent; this is shown in panel (a) of Fig. 2-3.

### Transformation to a Local $dq$ Reference Frame

When considering the structures of (2.47), (2.50), and (2.51), it is clear that significant simplification may occur by passing to a  $dq$  reference frame, i.e. rotating each expression in the direction of the rotor angle  $\delta$ . We use the convention of  $dq$  axes orientation from [105], so the rotational matrix defined as  $T_2$  is

$$T_2 = \begin{bmatrix} \cos(\delta) & \sin(\delta) \\ -\sin(\delta) & \cos(\delta) \end{bmatrix}. \quad (2.52)$$

This transformation is applied to the state space current injection equation  $\tilde{\mathbf{I}}_p = \tilde{\mathcal{V}}_p + \tilde{\mathcal{I}}_\tau + \tilde{\mathcal{I}}_E$  of (2.46). The superscript  $dq$  denotes variables given in the  $dq$  reference frame, while no superscript denotes variables in the real and imaginary reference frame. For instance,  $\mathbf{X} = [X_r \ X_i]^T$  is defined in the real and imaginary coordinate

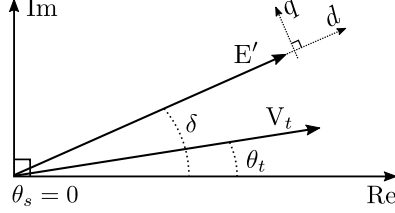


Figure 2-4: Orientation of the direct ( $d$ ) and quadrature ( $q$ ) axes.

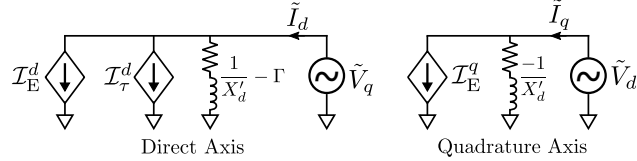


Figure 2-5: Circuit diagram interpretation of equation (2.53), where  $\mathcal{I}_\tau^d = -\gamma \frac{X_d'}{E'} \tilde{\tau}_m$ ,  $\mathcal{I}_E^d = \gamma \frac{V_t \sin(\varphi)}{E'} \tilde{E}'$ , and  $\mathcal{I}_E^q = \frac{1}{X_d'} \tilde{E}'$  as taken from (2.55) and (2.56). At non-source buses,  $\mathcal{I}_\tau^d = \mathcal{I}_E^d = \mathcal{I}_E^q = 0$  and all current flows are caused by terminal voltage deviations.

system while  $\mathbf{X}^{dq} = [X_d \ X_q]^T$  is defined in the  $dq$  coordinate system. Thus,

$$\tilde{\mathbf{I}}_p^{dq} = \mathcal{Y}^{dq} \tilde{\mathbf{V}}_p^{dq} + \mathcal{I}_\tau^{dq} + \mathcal{I}_E^{dq}, \quad (2.53)$$

where  $\mathcal{Y}^{dq} = T_2 \mathcal{Y} T_2^{-1}$  and  $\tilde{\mathbf{x}}^{dq} = T_2 \tilde{\mathbf{x}}$  for any vector  $\mathbf{x}$ . Fig. 2-4 provides a visualization of these transformations. In the new coordinate system, the direct ( $d$ ) axis is in line with  $\delta$ , and the quadrature ( $q$ ) axis is perpendicular to the direct axis. Once transformed, the the admittance matrix and negative current injections are given by

$$\mathcal{Y}^{dq} = \begin{bmatrix} 0 & \frac{1}{X_d'} - \gamma \\ -\frac{1}{X_d'} & 0 \end{bmatrix} \quad (2.54)$$

$$\mathcal{I}_\tau^{dq} = \begin{bmatrix} -\gamma \frac{X_d'}{E'} \\ 0 \end{bmatrix} \tilde{\tau}_m \quad (2.55)$$

$$\mathcal{I}_E^{dq} = \begin{bmatrix} \gamma \frac{V_t \sin(\varphi)}{E'} \\ \frac{1}{X_d'} \end{bmatrix} \tilde{E}'. \quad (2.56)$$

A conventional orthogonal circuit diagram interpretation of this result is given by Fig. 2-5. It is important to remember that  $\tilde{V}_d$ ,  $\tilde{V}_q$ ,  $\tilde{I}_d$ , and  $\tilde{I}_q$  are all complex phasors. This is a deviation from the standard power systems literature related to generator analysis (such as [158]) which uses orthogonal  $dq$  decomposition in order to treat  $V_q$  and  $V_d$  as real valued signals. We note that the purpose of performing this  $dq$  rotation is to build the intuition provided by equations (2.54-2.56) and Fig. 2-5. In general,

transforming voltages and current into a  $dq$  reference frame is not necessary.

### Extension of Methods to an Arbitrary Network Component

Although the proposed methods for quantifying the effective admittance and current injections of a generator are developed for a low order model, the same techniques may be employed for an arbitrarily complex model. We consider a power system component, shown in Fig. 2-6, whose dynamics are governed according to the Differential Algebraic Equation (DAE) set

$$\dot{\mathbf{x}} = \mathbf{f}(\mathbf{x}, \mathbf{u}, \mathbf{u}_v) \quad (2.57a)$$

$$\mathbf{y} = \mathbf{g}(\mathbf{x}, \mathbf{u}, \mathbf{u}_v), \quad (2.57b)$$

with state vector  $\mathbf{x}$ , terminal voltage input vector  $\mathbf{u}_v = [\mathbf{V}, \theta_t]$ , and terminal current output vector  $\mathbf{y} = [\mathbf{I}, \phi]$ . All other inputs, such as outside control signals, are collected in  $\mathbf{u}$ . During the modeling time period of interest, for a non-FO source generator, these other extraneous inputs are assumed constant:  $\dot{\mathbf{u}} = \mathbf{0}$ .

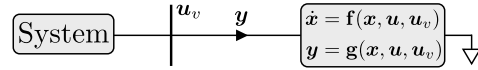


Figure 2-6: DAE modeled component tied to a larger power system.

We linearize (2.57) around a steady state operating point to linearly relate the voltage and current perturbations:

$$\Delta\dot{\mathbf{x}} = \mathbf{A}\Delta\mathbf{x} + \mathbf{B}\Delta\mathbf{u}_v \quad (2.58a)$$

$$\Delta\mathbf{y} = \mathbf{C}\Delta\mathbf{x} + \mathbf{D}\Delta\mathbf{u}_v, \quad (2.58b)$$

such that  $\mathbf{A} = \mathbf{f}_{\mathbf{x}}$ ,  $\mathbf{B} = \mathbf{f}_{\mathbf{u}_v}$ ,  $\mathbf{C} = \mathbf{g}_{\mathbf{x}}$ ,  $\mathbf{D} = \mathbf{g}_{\mathbf{u}_v}$ . Assuming (2.58) is BIBO stable [100], its Fourier transform admits the Frequency Response Function (FRF) of the component:

$$\tilde{\mathbf{y}}(\Omega) = \underbrace{(\mathbf{C}(j\Omega\mathbb{1} - \mathbf{A})^{-1}\mathbf{B} + \mathbf{D})}_{\mathcal{Y}(\Omega)} \tilde{\mathbf{u}}_v(\Omega), \quad (2.59)$$

where  $\Omega$  is the angular frequency of the input and output signals, and  $\mathcal{Y} \equiv \mathcal{Y}(\Omega) \in \mathbb{C}^{2 \times 2}$  is referred to as the admittance matrix<sup>3</sup> relating voltage  $\tilde{\mathbf{u}}_v(\Omega) \in \mathbb{C}^{2 \times 1}$  and current

---

<sup>3</sup>When referring to  $\mathcal{Y}(\Omega)$ , we will use the terms FRF and admittance interchangeably, depending

$\tilde{\mathbf{y}}(\Omega) \in \mathbb{C}^{2 \times 1}$  perturbations. The FRF  $\mathcal{Y}$  relates the Fourier transform of the inputs and the outputs across the full spectrum frequencies, where the Fourier transform of the time domain signal  $x(t)$ , for example, is given by  $\tilde{x}(\Omega) = \int_{-\infty}^{+\infty} x(t)e^{-j\Omega t}dt$ . In polar coordinates, (2.59) can be written more explicitly as

$$\underbrace{\begin{bmatrix} \tilde{I}(\Omega) \\ \tilde{\phi}(\Omega) \end{bmatrix}}_{\tilde{\mathbf{I}}_p(\Omega)} = \underbrace{\begin{bmatrix} \mathcal{Y}_{11} & \mathcal{Y}_{12} \\ \mathcal{Y}_{21} & \mathcal{Y}_{22} \end{bmatrix}}_{\mathcal{Y}(\Omega)} \underbrace{\begin{bmatrix} \tilde{V}(\Omega) \\ \tilde{\theta}(\Omega) \end{bmatrix}}_{\tilde{\mathbf{V}}_p(\Omega)}, \quad \Omega \in [0 \ \infty). \quad (2.60)$$

We note that the input and output perturbations of (2.59) can be given in polar ( $\tilde{V}, \tilde{\theta}, \tilde{I}, \tilde{\phi}$ ) or rectangular ( $\tilde{V}_r, \tilde{V}_i, \tilde{I}_r, \tilde{I}_i$ ) coordinates depending on convenience. Of course, generators are complex machines which may have a variety of controllers (AVR, PSS, etc.) and a multitude of states, but this process may be generalized for arbitrarily complex DAE systems  $\mathbf{f}(\cdot)$  and  $\mathbf{g}(\cdot)$  so long as terminal current can be written as a function of terminal voltage.

**Example: 6<sup>th</sup> Order Generator Model with AVR:** As a particular example, we choose to consider a generator model presented in the standardized test cases of [117]. This generator model may be approximated by the 6<sup>th</sup> order synchronous model presented in [129], where the  $d$  and  $q$  subscripts denote the Park reference frames. This model is chosen since it will be used to collect test results in 2.2.4:

$$\dot{\delta} = \Delta\omega \quad (2.61)$$

$$M\Delta\dot{\omega} = P_m - P_e - D\Delta\omega \quad (2.62)$$

$$T'_{d0}\dot{e}'_q = E_f - (X_d - X'_d - \gamma_d)i_d - e'_q \quad (2.63)$$

$$T'_{q0}\dot{e}'_d = (X_q - X'_q - \gamma_q)i_q - e'_d \quad (2.64)$$

$$T''_{d0}\dot{e}''_q = e'_q - e''_q - (X'_d - X''_d + \gamma_d)i_d \quad (2.65)$$

$$T''_{q0}\dot{e}''_d = e'_d - e''_d + (X'_q - X''_q + \gamma_q)i_q, \quad (2.66)$$

where  $\gamma_x = T''_{x0}X''_x(X_x - X'_x)/(T'_{x0}X'_x)$ ,  $x \in \{d, q\}$ . With stator resistance neglected, the electrical power is  $P_e = e_d i_d + e_q i_q$ , and the terminal currents ( $i_d, i_q$ ) can be written in terms of the terminal voltages ( $e_d = V_t \sin(\delta - \theta_t)$ ,  $e_q = V_t \cos(\delta - \theta_t)$ )

---

on the context of usage. In this thesis, though, we will be primarily concerned with the effects of the FRF matrix at the relevant forcing frequency  $\Omega_d$  of the FO.

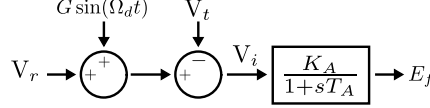


Figure 2-7: Voltage excitation system associated with source bus #1 in subsection 2.2.4. The forced oscillation source is given by  $G \sin(\Omega_d t)$ .

and the subtransient voltages ( $e_d''$ ,  $e_q''$ ):

$$\begin{bmatrix} i_d \\ i_q \end{bmatrix} = \begin{bmatrix} R & -X_q'' \\ X_d'' & R \end{bmatrix}^{-1} \begin{bmatrix} e_d'' - V_t \sin(\delta - \theta_t) \\ e_q'' - V_t \cos(\delta - \theta_t) \end{bmatrix}, \quad (2.67)$$

where  $R = 0$  when neglected. The real and imaginary *negative* current injections are computed by simply rotating  $i_d$  and  $i_q$  in rectangular space [158] and negating. Equation (2.68) is a time domain transformation and should not be confused with the phasor reference frame transformation of (2.52):

$$\begin{bmatrix} I_r \\ I_i \end{bmatrix} = - \begin{bmatrix} \sin(\delta) & \cos(\delta) \\ -\cos(\delta) & \sin(\delta) \end{bmatrix} \begin{bmatrix} i_d \\ i_q \end{bmatrix}. \quad (2.68)$$

Finally, since PMUs measure the magnitude and phase of voltage and current signals, it is numerically convenient to have the generator's FRF relate voltage magnitude and phase perturbations with current magnitude and phase perturbations. Therefore, the generator model needs some nonlinear function relating its state and algebraic variables to the current magnitude ( $I$ ) and current phase ( $\phi$ ):

$$I = \sqrt{I_r^2 + I_i^2} \quad (2.69)$$

$$\phi = \tan^{-1} \left( \frac{I_i}{I_r} \right). \quad (2.70)$$

Controllers may also be included in the generator model. The static voltage excitation system associated with the source generator of test case “F1” in [117] is approximated by the block diagram in Fig. 2-7 (limits excluded). The source of the forced oscillation is given by  $G \sin(\Omega_d t)$  with gain  $G$  and forcing frequency  $\Omega_d$ . This forcing function is not included in the system model; it is only shown for illustration. The exciter’s associated differential equation follows:

$$T_A \dot{E}_f = K_A (V_{\text{ref}} - V_t) - E_f. \quad (2.71)$$

Now that the generator's full set of nonlinear DAEs ( $\mathbf{f}$  and  $\mathbf{g}$ ) have been specified, with input vector  $\mathbf{u}_v = [V \ \theta]^T$  and output vector  $\mathbf{y} = [I \ \phi]^T$ , these DAEs can be linearized and the generator's FRF  $\mathcal{Y}$  can be built via (2.59).

### 2.2.2 Leveraging $\mathcal{Y}$ For Source Detection

In a deterministic power system where generator model parameters are fully known, measurement noise is negligible and perturbations are small, the FRF  $\mathcal{Y}$  can fully predict the measured spectrum of the generator output  $\tilde{\mathbf{I}}_p(\Omega)$  for a given measured spectrum input  $\tilde{\mathbf{V}}_p(\Omega)$  at all non-source generators. In this *ideal* system, the following simple test may be naively applied at each generator across the full spectrum of frequencies.

$$\tilde{\mathbf{I}}_p = \mathcal{Y}\tilde{\mathbf{V}}_p \rightarrow \text{Non-source generator} \quad (2.72)$$

$$\tilde{\mathbf{I}}_p \neq \mathcal{Y}\tilde{\mathbf{V}}_p \rightarrow \text{Source generator} \quad (2.73)$$

In other words, if the measured current spectrum  $\tilde{\mathbf{I}}_p$  and the predicted current spectrum  $\mathcal{Y}\tilde{\mathbf{V}}_p$  match, then the generator has no internal oscillation source. If, though,  $\tilde{\mathbf{I}}_p \neq \mathcal{Y}\tilde{\mathbf{V}}_p$  at some particular frequency, then a current source (forced oscillation) may be present in the generator at said frequency. To implement this test on any given generator, there must be a PMU present which is capable of measuring the generator's terminal voltages and currents so that the respective spectrums may be computed.

The realities of power system operation can prevent the naive tests of (2.72) and (2.73) from being directly implemented. There are three primary sources of potential error in this process. First, nonlinearities may prevent the admittance matrix, which is built on a linearized system model, from exactly predicting the generator dynamics. The extent of nonlinear system behavior depends on the size of the oscillation, but the associated error is typically small enough to be neglected. Secondly, in building the FRF, generator parameters (damping, time constants, etc.) may have a large degree of uncertainty. Accordingly, the results presented from tests on the 179-bus system consider this uncertainty. Additionally, this uncertainty is analyzed much more closely in the next section. Thirdly, despite the fact that IEEE Standard C37.242 specifies that PMU magnitude error must be below 0.1%, and timing error must be better than 1  $\mu\text{s}$  (or 0.02°) [2], additive measurement error from current and voltage transformer equipment may present additional error. Since measured voltage and current spectral

comparisons can breakdown severely when this nontrivial PMU measurement noise is present, the next section introduces a framework for dealing with the problem of additive measurement noise.

### Bounding Error Associated with PMU Measurement Noise

We define  $V(t)$ ,  $\theta(t)$ ,  $I(t)$  and  $\phi(t)$  to be the true voltage magnitude, voltage phase, current magnitude, and current phase time series vectors, respectively, at some generator bus. We further assume these vectors are perturbations from their respective steady state operating points. We now define the *measured* time series vectors to be  $\hat{X}(t)$ , where the true signals are corrupted by Additive White Gaussian Noise (AWGN) from  $\epsilon_X(t)$ :

$$\hat{X}(t) = X(t) + \epsilon_X(t), \quad X \in [V, \theta, I, \phi]. \quad (2.74)$$

In measuring the spectrum of  $\hat{X}(t)$ , we invoke the linearity property of the Fourier transform, such that

$$\mathcal{F}\{\hat{X}(t)\} = \tilde{\hat{X}}(\Omega) = \tilde{X}(\Omega) + \tilde{\epsilon}_X(\Omega). \quad (2.75)$$

The Fourier transform of AWGN will ideally have a flat magnitude spectrum (equal to  $\lambda_{\epsilon_X}$ ) and a uniformly distributed phase spectrum characterized by  $\mathcal{U}(0, 2\pi)$ :

$$\tilde{\epsilon}_X(\Omega) = \lambda_{\epsilon_X} e^{j\mathcal{U}(0, 2\pi)}, \quad \Omega \in [0, \infty). \quad (2.76)$$

In applying the admittance matrix transformation of (2.60) to calculate the difference in the measured ( $\tilde{\mathbf{I}}_p$ ) and the predicted ( $\mathcal{Y}\tilde{\mathbf{V}}_p$ ) currents at some non-source bus, the following error may be approximated:

$$\tilde{\mathbf{I}} - \mathcal{Y}\tilde{\mathbf{V}} = \begin{bmatrix} (\tilde{\mathbf{I}} + \tilde{\epsilon}_{\mathbf{I}}) - \mathcal{Y}_{11}(\tilde{\mathbf{V}} + \tilde{\epsilon}_{\mathbf{V}}) - \mathcal{Y}_{12}(\tilde{\theta} + \tilde{\epsilon}_{\theta}) \\ (\tilde{\phi} + \tilde{\epsilon}_{\phi}) - \mathcal{Y}_{21}(\tilde{\mathbf{V}} + \tilde{\epsilon}_{\mathbf{V}}) - \mathcal{Y}_{22}(\tilde{\theta} + \tilde{\epsilon}_{\theta}) \end{bmatrix} \quad (2.77a)$$

$$\approx \begin{bmatrix} \tilde{\epsilon}_{\mathbf{I}} - \mathcal{Y}_{11}\tilde{\epsilon}_{\mathbf{V}} - \mathcal{Y}_{12}\tilde{\epsilon}_{\theta} \\ \tilde{\epsilon}_{\phi} - \mathcal{Y}_{21}\tilde{\epsilon}_{\mathbf{V}} - \mathcal{Y}_{22}\tilde{\epsilon}_{\theta} \end{bmatrix} \quad (2.77b)$$

$$= \begin{bmatrix} \tilde{\epsilon}_{\mathbf{m}} \\ \tilde{\epsilon}_{\mathbf{p}} \end{bmatrix}, \quad (2.77c)$$

where the simplification in (2.77b) is due to the fact that, theoretically,  $\tilde{\mathbf{I}} - \mathcal{Y}_{11}\tilde{\mathbf{V}} - \mathcal{Y}_{12}\tilde{\theta} = 0$  and  $\tilde{\phi} - \mathcal{Y}_{21}\tilde{\mathbf{V}} - \mathcal{Y}_{22}\tilde{\theta} = 0$  for all frequencies. In (2.77c), the variables  $\tilde{\epsilon}_{\mathbf{m}}$

and  $\tilde{\epsilon}_{\mathbf{p}}$  have been defined which represent the aggregate measurement error spectrums associated with  $\tilde{\mathbf{I}}_p - \mathcal{Y}\tilde{\mathbf{V}}_p$ . We seek to quantify this error, at each frequency  $\Omega$ , with the  $l2$  norm such that

$$\|\tilde{\mathbf{I}}_p - \mathcal{Y}\tilde{\mathbf{V}}_p\|_2 = \sqrt{|\tilde{\epsilon}_{\mathbf{m}}|^2 + |\tilde{\epsilon}_{\mathbf{p}}|^2}. \quad (2.78)$$

As can been seen from (2.77b), this error norm will be maximized when the complex entries meet the phase conditions  $\angle\tilde{\epsilon}_I = -\angle(\mathcal{Y}_{11}\tilde{\epsilon}_V) = -\angle(\mathcal{Y}_{12}\tilde{\epsilon}_\theta)$  and  $\angle\tilde{\epsilon}_\phi = -\angle(\mathcal{Y}_{21}\tilde{\epsilon}_V) = -\angle(\mathcal{Y}_{22}\tilde{\epsilon}_\theta)$ . Since the measurement error spectrums have uniformly distributed phase angles  $\mathcal{U}(0, 2\pi)$ , this is a plausible scenario and it provides us with a theoretical upper bound on the measurement error for a generator with known model parameters and no forced oscillation:

$$\Sigma_2 := \sqrt{\max \{\tilde{\epsilon}_{\mathbf{m}}\}^2 + \max \{\tilde{\epsilon}_{\mathbf{p}}\}^2}, \quad (2.79)$$

where we give the following definitions for  $\max \{\tilde{\epsilon}_{\mathbf{m}}\}$  and  $\max \{\tilde{\epsilon}_{\mathbf{p}}\}$ :

$$\max \{\tilde{\epsilon}_{\mathbf{m}}\} = |\tilde{\epsilon}_I| + |\mathcal{Y}_{11}\tilde{\epsilon}_V| + |\mathcal{Y}_{12}\tilde{\epsilon}_\theta| \quad (2.80)$$

$$\max \{\tilde{\epsilon}_{\mathbf{p}}\} = |\tilde{\epsilon}_\phi| + |\mathcal{Y}_{21}\tilde{\epsilon}_V| + |\mathcal{Y}_{22}\tilde{\epsilon}_\theta|. \quad (2.81)$$

In (2.79),  $\Sigma_2$  is the maximum upper bound on the aggregate measurement error, and it is uniquely defined for all frequencies since both  $\tilde{\epsilon}_{\mathbf{m}}$  and  $\tilde{\epsilon}_{\mathbf{p}}$  are direct functions of frequency. If  $\|\tilde{\mathbf{I}}_p - \mathcal{Y}\tilde{\mathbf{V}}_p\|_2$  is significantly larger than  $\Sigma_2$  at some frequency, then PMU measurement error may not be the source of the error, and an internal forced oscillation may be to blame. In calculating (2.80) and (2.81), the operator must have a sense of the PMU measurement noise strength. Ideally, this noise strength is constant in the frequency domain, but realistically, it fluctuates for a time limited signal  $\epsilon_X(t)$ . Therefore, in estimating the measurement noise strength in any PMU signal, a system operator should be conservative in choosing values for  $\lambda_{\epsilon_X}$  from (2.76). One such conservative choice, which has been found via experimentation, is to set  $\lambda_{\epsilon_X}$  equal to twice the expected value of the magnitude of the Fast Fourier Transform (FFT) of its associated time domain signal  $\epsilon_X(t)$ , where  $\epsilon_X(t)$  is constructed by sampling length( $t$ ) times from  $\mathcal{N}(0, \sigma_{\text{PMU}}^2)$ . Therefore,

$$\lambda_{\epsilon_X} \approx 2 \cdot E[|\text{fft}\{\epsilon_X(t)\}|]. \quad (2.82)$$

Table 2.1: Definition of LSD Terms from (2.83)

$\tilde{\mathbf{I}}_p$	<b>Measured</b> $2 \times 1$ vector of complex valued current magnitude and phase variables $\tilde{\mathbf{I}}(\Omega)$ and $\tilde{\phi}(\Omega)$
$\tilde{\mathbf{V}}_p$	<b>Measured</b> $2 \times 1$ vector of complex valued voltage magnitude and phase variables $\tilde{\mathbf{V}}(\Omega)$ and $\tilde{\theta}(\Omega)$
$\mathcal{Y}$	<b>Modeled</b> $2 \times 2$ frequency dependent complex admittance matrix, as given by (2.59)
$\Sigma_2$	<b>Estimated</b> upper bound (frequency dependent) on measurement error effects, as given by the maximum $l_2$ norm of the vector in (2.77c)

### 2.2.3 Defining a Practical Source Location Technique

In computing the error between the measured and predicted currents at a given bus, (2.79) defines a useful approximate upper bound on the associated measurement error. As long as the strength of the measurement noise is known (or can be estimated, such as in [27]), this upper bound can be computed for all frequencies. Assuming an accurate FRF, significant deviations from this upper bound at any given frequency may indicate the presence of an internal current source (forced oscillation). To quantify the size of the spectral deviation at each frequency, we introduce a metric termed the Local Spectral Deviation (LSD). Its form is given as follows:

$$\text{LSD}(\Omega) = \|\tilde{\mathbf{I}}_p(\Omega) - \mathcal{Y}\tilde{\mathbf{V}}_p(\Omega)\|_2 - \Sigma_2(\Omega). \quad (2.83)$$

Table 2.1 summarizes the terms in (2.83) which is computed at all generators for which terminal PMU data data is available. Formally, the LSD calculates the difference in the prediction error and the maximum bound on the effects of measurement noise error. To apply the LSD, the operator should first determine the central forcing frequency  $\Omega_d$  of the system (there may be multiple forcing frequencies if the system is experiencing multiple forced oscillations). In Algorithm (1), the steps for using generator terminal data to determine whether or not a generator is the source of a forced oscillation are formalized. In this algorithm, the operator specified threshold  $\iota$  is used to determine if the LSD is large enough for a generator to be deemed a source.

We note that this algorithm should be applied in situations where an operator has a high degree of certainty that the detected oscillations are in fact forced oscillations (references such as [198] and [200] can be useful to this end); the method we have developed will not locate the source of negative damping in a system, and therefore it will be unhelpful in locating the source of a natural oscillation.

---

**Algorithm 1** Generator Source Detection Method

---

**START**

- 1: Use available generator model data to construct DEA sets (2.57a) and (2.57b).
  - 2: Build FRF  $\mathcal{Y}$  of (2.59) which relates polar voltage and polar current deviations
  - 3: Acquire PMU time series vectors  $V(t)$ ,  $\theta(t)$ ,  $I(t)$ ,  $\phi(t)$  from generator terminals
  - 4: Subtract estimated steady state operating points from these time series vectors
  - 5: Take the FFT of these perturbation vectors to build  $\tilde{\mathbf{I}}(\Omega)$  and  $\tilde{\mathbf{V}}(\Omega)$
  - 6: Identify forcing frequency (or frequencies)  $\Omega_d$
  - 7: Compute the LSD of (2.83) at  $\Omega_d$
  - 8: **if** LSD < 0 **then**
  - 9:     Prediction error is less than  $\Sigma_2$ : Generator **is not** a source
  - 10: **else if**  $0 < \text{LSD} < \iota$  **then**
  - 11:     Prediction error is larger than  $\Sigma_2$  but less than  $\iota$ : Generator **probably not** a source
  - 12: **else** Prediction error is larger than threshold
  - 13:     Generator **is** a source
  - end**
- 

## 2.2.4 Test Results

In this section, we present five sets of test results. First, we consider a 3-bus system of two 2<sup>nd</sup> order generators tied to an infinite bus. Second, we test our method on the modified WECC 179-bus system in the presence of a forced oscillation. Third, we test our method on the modified WECC 179-bus system in the presence of a natural oscillation. Fourth, we apply a rectangular forced oscillation in the WECC 179-bus system when a poorly damped mode is present. And fifth, we contrast the effectiveness of the DEF method and the FRF source location method in the context of a three-bus system with a constant impedance load.

### Radial Generators Tied to Infinite Bus

It is well known in the literature [135, 10] that relying on the location of the largest detected oscillations is an unreliable way for determining the source of a forced oscillation. Because of the excitation of local resonances, large power oscillations can occur at non-source generators. We demonstrate the effectiveness of our source location technique in the presence of resonance amplification occurring on a non-source generator by simulating the simple 3-bus system of two radial generators tied to an infinite bus as given by Fig. 2-8. In this system, the lines have  $X = 0.1$  and  $R = 0.01$ , and other system parameters are summarized in Table 2.2. A forced oscillation is applied to the mechanical torque of generator 1 via  $\tau_m = \tau_0 + \alpha \sin(\Omega_d t)$ . Additionally, ambient white noise is applied to the magnitude and the phase of the infinite bus voltage to mimic system fluctuations.

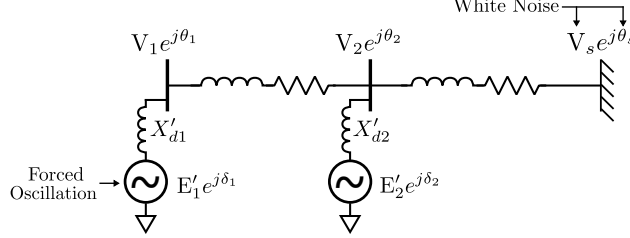


Figure 2-8: 3 Bus Diagram with Infinite Bus. Both generators are 2<sup>nd</sup> order, and a mechanically forced oscillation  $\tau_m = \tau_0 + \tilde{\tau}$  is placed on generator 1. White noise is applied to the phase and magnitude of the infinite bus voltage.

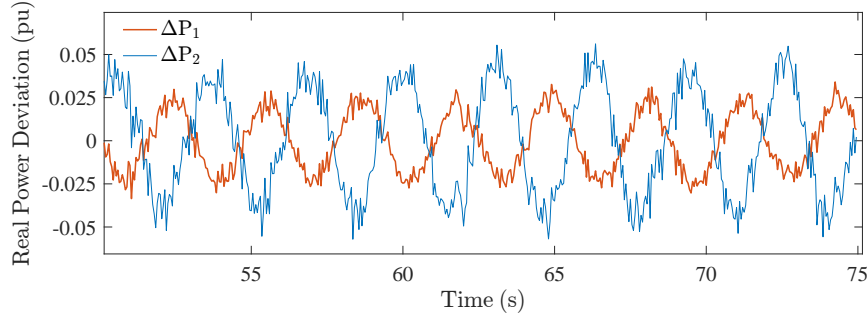


Figure 2-9: Active power injection deviations for generators 1 and 2.

The driving frequency of the forced oscillation  $\Omega_d$  is chosen by considering the eigenvalues of the system. To find these eigenvalues, the system DAEs of  $\dot{\mathbf{x}} = \mathbf{f}(\mathbf{x}, \mathbf{y})$  and  $0 = \mathbf{g}(\mathbf{x}, \mathbf{y})$  were linearized such that  $\Delta\dot{\mathbf{x}} = \mathbf{f}_x\Delta\mathbf{x} + \mathbf{f}_y\Delta\mathbf{y}$  and  $0 = \mathbf{g}_x\Delta\mathbf{x} + \mathbf{g}_y\Delta\mathbf{y}$ . The imaginary parts of the complex eigenvalues of the state matrix  $\mathbf{A}_s = \mathbf{f}_x - \mathbf{f}_y\mathbf{g}_y^{-1}\mathbf{g}_x$  yield the set of natural frequencies. The natural modes associated with generators 1 and 2 are  $\Omega_{d1} = 0.708 \frac{\text{rad}}{\text{sec}}$  and  $\Omega_{d2} = 1.915 \frac{\text{rad}}{\text{sec}}$ , respectively. We therefore choose to mechanically force the system at  $f_d = 2$  since this is close to, but not directly on top of, the natural mode of generator 2. Fig. 2-9 shows a time domain simulation plot of the power injection deviations at each generator. The standard deviation of power injections at generator 2 is almost twice as large as that of generator 1, and the forcing frequency of  $f_d = \frac{2}{2\pi}$  Hz can be seen underneath the system noise.

After collecting the time domain voltage and current data from the simulation, the predicted ( $\mathcal{Y}\tilde{\mathbf{V}}_p$ ) and measured ( $\tilde{\mathbf{I}}_p$ ) current spectrums were compared. For illustrative purposes, measurement noise is not applied and generator model parameter uncertainty is neglected such that  $\mathcal{Y}$  is known exactly for both generators. For a small frequency range, the magnitude spectrum comparisons are given by Fig. 2-10. There are two important observations concerning these comparisons. First, the spectral peaks of generator 2 (the non-source generator) at the forcing frequency of  $f_d = 0.32$

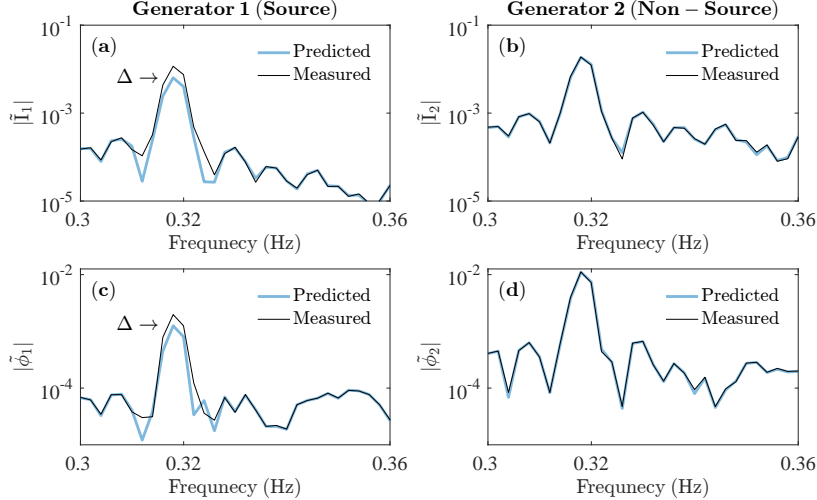


Figure 2-10: Spectral magnitude of current magnitude (panels **(a)** & **(b)**) and current phase (panels **(c)** & **(d)**) perturbations are given for each generator. The forcing frequency is located at  $f_d = 0.32$ . The  $\Delta$  symbol in panels **(a)** and **(c)** highlight the locations of significant deviations between the predicted and expected spectrums.

Table 2.2: Generator Parameters

	$M$	$D$	$X'_d$	$E'$	$V_t$	$\varphi$
Gen 1	4	1	0.25	1.019	1	0.248
Gen 2	1	0.25	0.2	1.031	1	0.117

are much larger than the spectral peaks of generator 1 (the source generator) due to resonance. Second, the predicted and measured spectrums at the forcing frequency of the source generator (seen in panels **(a)** & **(c)**) misalign significantly. From direct visual inspection of Fig. 2-10, it is clear that a modest internal oscillation is present on generator 1 which is causing deviations between the measured and the predicted spectrums (the LSD is not computed since measurement noise is not applied in this test).

### WECC 179-Bus System (Forced Oscillation)

For further validation, we apply these methods on data collected from the WECC 179-bus system in the presence of multiple forced oscillations. As suggested in [117], the standardized test case files were downloaded and simulated using Power Systems Analysis Toolbox (PSAT) [129]. We chose to investigate the performance of our methods on a modified version of test case “F1”. In “F1”, a scaled 0.86 Hz sinusoid is added to the reference signal of the AVR attached to the source generator at bus 4 (see [117] for a full system map). In the system, all loads are constant power while all

non-source generators are modeled as 2<sup>nd</sup> order classical machines with parameters  $D = 4$ ,  $X'_d = 0.25$ , and various inertias around  $H = 3$  (machine base). The source generator is a sixth order synchronous machine with an Automatic Voltage Regulator (AVR) modeled by Fig. 2-7. To engender a realistic testing scenario, we modify this test case in three major ways.

1. Load fluctuations are added to all PQ loads. The dynamics of these fluctuations are modeled by the Ornstein-Uhlenbeck process [66] of

$$\dot{\mathbf{u}}(t) = -E_\tau \mathbf{u}(t) + \mathbb{1}\boldsymbol{\xi}, \quad (2.84)$$

$E_\tau$  is a diagonal matrix of inverse time correlations and  $\boldsymbol{\xi}$  is a vector of zero-mean independent Gaussian random variables (standard deviation  $\sigma = 2.5e-3$ ). The noise vector  $\mathbf{u}(t)$  is added to the PQ loads such that

$$\mathbf{S}(t) = \mathbf{S}_0 (1 + \mathbf{u}(t)) \quad (2.85)$$

where  $\mathbf{S}(t) = \mathbf{P}(t) + j\mathbf{Q}(t)$ .

2. Two additional forced oscillations are added to the system (along with the AVR oscillation at generator bus 4). Each new oscillation is added to the mechanical torque of a 2<sup>nd</sup> order system generator according to

$$\tau_m = \tau_0(1 + \alpha_i \sin(\Omega_{d_i} t)). \quad (2.86)$$

These forced oscillations are arbitrarily added to generator buses 13 and 65, and in each case  $\alpha_i = 0.05$ . One of these oscillations is applied at  $f_d = 0.5$  Hz and the second is applied at  $f_d = 2.0$  Hz.

3. PMU measurement noise is added to the simulation data. AWGN with a standard deviation of  $\sigma = 0.3$  (% pu) is applied to all PMU times series vectors. This value of  $\sigma$  was chosen since the associated distribution tails realistically extend up to  $\pm 1\%$  pu. For a visualization of the effect of PMU measurement noise in the presence of system dynamics, Fig. 2-11 shows the bus voltage magnitude of a generator bus (bus 70). The applied noise greatly corrupts the FFT calculations.

After simulating the system for 100s, the PMU data from each generator were collected and analyzed according to Algorithm (1). In building the FRF of (2.59) for each

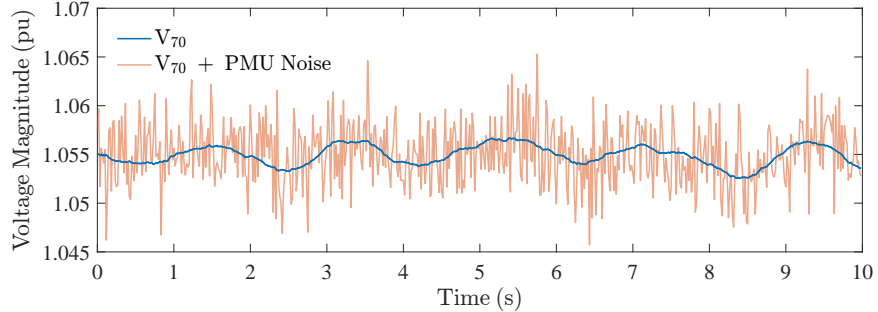


Figure 2-11: Actual and measured voltage magnitude at bus 70 (generator).

generator, it was assumed generator model parameters were initially known precisely (the end of this subsection will consider parameter uncertainty). Fig. 2-12 shows a sample of the simulation results associated with generator bus 9 (a non-source generator). These results show three spectral lines in each panel: (i) a measured spectrum magnitude, (ii) a predicted spectrum magnitude, and (iii) a maximum bound on the associated PMU measurement error  $\Sigma_2$ . (2.79) was used to compute  $\Sigma_2$  along with the approximation given by (2.82). We further assume that  $\sigma_{\text{PMU}}^2$  is roughly known for each PMU. Fig. 2-12 shows that the measured and predicted current (phase and magnitude) spectrums begin to deviate sharply for frequencies higher than 1 Hz. This is due to the fact that the admittance matrix amplifies the mid and high frequency measurement noise, which begins to dominate the voltage signal. Fig. 2-13 shows that the prediction error, though, is always lower than the measurement error bound. This implies that the generator at bus 9 is not an oscillation source.

The results of Figs. 2-12 and 2-13, which are associated with a non-source bus, can be contrasted to Figs. 2-14 and 2-15, which are associated with source bus 4. At this generator, the AVR reference is oscillated at  $f_d = 0.86$  Hz. This causes large observable differences in the measured and predicted magnitude spectrums. In Figs. 2-16 and 2-17, the prediction error and measurement noise error bounds are also contrasted at generators 13 and 65 (both source generators). As can be seen, there is significant spectral error at the forcing frequencies which the measurement noise cannot account for. This implies that both of these generators are sources of forced oscillations.

After analyzing the generator spectrums, the LSD can be quantified at each forcing frequency across all 29 system generators. These results are given in Fig 2-18. In plotting the LSD indices for each generator at each forcing frequency, the largest spectral deviations are easily found at the correct source generators. We do not formally define a threshold parameter  $\iota$ , which is required in the final steps of Algorithm

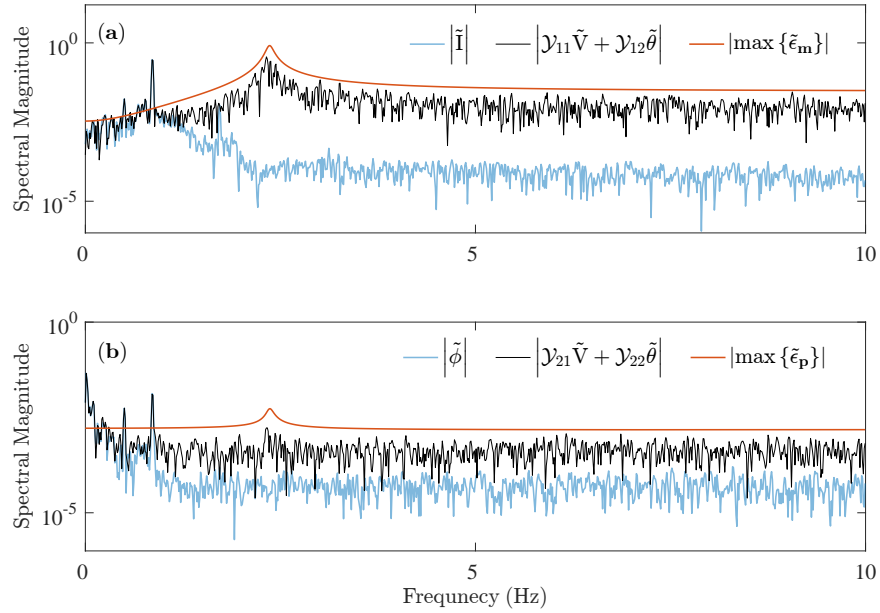


Figure 2-12: The spectral magnitude of the measured current magnitude (panel (a)) and the measured current phase (panel (b)) perturbations at generator bus 9 are given by the blue traces. The associated predicted spectral magnitudes are given by the black traces. Finally, the orange traces give the estimated maximum PMU measurement noise errors.

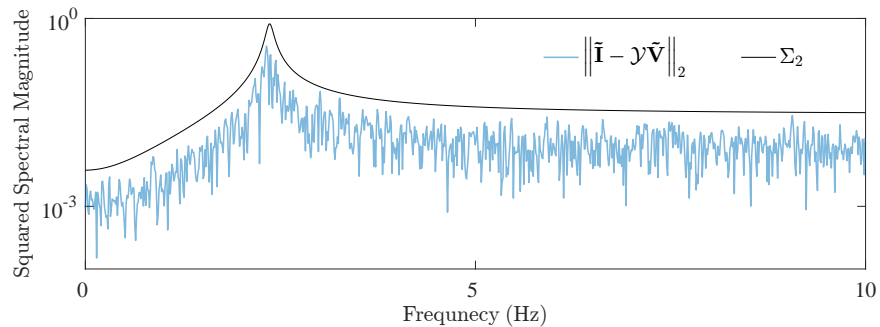


Figure 2-13: The prediction error  $\|\tilde{\mathbf{I}}_p - \mathcal{Y}\tilde{\mathbf{V}}_p\|_2$  and the maximum measurement noise error  $\Sigma_2$  associated with the non-source generator at bus 9 are plotted. Since there is no internal forced oscillation, prediction error is mostly caused by measurement error. Accordingly, the prediction error is bounded by the conservative maximum measurement noise error estimate  $\Sigma_2$ .

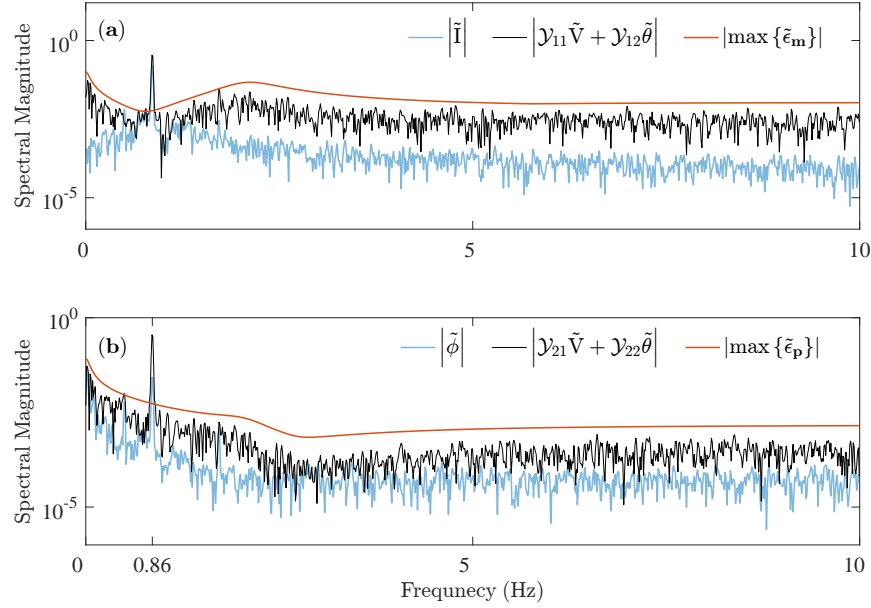


Figure 2-14: The spectral magnitude of the measured current magnitude (panel (a)) and the measured current phase (panel (b)) perturbations at generator bus 4 are given by the blue traces. The associated predicted spectral magnitudes are given by the black traces. Finally, the orange traces give the estimated maximum PMU measurement noise errors.

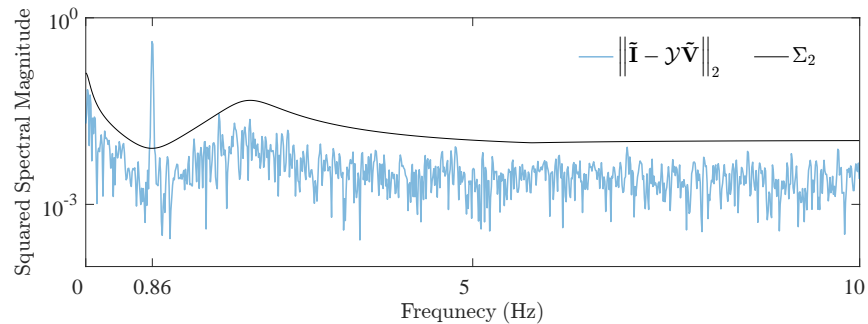


Figure 2-15: The prediction error  $\|\tilde{\mathbf{I}}_p - \mathcal{Y}\tilde{\mathbf{V}}_p\|_2$  and the maximum measurement noise error  $\Sigma_2$  associated with the source generator at bus 4 are plotted. Since there is an internal forced oscillation at  $f_d = 0.86$  Hz, the prediction error greatly exceeds the measurement noise error bound at this frequency.

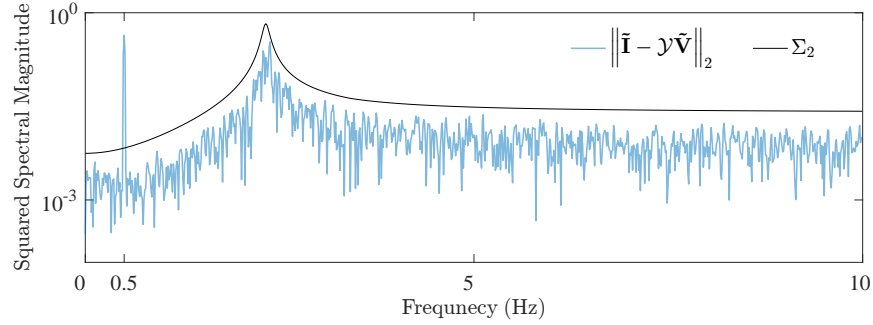


Figure 2-16: The prediction error  $\|\tilde{\mathbf{I}}_p - \mathcal{Y}\tilde{\mathbf{V}}_p\|_2$  and the maximum measurement noise error  $\Sigma_2$  associated with the source generator at bus 13 are plotted. Since there is an internal forced oscillation at  $f_d = 0.5$  Hz, the prediction error greatly exceeds the measurement noise error bound at this frequency.

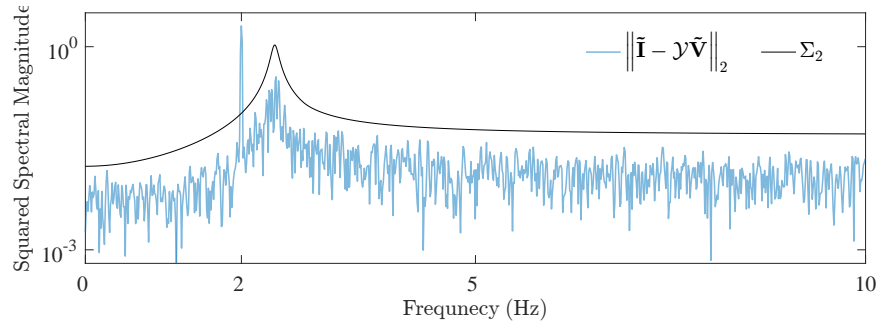


Figure 2-17: The prediction error  $\|\tilde{\mathbf{I}}_p - \mathcal{Y}\tilde{\mathbf{V}}_p\|_2$  and the maximum measurement noise error  $\Sigma_2$  associated with the source generator at bus 65 are plotted. Since there is an internal forced oscillation at  $f_d = 2.0$  Hz, the prediction error greatly exceeds the measurement noise error bound at this frequency.

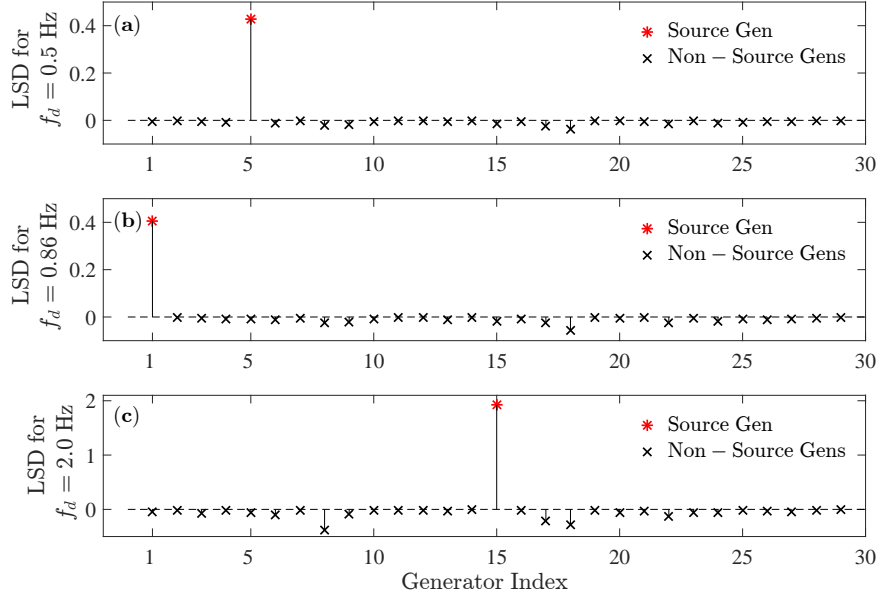


Figure 2-18: The LSD is computed at each generator for  $f_d = 0.5$  Hz (panel (a)),  $f_d = 0.86$  Hz (panel (b)), and  $f_d = 2.0$  Hz (panel (c)). At each frequency, the correct generator is located, despite strong PMU measurement noise. Generator index 1 corresponds to the generator at bus 4, generator index 5 corresponds to the generator at bus 13, and generator index 15 corresponds to the generator at bus 65.

(1), since it would have to be found empirically, by a system operator, via PMU data collected over time. We currently do not have access to such data.

Although the structure of the generator models may be reasonably accurate, the generator model parameters themselves may be known to a lesser degree of accuracy. To consider the effects of generator parameter uncertainty, the LSD is re-quantified for each generator, but in building the FRF of (2.59), generator parameter uncertainty is introduced over 100 trials. Parameter uncertainty includes all damping, reactance, time constant, and AVR variables. Inertia uncertainty is not considered since this is a static and typically very well defined parameter. All parameters are altered by a percentage chosen from a normal distribution characterized by  $\mu = 0$  and  $\sigma = 10\%$ ; this was the largest standard deviation for which parameters uncertainty was tolerable. The results, given by Fig. 2-19, show that the LSD metric is fairly robust to model parameter uncertainty for  $\sigma \leq 10\%$ , although the next section of this chapter will refine the source location method for enhanced accuracy in the face of uncertainty. In general, this parameter uncertainty analysis indicates that a reasonably accurate generator model is necessary to employ these frequency response methods at any particular generator.

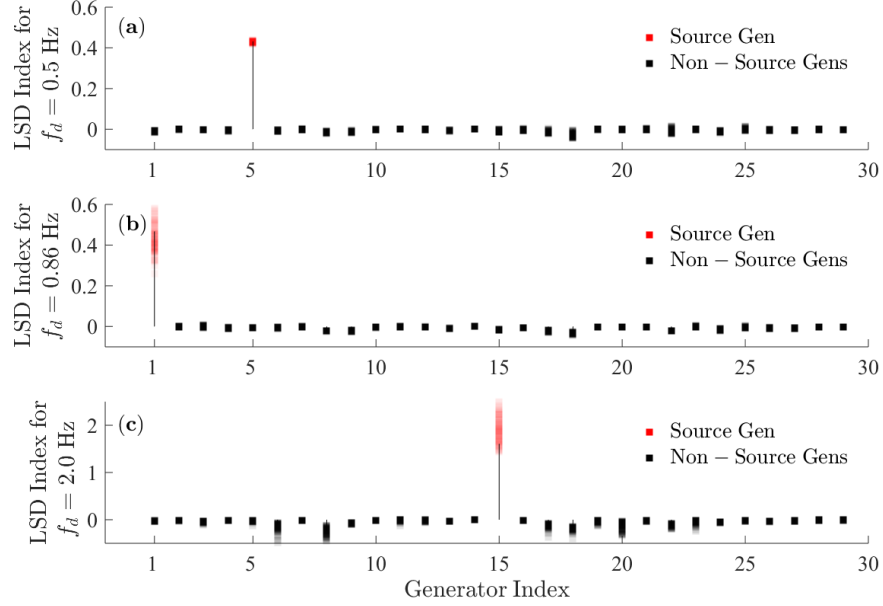


Figure 2-19: The LSD is computed at each generator for  $f_d = 0.5$  Hz (panel (a)),  $f_d = 0.86$  Hz (panel (b)), and  $f_d = 2.0$  Hz (panel (c)) over 100 trials to consider the impact of generator parameter uncertainty.

### WECC-179 Bus System (Natural Oscillation)

As a third test, the admittance matrix source location technique was applied in the presence of a natural oscillation (no forced oscillation sources). We used test case “ND1” from [117], where a natural oscillation is excited in the WECC 179-bus system. In “ND1”, all generators are modeled as 2<sup>nd</sup> order, and most are assigned a damping parameter of  $D = 4$ . The generators at buses 45 and 159, though, are assigned  $D = -1.5$  and  $D = 1$ , respectively, such that there exists a poorly damped mode with damping ratio  $\zeta = 0.01$ . To excite the system’s underdamped mode, a fault is applied at bus 159 for 0.05s. This system was simulated for 100 seconds with the same load dynamics and PMU measurement noise assumptions as were used in simulating test case “F1”. The bus voltage magnitude from generator buses 45 and 159 (oscillations are strongest at these generators) are given before, during, and after the fault by Fig. 2-20. As can be inferred from this plot, the excited underdamped natural mode of this system has frequency  $f_n = 1.41$  Hz.

Since the persisting oscillations are caused by the excitation of a poorly damped mode, we say the system is experiencing a natural oscillation rather than a forced oscillation. Therefore, the source location technique should indicate that no generator contains an internal forcing function. To test this theory, the prediction error aggre-

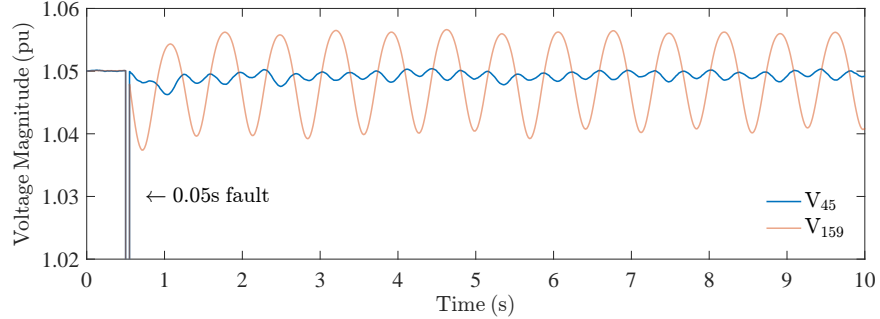


Figure 2-20: The voltage magnitude at buses 45 and 159 are plotted before, while, and briefly after the system experiences a fault. Measurement noise is not shown.

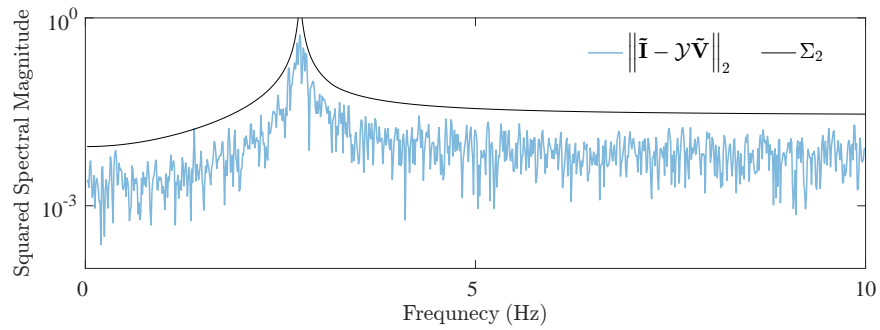


Figure 2-21: The prediction error  $\|\tilde{\mathbf{I}}_p - \gamma \tilde{\mathbf{V}}_p\|_2$  and the noise error bound  $\Sigma_2$  associated with generator 45 are plotted for test case ND1. The prediction error slightly exceeds the noise error bound at  $f = 1.41$  Hz.

gate  $\|\tilde{\mathbf{I}}_p - \gamma \tilde{\mathbf{V}}_p\|_2$  and the noise error bound  $\Sigma_2$  were calculated via Algorithm (1) and plotted for generator buses 45 and 159 (see Figs. 2-21 and 2-22, respectively). In each of these cases, the prediction error slightly exceeds the noise error at  $f_n = 1.41$  Hz. This deviation is very small, though, relative to the strength of the oscillation, and is likely due to slight nonlinearity of the generator responses (generator current angular perturbations are very large).

To further analyze the system, the LSDs were calculated at each generator (we again assumed PMU data were available). Since the LSD is a function of frequency, and there is no forcing frequency, we computed the LSDs at all generators in the range of  $f = 1.38$  to  $f = 1.42$  Hz. We then plot the maximum LSD in this frequency band for each generator. This result is shown in Fig. 2-23. In this plot, the maximum LSDs at generators 13 (bus 45) and 28 (bus 159) are seen to cross the zero threshold. Given the strength of the oscillation, as seen in Fig. 2-20, and the very small deviation between the prediction and the measurement, none of the sampled generators could be forced oscillation source candidates. More formally, all calculated LSD values are

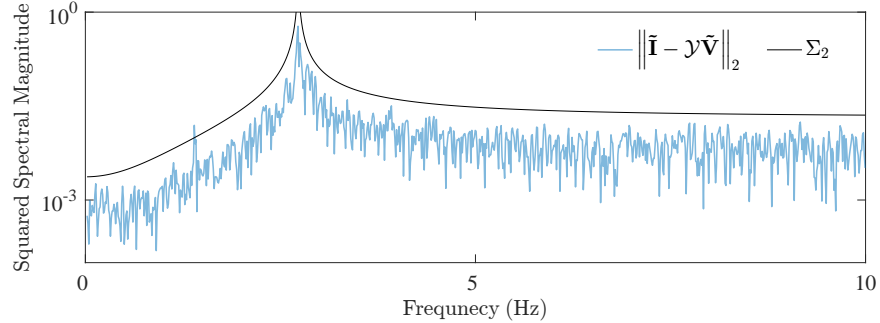


Figure 2-22: The prediction error  $\|\tilde{\mathbf{I}}_p - \mathcal{Y}\tilde{\mathbf{V}}_p\|_2$  and the noise error bound  $\Sigma_2$  associated with generator 159 are plotted for test case ND1. The prediction error slightly exceeds the noise error bound at  $f = 1.41$  Hz.

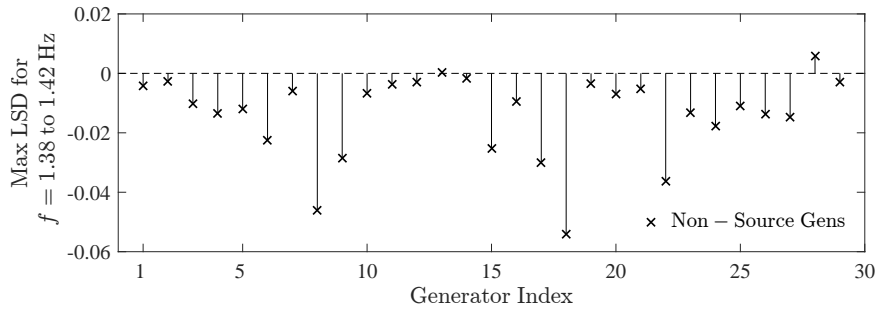


Figure 2-23: The maximum LSD, from  $f = 1.38$  to  $f = 1.42$ , is plotted for each generator. The maximum LSDs at generators 13 (bus 45) and 28 (bus 159) are slightly positive, but are still sufficiently small.

smaller than any realistically chosen  $\iota$  parameter which would represent the threshold for determining if a generator is the source of a forced oscillation. We may thus conclude that either the system is being forcibly oscillated by some non-generator piece of equipment or load, or that a natural oscillation is driving the system's periodic dynamics.

### WECC-179 Bus System (Forced + Natural Oscillation)

As a fourth test case, we used the natural oscillation test case “ND2” and we added the forced oscillation described in test case “F63” (both are described in [117]). Specifically, we set the damping parameters of the generators at buses 35 ( $D_{35} = 0.5$ ) and 65 ( $D_{65} = -1$ ) such that there exists a poorly damped mode ( $\zeta = 0.02\%$ ) at 0.37 Hz. Additionally, we forcibly oscillated generator 79’s AVR reference voltage with a additive *square wave* of frequency 0.40 Hz. In this particular situation, the presence of a negative damping at generator 65 can cause the generator to be viewed as a source of

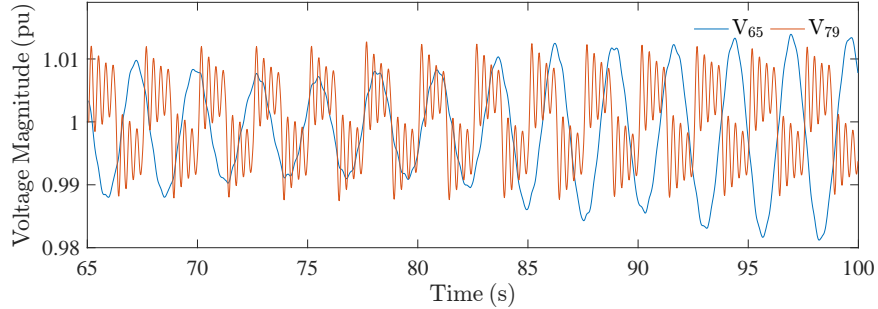


Figure 2-24: The voltage magnitude at buses 65 and 79 are plotted over 35 seconds. The natural mode frequency of 0.37 Hz, the forcing frequency of 0.40 Hz, and the resulting beat frequency can all be seen clearly. Measurement noise is not shown.

the so called “transient energy” in the DEF method. Accordingly, the DEF method will locate this generator as the source of the negative damping. Our FRF method, though, may be used in a complimentary fashion to find the forced oscillation source.

The voltage magnitudes at buses 65 and 79 are shown in Fig. 2-24 over 35 seconds. Generator 79’s response to the additive square wave on the AVR reference is evident. In this test, the forced oscillation frequency is only slightly larger than the natural frequency of the poorly damped mode. This elicits a strong response from the generator at bus 65. Accordingly, we compare the prediction error and measurement noise bound at both generators across the full spectrum of frequencies. In Fig. 2-25, the prediction error is seen to be totally contained by the measurement noise error bound at generator 65. This is true for all other generators (aside from generator 79) in the system as well. The resulting negative LSDs at all of these generators, across all frequencies, along with the massively positive LSD at generator 79, indicates there is only one forced oscillation source. This is shown by Fig. 2-27. Further evidence that generator 79 is the source of the oscillation can be seen by the Fig. 2-26. There are a series of prediction error spikes which violate the measurement noise error bound. The statistical signatures of these spikes further indicate that the forcing function is a square wave. To understand why, equation (2.87) gives the Fourier series of a pure square wave  $g_s(t)$  with fundamental frequency  $f$ . This series contains frequencies  $f$ ,  $3f$ ,  $5f$ , and so on, just as spectral deviations in Fig. 2-26 occur at  $f = 0.4$ ,  $1.2$ ,  $2.0$  and  $2.8$  Hz:

$$g_s(t) = \frac{4}{\pi} \sum_{n=1,3,5\dots}^{\infty} \frac{\sin(2\pi n f t)}{n}. \quad (2.87)$$

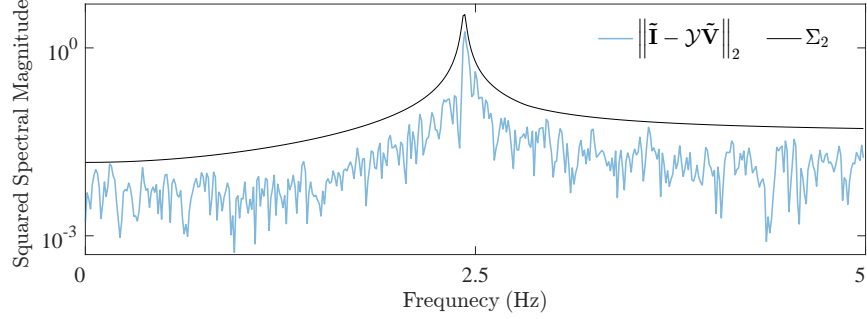


Figure 2-25: The prediction error  $\|\tilde{\mathbf{I}}_p - \mathcal{Y}\tilde{\mathbf{V}}_p\|_2$  and the noise error bound  $\Sigma_2$  associated with generator 65 are plotted for the test case where an underdamped natural mode is excited by a forced oscillation. Despite a strong oscillatory response from generator 65 at 0.37 Hz, the prediction error is entirely contained by the measurement noise error bound for all frequencies.

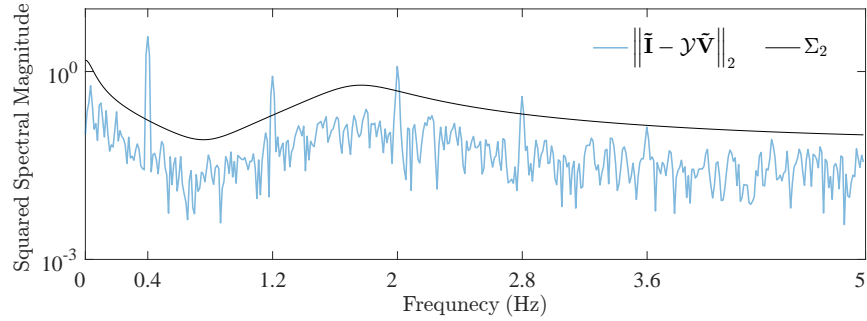


Figure 2-26: The prediction error  $\|\tilde{\mathbf{I}}_p - \mathcal{Y}\tilde{\mathbf{V}}_p\|_2$  and the noise error bound  $\Sigma_2$  associated with generator 79, the source bus, are plotted for the test case where an underdamped natural mode is excited by a forced oscillation. The prediction error violates the measurement noise error at  $f = 0.4, 1.2, 2.0 Hz.$

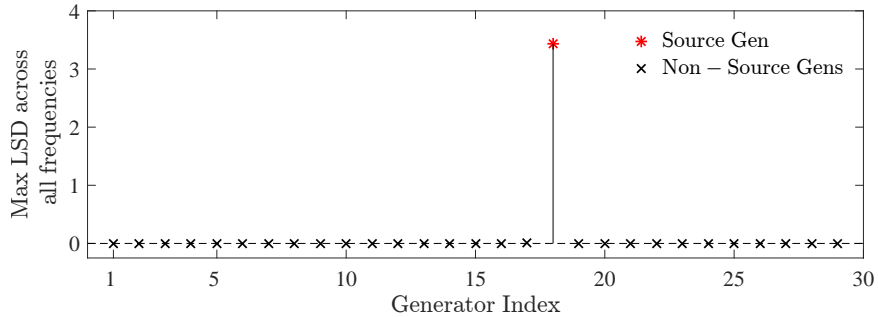


Figure 2-27: The LSD is computed at each generator across the full range of measured frequencies for the natural + forced oscillation test case. Only the largest LSD for each generator is plotted here, though. Generator index 18, which corresponds to the generator at bus 79, is correctly identified as the source generator.

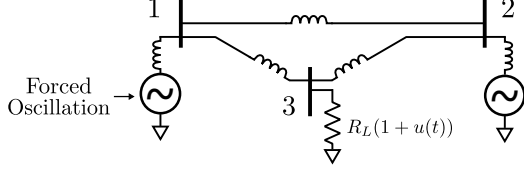


Figure 2-28: 3 bus system with two 2<sup>nd</sup> order generators and a resistive load. Resistive Ornstein-Uhlenbeck noise is added to mimic system fluctuations.

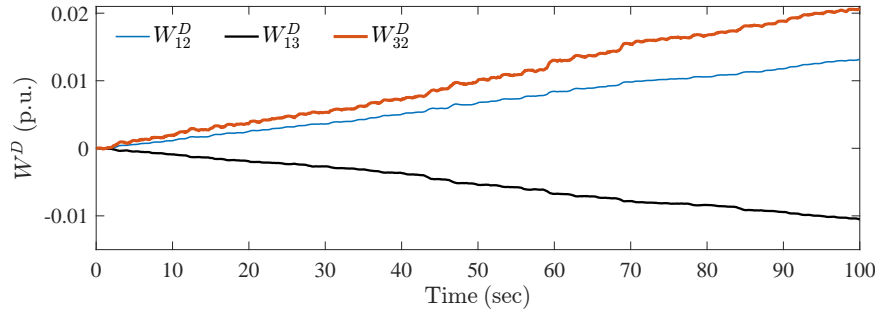


Figure 2-29: The DEF is computed for lines {12}, {13}, and {32}.

### 3-Bus System with Constant Impedance

As indicated in [36], network resistances embedded in system transfer conductances (shunt and series) and constant impedance loads may act as the source of transient energy from the viewpoint of the DEF method. The simplest system known to exhibit this phenomena [36] can be modeled as a two generator system with some constant impedance load (or shunt), as given by Fig. 2-28. In this system, we apply light Ornstein-Uhlenbeck noise of (2.84) to the resistive load in order to mimic system fluctuations, and we apply a FO of  $\Omega_d = 2 \frac{\text{rad}}{\text{sec}}$  to the torque on generator 1.

After simulating this system and adding white PMU measurement noise with  $\sigma = 0.1$  (% pu), the flow of dissipating energy was computed according to [122, eq. (3)]. The results are given by Fig. 2-29. According to the notation introduced in [122, eq. (5)], we found that  $DE_{12}^* = 0.61$ ,  $DE_{13}^* = -0.48$ , and  $DE_{32}^* = 0.94$ . These results indicate that energy is flowing from the resistive load at bus 3 to the two generator buses. Energy is also flowing from the generator 1 (the source bus) to generator 2 (the system sink). These results do not accurately locate the source of the oscillation due to the resistive load. The reasons why are explained in [36] and shall not be investigated here. We then applied the FRF method to both generators. In building the FRF of  $\mathcal{Y}$ , reactance and damping parameters were perturbed by a percentage pulled from a normal distribution with standard deviation  $\sigma = 0.05\%$ . The FO is clearly located at generator 1 due to the significantly positive LSD at 0.32Hz in panel

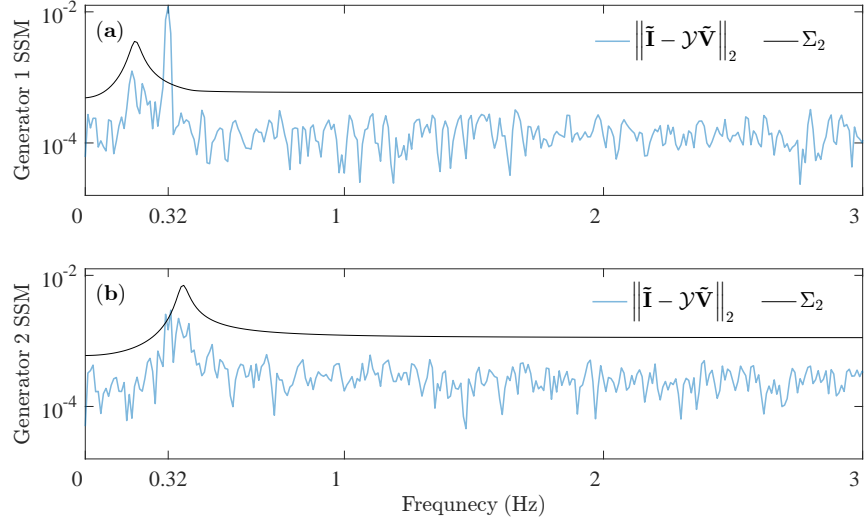


Figure 2-30: The prediction error  $\|\tilde{\mathbf{I}}_p - \mathcal{Y}\tilde{\mathbf{V}}_p\|_2$  (given as the Squared Spectral Magnitude (SSM)) and the noise error bound  $\Sigma_2$  associated with generator 1 (panel (a)) and generator 2 (panel (b)) are given.

(a) of Fig. 2-30. Conversely, the LSD at 0.32 Hz on generator 2 is effectively 0. Since the FRF method presented in this section is invariant to network dynamics, it is not constrained by load modeling assumptions.

## 2.3 A Bayesian Approach to FO Source Location Given Uncertain Generator Parameters

In this section, we address the challenges associated with the application of Algorithm 1 when certain modeling parameters of the generators in the system are poorly known. While many physical parameters, such as as inertia and armature reactance, have a higher probability of being known by system operators, other necessary parameters, such as controller gains and time constants, and even the equilibrium point around which the generator must be linearized, may have a higher degree of uncertainty. Indeed, the so-called power angle  $\varphi = \delta - \theta$ , which is necessary for linearization, is only ever known by system operators through the output of a (potentially erroneous) state estimation routine. For more details, please refer to the literature review in the introductory chapter.

### 2.3.1 Problem Formulation

In this subsection, we leverage a Maximum A Posteriori (MAP) framework for locating the sources of FOs. Then, we present an explicit procedure for relaxing and solving the posed MAP problem.

#### Generator Admittance Prediction Aberrations

As in the previous section, we consider a generator<sup>4</sup> connected to a power system and assume PMU data from the generator's terminal bus are available. We also assume the generator is operating with steady state terminal voltage phasor  $V_0 e^{j\theta_0}$  and current phasor  $I_0 e^{j\phi_0}$ . We respectively define  $V(t)$ ,  $\theta(t)$ ,  $I(t)$  and  $\phi(t)$  to be the *measured* voltage magnitude, voltage phase, current magnitude and current phase *deviations* from steady state. The Fourier transform  $\mathcal{F}$  of these signals is

$$\tilde{X}(\Omega) = \int_{-\infty}^{\infty} X(t) e^{j\Omega t} dt, \quad X \in \{V, \theta, I, \phi\}, \quad (2.88)$$

where, again, the frequency  $\Omega$  has nothing to do with the fundamental AC frequency of 50 or 60 Hz; the transformation in (2.88) is performed on phasors with AC frequencies already excluded. We now consider the FRF  $\mathcal{Y} \equiv \mathcal{Y}(\Omega)$  from (2.60) which relates a generator's terminal voltage (magnitude and phase) perturbations to its terminal current (magnitude and phase) perturbations in the frequency domain. We note, however, that the equality in (2.60) changes to an approximation whenever dealing with measured signals, because measurement noise will always prevent (2.60) from constituting an exact relationship. From (2.60), we refer to the vector  $\tilde{\mathbf{I}}_p(\Omega)$  as the current *measurement*, since it is directly measured by PMUs. Similarly, we refer to the vector  $\mathcal{Y}(\Omega)\tilde{\mathbf{V}}_p(\Omega)$  as the current *prediction*, since the measured voltage vector  $\tilde{\mathbf{V}}_p(\Omega)$  is multiplied by an admittance matrix model to yield a current estimate. The error between the measured ( $\tilde{\mathbf{I}}_p(\Omega)$ ) and predicted ( $\mathcal{Y}(\Omega)\tilde{\mathbf{V}}_p(\Omega)$ ) currents, at each frequency  $\Omega$ , may be quantified via the  $\ell_2$  norm:

$$\text{prediction error}(\Omega) = \left\| \tilde{\mathbf{I}}_p(\Omega) - \mathcal{Y}(\Omega)\tilde{\mathbf{V}}_p(\Omega) \right\|_2. \quad (2.89)$$

For small perturbations, the primary contributors to the prediction error are PMU measurement noise, generator model parameter inaccuracies, and unmodeled generator inputs such as external perturbations. Any FO at a source bus, though, acts as

---

<sup>4</sup>While this section exclusively considers generators as the sources of FOs, the given framework may be extended to any dynamic system component.

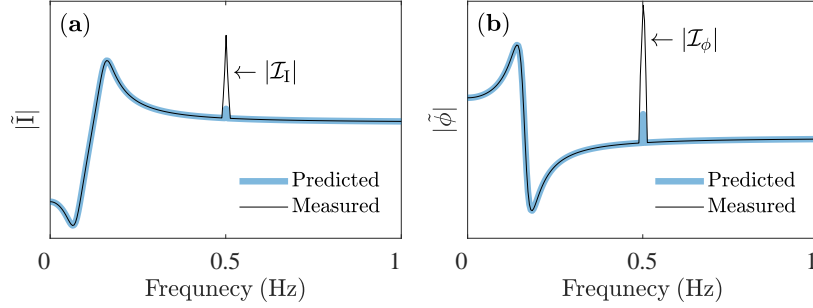


Figure 2-31: The modulus of the measured and predicted current magnitude  $\tilde{\mathbf{I}}$  and current phase  $\tilde{\phi}$  spectrums at a source generator are plotted in panels (a) and (b), respectively. At the forcing frequency of  $f_d = 0.5$  Hz, the current injection magnitudes  $|\mathcal{I}_l|$  and  $|\mathcal{I}_\phi|$  can be seen as deviations from the predicted terminal current spectrum.

a current injection represented by  $\mathcal{I}(\Omega) \in \mathbb{C}^{2 \times 1}$ , where  $\mathcal{I}(\Omega) = [\mathcal{I}_l(\Omega) \ \mathcal{I}_\phi(\Omega)]^T$  is used to denote the complex current magnitude ( $\mathcal{I}_l(\Omega)$ ) and complex current phase ( $\mathcal{I}_\phi(\Omega)$ ) injections:

$$\tilde{\mathbf{I}}_p(\Omega) \approx \mathcal{Y}(\Omega) \tilde{\mathbf{V}}_p(\Omega) + \mathcal{I}(\Omega). \quad (2.90)$$

This relation is illustrated at Fig. 2-3. Since FOs are usually dominant at some forcing frequency  $\Omega_d$  and nonexistent elsewhere in the frequency spectrum (neglecting nonlinear harmonics), the current injection  $\mathcal{I}$  will be equal to  $\mathbf{0}$  for all frequencies  $\Omega \neq \Omega_d$ . At any generator which is not the FO source, the current injection is zero for all  $\Omega$ . An example of the measured and predicted current spectrums associated with a source generator (in the absence of measurement noise and model uncertainty) is shown by Fig. 2-31. Panels (a) and (b) show the presence of the FO current injection magnitudes which cause deviation between the measured and predicted current spectrums. At non-source generators, these injections do not exist and the measurements and predictions match.

### Constructing the System Likelihood Function

Identifying the source of a FO based on a generator's FRF relies on the knowledge of the generator model in order to construct its  $\mathcal{Y}$ -matrix. If the generator model parameters are not known with sufficient accuracy, the method cannot be applied directly. However, since the current injection function  $\mathcal{I}$  is only non-zero in a narrow band around the forcing frequency  $\Omega_d$ , one can use the generator's measured response in the remainder of the spectrum in order to identify its parameters. This

is accomplished by employing the MAP framework.

Since the measurement noise associated with PMU data is approximately white [27], a likelihood function, which is similar to (2.12) constructed in the background chapter, may be constructed for the system in (2.90), where “system” in this subsection refers to a single generator. To build this likelihood function, the expanded right hand side (RHS) of (2.90) is subtracted from the expanded left hand side (LHS). Assuming an accurate admittance matrix, the system dynamics cancels out and only measurement noise terms are left over on the RHS of (2.91):

$$\begin{bmatrix} \tilde{\mathbf{I}} \\ \tilde{\phi} \end{bmatrix} - \left( \begin{bmatrix} \mathcal{Y}_{11} & \mathcal{Y}_{12} \\ \mathcal{Y}_{21} & \mathcal{Y}_{22} \end{bmatrix} \begin{bmatrix} \tilde{\mathbf{V}} \\ \tilde{\theta} \end{bmatrix} + \begin{bmatrix} \mathcal{I}_\mathbf{I} \\ \mathcal{I}_\phi \end{bmatrix} \right) = \begin{bmatrix} \tilde{\epsilon}_\mathbf{I} \\ \tilde{\epsilon}_\phi \end{bmatrix} - \begin{bmatrix} \mathcal{Y}_{11} & \mathcal{Y}_{12} \\ \mathcal{Y}_{21} & \mathcal{Y}_{22} \end{bmatrix} \begin{bmatrix} \tilde{\epsilon}_\mathbf{V} \\ \tilde{\epsilon}_\theta \end{bmatrix} \quad (2.91)$$

where  $\tilde{\epsilon}_X, X \in \{\mathbf{V}, \theta, \mathbf{I}, \phi\}$  is a complex random variable associated with the frequency domain representation of the AWGN distribution  $\epsilon_X$ . Accordingly, measured signal  $X(t)$  and its associated true signal  $\bar{X}(t)$  are related by

$$X(t) = \bar{X}(t) + \epsilon_X, \quad X \in \{\mathbf{V}, \theta, \mathbf{I}, \phi\}. \quad (2.92)$$

We now assume  $\epsilon_X$  is sampled  $2K+1$  times with sample rate  $f_s$ . The values are placed into discrete vector  $\epsilon_X[n]$ , and its Discrete Fourier Transform<sup>5</sup> (DFT) is taken. The resulting single-sided output,  $\tilde{\epsilon}_X[w]$ , will be a function of the  $K+1$  frequencies

$$\Omega_w = 2\pi \times \left[ 0, \frac{f_s}{2K+1}, \frac{2 \cdot f_s}{2K+1}, \dots, \frac{K \cdot f_s}{2K+1} \right]. \quad (2.93)$$

Since the input distribution to the DFT is a Gaussian, the output will be a frequency dependent set of complex Gaussians which are IID across frequency. Accordingly,  $\tilde{\epsilon}_X$  in fact does not depend on frequency since  $\tilde{\epsilon}_X[w_1]$  and  $\tilde{\epsilon}_X[w_2]$  are distributed identically. Additionally,  $\tilde{\epsilon}_X$  can be split into its real and imaginary components via  $\tilde{\epsilon}_X = \tilde{\epsilon}_{X_r} + j\tilde{\epsilon}_{X_i}$ , where  $\tilde{\epsilon}_{X_r}$  and  $\tilde{\epsilon}_{X_i}$  are both real valued, IID Gaussians with  $E[\tilde{\epsilon}_{X_r}] = E[\tilde{\epsilon}_{X_i}] = 0$ . By the central limit theorem and basic statistics, the variances of  $\tilde{\epsilon}_{X_r}$  and  $\tilde{\epsilon}_{X_i}$ , which are essential for eventually building the likelihood covariance matrix, can be computed:

$$E\{\tilde{\epsilon}_{X_r}^2\} = E\{\tilde{\epsilon}_{X_i}^2\} = \frac{4(2K+1)}{2} E\{\epsilon_X^2\}. \quad (2.94)$$

---

<sup>5</sup>We define the  $2K+1$  point double sided DFT of  $x[n]$  as  $\tilde{x}[w] = \sum_{k=0}^{2K} x[n] e^{-j \frac{2\pi w n}{2K+1}}$  where  $w = 0, 1, \dots, 2K$ .

To continue building the likelihood function, (2.91) must be separated into its real and imaginary parts in order to preserve the Gaussian nature of the measurement noise. It is important to note that there are no measurement noise terms associated with the current injections since vector  $\mathcal{I}$  is not measured but is instead a mathematical artifact which represents the current flow attributed to a FO. For notational convenience, the LHS of (2.91) may be rewritten in terms of the complex variables  $\tilde{M} = \tilde{M}_r + j\tilde{M}_i$  (magnitude) and  $\tilde{P} = \tilde{P}_r + j\tilde{P}_i$  (phase) while the RHS of (2.91) may be rewritten in terms of the corresponding complex noise variables  $\tilde{N} = \tilde{N}_r + j\tilde{N}_i$  and  $\tilde{Q} = \tilde{Q}_r + j\tilde{Q}_i$ :

$$\begin{bmatrix} \tilde{M}_r + j\tilde{M}_i \\ \tilde{P}_r + j\tilde{P}_i \end{bmatrix} = \begin{bmatrix} \tilde{N}_r + j\tilde{N}_i \\ \tilde{Q}_r + j\tilde{Q}_i \end{bmatrix}. \quad (2.95)$$

Equation (2.95) is valid across all frequencies. Explicitly, the residual expressions on the LHS of (2.95) take on the following forms:

$$\tilde{M}_r = \tilde{I}_r - \mathcal{Y}_{11r}\tilde{V}_r + \mathcal{Y}_{11i}\tilde{V}_i - \mathcal{Y}_{12r}\tilde{\theta}_r + \mathcal{Y}_{12i}\tilde{\theta}_i - \mathcal{I}_{I_r} \quad (2.96)$$

$$\tilde{M}_i = \tilde{I}_i - \mathcal{Y}_{11i}\tilde{V}_r - \mathcal{Y}_{11r}\tilde{V}_i - \mathcal{Y}_{12i}\tilde{\theta}_r - \mathcal{Y}_{12r}\tilde{\theta}_i - \mathcal{I}_{I_i} \quad (2.97)$$

$$\tilde{P}_r = \tilde{\phi}_r - \mathcal{Y}_{21r}\tilde{V}_r + \mathcal{Y}_{21i}\tilde{V}_i - \mathcal{Y}_{22r}\tilde{\theta}_r + \mathcal{Y}_{22i}\tilde{\theta}_i - \mathcal{I}_{\phi_r} \quad (2.98)$$

$$\tilde{P}_i = \tilde{\phi}_i - \mathcal{Y}_{21i}\tilde{V}_r - \mathcal{Y}_{21r}\tilde{V}_i - \mathcal{Y}_{22i}\tilde{\theta}_r - \mathcal{Y}_{22r}\tilde{\theta}_i - \mathcal{I}_{\phi_i} \quad (2.99)$$

where the subscripts r and i denote the real and imaginary parts of the admittance matrix entries, complex frequency domain signals, and current injection terms. The noise-related expressions, on the RHS of (2.95), take on the following forms:

$$\tilde{N}_r = \tilde{\epsilon}_{I_r} - \mathcal{Y}_{11r}\tilde{\epsilon}_{V_r} + \mathcal{Y}_{11i}\tilde{\epsilon}_{V_i} - \mathcal{Y}_{12r}\tilde{\epsilon}_{\theta_r} + \mathcal{Y}_{12i}\tilde{\epsilon}_{\theta_i} \quad (2.100)$$

$$\tilde{N}_i = \tilde{\epsilon}_{I_i} - \mathcal{Y}_{11i}\tilde{\epsilon}_{V_r} - \mathcal{Y}_{11r}\tilde{\epsilon}_{V_i} - \mathcal{Y}_{12i}\tilde{\epsilon}_{\theta_r} - \mathcal{Y}_{12r}\tilde{\epsilon}_{\theta_i} \quad (2.101)$$

$$\tilde{Q}_r = \tilde{\epsilon}_{\phi_r} - \mathcal{Y}_{21r}\tilde{\epsilon}_{V_r} + \mathcal{Y}_{21i}\tilde{\epsilon}_{V_i} - \mathcal{Y}_{22r}\tilde{\epsilon}_{\theta_r} + \mathcal{Y}_{22i}\tilde{\epsilon}_{\theta_i} \quad (2.102)$$

$$\tilde{Q}_i = \tilde{\epsilon}_{\phi_i} - \mathcal{Y}_{21i}\tilde{\epsilon}_{V_r} - \mathcal{Y}_{21r}\tilde{\epsilon}_{V_i} - \mathcal{Y}_{22i}\tilde{\epsilon}_{\theta_r} - \mathcal{Y}_{22r}\tilde{\epsilon}_{\theta_i} \quad (2.103)$$

where the real and imaginary components of the measurement noise distributions, as characterized by (2.94), have been employed explicitly. In equating the real and imaginary parts of (2.95), four equations are yielded:  $\tilde{M}_r = \tilde{N}_r$ ,  $\tilde{M}_i = \tilde{N}_i$ ,  $\tilde{P}_r = \tilde{Q}_r$ , and  $\tilde{P}_i = \tilde{Q}_i$ . Assuming each of these can be written for the  $K + 1$  frequencies of (2.93), then (2.95) may be used to generate a total of  $4(K + 1)$  equations. It is thus

useful to define the following  $\mathbb{R}^{K+1}$  function vectors:

$$\left. \begin{aligned} \mathbf{Z}_r &:= \left[ \tilde{Z}_r[0], \dots, \tilde{Z}_r[K] \right]^T \\ \mathbf{Z}_i &:= \left[ \tilde{Z}_i[0], \dots, \tilde{Z}_i[K] \right]^T \end{aligned} \right\}, \quad Z \in \{M, N, P, Q\} \quad (2.104)$$

where each vector entry is a function of one of the  $K+1$  frequencies from vector (2.93). The full noise function vector  $\mathbf{L}$  is now defined which represents the concatenation of the four individual noise function vectors:

$$\mathbf{L} = [\mathbf{N}_r^T \ \mathbf{N}_i^T \ \mathbf{Q}_r^T \ \mathbf{Q}_i^T]^T. \quad (2.105)$$

The residual function vector  $\mathbf{R}$  may be defined similarly:

$$\mathbf{R} = [\mathbf{M}_r^T \ \mathbf{M}_i^T \ \mathbf{P}_r^T \ \mathbf{P}_i^T]^T. \quad (2.106)$$

The  $4(K+1) \times 4(K+1)$  covariance matrix of  $\mathbf{L}$  is thus

$$\Sigma_{\mathbf{L}} = E\{\mathbf{L}\mathbf{L}^T\} \quad (2.107)$$

$$= \begin{bmatrix} \Sigma_{\mathbf{N}_r} & \mathbf{0} & \Sigma_{\mathbf{N}_r \mathbf{Q}_r} & \Sigma_{\mathbf{N}_r \mathbf{Q}_i} \\ \mathbf{0} & \Sigma_{\mathbf{N}_i} & \Sigma_{\mathbf{N}_i \mathbf{Q}_r} & \Sigma_{\mathbf{N}_i \mathbf{Q}_i} \\ \Sigma_{\mathbf{Q}_r \mathbf{N}_r} & \Sigma_{\mathbf{Q}_r \mathbf{N}_i} & \Sigma_{\mathbf{Q}_r} & \mathbf{0} \\ \Sigma_{\mathbf{Q}_i \mathbf{N}_r} & \Sigma_{\mathbf{Q}_i \mathbf{N}_i} & \mathbf{0} & \Sigma_{\mathbf{Q}_i} \end{bmatrix} \quad (2.108)$$

where the zero matrices  $\mathbf{0}$  are inserted due to the fact that  $E\{\tilde{N}_r \tilde{N}_i\} = E\{\tilde{Q}_r \tilde{Q}_i\} = 0$ , by inspection, for all frequencies. By direct extension,  $\Sigma_{\mathbf{N}_r \mathbf{N}_i} = \Sigma_{\mathbf{Q}_r \mathbf{Q}_i} = \mathbf{0}$ . Each of the non-zero sub-covariance matrices in (2.108) will be diagonal due to the fact that the frequency domain representation of measurement noise at the  $k^{\text{th}}$  frequency is uncorrelated with everything except for itself at the particular  $k^{\text{th}}$  frequency.

The multivariate Gaussian likelihood function may now be constructed. In Bayesian analysis, the likelihood probability density function (PDF)  $p_{\text{likely}}$  quantifies the likelihood of the observed data in  $\mathbf{d}$  given some set of model parameters in  $\Theta$ . In this context,  $\Theta$  is a vector filled with the generator parameters  $\Theta_g$  which are necessary to construct  $\mathcal{Y}$  (such as reactances, time constants or AVR gains) and the current injection terms  $\Theta_{\mathcal{I}}$ :

$$\Theta = \begin{cases} \Theta_g & \Rightarrow \text{generator parameters} \\ \Theta_{\mathcal{I}} & \Rightarrow \text{current injection terms.} \end{cases} \quad (2.109)$$

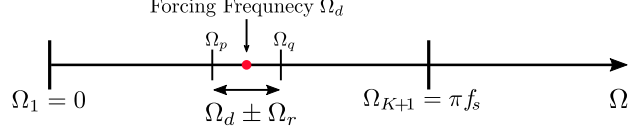


Figure 2-32: The frequencies between  $\Omega_p = \Omega_d - \Omega_r$  and  $\Omega_q = \Omega_d + \Omega_r$  represent the frequency range over which the FO has significant effect on the system.  $\Omega_r$  is half the range over which the forcing frequency has effect.

Entirely analogous to (2.12), the likelihood function itself is

$$p_{\text{likely}}(\mathbf{d}|\Theta) = \frac{e^{-\frac{1}{2}\mathbf{R}^T \boldsymbol{\Sigma}_L^{-1} \mathbf{R}}}{\sqrt{(2\pi)^{4(K+1)} \det(\boldsymbol{\Sigma}_L)}}. \quad (2.110)$$

### Constructing the System Prior Function

Typically, the generator model parameter values in the vector  $\Theta_g \in \mathbb{R}^m$  are not certain, and it is common to quantify this initial certainty with another multivariate Gaussian PDF [140]:

$$p_{\text{prior1}}(\Theta_g) = \frac{e^{-\frac{1}{2}(\Theta_g - \bar{\Theta}_g)^T \boldsymbol{\Sigma}_g^{-1} (\Theta_g - \bar{\Theta}_g)}}{\sqrt{(2\pi)^m \det(\boldsymbol{\Sigma}_g)}} \quad (2.111)$$

where  $\bar{\Theta}_g$  is the mean vector of prior generator parameter constants and  $\boldsymbol{\Sigma}_g$  is the corresponding diagonal covariance matrix. High model parameter confidence corresponds to low variance values. Also contained in  $\Theta$  is the vector  $\Theta_{\mathcal{I}} \in \mathbb{R}^{4v}$ :

$$\Theta_{\mathcal{I}} = \begin{cases} \mathcal{I}_{I_r}(\Omega) \\ \mathcal{I}_{I_i}(\Omega) \\ \mathcal{I}_{\phi_r}(\Omega) \\ \mathcal{I}_{\phi_i}(\Omega) \end{cases}, \quad \Omega \in \{\Omega_p \dots \Omega_q\} \quad (2.112)$$

where  $\mathcal{I}_{I_r}$ ,  $\mathcal{I}_{I_i}$ ,  $\mathcal{I}_{\phi_r}$  and  $\mathcal{I}_{\phi_i}$  are used in (2.96)-(2.99). By leveraging prior knowledge about the central FO frequency  $\Omega_d$ , we define these injections to exist only across the small range of DFT frequencies where the FO energy is dominant:  $\Omega_p$  through  $\Omega_q$  as shown by Fig. 2-32. In defining  $v$  discrete frequencies in this range, there are a total of  $4v$  current injection parameters (per FO) at each generator to include in (2.112). The prior distribution for these parameters will be taken as an unconditional IID Laplace distribution [138] (this choice shall be justified at the end of subsection

2.3.1):

$$p_{\text{prior2}}(\Theta_{\mathcal{I}}) = \prod_{j=1}^{4v} \frac{\lambda}{2} e^{-\lambda|\Theta_{\mathcal{I}_j}|} \quad (2.113)$$

where  $\Theta_{\mathcal{I}_j}$  refers to the  $j^{\text{th}}$  current injection variable from (2.112). The generator's full prior is the product of the generator parameter prior (2.111) and the current injection prior (2.113).

### Applying the MAP Formulation to the Forced Oscillation Source Location Problem

By leveraging the given likelihood and prior functions, a Bayesian framework, via MAP optimization, can be used to locate the sources of FOs in the context of a power system with poorly known generator parameters. The posterior distribution, which represents the likelihood of the model parameters given the data that have been observed, is computed through the application of Bayes' rule at each generator:

$$p_{\text{post}}(\Theta|\mathbf{d}) \propto p_{\text{likely}}(\mathbf{d}|\Theta)p_{\text{prior1}}(\Theta_g)p_{\text{prior2}}(\Theta_{\mathcal{I}}). \quad (2.114)$$

We now seek to maximize the posterior since  $\max\{p_{\text{post}}\}$  corresponds to maximum confidence in the model parameters for a given set of observed data. Maximizing this distribution is equivalent to minimizing the negative of its natural log<sup>6</sup>:

$$\Theta_{\text{MAP}} = \underset{\Theta \in \mathbb{R}^z}{\operatorname{argmin}} \{-\log(p_{\text{post}}(\Theta|\mathbf{d}))\} \quad (2.115)$$

$$= \underset{\Theta \in \mathbb{R}^z}{\operatorname{argmin}} \left\{ \|\Theta_g - \bar{\Theta}_g\|_{\Sigma_g^{-1}}^2 + \mathbf{R}^T \Sigma_{\mathbf{L}}^{-1} \mathbf{R} + \lambda \|\Theta_{\mathcal{I}}\|_1 \right\} \quad (2.116)$$

where  $\|\mathbf{x}\|_1 = \sum_i |x_i|$  and  $z = m + 4v$ . The unconstrained optimization problem formulated by (2.115) is similar in structure to the LASSO problem [30] with the regularization parameter  $\lambda$  acting as a penalty on non-sparse solutions for the vector  $\Theta_{\mathcal{I}}$ , although the admittance matrix  $\mathbf{Y}$  contained in  $\mathbf{R}$  is highly nonlinear. Generally, optimization problems with objective functions which are formulated as

$$\min_{\mathbf{x}, \mathbf{y}} L(\mathbf{x}, \mathbf{y}) + \lambda \|\mathbf{y}\|_1 \quad (2.117)$$

---

<sup>6</sup>To make this statement, we assume the determinant of the covariance matrix in (2.110) is roughly constant across plausible model parameters.

are non-differentiable when elements of  $\mathbf{y}$  are zero. A workaround for solving (2.117) transforms the unconstrained problem into a constrained problem [160] by introducing slack variables in the vector  $\mathbf{u}$  such that (2.117) may be restated as

$$\begin{aligned} \min_{\mathbf{x}, \mathbf{y}, \mathbf{u}} \quad & L(\mathbf{x}, \mathbf{y}) + \lambda \sum_i u_i \\ \text{s.t.} \quad & -\mathbf{u} \leq \mathbf{y} \leq \mathbf{u}. \end{aligned} \tag{2.118}$$

The unconstrained FO optimization problem may be restated similarly, where slack variable vector  $\mathbf{s}$  has been introduced:

$$\begin{aligned} \text{Minimize} \quad & \|\Theta_g - \bar{\Theta}_g\|_{\Sigma_g^{-1}}^2 + \mathbf{R}^T \Sigma_{\mathbf{L}}^{-1} \mathbf{R} + \lambda \sum_{i=1}^{4v} s_i \\ \text{subject to} \quad & -\mathbf{s} \leq \Theta_{\mathcal{I}} \leq \mathbf{s}. \end{aligned} \tag{2.119}$$

This optimization problem is written for a single generator. We now consider a power system with  $g$  generators of which one, or more, may be the source(s) of the FO(s); PMU data from each generator is assumed to be available. In defining the scalar cost function  $f_i = \|\Theta_g - \bar{\Theta}_g\|_{\Sigma_g^{-1}}^2 + \mathbf{R}^T \Sigma_{\mathbf{L}}^{-1} \mathbf{R} + \lambda \mathbf{1}^T \mathbf{s}$  associated with the  $i^{\text{th}}$  generator, we may minimize the sum of these cost functions over  $g$  generators:

$$\begin{aligned} \text{Minimize} \quad & \sum_{i=1}^g f_i \\ \text{subject to} \quad & -\mathbf{s}_i \leq \Theta_{\mathcal{I}_i} \leq \mathbf{s}_i, \quad i \in \{1 \dots g\}. \end{aligned} \tag{2.120}$$

Particularly useful is that (2.120) may be solved as a set of  $g$  *uncoupled* optimization problems: one for each generator. This is made possible due to a relaxation introduced in choosing the current injection prior of (2.113), which is now explained. If a system operator knows that a FO is occurring in a system, but the source generator is unknown, then the *most appropriate* prior distribution for (2.112) would be one which introduces an  $\ell_0$  norm constraint on current injections among all system generators; this would constrain the number of non-zero current injections found in the system to be equal to the number of occurring FOs. Aside from the NP-harness associated with such a formulation [30], an  $\ell_0$  norm constraint would require that the generator posterior distributions be optimized simultaneously, thus coupling the optimization problems of (2.120) and introducing large computational burden. As a relaxed alternative, a Laplace prior [138] is chosen to quantify the initial confidence in the current injection parameters because it ultimately introduces an  $\ell_1$  norm penalty in (2.115).

This  $\ell_1$  norm penalty naturally encourages sparse regression parameter selection [138] and introduces the benefit of uncoupled optimization despite inheriting the drawback of relaxed sparsity. As evidenced by LASSO's popularity, this is a common relaxation approach [30] applied to problems which seek sparse parameter recovery.

## A Numerical Procedure for MAP Solution

In numerically solving (2.120), the problem becomes computationally burdensome if the true likelihood covariance matrix of (2.108) is used in the objective function. Since  $\Sigma_L$  depends directly on the model parameters in  $\mathcal{Y}$ , obtaining an analytical solution for  $\Sigma_L^{-1}$ , such that it can be used in computing the necessary gradients and Hessians, is computationally intensive. In order to minimize (2.119), the following heuristic steps effectively balance formulation fidelity with tractability:

1. At the  $i^{\text{th}}$  iterative optimization step,  $\Sigma_L$  is numerically evaluated with the  $i^{\text{th}}$  parameter values of  $\Theta_g$  such that  $\bar{\Sigma}_{L_i} \equiv \Sigma_L|_{\Theta_{g_i}}$
2. Constant matrix  $\bar{\Sigma}_{L_i}$  replaces analytical matrix  $\Sigma_L$  in (2.119)
3. One iterative step is taken in the direction which minimizes this altered cost function, thus computing  $\Theta_{g_{i+1}}$
4. Returning to step 1, these steps are repeated for the  $(i+1)^{\text{th}}$  iteration, etc.

This process is applied for the covariance matrices of all  $g$  generators in (2.120). In treating these matrices as numerically constant at each optimization step, the objective function for a single  $i^{\text{th}}$  generator may now be restated as

$$f_i = \|\Theta_g - \bar{\Theta}_g\|_{\Sigma_g^{-1}}^2 + \mathbf{R}^T \bar{\Sigma}_L^{-1} \mathbf{R} + \lambda \mathbf{1}^T \mathbf{s}. \quad (2.121)$$

Since  $\frac{d}{d\Theta}(\bar{\Sigma}_L^{-1}) = \mathbf{0}$ , Hessian element  $i, j$  associated with  $C := \mathbf{R}^T \bar{\Sigma}_L^{-1} \mathbf{R}$  is therefore simply

$$\frac{d^2 C}{d\Theta_j d\Theta_i} = 2 \left( \frac{d^2 \mathbf{R}^T}{d\Theta_j d\Theta_i} \bar{\Sigma}_L^{-1} \mathbf{R} + \frac{d\mathbf{R}^T}{d\Theta_j} \bar{\Sigma}_L^{-1} \frac{d\mathbf{R}}{d\Theta_i} \right). \quad (2.122)$$

An interior point method may be used to solve the optimization problem set up by (2.120) with objective function (2.121).

### 2.3.2 Defining a Forced Oscillation Source Location Algorithm

In this section, the formulations introduced in [39] and Section 2.3.1 are tied together to explicitly define a FO source location algorithm. For enhanced effectiveness, a two-stage Bayesian update optimization scheme is introduced. This two-stage scheme allows the optimizer to primarily focus on generator parameter selection in stage 1 (by excluding data in the bandwidth of the FO) and current injection selection in stage 2 (by tightening the variances of the generator parameters based on the results of stage 1).

#### Stage 1

In stage 1, current injections are *not* considered. This is made possible if the system operator has prior knowledge about the location, in the frequency spectrum, of the current injections (FOs). By instructing the optimizer to ignore current injection variables  $\Theta_I$  and all data in the FO range of Fig. 2-32, the optimizer is able to tune generator parameters without considering current injections. Since this optimization formulation does not incorporate injection variables, it is thus unconstrained and has the following form across  $g$  generators:

$$\begin{aligned} \text{Minimize} \quad & \sum_{i=1}^g f_i \\ f_i = & \left\| \Theta_g - \bar{\Theta}_g \right\|_{\Sigma_g^{-1}}^2 + \mathbf{R}^T \bar{\Sigma}_{\mathbf{L}}^{-1} \mathbf{R}. \end{aligned} \quad (2.123)$$

In populating the residual function vector  $\mathbf{R}$  with PMU data, an important practical consideration which should be accounted for is the time window associated with the data. Since the methods of this chapter are based on linear analysis, the FRF is a direct function of the equilibrium of the system. If this equilibrium shifts significantly, parameter estimation and current injection determination will not be possible. To minimize these nonlinear affects, a short time window (on the order of a few minutes) should be employed to ensure that the analysis is unaffected by equilibrium swings.

Once the optimizer has converged to some local minimum (termed  $\Theta_{MAP1}$ ) and stage 1 is complete, the resulting posterior distribution will have mean  $\Theta_{MAP1}$  and covariance matrix  $\Sigma_{\Theta_{MAP1}}$  equal to the inverse Hessian  $\mathbf{H}^{-1}$  of (2.123) evaluated at the solution  $\Theta_{MAP1}$  [140].

## Stage 2

Stage 1 is effectively a Bayesian update for the generator parameters. In stage 2, the prior variances associated with the generator parameters in  $\Sigma_g$  are set equal to the diagonal values of the inverse Hessian  $\mathbf{H}^{-1}$  from stage 1, and the mean values of the generator parameters in  $\bar{\Theta}_g$  are set equal to  $\Theta_{\text{MAP1}}$ . Additionally, the full set of data in  $\tilde{\mathbf{V}}_p$  and  $\tilde{\mathbf{I}}_p$  is included in building the likelihood function, and the current injection variables are introduced into the framework. Again, current injections outside the range of  $\Omega_d \pm \Omega_r$  may be neglected if it is known a priori that the FO is not occurring in these frequency bands. Otherwise, the optimization problem and solution in stage 2 are fully characterized by the formulation introduced in subsections 2.3.1 and 2.3.1. The value of  $\lambda$  from (2.119) should be set sufficiently high such that the optimizer finds a sparse set of current injection parameters. Although a cross-validation approach should typically be employed to choose this regularization parameter, our ultimate desire is to locate the sources of FOs rather than build the most accurate predictive model possible, meaning increased regularization may be permissible.

The full set of steps necessary to implement this FO source location procedure are outlined in Algorithm 2; several of these steps reference equations from [39]. This algorithm concludes by comparing the size of the current injection solutions in  $\Theta_T$  to an operator specified threshold parameter  $\iota$ .

### 2.3.3 Test Results

In this section, we test our FO source location method on two test cases. First, we consider a 4-bus power system (Fig. 2-33), and we apply a sinusoidal oscillation to the mechanical torque supplied to one of the generators. Second, we apply two FOs to generators in the WECC 179-bus power system. In each test, white measurement noise is added to all PMU data (magnitude and phase) to achieve an SNR<sup>7</sup> of 45 dB in accordance with [27]. For model explanation brevity, all simulation code has been publicly posted online<sup>8</sup> for open source access.

---

<sup>7</sup>In setting the SNR, the signal power of all angular data is found after angles are subtracted from the angle associated with the system's so-called center of inertia angle  $\theta_{\text{coi}}$  where  $\theta_{\text{coi}} = (\sum H_i \delta_i) / (\sum H_i)$  [129].

<sup>8</sup><https://github.com/SamChevalier/FOs>

---

**Algorithm 2** MAP FO Source Detection Method

---

**START**

- 1: **for** each of the  $g$  generators **do**
  - 2:   Analytically construct FRF  $\mathcal{Y}$  of (2.59) via DAE sets (2.57a)-(2.57b)
  - 3:   Take DFT of generator PMU data  $V(t)$ ,  $\theta(t)$ ,  $I(t)$ , and  $\phi(t)$  to yield  $\tilde{\mathbf{I}}_p(\Omega)$  and  $\tilde{\mathbf{V}}_p(\Omega)$
  - 4:   Define parameter prior means  $\bar{\Theta}_g$  and variances  $\Sigma_g$
  - 5:   Use (2.94) and (2.100)-(2.103) to build the likelihood covariance matrix of (2.108)
  - end**
  - 6: **MAP Stage 1**
  - 7: Identify the range of frequencies  $\Omega_d \pm \Omega_r$  where the forced oscillation has significant effect and remove corresponding data from  $\tilde{\mathbf{I}}_p(\Omega)$  and  $\tilde{\mathbf{V}}_p(\Omega)$
  - 8: Iterate to local min ( $\Theta_{\text{MAP1}}$ ) of (2.123)
    - Continuously update covariance matrix at each iteration, as described in 2.3.1
  - 9: **MAP Stage 2**
  - 10: Update generator parameter prior means and variances with  $\Theta_{\text{MAP1}}$  and  $\mathbf{H}^{-1}$  of (2.123)
  - 11: Iterate to local min ( $\Theta_{\text{MAP2}}$ ) of (2.120), neglecting injection variables outside  $\Omega_d \pm \Omega_r$
  - 12: Via (2.109) and (2.112), parse  $\Theta_{\text{MAP2}}$  for generator  $i$  injection vector  $\mathcal{I}_i = [\mathcal{I}_{I_i}^T \mathcal{I}_{\phi_i}^T]^T$
  - 13: **if**  $\|\mathcal{I}_i\|_\infty > \iota$  **then**
  - 14:   Source found at generator  $i$
  - 15: **else**
  - 16:   No source found at generator  $i$
  - end**
- 

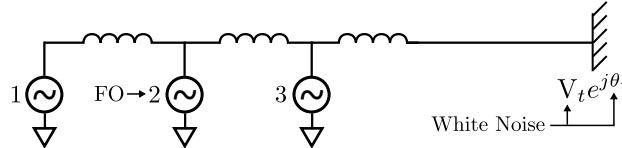


Figure 2-33: Three 3<sup>rd</sup> order generators (with AVR) are radially tied to an infinite bus with white noise. An FO is applied to generator 2's torque.

### Three Generators Tied to an Infinite Bus

In this test case, three 3<sup>rd</sup> order generators, each outfitted with first order automatic voltage regulators (AVRs), were radially tied to an infinite bus, as given by Fig. 2-33. At the infinite bus, white noise was applied to simulate stochastic system fluctuations. The mechanical torque applied to generator 2 was forcibly oscillated via  $\tau_m(t) = \tau_0(1 + 0.05 \sin(2\pi 0.5t))$ .

After 120 seconds of simulation, we built the generator admittance matrices using AVR and generator parameter ( $D$ ,  $H$ ,  $X_d$ ,  $X'_d$ ,  $X_q$ ,  $T'_{d0}$ ,  $K_A$ , and  $T_A$ ) values which were numerically perturbed by a percentage value randomly chosen from  $\mathcal{U}(-75, 75)$ . These perturbed parameter values represent the prior means placed into  $\bar{\Theta}_g$  for MAP stage 1. Fig. 2-34 compares the predicted current  $\mathcal{Y}\tilde{\mathbf{V}}_p$  with the measured current  $\tilde{\mathbf{I}}_p$ .

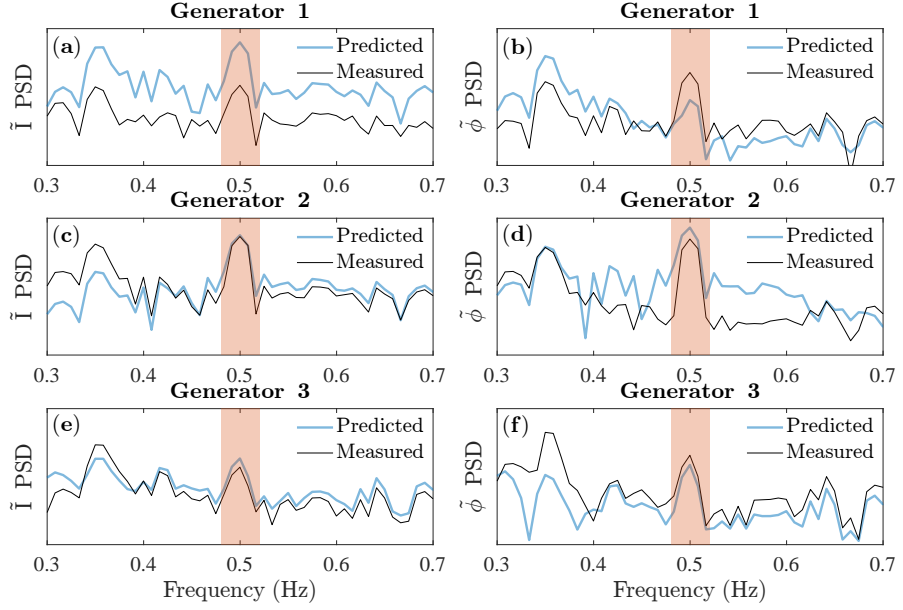


Figure 2-34: Shown are the measured ( $\tilde{I}_p$ ) and predicted ( $\mathcal{Y}\tilde{\mathbf{V}}_p$ ) current magnitude ( $\tilde{I}$ ) and current phase ( $\tilde{\phi}$ ) power spectral density (PSD) across a range of frequencies around the forcing frequency (0.5 Hz) before optimization has occurred. Panels (a) and (b) correspond to generator 1, panels (c) and (d) correspond to generator 2, and panels (e) and (f) correspond to generator 3.

across a small range of frequencies before MAP is solved. At all generators, there is significant spectral deviation between the measurements and predictions. From this data alone, it is not clear which is the source generator of the FO.

Next, stage 1 of the Bayesian update was run, where data in the range of the FO (the red shaded band in Fig. 2-34) was taken out of the problem altogether and current injections were not considered. After converging to  $\Theta_{\text{MAP1}}$ , the new set of generator parameters was used to compute the predicted spectrums in Fig. 2-35. Strong agreement between the measured and predicted spectrums is evident outside of the red band of the forcing frequency (which were not included in the stage 1 optimization).

In running stage 2 of the optimization, the current injection variables were reintroduced and the full set of frequencies were optimized over. The results are summarized in Fig. 2-36 which shows the norm of the current injections found at each frequency at each generator. For clarity, we plot

$$\|\mathcal{I}\| = \sqrt{\mathcal{I}_{I_r}^2 + \mathcal{I}_{I_i}^2 + \mathcal{I}_{\phi_r}^2 + \mathcal{I}_{\phi_i}^2}. \quad (2.124)$$

In viewing these results, the size of the current injections identified by MAP at gen-

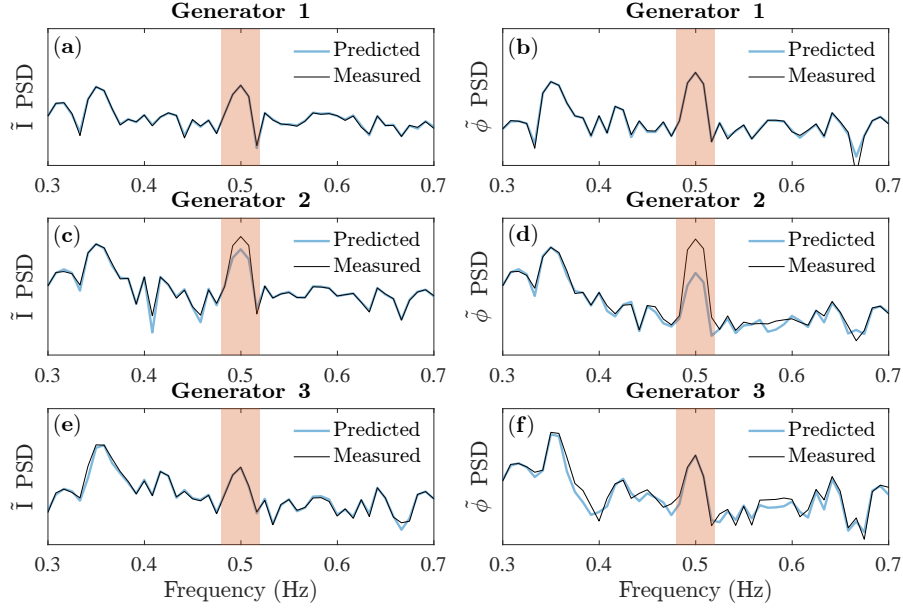


Figure 2-35: Shown are the measured ( $\tilde{I}_p$ ) and predicted ( $\mathcal{Y}\tilde{\mathbf{V}}_p$ ) current magnitude ( $\tilde{I}$ ) and current phase ( $\tilde{\phi}$ ) power spectral density (PSD) around the forcing frequency (0.5 Hz) after stage 1 of the optimizer has been run.

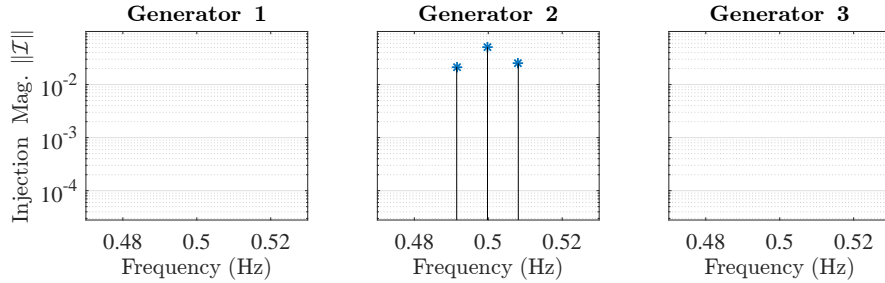


Figure 2-36: Shown are the stage 2 current injection results, as quantified by (2.124).

erator 2's forcing frequency of 0.5 Hz are sufficiently large enough, when compared to the other generators (which are many orders of magnitude smaller), to clearly indicate the presence of a forcing function at this generator.

## Two Forced Oscillations in the WECC 179-bus System

In conjunction with the IEEE Task Force on FOs, Maslennikov *et al.* developed a set of standardized test cases to validate various FO source detection algorithms [117]. For further testing, we applied the methods presented in this section on data collected from a modified version of test case “F1” in [117], in which the Automatic Voltage Regulator (AVR) reference signal at a generator (generator 1) in the WECC 179-bus system was forcibly oscillated at 0.86 Hz. In modifying the system, a second FO

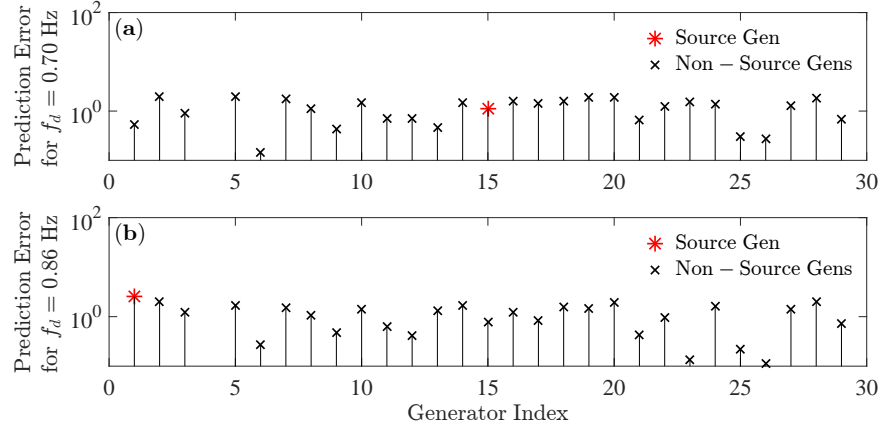


Figure 2-37: The prediction error, as quantified by the percent difference in the measured and predicted currents in (2.125), are shown for the system forcing frequencies of 0.70 Hz in panel (a) and 0.86 Hz in panel (b).

of frequency 0.7 Hz was added to the mechanical torque of the generator (generator 15) at bus 65. Additionally, PMU measurement noise was added as described previously and Ornstein-Uhlenbeck noise (with parameters taken from [66]) was added to all constant power loads, as described in [39]. After simulating the system, the admittance matrices for all system generators were constructed by parameters which were perturbed as in the previous subsection. For the second order generator model, parameters  $H$ ,  $D$ ,  $X'_d$  and  $E'$  were perturbed. For the third order generator model, the time constant, reactance, inertia, and AVR gain parameters were perturbed.

Next, the measured and predicted spectrums were compared at both of the forcing frequencies of  $f_d = 0.70$  Hz and  $f_d = 0.86$  Hz. To visualize the initial prediction error, the *percent difference* between measured and predicted currents are quantified via

$$\text{Prediction Error \% Difference} \Rightarrow \frac{\|\tilde{\mathbf{I}}_p - \mathcal{Y}\tilde{\mathbf{V}}_p\|}{\frac{1}{2}\|\tilde{\mathbf{I}}_p\| + \frac{1}{2}\|\mathcal{Y}\tilde{\mathbf{V}}_p\|} \quad (2.125)$$

and plotted in Fig. 2-37. The true source generator is identified in each panel, but because prediction error is sufficiently large due to parameter inaccuracies, it is not readily identifiable.

Stage 1 of the algorithm was then run. The results are given for two representative generators: a non-source generator at bus 9 (Fig. 2-38) and a source generator at bus 65 (Fig. 2-39). Panel (a) in Fig. 2-38 seems to indicate that generator 3 might be the source of the 0.86 Hz FO due to the large measurement/prediction deviations at this frequency, but the optimizer is able to reconcile the spectrums in panel (b). Panel (b) in Fig. 2-39, however, shows a significant gap between the measured and predicted

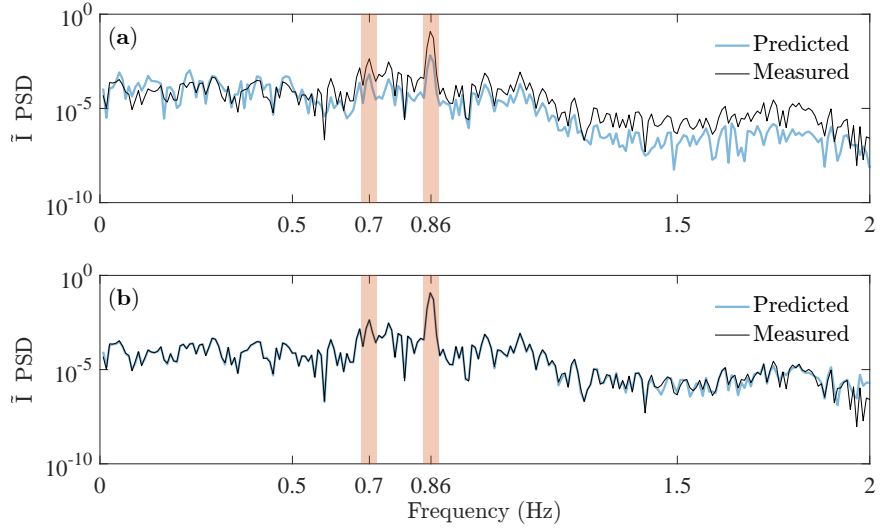


Figure 2-38: The predicted current magnitude spectrum is plotted in panel (a) for generator 3 (located at bus 9) before stage 1 of the optimization procedure. The predicted current magnitude spectrum is replotted in panel (b) after stage 1 is completed. Generator 3 is not a FO source.

spectrums at 0.70 Hz caused by the FO. Due to the physically meaningful way in which the covariance matrix is constructed, the amplification of the measurement noise at the points of FRF resonance does not prevent the optimizer from converging to the true set of generator parameters, but the effect can become troublesome if the SNR of the PMU data drops too low.

Finally, stage 2 of the optimization was run. Fig. 2-40 shows the magnitude of the current injections, as quantified by (2.124), found by the optimizer. Although no threshold has been established, it is clear that generator 15 is the source of the 0.70 Hz oscillation and that generator 1 is the source of the 0.86 Hz oscillation. In general, as the PMU measurement SNR is driven higher, the injections found by the  $\ell_1$  norm minimization in (2.115) at non-source generators are driven to 0.

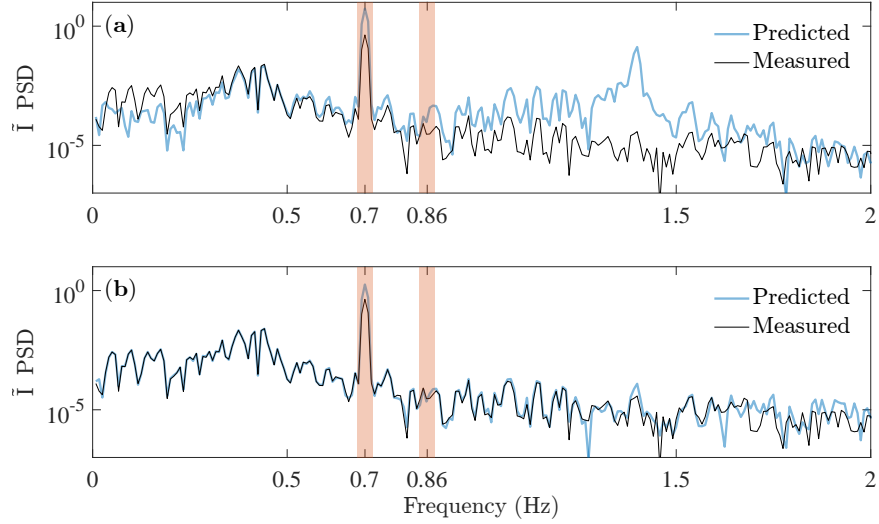


Figure 2-39: The predicted current magnitude spectrum is plotted in panel **(a)** for generator 15 (located at bus 65) before stage 1 of the optimization procedure. The predicted current magnitude spectrum is replotted in panel **(b)** after stage 1 in completed. Generator 65 is a FO source at 0.70 Hz.

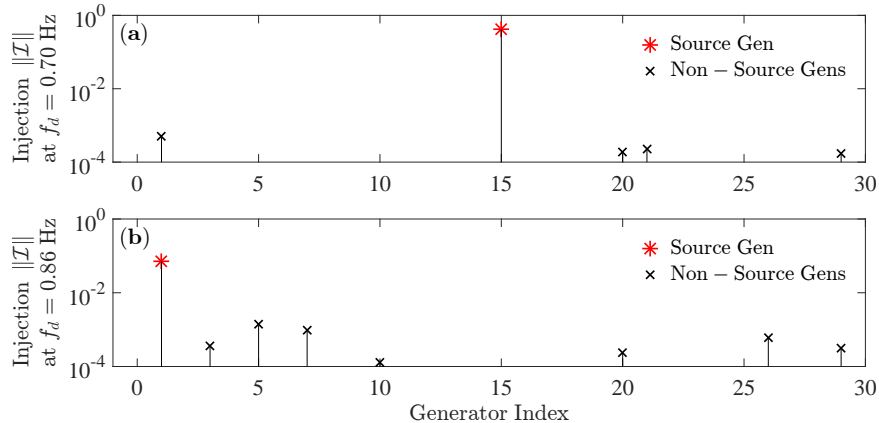


Figure 2-40: Current injection magnitudes of (2.124) found by the optimizer in stage 2 at both forcing frequencies.

## 2.4 A Dissipativity Interpretation of Energy-Based FO Source Location Methods

In this section, we leverage the equivalent circuit transformation of (2.46), along with the concept of dissipativity, in order to analyze quadratic energy-based FO source location methods, such as the popular DEF method [122]. Throughout this section,

we will make frequent use of Definition 1 and the proposed acronym of DQR. For convenience, we recall that if a dynamical system is DQR (i.e. Dissipative with respect to a Quadratic supply Rate), then it will satisfy the time domain integral (2.20). Furthermore, we note that a linear system is DQR in the time domain if its FRF is *positive real* in the frequency domain; refer to subsection 2.1.3 for more details. Before presenting the analysis, we define a DQR-transformation.

**Definition 4.** Consider MIMO transfer function  $\mathbf{H}(s) \in \mathbb{R}^{2 \times 2}$  which relates inputs  $\tilde{\mathbf{u}}(s)$  and output  $\tilde{\mathbf{y}}(s)$  via  $\tilde{\mathbf{y}}(s) = \mathbf{H}(s)\tilde{\mathbf{u}}(s)$ , where  $\mathbf{H}(s)$  may not be positive real. If nonsingular matrices  $\mathbf{M}(s)$  and  $\mathbf{\Gamma}(s)$  render matrix  $\mathbf{M}(s)\mathbf{H}(s)\mathbf{\Gamma}(s)$  positive real, then  $\mathbf{M}(s)$  and  $\mathbf{\Gamma}(s)$  are referred to as **DQR-transformation** matrices.

The motivation for providing this definition is the link between the positive realness of the resulting transfer function  $\mathbf{M}(s)\mathbf{H}(s)\mathbf{\Gamma}(s)$  and the DQR-ness of the associated system in the time domain:

$$\mathbf{M}(s)\mathbf{H}(s)\mathbf{\Gamma}(s) \text{ is Positive Real} \Leftrightarrow \mathcal{L}^{-1}\{\mathbf{M}(s)\mathbf{H}(s)\mathbf{\Gamma}(s)\} \text{ is DQR.} \quad (2.126)$$

### 2.4.1 A DQR Interpretation of the DEF Method

In this subsection, we interpret the traditional DEF time domain integral as a test of dissipativity (i.e. in a DQR sense), and then we offer a frequency domain interpretation via the LHS of (2.126).

**Definition 5.** Consider a linear system in the frequency domain characterized by  $\tilde{\mathbf{y}} = (\mathbf{C}(j\Omega_d \mathbb{1} - \mathbf{A})^{-1}\mathbf{B} + \mathbf{D})\tilde{\mathbf{u}}$ , where  $\Omega_d$  is a forcing frequency. To be consistent with the DEF literature, we refer to  $P^* = \operatorname{Re}\{\tilde{\mathbf{u}}^\dagger \tilde{\mathbf{y}}\}$  as **dissipating power**, and we refer to the corresponding time domain integral  $E^* = \int_0^t \mathbf{u}^T(\tau) \mathbf{y}(\tau) d\tau$  as **dissipating energy**. By positive realness,  $E^* > 0 \Leftrightarrow P^* > 0$ .

#### Common Shunt Components

We first derive or recall the FRFs associated with three of the primary dynamical elements in classical power systems [13]: constant impedances ( $\mathcal{Y}_z$ ), constant power loads ( $\mathcal{Y}_p$ ), and 2<sup>nd</sup> order synchronous generators ( $\mathcal{Y}_g$ ). We first consider a constant impedance shunt element whose admittance is given by  $G_z + jB_z = (R_z + jX_z)^{-1}$ . If positive current flows into the element, then Ohm's law yields

$$I_r(t) + jI_i(t) = (G_z + jB_z)(V_r(t) + jV_i(t)). \quad (2.127)$$

Writing the time domain signals as the sum of a steady state component plus a perturbation (e.g.  $I_r(t) = I_r + \Delta I_r(t)$ ), the linear expression (2.127) can be used to relate input and output perturbations:

$$\begin{bmatrix} \Delta I_r \\ \Delta I_i \end{bmatrix} = \begin{bmatrix} G_z & -B_z \\ B_z & G_z \end{bmatrix} \begin{bmatrix} \Delta V_r \\ \Delta V_i \end{bmatrix}. \quad (2.128)$$

Constant power loads are quadratic, with real and reactive components given by

$$P + jQ = (V_r + jV_i)(I_r + jI_i)^* \quad (2.129)$$

$$P = V_r I_r + V_i I_i \quad (2.130)$$

$$Q = V_i I_r - V_r I_i. \quad (2.131)$$

By solving this set of equations for  $I_r$  and  $I_i$  and then linearizing around some equilibrium point, the perturbation relationships are given by

$$\begin{bmatrix} \Delta I_r \\ \Delta I_i \end{bmatrix} = \begin{bmatrix} -G_p & B_p \\ B_p & G_p \end{bmatrix} \begin{bmatrix} \Delta V_r \\ \Delta V_i \end{bmatrix}, \quad (2.132)$$

where  $G_p = \frac{V_r I_r - V_i I_i}{V_r^2 + V_i^2}$  and  $B_p = \frac{-V_i I_r - I_i V_r}{V_r^2 + V_i^2}$  are defined for convenience. Since (2.128) and (2.132) are linear relationships with constant coefficients, taking the Fourier transform of these perturbation systems yields

$$\begin{bmatrix} \tilde{I}_r \\ \tilde{I}_i \end{bmatrix} = \underbrace{\begin{bmatrix} G_z & -B_z \\ B_z & G_z \end{bmatrix}}_{\mathcal{Y}_z} \begin{bmatrix} \tilde{V}_r \\ \tilde{V}_i \end{bmatrix} \quad (2.133)$$

$$\begin{bmatrix} \tilde{I}_r \\ \tilde{I}_i \end{bmatrix} = \underbrace{\begin{bmatrix} -G_p & B_p \\ B_p & G_p \end{bmatrix}}_{\mathcal{Y}_p} \begin{bmatrix} \tilde{V}_r \\ \tilde{V}_i \end{bmatrix}, \quad (2.134)$$

where  $\tilde{I}_r \equiv \tilde{I}_r(\Omega) = \mathcal{F}(\Delta I_r(t))$ , for example. Finally, the equations relating voltages and currents in a classical generator are nonlinear and differential, and the associated FRF is given by (2.47). We denote this FRF as  $\mathcal{Y}_g$ , which we restate here in a slightly

different, and more useful, form:

$$\mathcal{Y}_g = \gamma(\Omega) \underbrace{\begin{bmatrix} \sin(\delta) \cos(\delta) & -\cos^2(\delta) \\ \sin^2(\delta) & -\sin(\delta) \cos(\delta) \end{bmatrix}}_{T_\delta} + \underbrace{\begin{bmatrix} 0 & \frac{1}{X_d'} \\ \frac{-1}{X_d'} & 0 \end{bmatrix}}_{T_X} \quad (2.135)$$

$$\gamma(\Omega) = \frac{E'^2}{X_d'^2} \frac{\left( M(j\Omega)^2 + \frac{V_t E'}{X_d'} \cos(\varphi) \right) - j(\Omega D)}{\left( \frac{V_t E'}{X_d'} \cos(\varphi) - M\Omega^2 \right)^2 + (\Omega D)^2}, \quad (2.136)$$

where  $\delta$  is the generator's absolute rotor angle and  $\gamma \equiv \gamma(\Omega) \in \mathbb{C}^1$  is a complex frequency dependent parameter.

### Deriving DQR-Transformation Matrices associated with the DEF method

Originally developed from an energy function perspective [35, 177], the DEF method has a natural interpretation from the perspective of dissipativity. In this section, this interpretation is offered explicitly. The DEF is not re-derived here, but is instead stated in its most basic form and manipulated. The DEF integral is given by

$$W_{DE} = \int \text{Im}\{\tilde{I}^* d\tilde{V}\} \quad (2.137)$$

where  $\tilde{I}$  is the complex current flowing into an element (negative injection), and  $d\tilde{V}$  is the corresponding complex voltage differential. This expression may be manipulated:

$$W_{DE} = \int \text{Im}\{(I_r - jI_i)(dV_r + jdV_i)\} \quad (2.138a)$$

$$= \int (I_r dV_i - I_i dV_r) \quad (2.138b)$$

$$= \int \left( I_r \frac{dV_i}{dt} dt - I_i \frac{dV_r}{dt} dt \right) \quad (2.138c)$$

$$= \int \left( I_r \dot{V}_i + (-\dot{V}_r) I_i \right) dt. \quad (2.138d)$$

Assume now that the system underlying (2.138d) is linear with small signal inputs  $\dot{V}_i, -\dot{V}_r$  and outputs  $I_r, I_i$ . In this case,  $W_{DE}$  represents a dissipating energy  $E^* = \int (I_r \dot{V}_i + (-\dot{V}_r) I_i) dt$  (by Def. 5), and the corresponding FRF  $\mathcal{Y}_d$  associated with this system will satisfy

$$\begin{bmatrix} \tilde{I}_r \\ \tilde{I}_i \end{bmatrix} = \mathcal{Y}_d \begin{bmatrix} \dot{\tilde{V}}_i \\ -\dot{\tilde{V}}_r \end{bmatrix} \quad (2.139)$$

in the frequency domain. By the definition of positive realness, the integral (2.138d) associated with this system will be **positive** if  $\mathcal{Y}_d$  is a **positive real** admittance.

The DEF method is concerned with defining an energy function such that all elements in the power system “dissipate” energy unless they are the source, and accordingly, the convention used in [123, 118] is for (2.138d) to be negative if a power system element is not the source of an oscillation. Alternatively stated, positive values of  $W_{DE}$  in [123, 118] indicate the injection of energy from a FO source. To be consistent with the literature on dissipativity, this chapter assumes the opposite convention: the dissipating energy integral associated with DQR, non-source power system elements will be positive. The following theorem provides the DQR-transformation which is equivalent to the DEF integral of (2.137).

**Theorem 1.** Consider an element of a power system whose FRF  $\mathcal{Y}$  satisfies

$$\begin{bmatrix} \tilde{I}_r \\ \tilde{I}_i \end{bmatrix} = \mathcal{Y} \begin{bmatrix} \tilde{V}_r \\ \tilde{V}_i \end{bmatrix}. \quad (2.140)$$

The DEF integral of (2.137) associated with this element will be nonnegative if

$$\mathbf{M}\mathcal{Y}\boldsymbol{\Gamma} + (\mathbf{M}\mathcal{Y}\boldsymbol{\Gamma})^\dagger \succeq 0, \quad (2.141)$$

where DQR-transformation matrices  $\mathbf{M}$  and  $\boldsymbol{\Gamma}$  are defined as

$$\mathbf{M} = \begin{bmatrix} 1 & 0 \\ 0 & 1 \end{bmatrix} \quad (2.142a)$$

$$\boldsymbol{\Gamma} = \begin{bmatrix} 0 & -\frac{1}{j\Omega} \\ \frac{1}{j\Omega} & 0 \end{bmatrix}. \quad (2.142b)$$

*Proof.* We transform (2.140) via (2.142a) and (2.142b):

$$\mathbf{M} \begin{bmatrix} \tilde{I}_r \\ \tilde{I}_i \end{bmatrix} = (\mathbf{M}\mathcal{Y}\boldsymbol{\Gamma}) \boldsymbol{\Gamma}^{-1} \begin{bmatrix} \tilde{V}_r \\ \tilde{V}_i \end{bmatrix} \quad (2.143a)$$

$$\begin{bmatrix} \tilde{I}_r \\ \tilde{I}_i \end{bmatrix} = (\mathcal{Y}\boldsymbol{\Gamma}) \begin{bmatrix} j\Omega \tilde{V}_i \\ -j\Omega \tilde{V}_r \end{bmatrix} \quad (2.143b)$$

In the frequency domain,  $j\Omega \tilde{V}_i = \mathcal{F}\{\dot{V}_i\}$  and  $-j\Omega \tilde{V}_r = -\mathcal{F}\{\dot{V}_r\}$ , so

$$\underbrace{\begin{bmatrix} \tilde{I}_r \\ \tilde{I}_i \end{bmatrix}}_{\tilde{\mathbf{I}}} = (\mathcal{Y}\boldsymbol{\Gamma}) \underbrace{\begin{bmatrix} \tilde{\dot{V}}_i \\ -\tilde{\dot{V}}_r \end{bmatrix}}_{\tilde{\mathbf{V}}}. \quad (2.144)$$

Positive realness of  $\mathcal{Y}\Gamma$  ensures that

$$\operatorname{Re} \left\{ \tilde{\mathbf{V}}^\dagger \tilde{\mathbf{I}} \right\} = \operatorname{Re} \left\{ \tilde{\mathbf{V}}^\dagger (\mathcal{Y}\Gamma) \tilde{\mathbf{V}} \right\} \geq 0, \quad \forall \tilde{\mathbf{V}} \in \mathbb{C}^{2 \times 1}. \quad (2.145)$$

In the time domain, this further implies that

$$\int_0^t \mathbf{V}^T(\tau) \mathbf{I}(\tau) d\tau \geq 0, \quad (2.146)$$

where  $\mathcal{F}\{\mathbf{V}\} = \tilde{\mathbf{V}}$  and  $\mathcal{F}\{\mathbf{I}\} = \tilde{\mathbf{I}}$ . Since the inputs and outputs of (2.144) are identical to those of (2.139), which come from the manipulated DEF integral of (2.138d), then positive realness of  $\mathbf{M}\mathcal{Y}\Gamma + (\mathbf{M}\mathcal{Y}\Gamma)^\dagger$  implies a positive DEF integral.  $\square$

### Testing if Classical Network Components are DQR

We apply the results of Theorem 1 to consider whether loads and generators satisfy the DQR property. For notational simplicity, we define

$$K_x = \frac{1}{2}(\mathbf{M}\mathcal{Y}_x\Gamma + (\mathbf{M}\mathcal{Y}_x\Gamma)^\dagger), \quad (2.147)$$

where the DQR-transformation matrices  $\mathbf{M}$ ,  $\Gamma$  are given by (2.142a), (2.142b).

**Lemma 1.** *The DQR-transformation from Theorem 1 renders linearized constant power loads lossless.*

*Proof.* The eigenvalues of (2.147) for  $\mathcal{Y} = \mathcal{Y}_p$ , from (2.134), are

$$\lambda \{K_p\} = \lambda \left\{ \frac{1}{2} (\mathcal{Y}_p\Gamma + \Gamma^\dagger \mathcal{Y}_p^\dagger) \right\} \quad (2.148a)$$

$$= \lambda \left\{ \frac{1}{2} (\mathcal{Y}_p\Gamma - \mathcal{Y}_p\Gamma) \right\} \quad (2.148b)$$

$$= \{0, 0\} \quad (2.148c)$$

Since the eigenvalues are both 0, then  $\operatorname{Re}\{\tilde{\mathbf{V}}^\dagger \tilde{\mathbf{I}}\} = 0$  and the constant power loads are rendered lossless.  $\square$

**Lemma 2.** *The DQR-transformation from Theorem 1 renders linearized classical generator models DQR, but not strictly DQR.*

*Proof.* The eigenvalues of (2.147) for  $\mathcal{Y} = \mathcal{Y}_g$ , from (2.135), are:

$$\lambda \{K_g\} = \lambda \left\{ \frac{1}{2} (\mathcal{Y}_g \Gamma + \Gamma^\dagger \mathcal{Y}_g^\dagger) \right\} \quad (2.149)$$

$$= \left\{ -\frac{\text{Im}\{\gamma\}}{\Omega}, 0 \right\} \quad (2.150)$$

$$= \left\{ \frac{D \frac{E'^2}{X_d'^2}}{\left( \frac{V_t E'}{X_d'} \cos(\varphi) - M \Omega^2 \right)^2 + (\Omega D)^2}, 0 \right\}. \quad (2.151)$$

Since one eigenvalue is strictly positive (assuming positive damping) and one eigenvalue is 0, then  $\text{Re}\{\tilde{\mathbf{V}}^\dagger \tilde{\mathbf{I}}\} \geq 0$  and the generator is rendered DQR.  $\square$

**Lemma 3.** *The DQR-transformation from Theorem 1 renders constant impedance loads indefinite non-DQR in terms of dissipating energy injection.*

*Proof.* The eigenvalues of (2.147) for  $\mathcal{Y} = \mathcal{Y}_z$ , from (2.133), are:

$$\lambda \{K_z\} = \lambda \left\{ \frac{1}{2} (\mathcal{Y}_z \Gamma + \Gamma^\dagger \mathcal{Y}_z^\dagger) \right\} \quad (2.152)$$

$$= \left\{ -\frac{G_z}{\Omega}, +\frac{G_z}{\Omega} \right\}. \quad (2.153)$$

Since the eigenvalues are equal in magnitude but opposite in sign,  $K_z$  is an indefinite Hermitian matrix, and  $P^* = \text{Re}\{\tilde{\mathbf{V}}^\dagger \tilde{\mathbf{I}}\}$  can be positive or negative. Accordingly, conductive elements render an indefinite dissipating energy injection.  $\square$

The results of Lemma 3 may be used to compute the conditions under which a conductance (shunt or series) will inject positive or negative dissipating energy. To do so, we manipulate the dissipating power  $\text{Re}\{\tilde{\mathbf{V}}^\dagger \tilde{\mathbf{I}}\}$ :

$$P^* = \text{Re} \left\{ \tilde{\mathbf{V}}^\dagger \begin{bmatrix} 0 & -\frac{jG_z}{\Omega} \\ \frac{jG_z}{\Omega} & 0 \end{bmatrix} \tilde{\mathbf{V}} \right\} \quad (2.154)$$

$$= -\frac{G_z}{\Omega} \text{Im} \left\{ \tilde{V}_i^\dagger \tilde{V}_r - \tilde{V}_r^\dagger \tilde{V}_i \right\}. \quad (2.155)$$

We switch to a polar representation of the voltage perturbation phasors so that  $\tilde{V}_r = j\Omega |\tilde{V}_r| e^{j\theta_r}$  and  $\tilde{V}_i = j\Omega |\tilde{V}_i| e^{j\theta_i}$  (see [123, Fig. 2] for an interpretation):

$$P^* = G_z \Omega \left| \tilde{V}_i \right| \left| \tilde{V}_r \right| \text{Im} \left\{ e^{j(\theta_r - \theta_i)} - e^{-j(\theta_r - \theta_i)} \right\} \quad (2.156)$$

$$= 2G_z \Omega \left| \tilde{V}_i \right| \left| \tilde{V}_r \right| \sin(\theta_r - \theta_i) \quad (2.157)$$

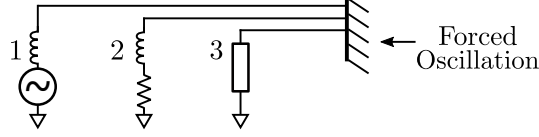


Figure 2-41: A generator (element 1), a constant impedance load (element 2), and a constant power load (element 3) are tied to an oscillating infinite bus.

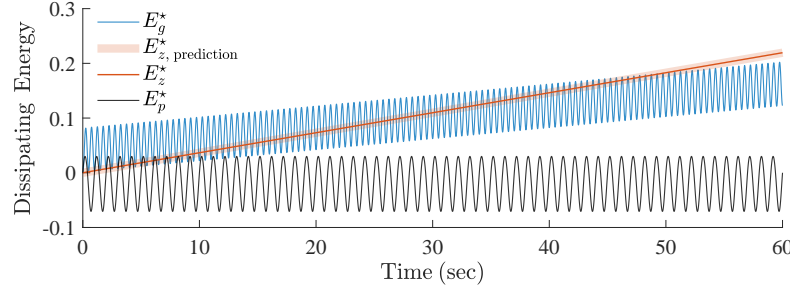


Figure 2-42: Simulated DEFs associated with the generator, impedance, and constant power load from Fig. 2-41. Real voltage perturbations lead the phase of imaginary voltage perturbations at the infinite bus, and generator damping is positive.

Therefore, the sign of the dissipating energy injection depends on  $\sin(\theta_r - \theta_i)$ , i.e.  $\sin$  of the phase shift between the input voltage perturbations. This can be shown to be consistent with the conditions given in [36] for energy injection.

## Simulation Results

To test the results presented in Theorems 1-3, we consider a situation in which a forced oscillation is applied by an infinite bus to the three power system elements in consideration, as depicted by Fig. 2-41. For the sake of model explanation brevity, all simulation code has been publicly posted online<sup>9</sup>. Two tests were run: in the first test, the phase of  $\tilde{V}_r$  at the infinite bus *led* the phase of  $\tilde{V}_i$  by  $\frac{\pi}{5}$ , and the damping of the generator was assigned positive and large. The dissipating energy integrals were computed according to (2.138d). Additionally, the dissipating energy injected by the constant impedance load was predicted by integrating the analytical expression given in (2.157). These results are shown in Fig. 2-42, where the energy dissipation is positive for the impedance load and the generator. The dissipating energy of the constant power load is lossless.

In the second test, the phase of  $\tilde{V}_r$  at the infinite bus *lagged* the phase of  $\tilde{V}_i$  by  $\frac{\pi}{5}$ , and the damping of the generator was assigned a slightly negative value. These

<sup>9</sup><https://github.com/SamChevalier/PassiveFOs>

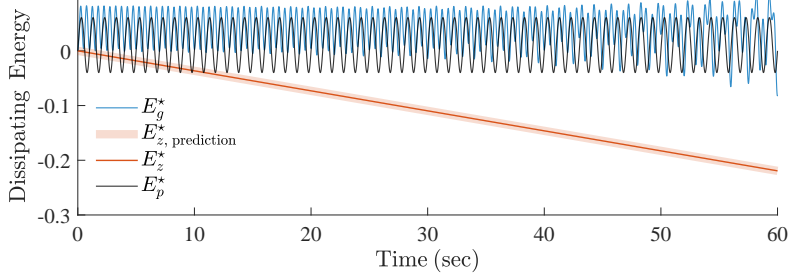


Figure 2-43: Simulated DEFs associated with the generator, impedance, and constant power load from Fig. 2-41. Real voltage perturbations lag the phase of imaginary voltage perturbations at the infinite bus, and generator damping is slightly negative.

results are shown in Fig. 2-43, where the energy dissipation of the impedance load has switched signs and is now negative. The constant power load is still lossless, and the generator, when stable, has a slight negative trend and therefore injects negative dissipating energy. This is predicted by the non-zero eigenvalue in (2.151).

#### 2.4.2 Deriving a “Perturbative” Network Model

In this subsection, we introduce a linearized network model which is particularly useful for analyzing FO propagation in power systems. We refer to it as a “perturbative” model since it captures the network’s response to small<sup>10</sup> perturbations.

##### Network Modeling

Consider a power system network whose graph  $\mathcal{G}(\mathcal{V}, \mathcal{E})$  has edge set  $\mathcal{E}$ ,  $|\mathcal{E}| = m$ , vertex set  $\mathcal{V}$ ,  $|\mathcal{V}| = n$ , and directed nodal incidence matrix  $E \in \mathbb{R}^{m \times n}$  [12]. In power system modeling, it is standard practice to use the incidence matrix to build the nodal admittance matrix  $Y_b$  from the primitive admittance matrix  $Y_p$  via  $Y_b = E^\dagger Y_p E$  [131]. This procedure is possible because the admittances in  $Y_p$  are complex values  $\in \mathbb{C}^1$ . In the following analysis, all admittances in the form of (2.59) must be expressed in  $2 \times 2$  matrix form (i.e.  $\mathcal{Y} \in \mathbb{C}^{2 \times 2}$ ). Accordingly, we need an incidence matrix which can relate  $2 \times 2$ , rather than  $1 \times 1$ , admittance values. We thus build a so-called “augmented” incidence matrix  $E_a \in \mathbb{R}^{2m \times 2n}$ . This matrix is constructed by taking  $E$  and replacing all values of 1 with the  $2 \times 2$  identity matrix  $\mathbb{1}_2$  and all values of 0 with

---

<sup>10</sup>Similar to the other tools in this chapter, the following framework is valid when FOs are sufficiently “small”, such that quadratic nonlinearities may be neglected.

a  $2 \times 2$  zero matrix  $\mathbf{0}$ :

$$E = \begin{bmatrix} 1 & -1 & \dots \\ 0 & 1 & \\ \vdots & & \ddots \end{bmatrix} \Leftrightarrow E_a = \begin{bmatrix} \mathbb{1}_2 & -\mathbb{1}_2 & \dots \\ \mathbf{0} & \mathbb{1}_2 & \\ \vdots & & \ddots \end{bmatrix}. \quad (2.158)$$

Considering voltage and current perturbation phasors such as  $\tilde{\mathbf{u}}_v$  and  $\tilde{\mathbf{y}}$  from (2.59), we define the vector  $\mathbf{V}_b \in \mathbb{C}^{2n \times 1}$  as the vector of rectangular bus voltage perturbation phasors, and we define the vector  $\mathbf{I}_l \in \mathbb{C}^{2m \times 1}$  as the vector of rectangular line current perturbation phasors, where the convention of the positive line current flows agrees with the direction of the augmented incidence matrix:

$$\mathbf{V}_b = \begin{bmatrix} \tilde{V}_{r,1} \\ \tilde{V}_{i,1} \\ \vdots \\ \tilde{V}_{r,n} \\ \tilde{V}_{i,n} \end{bmatrix}, \quad \mathbf{I}_l = \begin{bmatrix} \tilde{I}_{r,1} \\ \tilde{I}_{i,1} \\ \vdots \\ \tilde{I}_{r,m} \\ \tilde{I}_{i,m} \end{bmatrix}. \quad (2.159)$$

Admittance matrices  $\mathcal{Y}_{l,1}, \dots, \mathcal{Y}_{l,m}$ ,  $\mathcal{Y}_{l,i} \in \mathbb{R}^{2 \times 2}$ , associated with the  $m$  transmission lines, are placed diagonally in the matrix  $\mathcal{Y}_L \in \mathbb{R}^{2m \times 2m}$  such that

$$\mathcal{Y}_L = \begin{bmatrix} \mathcal{Y}_{l,1} & & \mathbf{0} \\ & \ddots & \\ \mathbf{0} & & \mathcal{Y}_{l,m} \end{bmatrix}. \quad (2.160)$$

Transformers with off-nominal tap ratios, such as tap changers, are discussed in Appendix A.1. Line current and bus voltage perturbations obey Ohm's law:

$$\mathcal{Y}_L E_a \mathbf{V}_b = \mathbf{I}_l. \quad (2.161)$$

Admittance matrices  $\mathcal{Y}_{s,1}, \dots, \mathcal{Y}_{s,n}$ ,  $\mathcal{Y}_{s,i} \in \mathbb{C}^{2 \times 2}$ , associated with shunt elements at each of the  $n$  buses, are placed diagonally in the matrix  $\mathcal{Y}_S \in \mathbb{C}^{2n \times 2n}$ , such that

$$\mathcal{Y}_S = \begin{bmatrix} \mathcal{Y}_{s,1} & & \mathbf{0} \\ & \ddots & \\ \mathbf{0} & & \mathcal{Y}_{s,n} \end{bmatrix}. \quad (2.162)$$

These shunt admittances are not simply capacitors or inductors; they can represent generators, loads, or any other terminal element in the system and can be constructed

via (2.59). If multiple elements are connected in parallel, such as a generator and its station load, their admittances can be modeled independently and summed to compute the aggregate shunt admittance. The shunt matrix  $\mathcal{Y}_S$  may be used to compute the shunt current injections<sup>11</sup>  $\mathbf{I}_s \in \mathbb{C}^{2n \times 1}$  via

$$\mathbf{I}_s = \mathcal{Y}_S \mathbf{V}_b. \quad (2.163)$$

When analyzing a network with this representation, FOs show up like current sources at their respective source buses. For a system experiencing a *single* FO, there will be a *single* current source  $\mathcal{I} \in \mathbb{C}^{2 \times 1}$  driving the entire network. We define a sparse FO vector of current injections  $\mathbf{J} \in \mathbb{C}^{2n \times 1}$  whose structure will take the form

$$\mathbf{J} = [\mathbf{0}, \dots \mathbf{0}, \mathcal{I}^T, \mathbf{0}, \dots \mathbf{0}]^T. \quad (2.164)$$

If bus  $k$  is the source of the FO, then  $\mathcal{I}$  will be located in elements  $\mathbf{J}_{2k-1}$  and  $\mathbf{J}_{2k}$ . Source injections in  $\mathbf{J}$  obey the same current convention as  $\mathbf{I}_s$ . The network obeys KCL, i.e., all nodal currents sum to 0:

$$\mathbf{J} + \mathbf{I}_s + E_a^\dagger \mathbf{I}_l = \mathbf{0}. \quad (2.165)$$

We define  $\mathbf{I}_I \equiv E_a^\dagger \mathbf{I}_l$  to be the aggregate current injection at each node: it represents the sum of the source current injection at each bus plus the shunt current flowing to ground. Via conservation of current at each bus, we have

$$-\mathbf{J} = \mathbf{I}_I + \mathbf{I}_s \quad (2.166a)$$

$$= E_a^\dagger \mathbf{I}_l + \mathcal{Y}_S \mathbf{V}_b \quad (2.166b)$$

$$= (E_a^\dagger \mathcal{Y}_L E_a + \mathcal{Y}_S) \mathbf{V}_b. \quad (2.166c)$$

The block-Hermitian dynamic nodal admittance (or augmented dynamic Y-bus) matrix  $\mathcal{Y}_B \in \mathbb{C}^{2n \times 2n}$  is thus defined to be

$$\mathcal{Y}_B = E_a^\dagger \mathcal{Y}_L E_a + \mathcal{Y}_S. \quad (2.167)$$

Assuming there is a single FO in the system, it is instructive to rewrite (2.166c) with partitioned matrices and vectors, where the system has been renumbered such that

---

<sup>11</sup>Shunt currents flowing out of the circuit to ground are defined as positive.

the source bus is bus 1, and the current injection has a value of  $\mathcal{I} \in \mathbb{C}^{2 \times 1}$ :

$$-\mathbf{J} = \mathcal{Y}_B \mathbf{V}_b \quad (2.168a)$$

$$\begin{bmatrix} -\mathcal{I} \\ \mathbf{0} \end{bmatrix} = \begin{bmatrix} \mathcal{Y}_{B1} & \mathcal{Y}_{B2} \\ \mathcal{Y}_{B3} & \mathcal{Y}_{B4} \end{bmatrix} \begin{bmatrix} \mathbf{V}_s \\ \mathbf{V}_{ns} \end{bmatrix}, \quad (2.168b)$$

where  $\mathbf{V}_s \in \mathbb{C}^{2 \times 1}$  represents voltage perturbations at the source bus,  $\mathbf{V}_{ns} \in \mathbb{C}^{(2n-2) \times 1}$  represents voltage perturbations at all other buses, and  $\mathbf{V}_b = \mathbf{V}_s^\top \mathbf{V}_{ns}$ . While  $\mathcal{I}$  represents the true source current injection, we may also define  $\mathcal{I}'$  as the sum of the source current at the source bus plus its shunt injection:

$$\mathcal{I}' = \mathcal{I} + \mathcal{Y}_{s,1} \mathbf{V}_s. \quad (2.169)$$

Correspondingly, we say that  $\mathcal{Y}'_{B1}$  contains no shunt element, and  $\mathcal{I}'$  is the current *directly measured at the source bus flowing into the network*; we note that it is equal to the first two elements of  $\mathbf{I}_I$ . We now restate (2.168a)-(2.168b) with this update:

$$-\mathbf{J}' = \mathcal{Y}'_B \mathbf{V}_b \quad (2.170a)$$

$$\begin{bmatrix} -\mathcal{I}' \\ \mathbf{0} \end{bmatrix} = \begin{bmatrix} \mathcal{Y}'_{B1} & \mathcal{Y}_{B2} \\ \mathcal{Y}_{B3} & \mathcal{Y}_{B4} \end{bmatrix} \begin{bmatrix} \mathbf{V}_s \\ \mathbf{V}_{ns} \end{bmatrix}. \quad (2.170b)$$

A graphical interpretation of (2.170) is given in Fig. (2-44), where a time domain power system model is contrasted to its frequency domain perturbative model.

A simple Kron reduction can be performed in order to determine the effective admittance “seen” by the current source:

$$-\mathcal{I}' = \underbrace{\left( \mathcal{Y}'_{B1} - \mathcal{Y}_{B2} \mathcal{Y}_{B4}^{-1} \mathcal{Y}_{B3} \right)}_{\mathcal{Y}_N} \mathbf{V}_s, \quad (2.171)$$

where  $\mathcal{Y}_N \in \mathbb{C}^{2 \times 2}$  is an aggregate network admittance matrix and  $\mathbf{V}_s$  is the resulting voltage caused by the current injection  $\mathcal{I}'$  interacting with the aggregate network dynamics codified in  $\mathcal{Y}_N$ . In this model, since voltage perturbations are considered a response to rogue current injections, it is helpful to rewrite (2.171) with voltage as a function of current, i.e.  $\mathbf{V}_s = -\mathcal{Z}_N \mathcal{I}'$ , where  $\mathcal{Z}_N = \mathcal{Y}_N^{-1}$  is the aggregate network impedance. In other words, the current injection  $\mathcal{I}'$  *gives rise* to the network voltages, and the vector  $\mathbf{V}_b$  in (2.170a) is not arbitrary: the Kron reduction of (2.171) is only meaningful when  $\mathbf{V}_b$  acts as a solution to the linear system  $-\mathbf{J}' = \mathcal{Y}'_B \mathbf{V}_b$ , i.e.

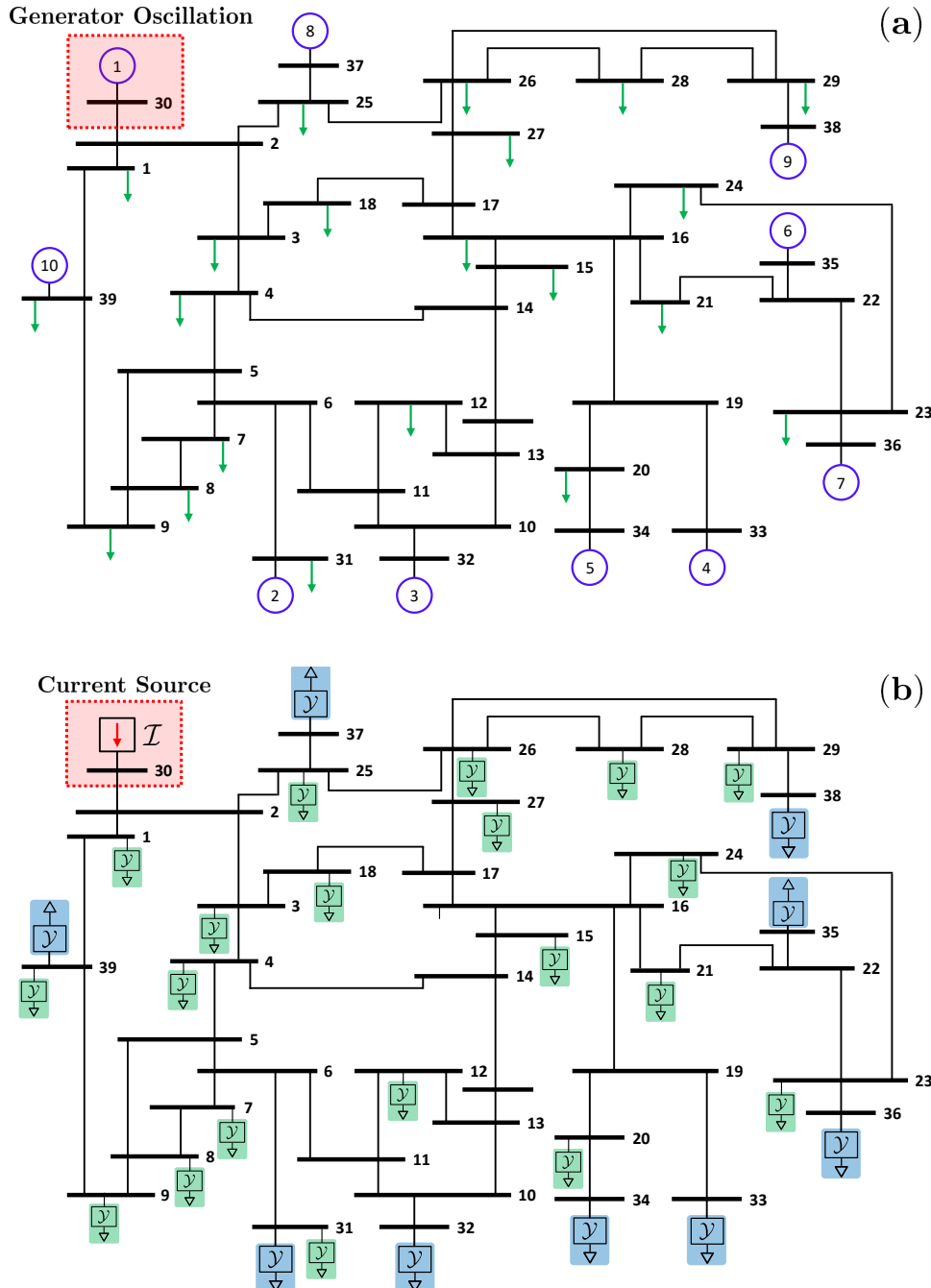


Figure 2-44: Panel (a) shows a model of the IEEE 39-bus power system in the time domain, where blue circles are generators, green arrows are loads, and an oscillation source is located in the upper left corner. Panel (b) shows the same system in the frequency domain, at  $\Omega = \Omega_d$ , where loads, generators and sources have become admittances, and the oscillation source has been transformed into a current injection  $\mathcal{I}$ , which excites the entire circuit. Accordingly, panel (b) is entirely *analogous* to an AC circuit in oscillatory steady-state excited by a single current injection source.

$$\mathbf{V}_b = -(\mathcal{Y}'_B)^{-1} \mathbf{J}'.$$

**Definition 6.** We refer to the admittance matrix  $\mathcal{Y}_N$  of (2.171) as the system's dynamic Ward equivalent (**DWE**) admittance.

### Quadratic “Energy” Considerations in the Perturbative Network

As with any network which obeys Kirchhoff's laws, Tellegen's theorem is also obeyed: the sum of the products of branch (including shunt branches) potential differences and branch flows is equal to 0. Accordingly,

$$0 = (E_a \mathbf{V}_b)^\dagger \mathbf{I}_l + \mathbf{V}_b^\dagger (\mathbf{I}_s + \mathbf{J}) \quad (2.172a)$$

$$= \mathbf{V}_b^\dagger (E_a^\dagger \mathbf{I}_l + \mathbf{I}_s + \mathbf{J}) \quad (2.172b)$$

$$= \mathbf{V}_b^\dagger (\mathcal{Y}_B - \mathcal{Y}_B) \mathbf{V}_b, \quad (2.172c)$$

where (2.172a) is the statement of Tellegen's theorem, (2.172b) is the conservation of current, and (2.172c) is the resulting proof. As a consequence of this theorem, there exist a family of quadratic functionals for which conservation laws can be formulated. An obvious one is the “real power”,  $\text{Re}\{\mathbf{VI}^\dagger\}$ , that is consumed only on the elements with positive resistance. In the context of FOS, an alternative interpretation of the conservation of power can be acquired by manipulating (2.170b) in order to define another (arbitrary) type of quadratic power<sup>12</sup>. The key observation is that this new quadratic power will be conserved throughout the network. To show why, we consider matrix  $\mathcal{Q} \in \mathbb{C}^{2n \times 2n}$  with block diagonal sub-matrices  $\mathcal{Q}_b \in \mathbb{C}^{2 \times 2}$ :

$$\mathcal{Q} = \begin{bmatrix} \mathcal{Q}_b & \mathbf{0} \\ \mathbf{0} & \ddots \\ \mathbf{0} & \mathcal{Q}_b \end{bmatrix}. \quad (2.173)$$

We now left multiply (2.170a) by  $\mathbf{V}_b^\dagger \mathcal{Q}$ , which represents the application of a quadratic energy function:

$$-\mathbf{V}_b^\dagger \mathcal{Q} \mathbf{J}' = \mathbf{V}_b^\dagger \mathcal{Q} \mathcal{Y}'_B \mathbf{V}_b \quad (2.174a)$$

$$-\mathbf{V}_s^\dagger \mathcal{Q}_b \mathcal{I}' = \mathbf{V}_b^\dagger (\mathcal{Q} E_a^\dagger \mathcal{Y}_L E_a) \mathbf{V}_b + \mathbf{V}_b^\dagger (\mathcal{Q} \mathcal{Y}'_S) \mathbf{V}_b. \quad (2.174b)$$

---

<sup>12</sup>The term “quadratic power” is used since we are multiplying voltages and currents, but the quadratic quantity doesn't necessarily have the interpretation of physical power. It can also be interpreted as an “energy function”. Quadratic energy and quadratic power are therefore used interchangeably.

Different choices for matrix  $\mathcal{Q}_b$  correspond to different energy function applications, but in each case, the quadratic quantity is conserved. For example, if  $\mathcal{Q}_b$  is chosen such that

$$\mathcal{Q}_b = \begin{bmatrix} 0 & -\frac{1}{j\Omega} \\ \frac{1}{j\Omega} & 0 \end{bmatrix}, \quad (2.175)$$

then the associated energy function corresponds to the DEF method [40]. Under DEF assumptions, lines and loads are rendered lossless, i.e  $(\mathcal{Q}_b\mathcal{Y}) + (\mathcal{Q}_b\mathcal{Y})^\dagger = \mathbf{0}$ . Thus, in taking the real part, (2.174b) simplifies to

$$\underbrace{\text{Re}\{\mathbf{V}_s^\dagger \mathcal{Q}_b \mathcal{I}'\}}_{\text{Source Energy}} + \sum_{i=2}^n \underbrace{\text{Re}\{\mathbf{V}_{ns,i}^\dagger (\mathcal{Q}_b \mathcal{Y}_{s,i}) \mathbf{V}_{ns,i}\}}_{\text{Generator Damping Contributions}} = 0, \quad (2.176)$$

where  $\mathbf{V}_s$  and  $\mathbf{V}_{ns,i}$  are the source and  $i^{\text{th}}$  non-source bus voltage perturbation vectors, respectively. The formulation of (2.176) further clarifies the DEF's functionality: since all the damping energy consumed by generators is positive [40], the source energy is necessarily negative and can be traced back to the single, negative source. The DEF technique, therefore, is based on tracking a particular type of quadratic power in the network. When constructing the system's quadratic energy function, we are not restricted to choosing just a  $\mathcal{Q}$  matrix. We may also introduce matrix  $\mathcal{P}$  whose structure matches  $\mathcal{Q}$ . For example, we may set  $\mathbf{U}_b = \mathcal{P}^{-1}\mathbf{V}_b$ , left multiply (2.170a) by  $\mathbf{U}_b^\dagger \mathcal{Q}$ , and insert a  $\mathcal{P}\mathcal{P}^{-1}$  term. Updating (2.176) yields

$$\underbrace{\text{Re}\{\mathbf{U}_s^\dagger \mathcal{Q}_b \mathcal{I}'\}}_{\text{Source Energy}} + \sum_{i=2}^n \underbrace{\text{Re}\{\mathbf{U}_{ns,i}^\dagger (\mathcal{Q}_b \mathcal{Y}_{s,i} \mathcal{P}_b) \mathbf{U}_{ns,i}\}}_{\text{Generator Damping Contributions}} = 0. \quad (2.177)$$

## Energy Function Analysis

The DEF method can be interpreted as the application of a specific quadratic energy function to all elements of a network. Reference [40], though, shows that the DEF energy function is inadequate for lossy network elements. While it may be tempting to develop a new DQR-transformation which is suitable for lossy networks, in this section, we prove that no constant quadratic energy function exists for the classical model of a multimachine power system. For coherency, we first offer the following clarification of how we use the terms "lossy" and "lossless" in this section.

**Definition 7.** In keeping with the conventional nomenclature for both power systems and dissipativity literature, we offer the following definitions for lossy and lossless:

- **Lossy:** A lossy element is an element which contains resistance; a lossy system is a system which contains resistive transmission lines.
- **Lossless<sup>13</sup>:** The term lossless describes a FRF whose Hermitian part is  $\mathbf{0}$ . If  $\mathcal{Y} + \mathcal{Y}^\dagger = \mathbf{0}$ ,  $\mathcal{Y}$  is said to be lossless; if  $\mathbf{M}\mathcal{Y} + (\mathbf{M}\mathcal{Y})^\dagger = \mathbf{0}$ ,  $\mathbf{M}\mathcal{Y}$  is said to be lossless. This is further specified just below relation (2.23) in the background.

### Basis Matrices

To aide in the energy function analysis and inference techniques, we define a useful set of basis matrices.

**Definition 8.** We define orthogonal ( $A^{-1} = A^\dagger$ ) basis matrices

$$\begin{aligned}\overline{T}_1 &= \begin{bmatrix} 1 & 0 \\ 0 & 1 \end{bmatrix}, & \overline{T}_2 &= \begin{bmatrix} 1 & 0 \\ 0 & -1 \end{bmatrix}, \\ \overline{T}_3 &= \begin{bmatrix} 0 & 1 \\ 1 & 0 \end{bmatrix}, & \overline{T}_4 &= \begin{bmatrix} 0 & -1 \\ 1 & 0 \end{bmatrix},\end{aligned}$$

and the set  $\mathbb{T} = \{\overline{T}_1, \overline{T}_2, \overline{T}_3, \overline{T}_4\}$ . Set  $\mathbb{T}$  spans region  $\mathbb{R}^{2 \times 2}$ :

$$\text{span}(\mathbb{T}) = \left\{ \sum_{i=1}^4 \lambda_i \overline{T}_i \mid \overline{T}_i \in \mathbb{T}, \lambda_i \in \mathbb{R}^1 \right\} = \mathbb{R}^{2 \times 2}. \quad (2.179)$$

**Lemma 4.** There exists no non-singular matrix  $\Gamma \in \mathbb{C}^{2 \times 2}$  for which, simultaneously,

$$\text{Re} \{ \mathbf{v}^\dagger (\overline{T}_i \Gamma) \mathbf{v} \} \geq 0, \forall \mathbf{v} \in \mathbb{C}^{2 \times 1}, \forall i \in \{1\} \quad (2.180)$$

$$\text{Re} \{ \mathbf{v}^\dagger (\overline{T}_i \Gamma) \mathbf{v} \} = 0, \forall \mathbf{v} \in \mathbb{C}^{2 \times 1}, \forall i \in \{2, 3, 4\}. \quad (2.181)$$

*Proof.* We write  $\Gamma$  as the sum of its diagonal ( $\Gamma_d$ ) and off-diagonal ( $\Gamma_o$ ) component matrices:  $\Gamma = \Gamma_d + \Gamma_o$ . Since  $\text{Re}\{\mathbf{v}^\dagger (\overline{T}_i \Gamma) \mathbf{v}\} = 0$ ,  $\forall \mathbf{v} \in \mathbb{C}^{2 \times 2}$  is equivalent to stating that  $\overline{T}_i \Gamma + (\overline{T}_i \Gamma)^\dagger = \mathbf{0}$ , the constraints on  $\Gamma$  caused by  $\overline{T}_2$ ,  $\overline{T}_3$ , and  $\overline{T}_4$  from (2.181) may be stated as

$$\overline{T}_2 \rightarrow \Gamma_d = -\Gamma_d^\dagger, \quad \Gamma_o = \Gamma_o^\dagger, \quad (2.182)$$

$$\overline{T}_3 \rightarrow K\Gamma_d = -\Gamma_d^\dagger K, \quad K\Gamma_o = -\Gamma_o^\dagger K, \quad (2.183)$$

$$\overline{T}_4 \rightarrow K\Gamma_d = \Gamma_d^\dagger K, \quad K\Gamma_o = -\Gamma_o^\dagger K, \quad (2.184)$$

---

<sup>13</sup>While “lossless” certainly can also refer to a transmission network with purely reactive lines, we do not invoke that definition anywhere in this section.

where  $K \equiv \bar{T}_3$  is defined to be the reversal matrix in [89]. Accordingly,  $\Gamma_d$  must be simultaneously skew-Hermitian, skew-perhermitian and perhermitian, respectively [89]. Necessarily,  $\Gamma_d = \mathbf{0}$ . The matrix  $\Gamma_o$  must be simultaneously Hermitian and skew-perhermitian. Necessarily,  $j\beta\bar{T}_4$ ,  $\beta \in \mathbb{R}^1$ , is the only matrix which fits this description. We define

$$\Gamma^* = j\beta\bar{T}_4 \quad (2.185)$$

as the only matrix which uniformly satisfies (2.181). We apply  $\Gamma = \Gamma^*$  to (2.180) and consider the eigenvalues of the matrix  $\bar{T}_1\Gamma^* + (\bar{T}_1\Gamma^*)^\dagger = 2\beta j\bar{T}_4$ :

$$\det [2\beta j\bar{T}_4 - \text{diag}\{\lambda\}] = \lambda^2 - 4\beta^2, \quad (2.186)$$

$$\lambda = \pm 2\beta \quad (2.187)$$

which violates (2.180). Since  $\bar{T}_1\Gamma^* + (\bar{T}_1\Gamma^*)^\dagger$  is an indefinite matrix but  $\Gamma^*$  is the only matrix which satisfies (2.181), the theorem has been proved.  $\square$

**Corollary 1.**  $\Gamma^*$  is a solution to  $P\Gamma^* + (P\Gamma^*)^\dagger = \mathbf{0}$  for any matrix  $P$  which may be written as  $P = \sum_{i=2}^4 \alpha_i \bar{T}_i$ ,  $\alpha_i \in \mathbb{R}^1$ .

**Corollary 2.** The results of Lemma 4 stand if  $\bar{T}_i$  is right multiplied by transformation matrix  $\mathbf{M}$  instead of left multiplied by transformation matrix  $\Gamma$ . There exists no non-singular matrix  $\mathbf{M} \in \mathbb{C}^{2 \times 2}$  for which the following simultaneously hold:

$$\text{Re} \{ \mathbf{v}^\dagger (\mathbf{M}\bar{T}_i) \mathbf{v} \} \geq 0, \forall \mathbf{v} \in \mathbb{C}^{2 \times 2}, \forall i \in \{1\} \quad (2.188)$$

$$\text{Re} \{ \mathbf{v}^\dagger (\mathbf{M}\bar{T}_i) \mathbf{v} \} = 0, \forall \mathbf{v} \in \mathbb{C}^{2 \times 2}, \forall i \in \{2, 3, 4\} \quad (2.189)$$

**Corollary 3.** By employing both non-singular matrices  $\Gamma \in \mathbb{C}^{2 \times 2}$  and  $\mathbf{M} \in \mathbb{C}^{2 \times 2}$ , the solution to

$$\text{Re} \{ \mathbf{v}^\dagger (\mathbf{M}\bar{T}_i\Gamma) \mathbf{v} \} = 0, \forall \mathbf{v} \in \mathbb{C}^{2 \times 1}, \forall i \in \{2, 3, 4\} \quad (2.190)$$

must take the form  $\Gamma = (j\beta\bar{T}_4)\mathbf{M}^\dagger$  for any  $\mathbf{M} \in \mathbb{C}^{2 \times 2}$ . This may be seen via the following manipulation:

$$\mathbf{0} = \mathbf{M}\bar{T}_i\Gamma + (\mathbf{M}\bar{T}_i\Gamma)^\dagger, \quad \forall i \in \{2, 3, 4\} \quad (2.191a)$$

$$= \bar{T}_i(\Gamma\mathbf{M}^{\dagger-1}) + (\mathbf{M}^{-1}\Gamma^\dagger)\bar{T}_i^\dagger, \quad \forall i \in \{2, 3, 4\}. \quad (2.191b)$$

Since (2.191b) may only be solved by  $\Gamma\mathbf{M}^{\dagger-1} = j\beta\bar{T}_4$ , per Lemma 4, we have that  $\Gamma = (j\beta\bar{T}_4)\mathbf{M}^\dagger$  must be satisfied.

## Quadratic Energy Functions in a Classical Power System

We now assume the classical model of a lossy multimachine power system model [13] and allow for constant power loads to be present. The forms of the FRFs associated with constant power loads ( $\mathcal{Y}_p$ ), constant impedance lines/shunts ( $\mathcal{Y}_z$ ), and classical generators ( $\mathcal{Y}_g$ ) are given by (2.133)-(2.135). The set of plausible FRFs associated with these three elements may be constructed according to the following basis matrix combinations:

$$\mathcal{Y}_p = \sum_{i=2,3} a_i \bar{T}_i, \quad a_i \in \mathbb{R}^1 \quad (2.192a)$$

$$\mathcal{Y}_z = \sum_{i=1,4} a_i \bar{T}_i, \quad a_i \in \mathbb{R}^1 \quad (2.192b)$$

$$\mathcal{Y}_g = \sum_{i=2,3,4} (a_i + j b_i) \bar{T}_i, \quad a_i, b_i \in \mathbb{R}^1. \quad (2.192c)$$

In Appendix A.5, we prove that the classical generator admittance model, for a given frequency, can be constructed with only four coefficients. Notwithstanding, we now prove that a perturbative system model containing elements (2.192a)-(2.192c) cannot be rendered DQR under any quadratic DQR-transformation. In other words, there is no quadratic quantity that is dissipated by all elements present in common networks.

**Theorem 2.** *There exist no non-singular matrices  $\mathbf{M} \in \mathbb{C}^{2 \times 2}$  and  $\boldsymbol{\Gamma} \in \mathbb{C}^{2 \times 2}$  for which*

$$\mathbf{M}\mathcal{Y}\boldsymbol{\Gamma} + (\mathbf{M}\mathcal{Y}\boldsymbol{\Gamma})^\dagger \succeq 0, \quad \forall \mathcal{Y} \in \{\mathcal{Y}_p, \mathcal{Y}_z, \mathcal{Y}_g\}. \quad (2.193)$$

*Proof.* The FRF of a strictly reactive element, such as matrix  $T_X$  in (2.135), is  $\propto \bar{T}_4$  while the FRF of a strictly capacitive element is  $\propto -\bar{T}_4$ . The only way for  $\mathbf{M}\bar{T}_4\boldsymbol{\Gamma} + (\mathbf{M}\bar{T}_4\boldsymbol{\Gamma})^\dagger \succeq 0$  and  $-\mathbf{M}\bar{T}_4\boldsymbol{\Gamma} - (\mathbf{M}\bar{T}_4\boldsymbol{\Gamma})^\dagger \succeq 0$  to be simultaneously true is for  $\mathbf{M}\bar{T}_4\boldsymbol{\Gamma} + (\mathbf{M}\bar{T}_4\boldsymbol{\Gamma})^\dagger \equiv \mathbf{0}$ . Since both reactive and capacitive elements appear in classical power systems,  $\bar{T}_4$  must be lossless under the desired DQR-transformation.

We now consider some classical generator whose damping characteristics are sufficiently small ( $D \approx 0$ ), such that  $\gamma$  is a real parameter. In this case, the matrix  $\mathbf{M}\mathcal{Y}_g\boldsymbol{\Gamma} + (\mathbf{M}\mathcal{Y}_g\boldsymbol{\Gamma})^\dagger$  reduces to  $\mathbf{M}\gamma T_\delta\boldsymbol{\Gamma} + (\mathbf{M}\gamma T_\delta\boldsymbol{\Gamma})^\dagger$  since  $T_X$  must be a lossless element according to the previous conclusion about  $\bar{T}_4$ .

We define the squared electromechanical resonant frequency associated with the classical generator as  $\Omega_r^2 = \frac{VE'}{MX_d'} \cos(\varphi)$ . For some  $\epsilon$ ,  $\gamma(\Omega_r - \epsilon) = -\gamma(\Omega_r + \epsilon)$ . We must therefore ensure that  $\mathbf{M}\gamma T_\delta\boldsymbol{\Gamma} + (\mathbf{M}\gamma T_\delta\boldsymbol{\Gamma})^\dagger \succeq 0$  and  $-\mathbf{M}\gamma T_\delta\boldsymbol{\Gamma} - (\mathbf{M}\gamma T_\delta\boldsymbol{\Gamma})^\dagger \succeq 0$ , respectively, when ensuring the generator is DQR on either side of the resonant peak. The only way for these statements to be simultaneously true is for  $\mathbf{M}T_\delta\boldsymbol{\Gamma} + (\mathbf{M}T_\delta\boldsymbol{\Gamma})^\dagger \equiv \mathbf{0}$ . To accomplish this, we consider the numerical structure of  $T_\delta$  for two plausible

rotor angle values:  $\delta_1 = 0$  and  $\delta_2 = \frac{\pi}{4}$ :

$$T_\delta(\delta_1) = \begin{bmatrix} 0 & -1 \\ 0 & 0 \end{bmatrix} = \frac{1}{2} (\bar{T}_4 - \bar{T}_3), \quad (2.194)$$

$$T_\delta(\delta_2) = \begin{bmatrix} \frac{1}{2} & -\frac{1}{2} \\ \frac{1}{2} & -\frac{1}{2} \end{bmatrix} = \frac{1}{4} (\bar{T}_2 + \bar{T}_4). \quad (2.195)$$

Since  $\mathbf{M}\bar{T}_4\boldsymbol{\Gamma} + (\mathbf{M}\bar{T}_4\boldsymbol{\Gamma})^\dagger \equiv \mathbf{0}$ , then we must also require  $\mathbf{M}\bar{T}_3\boldsymbol{\Gamma} + (\mathbf{M}\bar{T}_3\boldsymbol{\Gamma})^\dagger \equiv \mathbf{0}$  from (2.194) and  $\mathbf{M}\bar{T}_2\boldsymbol{\Gamma} + (\mathbf{M}\bar{T}_2\boldsymbol{\Gamma})^\dagger \equiv \mathbf{0}$  from (2.195) in order to ensure that  $\mathbf{M}T_\delta\boldsymbol{\Gamma} + (\mathbf{M}T_\delta\boldsymbol{\Gamma})^\dagger \equiv \mathbf{0}$ . We are thus requiring that  $\text{Re}\{\tilde{\mathbf{v}}^\dagger (\mathbf{M}\bar{T}_i\boldsymbol{\Gamma}) \tilde{\mathbf{v}}\} = 0$ ,  $\forall \tilde{\mathbf{v}} \in \mathbb{C}^{2 \times 1}$ ,  $\forall i \in \{2, 3, 4\}$ . As stated in Corollary 3, the only way to achieve losslessness for basis matrices 2, 3 and 4 is for  $\boldsymbol{\Gamma} = (j\beta\bar{T}_4)\mathbf{M}^\dagger$ . By employing this transformation, Lemma 4 proves that the quadratic energy associated with any element containing  $\bar{T}_1$  will be rendered indefinite in sign. Since (2.192b) contains  $\bar{T}_1$  when resistance is present in the network, then there exists no nonsingular matrices  $\mathbf{M}$  and  $\boldsymbol{\Gamma}$  for which  $\mathbf{M}\mathcal{Y}\boldsymbol{\Gamma} + (\mathbf{M}\mathcal{Y}\boldsymbol{\Gamma})^\dagger \succeq 0$ ,  $\forall \mathcal{Y} \in \{\mathcal{Y}_p, \mathcal{Y}_z, \mathcal{Y}_g\}$ .  $\square$

**Corollary 4.** *By choosing  $\mathbf{M} = \bar{T}_1$ ,  $\beta = \frac{-1}{\Omega}$ , and  $\boldsymbol{\Gamma} = (j\beta\bar{T}_4)\mathbf{M}^\dagger$ , we arrive at the DQR-transformation implicitly employed by the DEF.*

**Corollary 5.** *Without resistive elements, the DEF method is a fully reliable source location technique in classical power systems.*

**Corollary 6.** *Since the linearized admittance matrix  $\mathcal{Y}$  associated with any ZIP load is purely real, i.e.  $\mathcal{Y} = \text{Re}\{\mathcal{Y}\}$ , the eigenvalues of its transformed Hermitian part will be equal and opposite in value:  $\lambda(\mathbf{M}\mathcal{Y}\boldsymbol{\Gamma} + (\mathbf{M}\mathcal{Y}\boldsymbol{\Gamma})^\dagger) = \pm\alpha$ , where  $\alpha = 0$  for constant power or purely reactive loads.*

If a network has no resistive elements and is truly DQR, no quadratic energy production can occur on regular network elements, so injections of energy have to be related to external sources, like FOs. This is why finding a DQR energy-like form is important, and why the “almost-DQR” form used by DEF has had so much success. To further show why the results of Theorem 2 are problematic for the DEF method, we consider the structure of (2.176): since the generator damping contributions are positive definite, the source energy is necessarily negative in a power system with no resistance. This is not true in a lossy power system. To show why not, we define

block matrices  $\underline{\mathbf{M}} \in \mathbb{C}^{2n \times 2n}$  and  $\underline{\Gamma} \in \mathbb{C}^{2n \times 2n}$ , where

$$\underline{\mathbf{M}} = \begin{bmatrix} \mathbf{M} & \mathbf{0} \\ \mathbf{0} & \mathbf{M} \end{bmatrix}, \quad \underline{\Gamma} = \begin{bmatrix} \Gamma & \mathbf{0} \\ \mathbf{0} & \Gamma \end{bmatrix},$$

and whose block diagonal matrices are given by  $\mathbf{M}$  and  $\Gamma = (j\beta \bar{T}_4)\mathbf{M}^\dagger$ , respectively. We left multiply (2.170a) by  $\underline{\mathbf{M}}$  and insert  $\underline{\Gamma}\underline{\Gamma}^{-1}$  on the RHS:

$$-\underline{\mathbf{M}}\mathbf{J}' = \underline{\mathbf{M}}(E_a^\dagger \mathcal{Y}_L E_a + \mathcal{Y}'_S) \underline{\Gamma}\underline{\Gamma}^{-1} \mathbf{V}_b. \quad (2.196)$$

Defining the transformed voltage vectors  $\mathbf{U}_b = \underline{\Gamma}^{-1} \mathbf{V}_b$  and  $\mathbf{U}_s = \underline{\Gamma}^{-1} \mathbf{V}_s$ , we left multiply (2.196) by  $\mathbf{U}_b^\dagger$  and simplify. We may group the dissipating power injections into their respective contributing groups (assuming lossless loads):

$$0 = \underbrace{\mathbf{U}_s^\dagger \underline{\mathbf{M}} \mathcal{I}'}_{\text{Source}} + \underbrace{\mathbf{U}_b^\dagger (\underline{\mathbf{M}} \mathcal{Y}'_S \underline{\Gamma}) \mathbf{U}_b}_{\text{Generator}} + \underbrace{\mathbf{U}_b^\dagger (\underline{\mathbf{M}} E_a^\dagger \mathcal{Y}_L E_a \underline{\Gamma}) \mathbf{U}_b}_{\text{Network}}. \quad (2.197)$$

The FO source term can produce only negative damping energy, i.e.  $\text{Re}\{\mathbf{U}_s^\dagger \underline{\mathbf{M}} \mathcal{I}'\} < 0$ , if the condition

$$\underline{\mathbf{M}}(\mathcal{Y}'_S + E_a^\dagger \mathcal{Y}_L E_a) \underline{\Gamma} + (\underline{\mathbf{M}}(\mathcal{Y}'_S + E_a^\dagger \mathcal{Y}_L E_a) \underline{\Gamma})^\dagger \succ 0 \quad (2.198)$$

is met. If it is not met, indefinitely signed resistive energy can dominate damper winding energy absorption and the source term can, in fact, appear as a positively damped element. In this plausible situation, the DEF method will fail. We note that violation of (2.198) is a necessary but not sufficient condition for DEF failure. Next, we explore these failure conditions more closely. First, we offer a definition of an associated system.

**Definition 9.** Consider classical power system  $\Sigma_c$  with ZIP loads, DQR generators, and a lossy transmission network. This system's voltage vector  $\mathbf{V}_b$  is  $\mathbf{V}_b = \mathbf{V}_s^\top \mathbf{V}_{ns}$ , where  $\mathbf{V}_{ns} = -\mathcal{Y}_4^{-1} \mathcal{Y}_3 \mathbf{V}_s$  from (2.170b). All voltage vectors are transformed such that  $\mathbf{U} = \underline{\Gamma}^{-1} \mathbf{V}$ . The Kron reduced admittance (DWE) seen by a FO source is  $\mathcal{Y}_N$  as in (2.171). The matrix  $\mathbf{N}_c = \frac{1}{2}(\mathbf{M} \mathcal{Y}_N \underline{\Gamma}) + \frac{1}{2}(\mathbf{M} \mathcal{Y}_N \underline{\Gamma})^\dagger$ , with matrices  $\mathbf{M}$  and  $\underline{\Gamma}$  from Corollary 3, will have two eigenvalues:  $\lambda_1$  and  $\lambda_2$ .

**Theorem 3.** Consider  $\mathbf{N}_c$  from  $\Sigma_c$ :

- (a) If condition (2.198) is met,  $\lambda_1, \lambda_2 > 0$ .
- (b) If  $\text{Re}\{\mathbf{U}_s^\dagger \mathbf{M} \mathcal{I}'\} > 0$  is measured, i.e. the DEF method has failed, condition (2.198) is violated and  $\lambda_1 \vee \lambda_2 < 0$ .

*Proof.* By modifying (2.197), we have  $-\mathbf{U}_s^\dagger \mathbf{M} \mathcal{I}' = \mathbf{U}_b^\dagger \underline{\mathbf{M}} (\mathcal{Y}'_S + E_a^\dagger \mathcal{Y}_L E_a) \underline{\boldsymbol{\Gamma}} \mathbf{U}_b$ , and with condition (2.198) met,  $-\mathbf{U}_s^\dagger \mathbf{M} \mathcal{I}' > 0$ . Since  $-\mathcal{I}' = \mathcal{Y}_N \mathbf{V}_s$ , we have that  $\mathbf{U}_s^\dagger \mathbf{M} \mathcal{Y}_N \boldsymbol{\Gamma} \mathbf{U}_s > 0$  by substitution, implying that  $\lambda \{(\mathbf{M} \mathcal{Y}_N \boldsymbol{\Gamma}) + (\mathbf{M} \mathcal{Y}_N \boldsymbol{\Gamma})^\dagger\} > 0, \forall \lambda \in \{\lambda_1, \lambda_2\}$ , proving proposition (a).

If  $\text{Re}\{\mathbf{U}_s^\dagger \mathbf{M} \mathcal{I}'\} > 0$ , then  $\mathbf{U}_s^\dagger \mathbf{N}_c \mathbf{U}_s < 0$  is directly implied. Accordingly,  $\lambda_1 \vee \lambda_2 < 0$ . By the conservation argument presented in the proof of proposition (a), if  $\mathbf{U}_s^\dagger \mathbf{N}_c \mathbf{U}_s < 0$ , then  $\text{Re}\{\mathbf{U}_b^\dagger \underline{\mathbf{M}} (\mathcal{Y}'_S + E_a^\dagger \mathcal{Y}_L E_a) \underline{\boldsymbol{\Gamma}} \mathbf{U}_b\} < 0$  implying the violation of condition (2.198), proving proposition (b).  $\square$

The effects of energy injections from resistive networks are further considered in Appendix A.6. These results, though, are not explicitly utilized in the following practical application subsection, so they are relegated to the appendix.

### 2.4.3 Practical Applications of the DQR Analysis

We now expound upon three practical applications of the analysis presented in this subsection. First, we explicitly state how to implement the DEF source location method via the proposed frequency domain methods. Second, we show how system operators can use the proposed framework to predict how the DEF method will perform in their respective networks without performing simulations. And third, we explain how the tools in this section can be used to understand how the addition of new grid components will affect performance of the DEF method. In all further analysis, we assume  $\mathbf{M} = -j\bar{T}_4$ .

#### Energy Flow Calculations in the Frequency Domain

In order to compute the dissipating power signal  $P^*$  in a system which is experiencing a FO event, we convert voltage and current PMU data into rectangular coordinates. Next, we take the FFT of these signals, thus constructing  $\tilde{\mathbf{V}}(\Omega) = [\tilde{V}_r(\Omega), \tilde{V}_i(\Omega)]^T$  and  $\tilde{\mathbf{I}}(\Omega) = [\tilde{I}_r(\Omega), \tilde{I}_i(\Omega)]^T$  at all relevant buses and lines. Finally, we evaluate these signals at the forcing frequency  $\Omega_d$  in order to compute the dissipating power injection at each bus or flow along each line:

$$P^* = \text{Re}\{\tilde{\mathbf{V}}(\Omega_d)^\dagger \mathbf{M} \tilde{\mathbf{I}}(\Omega_d)\}. \quad (2.199)$$

Positive  $P^*$  flowing out of an element indicates the presence of a non-DQR component (typically a FO source). We refer readers to Appendix A.2 for a discussion on the difficulties of dealing with rectangular coordinates in a realistic power system. Using this procedure, a map, such as the one presented in Fig. 2-46, can be constructed.

### Predicting Performance of DEF Source Location

The implicit goal of the DEF method is to locate the source of negative damping in the system. When resistive elements are introduced to the network, the goal becomes obfuscated because the source may appear DQR, and thus, positively damped. By Remark 13 though, the negative DWE of the source cannot be *physically* DQR. A key contribution of this section recognizes that while generators continue to be physically DQR, the source only appears<sup>14</sup> DQR when the DEF method fails in a classical power system.

Before system operators can consistently rely on using the DEF method for FO source location, it is important that they first test if the method will perform adequately in their respective networks. Algorithm 2.4.3 clarifies the exact analytical procedure which can be used to test if the DEF method will perform successfully for any given bus in the network at any given FO frequency. We note that this off-line analysis is not restricted to classical power systems: any system component can be incorporated so long as its dynamics can be analytically approximated and linearized. Additionally, the *type* of oscillation source is entirely arbitrary: the methods in Algorithm 2.4.3 predict the sign of the energy flowing from the source bus terminal as a function of how the system dynamically responds to the abstracted oscillation signal. It is thus similar to testing if condition (2.198) is violated.

### Analysis of Additional Grid Components

Until this point in the section, only the elements of a lossy classical power system have been considered, but it is important for system operators to consider how the addition of new elements will effect energy-based source location methods. If newly added elements are non-DQR, it is also important for system operators to test the degree of allowed penetration from these elements before energy-based source location methods will fail. In this subsection, we present examples of DQR analysis applied to three non-classical elements: frequency dependent loads, droop-controlled inverter

---

<sup>14</sup>The transformed FRF will have one positive and one negative eigenvalue.

---

**Algorithm 3** Reliability Test for Energy Flow Methods

---

**START**

```

1: Construct nonlinear model (2.57) for all shunts and linearize to build admittance (2.59)
2: Construct shunt matrix (2.162), incidence matrix (2.158) and line matrix (2.160)
3: Construct dynamic nodal admittance (2.167)
4: for each plausible FO frequency  $\Omega_d$  do
5:   for each plausible source bus  $i$  do
6:     Remove shunt admittance  $\mathcal{Y}_{s,i}$  from  $\mathcal{Y}_S$ 
7:     Partition network via (2.170) and Kron reduce via (2.171) to construct  $\mathcal{Y}_N$ 
8:     Compute  $\lambda_{1,2} = \lambda\{\mathbf{M}\mathcal{Y}_N + (\mathbf{M}\mathcal{Y}_N)^\dagger\}$ 
9:     Assume bus  $i$  generates FO of frequency  $\Omega_d$ :
10:    if  $\lambda_1, \lambda_2 \geq 0$  then
11:      • DEF will succeed
12:    else if  $\lambda_1, \lambda_2 \leq 0$  then
13:      • DEF will fail
14:    else
15:      • DEF will perform unreliably
  end
end

```

---

systems, and third order synchronous generators with first order Automatic Voltage Regulators (AVRs).

**Frequency Dependent Load:** Assuming power is an instantaneous function of voltage magnitude and frequency [129], we may write  $P(t)$  and  $Q(t)$  via

$$P(t) = P_0 (V/V_0)^{\alpha_p} (\omega/\omega_0)^{\beta_p} \quad (2.200a)$$

$$Q(t) = Q_0 (V/V_0)^{\alpha_q} (\omega/\omega_0)^{\beta_q}, \quad (2.200b)$$

where  $\omega = \omega_0 + \dot{\theta}$ . Since we are interested in the linearized responses of (2.200a) and (2.200b), we evaluate their partial derivatives at equilibrium ( $V_0, \omega_0 = 1$ ).

$$\begin{bmatrix} \Delta P \\ \Delta Q \end{bmatrix} = \begin{bmatrix} P_0 & 0 \\ 0 & Q_0 \end{bmatrix} \begin{bmatrix} \frac{\alpha_p}{V_0} & \beta_p \\ \frac{\alpha_q}{V_0} & \beta_q \end{bmatrix} \begin{bmatrix} \Delta V \\ \Delta \omega \end{bmatrix}. \quad (2.201)$$

Assuming sinusoidal perturbations, phasor notation yields

$$\underbrace{\begin{bmatrix} \tilde{P} \\ \tilde{Q} \end{bmatrix}}_{\tilde{\mathbf{s}}} = \underbrace{\begin{bmatrix} \frac{\alpha_p}{V_0} P_0 & \beta_p P_0 \\ \frac{\alpha_q}{V_0} Q_0 & \beta_q Q_0 \end{bmatrix}}_{\mathcal{Y}_a} \underbrace{\begin{bmatrix} 1 & 0 \\ 0 & j \end{bmatrix}}_{I_j} \underbrace{\begin{bmatrix} \tilde{V} \\ \tilde{\theta} \end{bmatrix}}_{\tilde{\mathbf{v}}_p} \quad (2.202)$$

where  $\tilde{\omega} = j\tilde{\theta}$ . Employing matrix  $T_1$  from Appendix A.2, we transform from polar to rectangular via  $\tilde{\mathbf{V}} = T_1 \tilde{\mathbf{V}}_p$  in (2.202):

$$\tilde{\mathbf{S}} = \mathcal{Y}_a I_j T_1^{-1} \tilde{\mathbf{V}}. \quad (2.203)$$

We next consider perturbations of  $P = V_r I_r + I_i V_i$  and  $Q = V_i I_r - V_r I_i$ . Treating  $\bar{V}_{i/r}$  and  $\bar{I}_{i/r}$  as steady state values, we linearize and convert to phasor notation:

$$\begin{bmatrix} \tilde{P} \\ \tilde{Q} \end{bmatrix} = \underbrace{\begin{bmatrix} \bar{I}_r & \bar{I}_i \\ -\bar{I}_i & \bar{I}_r \end{bmatrix}}_{A_I} \underbrace{\begin{bmatrix} \tilde{V}_r \\ \tilde{V}_i \end{bmatrix}}_{\tilde{\mathbf{V}}} + \underbrace{\begin{bmatrix} \bar{V}_r & \bar{V}_i \\ \bar{V}_i & -\bar{V}_r \end{bmatrix}}_{A_V} \underbrace{\begin{bmatrix} \tilde{I}_r \\ \tilde{I}_i \end{bmatrix}}_{\tilde{\mathbf{I}}}. \quad (2.204)$$

By equating (2.203) and (2.204),  $\tilde{\mathbf{I}}$  and  $\tilde{\mathbf{V}}$  are directly related by

$$\tilde{\mathbf{I}} = \underbrace{A_V^{-1} (\mathcal{Y}_a I_j T_1^{-1} - A_I)}_{\mathcal{Y}_b} \tilde{\mathbf{V}}. \quad (2.205)$$

Finally, we set  $\alpha_p = \alpha_q = 0$  to isolate the effects of frequency, and we compute eigenvalues  $\lambda_{1,2} = \lambda\{\mathbf{M}\mathcal{Y}_b + (\mathbf{M}\mathcal{Y}_b)^\dagger\}$ :

$$\lambda_{1,2} = \frac{\beta_p \cos(\varphi) \pm \sqrt{\frac{\beta_p^2}{2}(1+\cos(2\varphi)) + \frac{\beta_q^2}{2}(1-\cos(2\varphi))}}{I/V}. \quad (2.206)$$

where  $\varphi = \theta - \phi$ . In setting  $\beta \equiv \beta_p \approx \beta_q$ , (2.206) simplifies to

$$\lambda_{1,2} = \beta(\cos(\varphi) \pm 1)V/I. \quad (2.207)$$

Since power factor is usually close to unity, this case of frequency dependent load is *primarily DQR* for  $\beta > 0$  because the positive eigenvalue will be far larger than the negative eigenvalue. Otherwise, if  $\beta_p = 0$ , then the load behaves like a resistor (equal and opposite eigenvalues), but if instead  $\beta_q = 0$ , then the load is truly DQR for reasonable values of power factor.

**Droop-controlled Inverter:** We consider the dynamics of a droop-controlled inverter circuit; such circuits have the potential to dominate distributed energy resource

interconnections. As given by the inverse of (3.15), the circuit's impedance is

$$\mathcal{Z} = \begin{bmatrix} R_c + j\Omega L_c & -X_c - \frac{k_q}{1+j\tau\Omega} \\ X_c - \frac{k_p}{\tau\Omega^2-j\Omega} & R_c + j\Omega L_c \end{bmatrix}, \quad (2.208)$$

where  $k_p$  and  $k_q$  are the active and reactive power droop coefficients, and  $R_c$  is the coupling resistance. We seek to analyze the dissipativity of this system. Rather than invert (2.208), we consider the dissipativity of the impedance  $\mathcal{Z}$  directly. Appendix A.3 establishes the equivalence of dissipativity classifications between an admittance  $\mathcal{Y}$  and its associated impedance  $\mathcal{Z} = \mathcal{Y}^{-1}$  for transformation matrix  $\mathbf{M}$ . We thus compute the Hermitian part of  $\mathbf{M}\mathcal{Z}$ :

$$\mathbf{M}\mathcal{Z} + (\mathbf{M}\mathcal{Z})^\dagger = 2 \begin{bmatrix} \frac{k_p}{\Omega((\tau\Omega)^2+1)} & jR_c \\ -jR_c & \frac{k_q\tau\Omega}{(\tau\Omega)^2+1} \end{bmatrix}. \quad (2.209)$$

Since  $\tau$ ,  $\Omega$ , and the droop coefficients are all positive, if  $R_c$  is small, then the eigenvalues of (2.209) are simply

$$\lambda_{1,2} \approx \left\{ k_p \frac{2}{\Omega((\tau\Omega)^2+1)}, k_q \frac{2\tau\Omega}{(\tau\Omega)^2+1} \right\} \quad (2.210)$$

and the system is effectively DQR. If  $R_c$  is not neglected, though, the eigenvalue expressions become more cumbersome. Using the parameter values suggested in [182], we plot  $\lambda_1$  and  $\lambda_2$  as  $R_c$  is scaled via  $R_c = \alpha X_c$ ,  $\alpha \in \{0, 0.05, 0.1, 0.15, 0.2\}$ , for the matrix  $\mathbf{M}\mathcal{Y} + (\mathbf{M}\mathcal{Y})^\dagger$  (we plot admittance eigenvalues rather than impedance eigenvalues solely for graphical clarity). Fig. 2-45 shows the eigenvalues. Clearly, as coupling resistance decreases in value, the inverter behaves more DQR. The DEF method will thus perform more successfully when virtual + coupling resistance is minimized.

**Third Order Generator with First Order AVR:** We consider the dynamics of a third order synchronous machine with a first order ARV. The associated model [129]

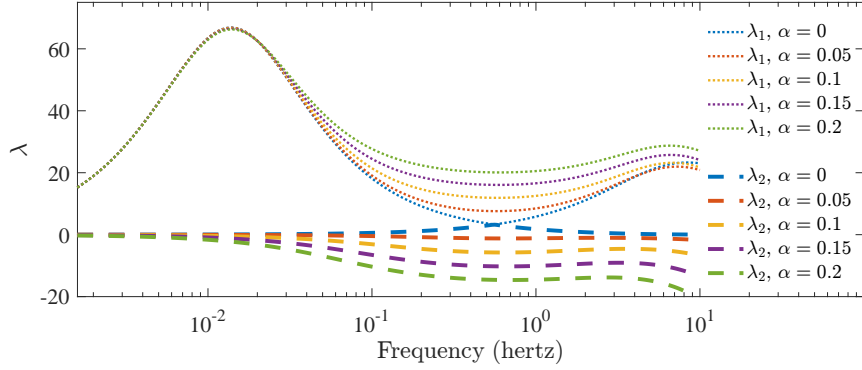


Figure 2-45: Plot of the eigenvalues of  $\mathbf{M}\mathcal{Y} + (\mathbf{M}\mathcal{Y})^\dagger$ , where  $\mathcal{Y}$  is associated with the dynamics of a droop-controlled inverter. For  $\alpha = 0$ , the system is fully DQR since both eigenvalues are positive.

is stated by

$$\dot{\delta} = \Delta\omega \quad (2.211a)$$

$$M\Delta\dot{\omega} = P_m - P_e - D\Delta\omega \quad (2.211b)$$

$$T'_{d0}\dot{e}'_q = E_f - (X_d - X'_d)i_d - e'_q \quad (2.211c)$$

$$T_a\dot{E}_f = K_a(V_r - V) - E_f, \quad (2.211d)$$

where  $V_r$  is the voltage reference set point,  $V e^{j\theta}$  is the terminal voltage phasor,  $i_d = (e'_q - e_q)/X'_d$ ,  $i_q = e_d/X_q$ ,  $e_d = V \sin(\delta - \theta)$  and  $e_q = V \cos(\delta - \theta)$ . Finally,  $P_e = e_d i_d + i_q e_q$ . We define output power variables  $P$  and  $Q$  as  $P = -P_e$  and  $Q = -(i_d e_q - i_q e_d)$ <sup>15</sup>.

In order to make analytical claims about the dissipativity of (2.211), we leverage the alternative DEF interpretation proposed in Appendix A.4. To make the analysis tractable, we choose to linearize the model about the generator's unloaded equilibrium point (i.e.  $\theta = \delta$ ,  $V = e_q$ ,  $e_d = 0$ , etc.). Although this configuration may be uncommon, the resulting linearized dynamics are sufficiently simplified for approximating generator dissipativity. Additionally, the resulting admittance matrix  $\mathcal{H}$  is diagonal, so the eigenvalues of  $\mathbf{K}^\dagger \mathcal{H} + (\mathbf{K}^\dagger \mathcal{H})^\dagger$  are trivial. We compute  $\mathcal{H}$  from Appendix A.4:

$$\mathcal{H} = \begin{bmatrix} \frac{\Omega(jM\Omega + D)}{DX_q\Omega + j(MX_q\Omega^2 - 1)} & 0 \\ 0 & \frac{K_a + 1 - \Omega^2 T_a T'_{d0} + j\Omega(T_a + T'_{d0})}{(\Omega T_a - j)(X_d j - \Omega T'_{d0} X'_d)} \end{bmatrix}. \quad (2.212)$$

---

<sup>15</sup>In keeping with the conventions of Section 2.4.2, positive currents flow from the network and into the machine.

Taking the eigenvalues of  $\mathbf{K}^\dagger \mathcal{H} + (\mathbf{K}^\dagger \mathcal{H})^\dagger$  is equivalent to taking the imaginary parts of the diagonals of matrix  $\mathcal{H}$ . The relationship between  $\tilde{P}$  and  $\tilde{\theta}$  (i.e.  $\lambda_1$ ) is thus DQR if  $\Omega D \geq 0$ . This will be true if damping  $D$  is positive. Interestingly, when the generator is *unloaded*, the damping provided by the field winding is of second order and thus has no mathematical impact on dissipativity between  $\tilde{P}$  and  $\tilde{\theta}$ . Via (2.212), the relationship between  $\tilde{Q}$  and  $\tilde{V}$  (i.e.  $\lambda_2$ ) is thus DQR if

$$(T'_{d0}\Omega^2 T_a^2 + T'_{d0})(X_d - X'_d) - K_a(T'_{d0}X'_d + X_d T_a) \geq 0. \quad (2.213)$$

This result has many interesting interpretations. For  $K_a$  small or  $T_a$  sufficiently large, the expression will always be DQR. Strong and fast AVR response thus causes the relationship between  $\tilde{Q}$  and  $\tilde{V}$  to lose dissipativity. For dissipativity to be guaranteed  $\forall \Omega$ , the AVR gain should have the upper bound

$$K_a \leq \frac{T'_{d0}(X_d - X'_d)}{T'_{d0}X'_d + X_d T_a}. \quad (2.214)$$

Of course, the claim that the generator will be DQR if  $D \geq 0$  and (2.214) are both satisfied is only true when the generator is unloaded. Loading effects are likely to be small, though, so these results are useful for guiding intuition related to when generators will lose dissipativity.

#### 2.4.4 Test Results

In this section, we present test results which illustratively validate the framework presented in Sections 2.4.2 and 2.4.2 and the practical applications presented in Section 2.4.3. We perform these tests in two systems which are altered to engender poor DEF performance. In the 39-bus New England system, the average R/X transmission line ratio was increased from 6% to 15%, and in the 179-bus WECC system, all constant power loads were converted into constant impedance loads. All simulation code is posted online<sup>16</sup> for open source access.

##### New England 39-bus Test System

Fig. 2-46 shows a diagram of the IEEE 39-bus New England system. In this system, generators are modeled as third order synchronous machines [158] with first order

---

<sup>16</sup><https://github.com/SamChevalier/Passivity-Enforcement-FOs>

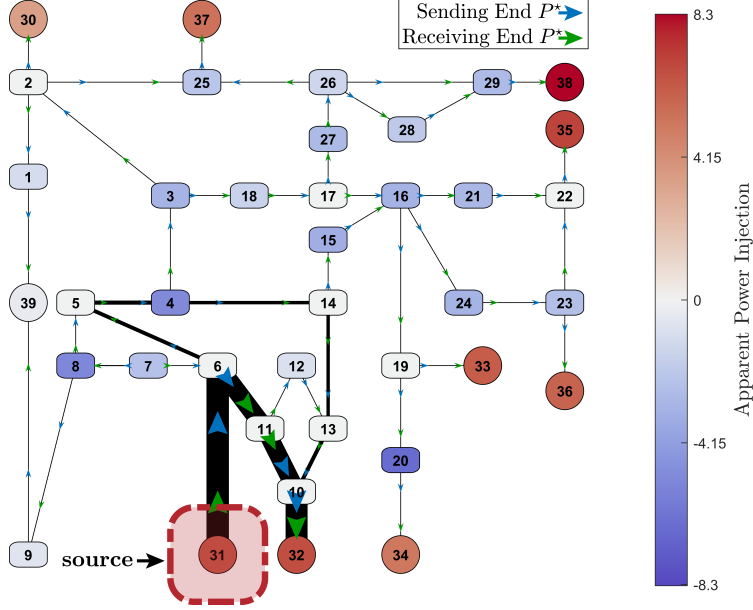


Figure 2-46: Dissipating power flow  $P^*$  in the IEEE 39-bus power system for an applied FO of 2 Hz. All line resistance has been removed. Circles represent generators while rounded rectangles represent loads. Line thickness and arrow size represent dissipating power flow magnitude.

AVRs<sup>17</sup>. Initially, loads were modeled as constant power (PQ) and system lines were modeled with no-loss (purely reactive). Following the steps in Algorithm 2.4.3, we computed the eigenvalues associated with bus 31's DWE  $\mathcal{Y}_N$  for a frequency of  $\Omega_d = 2\pi \times 2$ :

$$\lambda \{ \mathbf{M} \mathcal{Y}_N + (\mathbf{M} \mathcal{Y}_N)^\dagger \} = 0.007, 2.11. \quad (2.215)$$

Due to the two positive eigenvalues, any FO source originating at bus 31 with a frequency of 2 Hz will appear non- DQR: the DEF method should perform accurately in this system since condition (2.198) is satisfied. We then simulated the response of the system to a 2Hz perturbation originating at bus 31. System excitation and simulation were performed in the frequency domain. From the simulated data, dissipating power  $P^*$  was computed via (2.199) on all lines. The resulting flows are plotted in Fig. 2-46. Clearly, the source is readily identifiable.

Next, the model was altered such that the average<sup>18</sup> R/X ratio was increased from 6% to 15% for all lines. Additionally, all loads were converted to the model

---

<sup>17</sup>The gains and time constants of these AVRs were chosen to approximate the full regulator + exciter system model from [158].

<sup>18</sup>One outlier line, which has  $R \approx X$ , was excluded from this average.

described by (2.200) with  $\alpha$  and  $\beta$  parameters chosen randomly from  $\mathcal{U}(0, 2)$ . We again considered the eigenvalues associated with bus 31's DWE  $\mathcal{Y}_N$  for a frequency of  $\Omega_d = 2\pi \cdot 2$ :

$$\lambda \left\{ \mathbf{M} \mathcal{Y}_N + (\mathbf{M} \mathcal{Y}_N)^\dagger \right\} = -2.52, +4.77 \quad (2.216)$$

The oppositely signed eigenvalues show that the network can aggregate generate or consume dissipating power  $P^*$ , indicating unreliable DEF results. After computing the system's response to a 2Hz sinusoidal FO applied at bus 31's generator, the dissipating power  $P^*$  flowing in the network was plotted in Fig. 2-47. Based on arrow directionality, all generators are shown to be  $P^*$  sinks: there is no apparent generator source in the system. Loads present only a small contribution of dissipating power. Although it may appear as though bus 6, for example, is a source, the dissipating power flows are exactly conserved at this bus: all dissipating power flowing in from lines 7-6, 5-6, and 11-6 exactly flows out on line 6-31.

The reason there are no apparent sources is due to the highly active nature of the lines. For example, in the flow from bus 11 to bus 6, the sending end  $P^*$  is larger than the receiving end  $P^*$  (based on arrow sizes), and given the flow direction, the line is clearly a source of dissipating power. Similarly, on line 21-22, both arrows point away from the line, indicating positive dissipating power flows out of both ends of the line. Because condition (2.198) is not met in this network, the FO source is able to act as a dissipating power sink. In other words, since the network is producing more dissipating power than it can consume, the source provides additional “sink” slack. Therefore, the source cannot be readily identified by a system operator.

As a second test, we reconsidered the no-loss system whose eigenvalues are characterized by (2.215). At load buses 4, 8 and 16, we added identical droop-controlled inverter circuits whose parameter values are specified in [182]. However, we intentionally neglected resistive losses (i.e.  $R_c = 0$ ). Next, we scaled the nominal droop gain values of  $k_p = 1.3 \cdot 10^{-3}$  and  $k_q = 7.5 \cdot 10^{-3}$  by scalar  $\alpha \in [0 \ 10^4]$ . For each system configuration, the eigenvalues of the DWE seen at the source bus were computed per Algorithm 2.4.3. The results, shown in Table 2.3, confirm the prediction of (2.210). Across the full range of droop gain values, the eigenvalues of the source bus are both positive. Therefore, these components do not interfere with DEF performance. When losses are added back in, interference may occur.

As a final test on the 39-bus system, we again reconsidered the no-loss system whose eigenvalues are characterized by (2.215). Instead of adding loss, we tripled all

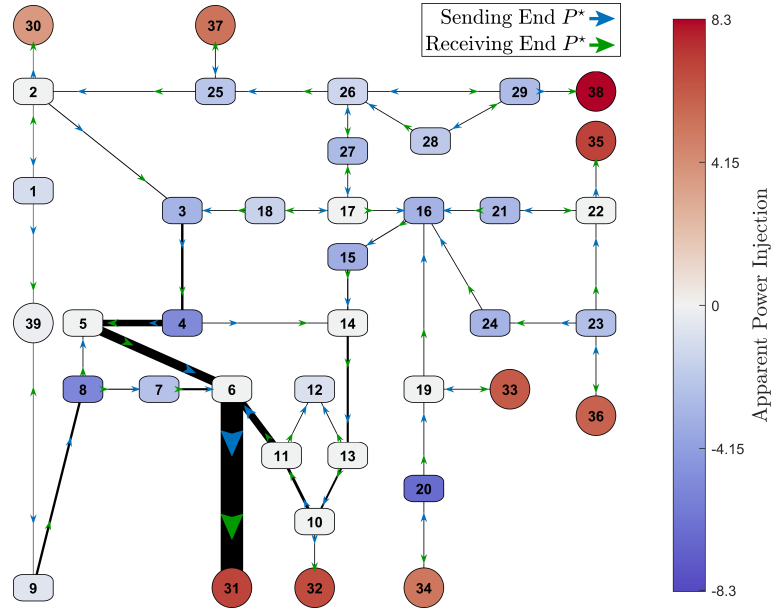


Figure 2-47: Dissipating power flow  $P^*$  in the lossy IEEE 39-bus power system. The source of the FO cannot be located using the energy-based DEF method in this situation.

Table 2.3: Eigenvalues of System with Droop-Controlled Inverters

	$\alpha=0$	$\alpha=10^0$	$\alpha=10^1$	$\alpha=10^2$	$\alpha=10^3$	$\alpha=10^4$
$\lambda_1$	0.007	0.007	0.008	0.01	0.05	0.4
$\lambda_2$	2.11	2.11	2.12	2.17	2.80	28.04

AVR gain values and decreased all AVR time constants by one third. Accordingly,

$$\lambda \{ \mathbf{M} \mathcal{Y}_N + (\mathbf{M} \mathcal{Y}_N)^\dagger \} = -0.1, +1.53. \quad (2.217)$$

As evidenced by the slightly negative eigenvalue, these changes caused generator dissipativity to be lost in at least some cases. This effect was predicted by (2.214).

### WECC 179-bus Test System

In the second test, we employed the 179-bus WECC system which was prepared by the IEEE Task Force on FOs [119]. Specifically, we employed test case number F1, where a 0.86 Hz FO is applied to the reference signal in a generator's AVR. We altered the system by converting all loads to constant impedance with some frequency dependence. We also applied Ornstein-Uhlenbeck noise on the load power terms  $P_0$  and  $Q_0$  from (2.200a)-(2.200b). Due to the load model modification, the natural frequencies of the system changed slightly. Thus, in order to engender better resonance, we increased the frequency of the FO by 0.1Hz, and we increased the damping at the source generator to ensure it acted as a FO sink in the DEF analysis. We simulated the system for 120 seconds with Power System Analysis Toolbox (PSAT) [129]. To show the strength of the resonance condition, we initially simulated the system with no load noise and plotted the time domain frequency response  $\omega$  of the system generators. Panel (a) of Fig. 2-48 shows that there are multiple generators with larger frequency oscillations than the source. Panel (b) shows the frequency dynamics of the system generators once load stochasticity is added.

Before investigating the dissipating energy flows in this large system, we first sought to further experimentally validate the propagation framework proposed in Section 2.4.2. To do so, we analytically constructed the full system model of (2.167). As predicted by this model, the complex current injection vector  $\mathbf{J} \in \mathbb{C}^{2n \times 1}$  from (2.168) should be sparse: non-zero elements should only come from unmodeled, extraneous perturbations. We thus simulated the WECC system with noisy loads and a strong FO source at bus 4. We then collected all voltage PMU data, generated the FFT evaluated at  $\Omega_d = 2\pi \times 0.96$ , constructed  $\mathbf{V}_b$  from (2.168) and the methods outlined in Appendix A.2, and predicted the current injection vector  $\mathbf{J}$  via  $\mathbf{J} = -\mathcal{Y}_B \mathbf{V}_b$ . Since there are two complex current injection components associated with each bus, we defined injection magnitude vector  $\bar{\mathbf{J}} \in \mathbb{R}^{n \times 1}$ . Its  $i^{\text{th}}$  element is given as the sum

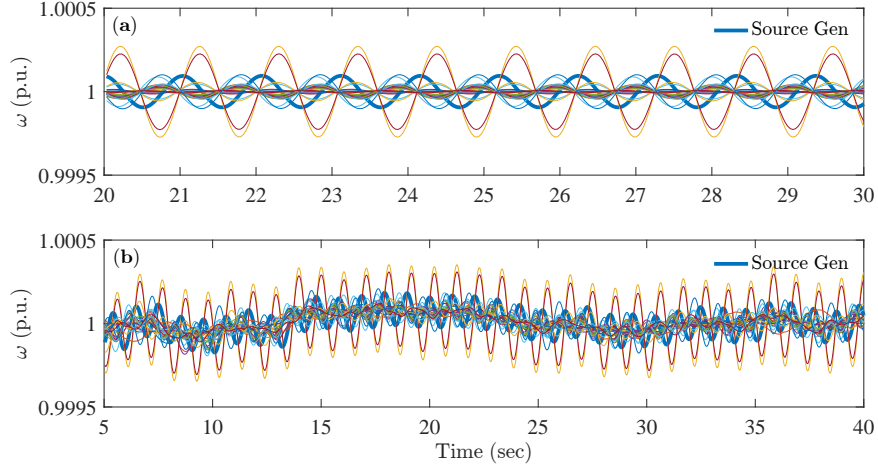


Figure 2-48: Shown are the generator frequency oscillations for all 29 system generators. Panel (a) shows 10s of time series data for when the FO is the only source of system excitation, and panel (b) shows 35s of time series data for when the FO and random load perturbations are both exciting the system.

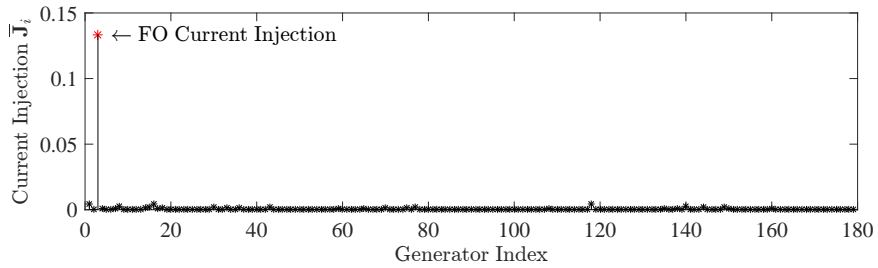


Figure 2-49: Plotted are the current injection magnitudes of (2.218). The perturbative model (2.168) predicts nodal current balances with a high degree of accuracy. Non-source current injections are due to extraneous load perturbations.

of the magnitudes of the current injections at the  $i^{\text{th}}$  bus:

$$\bar{J}_i = |\mathbf{J}_{2i-1}| + |\mathbf{J}_{2i}|. \quad (2.218)$$

We plot the injection magnitudes in Fig. 2-49. As expected, the primary current injection is located at the source bus, but there is a plethora of small, non-zero injections as well. These come from the random load perturbations which are applied at each time step. Fig. 2-49 thus serves to validate (2.167) as a useful model for analyzing FO propagation.

As stated, the FO source is located in the generator at bus 4. By converting all loads to constant impedance (with some frequency dependence), we were able to engender a system whose DWE  $\mathcal{Y}_N$  had oppositely signed eigenvalues. Via Algorithm

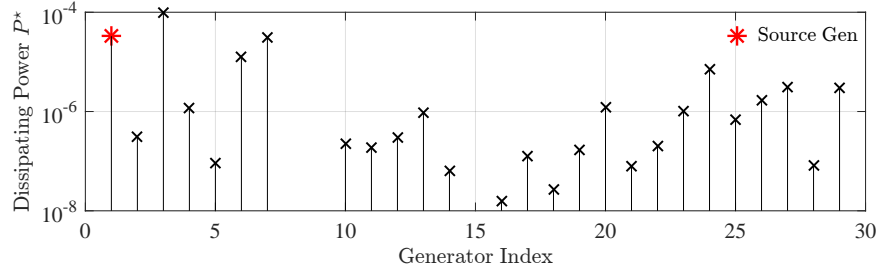


Figure 2-50: Plotted are the dissipating power injections across all 29 generators. All injections are positive, indicating the positive dissipation of  $P^*$ . Generators are listed in ascending order of corresponding bus number. Some magnitudes are too small to appear on the plot.

2.4.3,

$$\lambda \{ \mathbf{M} \mathcal{Y}_N + (\mathbf{M} \mathcal{Y}_N)^\dagger \} = -11.9, +39.6. \quad (2.219)$$

Again, these are the eigenvalues seen by the source bus when it looked into the system. Because one of the eigenvalues is negative, the source generator is capable of acting as a dissipating power sink. When the AVR oscillation was initially applied, simulation results showed that the generator acted like a source. When we simply increased the damping of the source generator though, we began to excite alternative eigenvalues of  $\mathcal{Y}_N$ , and the source generator became a sink. For a sufficiently high level of source damping, the dissipating power injections of Fig. 2-50 were observed at the generator buses. In this scenario, the DEF method fails due to the high level of resistance in the system. This unreliable DEF performance is predicted by the oppositely signed eigenvalues of (2.219).

It is instructive to note that the eigenvalues of (2.219) do not change as the damping at the source bus is altered. These eigenvalues are a product of the network, not the source. This is further confirmation that Algorithm 2.4.3 is agnostic to the type or cause of the FO; rather, Algorithm 2.4.3 predicts the network response to any perturbation originating from the selected source bus. Accordingly, frequency and topological location are the only important characteristics of the FO considered in the algorithm.



# Chapter 3

## Decentralized Small-Signal Stability Certification Standards for Microgrid Networks

The celebrated concept of dissipative dynamic systems [192, 193] allows for the formulation of stability certificates for an entire system through the separate consideration of its individual components: if every component of the system is dissipative, then the whole system is also dissipative irrespective to the way components are interconnected. In this chapter, we leverage this inherent notion of decentralization in order to propose a series of decentralized small-signal stability standards for microgrid networks. In the first section, we provide the mathematical background which will be necessary for solving the problems considered in this chapter. In the second section, we consider the case of DC networks, and we build up the necessary theory to develop such standards. In the third section, we extend the methodology to the generally more challenging case of AC microgrids.

### 3.1 Mathematical Background

In this section, the small-signal model of a constant power DC load is recalled. Next, a small-signal DC microgrid network model is stated, and the problem of certifying the network's stability is outlined.

### 3.1.1 Constant Power DC Load Model

DC-DC power electronic converters are designed with a control system which properly mitigates input voltage variations in order to provide a fairly constant load voltage. A common way to represent a lossless converter is using a single-pole, double-throw (SPDT) switch with a duty cycle  $D$ . Due to the switch, which operates with a frequency on the order of tens of kilohertz, the inductor current and capacitor voltage vary throughout a given cycle with small amplitude around their average values even in steady state. Therefore, to properly account for the low frequency variations, the so-called small-ripple approximation is used, where the system is averaged over a given period and switching variations are neglected.

While there are several common types of converters, we will focus on the buck converter due to its prevalence. The buck converter, consisting of an inductance  $L$ , capacitance  $C$  and constant resistance load  $R$ , has a step-down conversion ratio  $D$ . Since averaging is done over many switching periods, an ideal DC transformer, rather than a switch, is used in the small-signal model. Further buck converter details are provided in [58]. To maintain constant voltage at its output, a converter relies on feedback to modify the duty cycle following any variations in the input voltage. In this work, we consider a buck converter interfaced with a constant resistance load on its output and a control loop to stabilize the output voltage. In this way, it is seen from the network as a constant power load in steady state. This model is defined in Fig. 3-1. To characterize the small-signal behavior of the buck converter, we first examine the transfer function from the control input (duty cycle variation)  $d(s)$  to the output voltage  $v(s)$  [58]:

$$G_{vd}(s) = \frac{v(s)}{d(s)} = G_{d0} \frac{\omega_0^2}{s^2 + 2\zeta\omega_0 s + \omega_0^2} \quad (3.1)$$

with  $G_{d0} = V/D$ ,  $\omega_0 = 1/\sqrt{LC}$  and  $\zeta = \sqrt{L/C}/(2R)$ . In the presence of voltage control, the loop gain of the system is defined as  $T = G_{vd}(s)H(s)G_c(s)/V_m$ , where  $H$  is the sensor gain,  $G_c(s)$  is the compensator transfer function and  $V_m$  is the voltage of the pulse width modulation. The compensator is modeled as a simple lead-lag controller of the form

$$G_c(s) = G_{c\infty} \frac{(1 + \frac{\omega_L}{s})(1 + \frac{s}{\omega_z})}{(1 + \frac{s}{\omega_p})}. \quad (3.2)$$

The input admittance transfer function  $Y_{\mathcal{L},k}(s)$  can be written

$$Y_{\mathcal{L},k}(s) = \frac{i(s)}{v_g(s)} = \frac{1}{Z_N(s)} \frac{T(s)}{1 + T(s)} + \frac{1}{Z_D(s)} \frac{1}{1 + T(s)}, \quad (3.3)$$

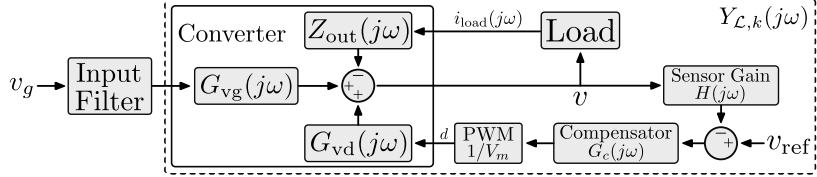


Figure 3-1: Definition of Small-Signal Load Model

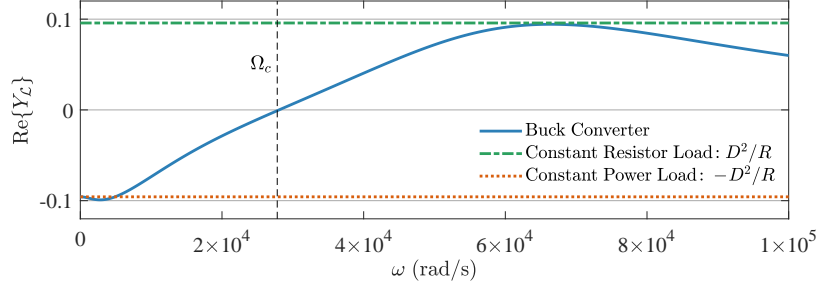


Figure 3-2: Shown are the real parts of the input admittance for a buck converter (blue), constant resistance load (green), and constant power load (orange).

where, for a buck converter,

- $Z_N = \frac{-R}{D^2}$  is the converter impedance when the load voltage perturbations  $v(s)$  are eliminated (i.e.  $d(s)$  is infinitely fast and the load acts like constant power), and
- $Z_D = \frac{R}{D^2} \frac{1+sL/R+s^2LC}{1+sRC}$  is the converter impedance in the absence of control input  $d(s)$  (i.e. the load acts like constant impedance).

In steady state,  $Z_D = -Z_N$ . This is shown quite clearly by the green and orange traces in Fig 3-2, where above  $\Omega_c$ ,  $\text{Re}\{Y_L(\omega)\} > 0$ , and the load behaves more like a passive impedance. In practice, converters are also equipped with an input filter to reject the high-frequency current components from converter switching actions. Improper input filter design can bring instability to an otherwise stable converter.

### 3.1.2 Network Modeling for Small-Signal Stability Analysis

To study the small-signal stability of the full DC microgrid, we leverage a network whose connected graph  $G(\mathcal{V}, \mathcal{E})$  has edge set  $\mathcal{E}$  with cardinality  $|\mathcal{E}| = m$ , vertex set  $\mathcal{V}$  with cardinality  $|\mathcal{V}| = n$ , and signed nodal incidence matrix  $E \in \mathbb{R}^{m \times n}$ . This network has a set of operating equilibrium voltages  $\mathbf{V}_0 \in \mathbb{R}^n$  and nodal current injections  $\mathbf{I}_0 \in \mathbb{R}^n$ . The vectors of voltage and current perturbations are written as  $\mathbf{v}(t) = \mathbf{V}(t) - \mathbf{V}_0$

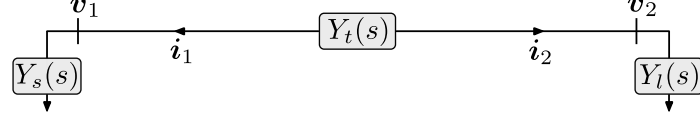


Figure 3-3: Simple 2 bus DC microgrid network. The source, load, and line dynamics are represented by  $Y_s(s)$ ,  $Y_l(s)$ , and  $Y_t(s)$ , respectively.

and  $\mathbf{i}(t) = \mathbf{I}(t) - \mathbf{I}_0$ , respectively. Finally, the Laplace domain representations of these signal vectors are written as  $\mathbf{v}(s) = \mathcal{L}\{\mathbf{v}(t)\}$  and  $\mathbf{i}(s) = \mathcal{L}\{\mathbf{i}(t)\}$ .

Next, we define the frequency dependant nodal admittance matrix according to the general rule

$$\mathbf{i}(s) = \mathbf{Y}(s)\mathbf{v}(s). \quad (3.4)$$

Matrix  $\mathbf{Y}(s)$  includes contributions from the network matrix  $\mathbf{Y}_N(s)$  and the diagonal shunt<sup>1</sup> matrix  $\mathbf{Y}_S$ . Written explicitly,

$$\mathbf{Y}(s) = \sum_{\{i,j\} \in \mathcal{E}} \mathbf{Y}_N^{(i,j)}(s) + \sum_{i \in \mathcal{V}} \mathbf{Y}_S^{(i)}(s), \quad (3.5)$$

where  $\mathbf{Y}_N^{(i,j)}$  is the matrix associated with the network connection between buses  $i$  and  $j$ , and  $\mathbf{Y}_S^{(i)}$  is the matrix associated with shunt elements at bus  $i$ . For example, the simple network illustrated in Fig. 3-3 can be decomposed and written as

$$\mathbf{Y} = \overbrace{\mathbf{Y}_N^{(1,2)}} + \overbrace{\mathbf{Y}_S^{(1)}} + \overbrace{\mathbf{Y}_S^{(2)}} \quad (3.6a)$$

$$= \begin{bmatrix} Y_t & -Y_t \\ -Y_t & Y_t \end{bmatrix} + \begin{bmatrix} Y_s & 0 \\ 0 & 0 \end{bmatrix} + \begin{bmatrix} 0 & 0 \\ 0 & Y_l \end{bmatrix}. \quad (3.6b)$$

If  $\mathbf{Y}_L(s)$  is the diagonal matrix of line admittances, then (3.5) can also be conventionally expressed via  $\mathbf{Y}(s) = E^T \mathbf{Y}_L(s) E + \mathbf{Y}_S(s)$ . In the absence of external perturbations,

$$\mathbf{0} = \mathbf{Y}(s)\mathbf{v}(s) \quad (3.7)$$

will always be satisfied, since the network obeys Kirchhoff's laws. In general, (3.7) may only be satisfied by nontrivial solutions of  $\mathbf{v}(s)$  when  $s = s_0$  is chosen such that  $\mathbf{Y}(s_0)$  is a singular matrix.

---

<sup>1</sup>Shunt elements are any elements which tie the network to ground, and they can include loads, sources, and network elements.

**Definition 10.**  $\mathbf{v}e^{s_0 t}$ ,  $\mathbf{v} \neq \mathbf{0}$ , is an eigenmode of  $\mathbf{Y}(s)$  if

$$\mathbf{0} = \mathbf{Y}(s_0) \mathbf{v} e^{s_0 t}. \quad (3.8)$$

In the following, both  $s_0$  and  $\mathbf{v}e^{s_0 t}$  will be referred to as the same eigenmode. As a necessary consequence of (3.8),  $\det[\mathbf{Y}(s_0)] = 0$  if  $s_0$  is an eigenmode. We now collect all values of  $s_0$  which satisfy Definition 10 and place them in the vector  $\mathbf{s}_0$ . The small-signal stability of system (3.4) can be gauged by computing the real parts of  $\mathbf{s}_0$ .

**Lemma 5.** System (3.7) is stable if

$$\operatorname{Re}\{s_0\} < 0, \forall s_0 \in \mathbf{s}_0. \quad (3.9)$$

*Proof.* In the absence of external perturbations, the solution to (3.7) will be a scaled sum of its eigenmodes. The decay rate of each eigenmode is given by  $\operatorname{Re}\{s_0\}$ . If (3.9) holds, then the solution will decay exponentially fast.  $\square$

### 3.1.3 Modeling Droop-Controlled Inverter-Based Components in AC Microgrids

In this section, we derive explicit expressions for the small-signal admittance matrices associated with both RL lines<sup>2</sup> and droop-controlled inverter-based generation sources in AC microgrids. A suitable modeling paradigm uses dynamic phasors  $\tilde{V}_{dq}(t)$  and  $\tilde{I}_{dq}(t)$ . These dynamics phasors are split into their real and imaginary parts in an arbitrary  $dq$  reference frame, and then their equilibrium points are discarded in order to capture their respective small signal perturbations  $v_d(t)$ ,  $v_q(t)$ ,  $i_d(t)$ , and  $i_q(t)$ . Please refer to Appendix C for additional details on dynamic phasor modeling.

#### RL Line Admittance

In the modeling paradigm of dynamic phasors, the admittance associated with an RL line, connecting nodes  $j$  and  $k$ , is given in (C.14) by [91]

$$\mathcal{Y}_{jk}(s) = \begin{bmatrix} Ls + R & -L\omega_0 \\ L\omega_0 & Ls + R \end{bmatrix}^{-1}. \quad (3.10)$$

---

<sup>2</sup>The corresponding admittance can also be used to characterize RL loads.

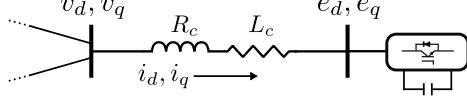


Figure 3-4: Inverter connected to a grid node:  $v_d$  and  $v_q$  are small-signal variations of grid node voltage while  $e_d$  and  $e_q$  are variations of inverter terminal voltage. The combined coupling and virtual inductance and resistance are  $L_c$  and  $R_c$  respectively.

### Inverter Input Admittance

We assume the inverter terminals are connected to a network bus via a certain impedance which, in general, is the combined virtual, coupling, and possibly connecting line impedance. We will refer to this combined impedance simply as coupling impedance and denote it as  $Z_c = R_c + sL_c$ . Let  $E_t$ ,  $\Theta_t$ , and  $\Omega_t$  denote the (non-small signal) magnitude, angle, and frequency of the inverter's terminal voltage. The following equations describe the time-domain dynamics of a droop-controlled inverter [184] (we omit the subscript  $i$  denoting the inverter number):

$$\frac{d\Theta_t}{dt} = \Omega_t - \Omega_0 \quad (3.11a)$$

$$\tau \frac{d\Omega_t}{dt} = \Omega^* - \Omega_t - k_p P \quad (3.11b)$$

$$\tau \frac{dE_t}{dt} = E^* - E_t - k_q Q, \quad (3.11c)$$

where  $P$  and  $Q$  are instantaneous values of real and reactive power discharged by the inverter, and  $k_p$  and  $k_q$  are frequency and voltage droop gain coefficients respectively. Constants  $\Omega^*$  and  $E^*$  are the frequency and magnitude set-points respectively, and  $\tau$  is the inverse of the power controller filter cut-off frequency  $w_{ci}$  (typically around 31.41 rad/s for 50 Hz grids). Control scheme (3.11) allows inverters to mimic synchronous machine dynamics; a detailed description of such control is provided in [146].

As previously, we let the lower-case letters denote small-signal variations of corresponding variable. Thus  $\theta$ ,  $\omega$ ,  $e$ ,  $p$ , and  $q$  are the variations of inverter terminal angle, frequency, voltage magnitude, real and reactive power output, respectively. In writing the small-signal representation of (3.11), we take into account that inverters typically operate at very low values of terminal angle and voltage variation due to small per unit values of coupling impedance (for details, see [184]). In this case, we

have the following simple relations (where we assume nominal voltage is 1 pu):

$$e_q = \theta, \quad e_d = e, \quad (3.12a)$$

$$p = i_d, \quad q = -i_q \quad (3.12b)$$

Where  $e_d$ ,  $e_q$ ,  $i_q$ , and  $i_d$  are the small-signal  $dq$  components of the inverter terminal voltage and current (Fig. 3-4). The small-signal approximation of (3.11) becomes:

$$\tau \frac{d^2 e_q}{dt^2} + \frac{de_q}{dt} = k_p i_d \quad (3.13a)$$

$$\tau \frac{de_d}{dt} + e_d = -k_q i_q. \quad (3.13b)$$

We can now construct the effective admittance matrix associated with the inverter controls that links inverter voltage and current via  $[i_d, i_q]^T = \mathcal{Y}_{ctrl}[e_d, e_q]^T$ , where

$$\mathcal{Y}_{ctrl}(s) = \begin{bmatrix} 0 & -\frac{k_q}{\tau s + 1} \\ \frac{k_p}{\tau s^2 + s} & 0 \end{bmatrix}^{-1}. \quad (3.14)$$

In order to get the full inverter input admittance, we note that the coupling impedance is connected in series with the inverter and has the admittance given by (3.10). Therefore, the input admittance associated with inverter  $i$  is given by

$$\mathcal{Y}_i(s) = \begin{bmatrix} R_c + sL_c & -X_c - \frac{k_q}{1 + \tau s} \\ X_c + \frac{k_p}{\tau s^2 + s} & R_c + sL_c \end{bmatrix}^{-1}, \quad (3.15)$$

where  $R_c$ ,  $L_c$ , and  $X_c = L_c \omega_0$  refer to coupling impedance parameters.

## AC Network Model

Finally, in the absence of external perturbations, we note that AC microgrid systems also satisfy (3.7). In order to differentiate between the nodal admittance matrices of AC and DC microgrid networks,  $\mathbf{Y}(s)$  is used to refer to the DC microgrid matrix, while  $\tilde{\mathbf{Y}}(s)$  is used to refer to the AC microgrid matrix. The entries of the AC system matrix will be  $2 \times 2$  admittance matrix terms, such as (3.10) and (3.15), and the voltage vector  $\mathbf{v}(s)$  will be filled with  $dq$  axis small-signal voltage perturbations:

$$\mathbf{v}(s) = [v_{d,1}(s), v_{q,1}(s), \dots, v_{d,n}(s), v_{q,n}(s)]^T. \quad (3.16)$$

## 3.2 Stability Certificates for DC Microgrids

### 3.2.1 From Centralized to Decentralized Stability Certificates

In this subsection, the proposed small-signal network model of (3.7) is “parameterized” by scaling its closed loop controller gains. Leveraging this parameterization, a decentralized stability certificate is derived. This certificate is then updated to accommodate networks where negative admittances are present at zero frequency. Finally, a simple, tractable example is given in order to illustrate the mechanics behind the proposed methods.

#### Centralized Stability Assessment via Parameterization

We choose to “parameterize” our network model with a homotopic scalar gain value  $\alpha \in [0, 1]$ , where  $\alpha = 1$  corresponds to a nominal (or desired) system configuration. Next, we appropriately multiply  $\alpha$  by all closed loop controller gains in the network which influence stability. For example, if the open loop admittance of a dynamical load is given by  $h(s)$ , and proportional feedback control is added, its closed loop admittance may be computed as

$$Y(s) = \frac{h(s)}{1 + K \cdot h(s)}. \quad (3.17)$$

When this closed loop admittance is parameterized, the transfer function may be written as

$$Y(s, \alpha) = \frac{h(s)}{1 + (\alpha \cdot K) \cdot h(s)}. \quad (3.18)$$

Clearly, when  $\alpha = 0$ , the closed feedback loop is broken. The primary feature of this parameterization scheme is that for  $\alpha = 0$ , the system is “definitely” stable, i.e. all of its eigenmodes are in the LHP. This claim can be certified by considering that, when  $\alpha = 0$ , all relevant controller gains (voltage regulation, power sharing, etc.) in the network are set to 0. When this occurs, all of the closed loop feedback mechanisms in the network are effectively broken. The system will thus be operating in a definitely stable, open loop configuration. When  $\alpha$  is scaled up to 1, then all of the controller gains have also been scaled up to their nominal values. As will be clarified, the scaling of  $\alpha$  from 0 to 1 can be thought of as a homotopy procedure, since it represents a smoothly varying parameterization of the system eigenmodes.

Using this parameterization scheme, matrix  $\mathbf{Y}(s, \alpha)$  represents the previously derived small-signal network model which has been parameterized with  $\alpha$ . The general strategy for proving the stability of the system  $\mathbf{Y}(s, \alpha)$  is based on the well-known “zero exclusion principle” and is closely related to the  $\mu$ -analysis, as is shown in the following stability lemma.

**Lemma 6.** *Assuming  $\mathbf{Y}(s, \alpha)$  is stable for  $\alpha = 0$ , then  $\mathbf{Y}(s, \alpha)$  is also stable for  $\alpha = 1$  if the determinant satisfies*

$$\det[\mathbf{Y}(s = j\omega, \alpha)] \neq 0, \quad \forall \omega \geq 0, \quad \forall \alpha \in [0, 1]. \quad (3.19)$$

*Proof.* For  $\alpha = 0$ , the real part of all eigenmodes will lie in the LHP. For the system to go unstable, an eigenmode must cross the imaginary axis. At the point of crossing,  $\exists \alpha, \omega \ni \det[\mathbf{Y}(s = j\omega, \alpha)] = 0$ , since one of the eigenmodes will necessarily have  $\text{Re}\{s_0\} = 0$ . If this does not occur, the system remains stable.  $\square$

To generalize this lemma, we introduce the rotational function

$$\mathcal{D}(\omega, \alpha) = e^{j\phi(\omega, \alpha)} \quad (3.20)$$

whose magnitude is unity and whose phase function  $\phi(\omega, \alpha)$  depends on both frequency and the parameterization value  $\alpha$ .

**Remark 3.** *The results of lemma 6 remain valid if  $\mathbf{Y}(s, \alpha)$  is multiplied by any nonzero function. Thus, we can write the generalization of condition (3.19) as*

$$\det[\mathcal{D}(\omega, \alpha)\mathbf{Y}(s = j\omega, \alpha)] \neq 0, \quad \forall \omega \geq 0, \quad \forall \alpha \in [0, 1]. \quad (3.21)$$

While (3.21) can guarantee the stability of the system  $\mathbf{Y}(s, \alpha)$ , it is centralized in nature, i.e., there is no way to relate the determinants of the subsystems with the determinant of the full system. Rather than require a nonzero determinant, a more restrictive condition is to require the positive definiteness of the matrix over the same range. While conservative, positive definiteness has a very useful additive property, i.e., if the matrices in a set are all positive definite, then so is their sum.

**Lemma 7.** *Assume network  $\mathbf{Y} \equiv \mathbf{Y}(s, \alpha)$  is stable for  $\alpha = 0$ . Set  $s = j\omega$ . If there exists  $\mathcal{D} \equiv e^{j\phi(\omega, \alpha)}$  for which*

$$\mathcal{D}\mathbf{Y} + (\mathcal{D}\mathbf{Y})^\dagger \succ 0, \quad \forall \omega \geq 0, \quad \forall \alpha \in [0, 1], \quad (3.22)$$

*then  $\mathbf{Y}(s, \alpha)$  is stable for all gain values up to  $\alpha = 1$ .*

*Proof.* Assume matrix  $\mathbf{Y}$  becomes singular for some allowed values of  $\omega, \alpha$ . Then  $\mathcal{D}\mathbf{Y}$  will also be singular, meaning  $\mathcal{D}\mathbf{Y} + (\mathcal{D}\mathbf{Y})^\dagger$  cannot be positive definite. If (3.22) is satisfied,  $\mathbf{Y}$  cannot become singular, and Lemma 6 holds.  $\square$

## Decentralized Stability Rules

As written, (3.22) is still a fully centralized stability certificate, because  $\mathbf{Y}$  is the full system matrix. The certificate can be converted to a decentralized stability certificate, though, by writing  $\mathbf{Y}$  as a summation of its network and shunt components, as in (3.5). To simplify notation, we introduce set  $\mathcal{C} = \mathcal{E} \cup \mathcal{V}$ ; it is defined to be the set of indices associated with all dynamical elements in the network. Furthermore,  $Y_k \equiv Y_k(s, \alpha)$ ,  $k \in \mathcal{C}$  refers to the  $k^{\text{th}}$  complex *scalar* transfer function element in the system (line, load, or source).

**Theorem 4.** *Assume network  $\mathbf{Y} \equiv \mathbf{Y}(s, \alpha)$  of (3.7) is stable for  $\alpha = 0$ . Set  $s = j\omega$ . If there exists  $\mathcal{D} \equiv e^{j\phi(\omega, \alpha)}$  for which*

$$\operatorname{Re}\{\mathcal{D}Y_k\} > 0, \quad \forall k \in \mathcal{C}, \quad \forall \omega \geq 0, \quad \forall \alpha \in [0, 1], \quad (3.23)$$

*then  $\mathbf{Y}(s, \alpha)$  is stable for all gain values up to  $\alpha = 1$ .*

*Proof.* Using (3.5), we break system  $D\mathbf{Y}$  into

$$D\mathbf{Y} = \underbrace{\sum_{i,j \in \mathcal{E}} \mathcal{D}\mathbf{Y}_N^{(i,j)}}_A + \underbrace{\sum_{i \in \mathcal{V}} \mathcal{D}\mathbf{Y}_S^{(i)}}_B. \quad (3.24)$$

Assume (3.23) holds true. By construction, matrix  $A_H = A + A^\dagger$  necessarily has a single  $\lambda = 0$  eigenvalue, and all others are positive. The eigenvector associated with this zero eigenvalue is equal to  $\mathbf{e} = [1, 1, \dots, 1]^T$ . Matrix  $B_H = B + B^\dagger$  is also a PSD matrix, but it is additionally diagonal, so  $\mathbf{e}^\dagger B_H \mathbf{e} > 0$ . Thus, (3.23) implies positive definiteness of  $\mathcal{D}\mathbf{Y} + (\mathcal{D}\mathbf{Y})^\dagger$ , which further implies the stability of  $\mathbf{Y}(s, \alpha)$  up to  $\alpha = 1$ .  $\square$

As a helpful simplification, we may use polar coordinates to write  $\theta_k \equiv \angle Y_k(\omega, \alpha)$  and  $|Y_k| \equiv |Y_k(\omega, \alpha)|$ . Thus, the positivity condition in (3.23) can be stated as

$$0 < \mathcal{D}Y_k + (\mathcal{D}Y_k)^\dagger \quad (3.25a)$$

$$= 2|Y_k| \operatorname{Re}\{e^{j(\phi(\omega, \alpha) + \theta_k)}\}. \quad (3.25b)$$

Using (3.25), we have the following corollary.

**Corollary 7.** *If there exists  $\phi \equiv \phi(\omega, \alpha)$  for which*

$$-\frac{\pi}{2} < \phi + \theta_k < \frac{\pi}{2}, \forall k \in \mathcal{C}, \forall \omega \geq 0, \forall \alpha \in [0, 1], \quad (3.26)$$

*and  $\mathbf{Y}(s, \alpha = 0)$  is stable, then  $\mathbf{Y}(s, \alpha = 1)$  is also stable.*

### The Problem of Negative Admittance at Zero Frequency

Assuming the network model is constructed using physical laws and physically realizable controllers, the admittance matrix  $\mathbf{Y}(s = j0, \alpha)$  will be a purely real matrix. Therefore, the angle  $\theta_k$  associated with all elements in this matrix will have an angle of either  $\theta_k = 0^\circ$  or  $\theta_k = 180^\circ$ . If any shunt element, such as a constant power load, has  $\theta_k = 180^\circ$  at  $s = j0$ , then condition (3.26) cannot be satisfied at this frequency, since any network line will necessarily have  $\theta_k = 0^\circ$ . Mathematically, this limiting case of  $s = j0$  cannot be ignored, since a negative real eigenmode (i.e. system pole) may potentially travel on the real axis and cross the imaginary axis at  $s = j0$ . Therefore, network singularity at zero frequency must be considered.

**Definition 11.** *System  $\mathbf{Y}(s, \alpha)$  is said to be **zero-frequency stable** if  $\det[\mathbf{Y}(s = j0, \alpha)] \neq 0, \forall \alpha \in [0, 1]$ . That is, no real eigenmode crosses into the RHP as  $\alpha$  is scaled from 0 to 1.*

We note, however, that  $\det[\mathbf{Y}(s = j0, \alpha)] = 0$  will occur at the point of maximum network loadability. Therefore, if this determinant is close to 0, then the system is operating on the tip of the so-called “nose curve”. Practical systems are engineered to operate far from this nose curve. We therefore offer the following assumption, which entirely precludes the possibility of a system encountering zero-frequency instability.

**Assumption 1.** *System (3.7) is assumed to operate far from the steady state nose curve and is therefore zero-frequency stable.*

With the addition of Assumption 1, we update Corollary 7.

**Corollary 8.** *If there exists  $\phi \equiv \phi(\omega, \alpha)$  for which*

$$-\frac{\pi}{2} < \phi + \theta_k < \frac{\pi}{2}, \forall k \in \mathcal{C}, \forall \omega > 0, \forall \alpha \in [0, 1], \quad (3.27)$$

*and Assumption 1 holds, and  $\mathbf{Y}(s, \alpha = 0)$  is stable, then  $\mathbf{Y}(s, \alpha)$  is also stable  $\forall \alpha \in [0, 1]$ .*

Per (3.27), the phase condition must be satisfied for all *positive*  $\omega$ , rather than all non-negative  $\omega$ , as in (3.26).

## Numerical Example

As an illustrative example, we consider the network in Fig. 3-3. We define the open-loop load dynamics via

$$h(s) = \frac{1}{s^2 + 2\zeta\omega_n s + \omega_n^2}. \quad (3.28)$$

A PI controller is then added in a negative feedback loop to yield the resulting admittance function

$$Y_l(s) = \frac{h(s)}{K(1 + \frac{1}{s\tau_i})h(s) + 1}. \quad (3.29)$$

The source is considered to be an ideal voltage source<sup>3</sup> connected through a short line. Thus, the admittances associated with the source and the network line are respectively given by

$$Y_s(s) = \frac{1/R_s}{1+s\tau}, \quad Y_t(s) = \frac{1/R_t}{1+s\tau}, \quad (3.30)$$

where, for simplicity, the time constant  $\tau$  is assumed equal in both admittances. We consider the stability of this system in two ways: first, using the non-conservative centralized approach of Lemma 6, and second, using the decentralized approach proposed by Corollary 8.

**Centralized Stability Approach:** In the centralized approach of Lemma 6, we may leverage the full, centralized network model. Rather than scaling  $\alpha$ , we directly scale gain value  $K$  to determine its maximal tolerable value. The determinant of system admittance matrix (3.6) is

$$\det[\mathbf{Y}] = (Y_s + Y_t)(Y_l + Y_t) - Y_t^2. \quad (3.31)$$

Satisfying  $(Y_s + Y_t)(Y_l + Y_t) - Y_t^2 = 0$  simplifies to

$$s^3 + (\tau R + 2\zeta\omega_n)s^2 + (\omega_n^2 + K + R)s + K/\tau_i = 0, \quad (3.32)$$

---

<sup>3</sup>Ideal voltage sources act as direct paths to ground in an admittance model.

where  $R \equiv R_s + R_l$ . By Routh-Hurwitz, an eigenmode will become unstable when  $K > \tau_i(\tau R + 2\zeta\omega_n)(\omega_n^2 + K + R)$ . This simplifies to

$$K > \frac{\tau_i(\tau R + 2\zeta\omega_n)(\omega_n^2 + R)}{1 - \tau_i(\tau R + 2\zeta\omega_n)} \equiv \hat{K} \quad (3.33)$$

assuming  $1 > \tau_i(\tau R + 2\zeta\omega_n)$ . When (3.33) is satisfied as an equality, the complex roots of (3.32) are

$$s = 0 \pm j\sqrt{(\omega_n^2 + R)/(R\tau\tau_i + 2\tau_i\zeta\omega_n - 1)} \equiv j\hat{\omega}. \quad (3.34)$$

Since  $\det[\mathbf{Y}(s = j\hat{\omega})] = 0$  for  $K = \hat{K}$ , this is the gain value for which stability is lost, and  $\hat{\omega}$  is the frequency of the system mode that becomes unstable. When applying the numerical values  $\omega_n = 2\pi$ ,  $\zeta = 0.1$ ,  $\tau = 0.1$ , and  $\tau_i = 0.25$ , we find  $\hat{K} = 20.77$  is the maximum tolerable gain value.

**Decentralized Stability Approach:** In the decentralized approach, we consider positive definiteness of the network elements independently via condition (3.27). To apply this corollary, we parameterize the load by setting  $K \rightarrow \alpha \cdot \hat{K}$ , so that for  $\alpha = 1$ , the system will definitely become marginally stable. Next, we independently define the phase functions  $\theta_t(\omega, \alpha)$  and  $\theta_l(\omega, \alpha)$  associated with parameterized admittance functions  $Y_t(\omega, \alpha)$ <sup>4</sup> and  $Y_l(\omega, \alpha)$ :

$$\theta_t(\omega, \alpha) = \tan^{-1}(-\omega\tau) \quad (3.35)$$

$$\theta_l(\omega, \alpha) = \tan^{-1}\left(\frac{\alpha \cdot \hat{K}/\tau_i - 2\zeta\omega_n\omega^2}{\omega(\omega_n^2 + \alpha \cdot \hat{K}) - \omega^3}\right). \quad (3.36)$$

Next, we plug these phase functions into inequality (3.26). We then plot the range of values which the unknown function  $\phi(\omega, \alpha)$  can permissibly take, for each element, as *continuous* functions of frequency and as *discrete* functions of  $\alpha$ . The results are shown in Fig. 3-5. In panel (f), it can clearly be seen that the inequality “breaks” at  $\omega \approx 7.59$ . This corresponds to  $\alpha = 0.871$  with a corresponding maximum controller gain of  $K \approx 18.1$ . When the sectors lose continuous overlap, the inequality is necessarily violated, and stability of the interconnection can no longer be guaranteed (even though the system damping ratio is still 0.8%). While  $K \approx 18.1$  is 12.9% conservative, this gain value guarantees stability not only for the circuit in Fig. 3-3, but also

---

<sup>4</sup>Since they have identical time constants, the line and the source phase functions are identical. Thus, only one of them is defined.

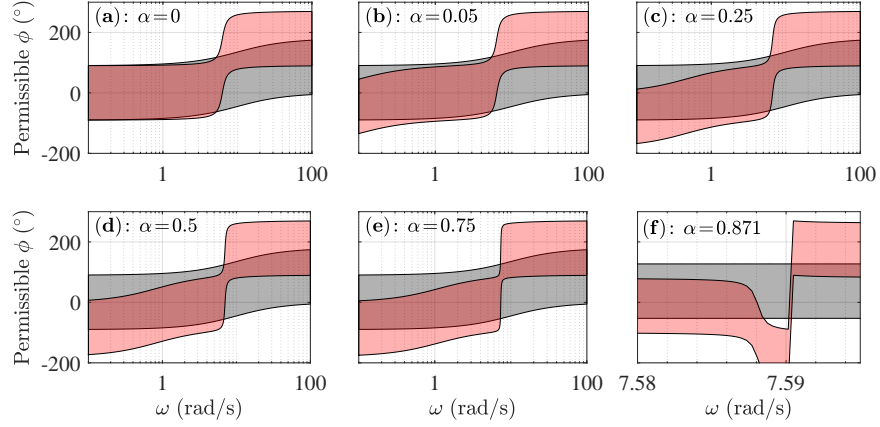


Figure 3-5: The shaded regions are the values that function  $\phi(\omega, \alpha)$  can take, according to inequality (3.27), for a continuum of frequency and controller gain values. The grey sector corresponds to the line phase function (3.35), while the red sector corresponds to the load phase function (3.36). Loss of overlap between these shaded regions indicates the non-existence of function  $\phi(\omega, \alpha)$ .

for an arbitrary interconnection of an arbitrary number of components in that circuit (assuming the system is still zero-frequency stable). Thus, it provides a generalized stability guarantee, rather than just a specific one.

### 3.2.2 Numerical Test Results

In this section, we consider a microgrid system consisting of three primary components: stiff battery-based voltage sources, RL lines, and constant resistance loads connected to buck converters. In the first subsection, we initialize the 8-bus microgrid system of Fig. 3-6. Next, we appropriately parameterize the buck converters. Finally, we analyze the small-signal stability of the network under two different controller configurations.

#### System Initialization

We first consider the equilibrium point of the network, since this operating point will influence the input voltage  $V$  for the loads. This initialization procedure is reviewed in Appendix B.2. To introduce variety into this network, the line lengths are chosen from a normal distribution with a small standard deviation:  $l_{ij} = 1 + \mathcal{N}(0, 0.1^2)$ . Solving (B.57) using the parameter values provided in Table 3.1, we get a solution with non-source nodal voltages ranging from 28.8V to 29.3V, as given in Table 3.2.

## Buck Converter Parameterization

In the microgrid system of Fig. 3-6, the loads are modeled as constant resistance and are interfaced with the network through buck converters. The nominal converter and controller parameters have been drawn from [58] and are defined in Table 3.1. The buck converter's transfer function, with the additional grounded filter capacitor from Fig. 3-1, can be parameterized by scaling the compensator gain  $G_{c\infty}$  from (3.2). Thus,

$$G_c(s, \alpha) \equiv \alpha \cdot G_c(s) \quad (3.37)$$

and the full transfer function can be written as

$$\begin{aligned} Y_{\mathcal{L}_c}(s, \alpha) &\triangleq \frac{V_m D^2}{V_m + G_c(s, \alpha) G_{vd}(s) H} \cdot \\ &\left( \frac{1 + sRC}{R + sL + s^2 RLC} - G_c(s, \alpha) \frac{G_{vd}(s) H}{RV_m} \right) + C_f s, \end{aligned} \quad (3.38)$$

where  $C_f$  represents the parallel filter capacitor. At non-zero frequencies, when  $\alpha \rightarrow 0$ , (3.38) relaxes to

$$Y_{\mathcal{L},c}(s, \alpha \rightarrow 0) = D^2 \left( \frac{1 + sRC}{R + sL + s^2 RLC} \right) + C_f s, \quad (3.39)$$

which is effectively a passive RLC transfer function. Thus, the associated parameterized system will be *definitely stable* when  $\alpha = 0$ . When  $s \rightarrow j0$ , the admittance relaxes to

$$Y_{\mathcal{L},c}(s \rightarrow j0, \alpha) = -D^2/R, \quad (3.40)$$

as would be expected from a constant power load. Since the zero frequency response of the load is negative, the conditions from Corollary 8 must be satisfied in order to certify the stability of the network in Fig. 3-6. In this system, the generators are assumed to be stiff, battery-based voltage sources. Accordingly, their only dynamics are captured by the interconnecting line. The phase response of the RL lines (including the source lines) is given according to

$$\theta_Z(\omega, \alpha) = \tan^{-1}(-\tau\omega), \quad (3.41)$$

	Parameter	Description	Value
Converter	$V$	Input Voltage	$28 \sim 30 \text{ V}$
	$R$	Load Resistance	$3 \Omega$
	$C$	Capacitance	$500 \mu\text{F}$
	$L$	Inductance	$50 \mu\text{H}$
	$D$	Duty Cycle	0.536
Controller	$G_{c\infty}$	Midband Gain	3.7
	$w_L$	Lead Zero	$2\pi \cdot 500 \text{ Hz}$
	$w_z$	Trailing Zero	$2\pi \cdot 1700 \text{ Hz}$
	$w_p$	Pole	$2\pi \cdot 14.5 \text{ kHz}$
	$H$	Sensor Gain	$1/3$
	$V_m$	Voltage of PWM	4
Network	$C_f$	Filter Capacitor	$500 \mu\text{F}$
	$l_{ij}$	Line Length	1.0 km
	$r$	Line Resistance	$0.2 \Omega/\text{km}$
	$\tau$	Line Time Constant	1 ms
	$V_s$	Source Voltage	30 V

Table 3.1: Converter, Controller, and Network Parameters

Bus 1	Bus 2	Bus 3	Bus 4	Bus 5	Bus 6	Bus 7	Bus 8
29.09	28.78	28.77	29.02	29.83	29.06	29.04	29.84

Table 3.2: Equilibrium DC Voltages of the Circuit in Fig. 3-6

where  $\tau = L/R$ . The phase response of (3.38) is analytically cumbersome, but it can be numerically computed as

$$\theta_{\mathcal{L}}(\omega, \alpha) = \tan^{-1} \left( \frac{\text{Im} \{ Y_{\mathcal{L}}(s = j\omega, \alpha) \}}{\text{Re} \{ Y_{\mathcal{L}}(s = j\omega, \alpha) \}} \right). \quad (3.42)$$

### Testing Network Stability

We now gauge the stability of the network under two buck converter controller configurations: a lead-lag filter, as in (3.3), and a common PI filter. In both cases, stability assessments are performed using an exact, centralized approach (i.e. root locus), and via the decentralized approach of Corollary 8.

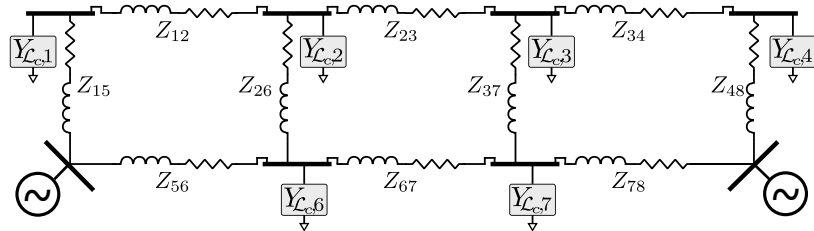


Figure 3-6: Meshed 8-bus microgrid with two stiff voltage sources and six loads.

**Lead-Lag Controller:** In this example,  $G_c(s)$  is the lead-lag controller specified in (3.3). According to [58], the stability of (3.3) is primarily controlled by the roots of  $1 + T(s)$ . With the parameters from Table 3.1, the lead-lag filter gives the bode plot of  $1 + T(s)$  a phase margin of  $\phi_m = 45.6^\circ$  and a gain margin of  $g_m = \infty$ . Using this controller, we first apply the decentralized approach of Corollary 8 by analyzing the phase functions (3.41) and (3.42). These results are shown in Fig. 3-7, where the phase functions are plotted from  $\alpha = 0$  up to  $\alpha = 10$  (i.e. scaling the gain  $G_{\infty}$  to 10 times its nominal value). As can be seen, there exists continuous overlap between the sectors; this is true for all loads in the system (results not shown), despite the small differences in equilibrium input voltages for the loads. Since the network is “definitely stable” for  $\alpha = 0$ , Corollary 8 is satisfied, and the system is *guaranteed stable under arbitrary interconnection*, assuming input voltages remain sufficiently close to those tested (i.e. within a few volts).

Next, we confirm these results using Lemma 5 and testing the system eigenmodes on a root locus plot as  $\alpha$  is scaled. To do so, we build the parameterized system admittance matrix  $\mathbf{Y}(s, \alpha) \in \mathbb{C}^{8 \times 8}$  and construct the  $N^{\text{th}}$  order polynomial  $\det[\mathbf{Y}(s, \alpha)] = 0$ , where  $N = 40$ . Finally, we employ the MATLAB root solver `roots(·)` to build the complex vector

$$\mathbf{s}(\alpha) = \{s \mid \det[\mathbf{Y}(s, \alpha)] = 0\}. \quad (3.43)$$

As shown in Fig. 3-8, no eigenmodes cross into the RHP for any value of  $\alpha \leq 10$ . Therefore, the conclusion of Corollary 8 is correct: the network is stable for any gain value  $G_{\infty}$ , even up to 10 times its nominal value. Of course, we have confirmed the prediction only for a single network configuration, but the results should generalize to an arbitrary network configuration. To further confirm this result, we set  $\alpha = 10$  and applied a 0.5 Volt step increase to the voltage source set point at bus 5. The resulting stable dynamic responses are shown in Fig. 3-9. The modeling procedure used to simulate these dynamics is reviewed in Appendix B.2.

**PI Controller:** In this test, we used a PI controller:

$$G_c(s) = G_i \left(1 + \frac{\omega_i}{s}\right). \quad (3.44)$$

Setting  $\omega_i = 2\pi 500$  and  $G_i = 0.015$ , the phase and gain margins of  $1 + T(s)$  were driven to  $\phi_m = 93.6^\circ$  and  $g_m = 12.3$  dB. The resulting phase function analysis results are shown in Fig. 3-10, where the phase functions are plotted from  $\alpha = 0$  up to

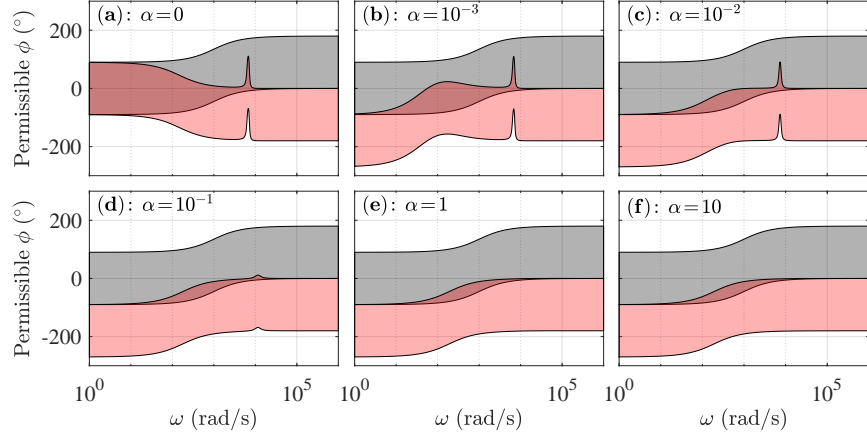


Figure 3-7: Plotted are the values that  $\phi(\omega, \alpha)$  can take, according to (3.27), for a continuum of frequency and gain values. The grey sector corresponds to the line phase function (3.41), while the red sector corresponds to the load phase function (3.42), where  $G_c(s)$  is a lead-lag controller.

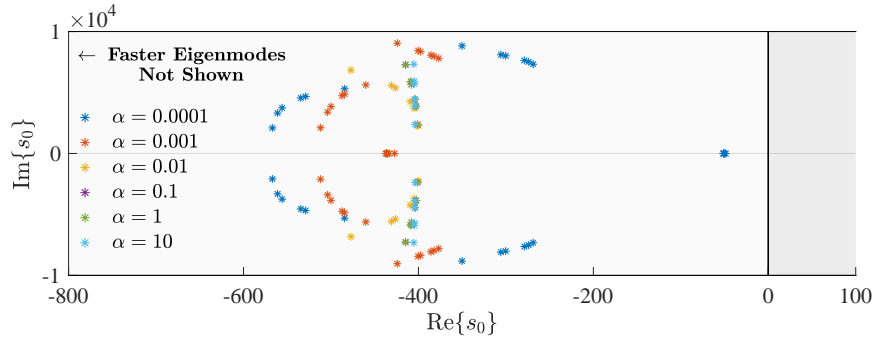


Figure 3-8: Eigenmode locus of the Fig. 3-6 microgrid via (3.43). All buck converters are outfitted with lead-lag controllers. Stability is never lost for  $\alpha \leq 10$ .

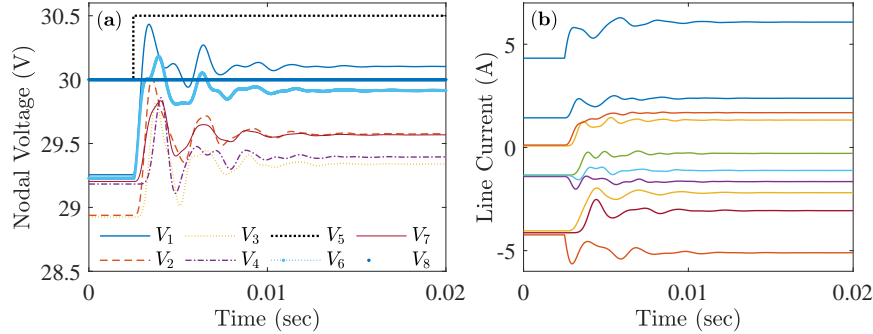


Figure 3-9: Shown are the nodal voltage (panel (a)) and line current (panel (b)) dynamic responses for a 0.5V step change in supply voltage at source bus 5. Despite the large controller gain values associated with  $\alpha = 10$ , system settling time is on the order of 10ms.

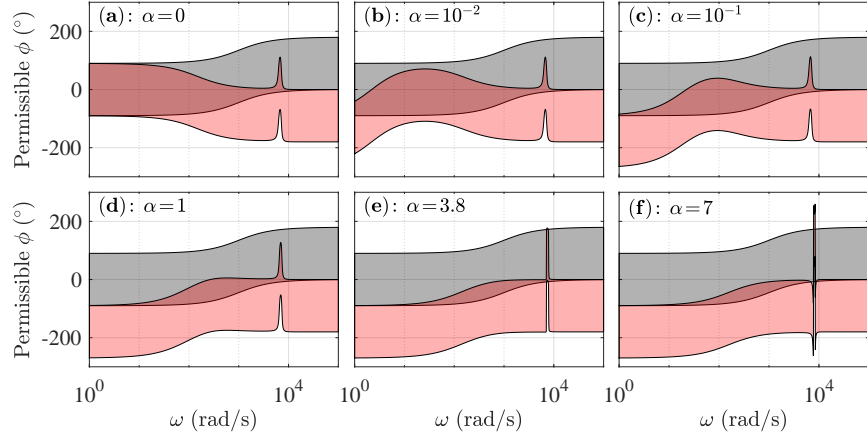


Figure 3-10: Plotted are the values that  $\phi(\omega, \alpha)$  can take, according to (3.27), for a continuum of frequency and gain values. The grey sector corresponds to the line phase function (3.41), while the red sector corresponds to the load phase function (3.42), where  $G_c(s)$  is a PI controller.

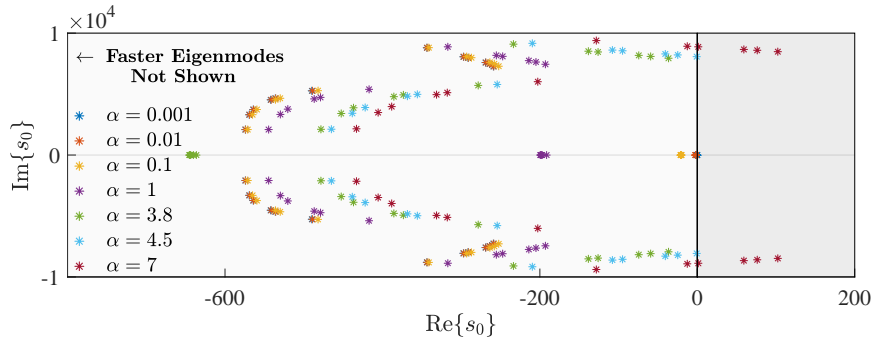


Figure 3-11: Eigenmode locus of the Fig. 3-6 microgrid via (3.43). All buck converters are outfitted with PI controllers. System stability is lost when  $\alpha > 4.5$ .

$\alpha = 7$  (i.e. scaling the gain  $G_{\infty}$  to 7 times its nominal value). As can be seen, there is a break in continuous overlap between the sectors at  $\alpha = 3.8$ , corresponding to a **maximum allowable controller gain** of  $3.8 \times 0.015 = 0.057$ . The root locus plot is shown in Fig. 3-11. The network is clearly still stable for  $\alpha = 3.8$ , but becomes marginally stable for  $\alpha = 4.5$ . Stability is clearly lost for larger value of  $\alpha$ , as shown by the eigenmodes of  $\alpha = 7$ , for example. Therefore, Corollary 8 is conservative by a margin of  $100 \times (1 - 3.8/4.7) \approx 20\%$  for this particular network configuration. In this context, the results of Fig. 3-10 can be interpreted alternatively: there exists some network configuration for which  $\alpha = 3.8$  is the maximum allowable gain factor.

### 3.2.3 Practical Applications to the Design and Operation of DC Microgrids

Although mathematical in nature, the results of Corollary 8 can lead to a plethora of (i) practical design guidelines for engineers and (ii) useful operational tools for non-expert microgrid users. Both are briefly considered.

#### Microgrid Design Tools

If an engineering team desires plug and play operability of a microgrid, they can follow the steps of Algorithm 4. This procedure can have three outcomes: it will either (i) confirm the plug-and-play operability of all desired elements, (ii) determine the maximum value of  $\alpha$  for which the system can operate, or (iii) identify the components which must be removed in order for the system to operate at  $\alpha = 1$  (i.e. nominal controller values).

Since the amount of overlap between phase curves implicitly parameterizes a stability margin, this procedure can also directly inform design constraints. For example, Fig. 3-7 was used to guarantee plug-and-play stability for constant power loads connected to RL lines. These results only hold, though, for the tested parameter values. If, for example, the time constant associated with the lines increased from  $\tau = 1$  ms to  $\tau = 7$  ms, all of the gray curves would shift backwards in frequency and overlap would be lost. Accordingly, an example of a practical design constraint follows:

- *For plug-and-play operability to be achieved in a network with buck converter loads, lines must be chosen such that their electromagnetic time constants satisfy  $\tau < 7$  ms.*

#### Microgrid Operational Tools

We consider a situation in which a variety of common microgrid components are collectively analyzed by Algorithm 4. Immediate analysis could be performed by design engineers or researchers, while future analysis could be performed directly by manufacturers. Any particular combination of microgrid elements which satisfy the criteria of Algorithm 4 can then be aggregated to form a particular “class”. For user simplicity, each class can be associated with a color (i.e. “red class”, “blue class”, etc.). Of course, any particular microgrid element can simultaneously belong to multiple classes, but mixing elements of certain classes could lead to instability. Depending on the needs of a microgrid, the designers could pre-determine the classes of elements which can

---

**Algorithm 4** Microgrid Design Procedure

---

**Require:** Candidate components  $\Sigma_i$  and potential input voltages  $V_j$

```
1: for each microgrid component  $\Sigma_i$  do
2:   for each potential input voltage  $V_j$  do
3:     for a sufficient number of  $\alpha \in [0, 1]$  values do
4:       Parameterize closed loop gains of  $\Sigma_i$  with  $\alpha$ 
5:       Compute or measure  $\Sigma_i$ 's phase response  $\theta_i(\alpha, V_j, \omega)$ 
6:     end
7:   end
8:   for each ascending value of  $\alpha$  do
9:     Plot  $\theta_i(\alpha, V_j, \omega) \pm 90^\circ$ ,  $\forall i, \forall j, \forall \omega > 0$ 
10:    if there exists continuous overlap between all phase plots then
11:      All components are plug-and-play stable for this  $\alpha$ 
12:    else
13:      either terminate at this  $\alpha$  or remove non-overlapping item
14:    end
15:  return Maximum  $\alpha$  and non-rejected  $\Sigma_i, V_j$  pairs
```

---

be plug-and-play added to the microgrid without compromising the stability of the network. Users of the microgrid, then, would only need to check if a load, for example, satisfies the class designation of the microgrid. If it does, it can be safely added (i.e. plugged in) to any arbitrary location in the network without compromising stability.

### 3.3 Decentralized Small-Signal Stability Certificates for AC Microgrids

We now offer a direct extension of the proposed standards to AC microgrid networks.

#### 3.3.1 Decentralized Stability of AC Microgrids

We consider an AC microgrid network model whose dynamics are codified by the system matrix  $\mathbf{Y}(s)$ . As reviewed in 3.1.3, in the absence of external perturbations, the system satisfies  $\mathbf{0} = \mathbf{Y}(s)\mathbf{v}(s)$ , just like in DC grids. In AC grids, though, the nodal voltages are characterized by two orthogonal components:

$$\mathbf{v}(s) = [v_{d,1}(s), v_{q,1}(s), \dots, v_{d,n}(s), v_{q,n}(s)]^T. \quad (3.45)$$

As noted in 3.1.3, the entries inside the system admittance matrix are all  $2 \times 2$  matrices:

$$\underline{\mathbf{Y}}(s) = E_a^\top \underbrace{\begin{bmatrix} \mathcal{Y}_{ij}(s) & & 0 \\ & \ddots & \\ 0 & & \mathcal{Y}_{kl}(s) \end{bmatrix}}_{\underline{\mathbf{Y}}_L(s)} E_a + \underbrace{\begin{bmatrix} \mathcal{Y}_1(s) & & 0 \\ & \ddots & \\ 0 & & \mathcal{Y}_n(s) \end{bmatrix}}_{\underline{\mathbf{Y}}_S(s)} \quad (3.46)$$

where  $E_a$  is the augmented admittance matrix from (2.158), and each  $\mathcal{Y}(s) \in \mathbb{C}^{2 \times 2}$  (for all system components). We note that (3.46) obeys Lemma 5, and the associated parameterized matrix  $\underline{\mathbf{Y}}(s, \alpha)$  obeys Lemma 6, which we restate as Lemma 8.

**Lemma 8.** *Assume network  $\underline{\mathbf{Y}} \equiv \underline{\mathbf{Y}}(s, \alpha)$  is stable for  $\alpha = 0$ . Set  $s = j\omega$ . If*

$$\underline{\mathbf{Y}} + \underline{\mathbf{Y}}^\dagger \succ 0, \quad \forall \omega \geq 0, \quad \forall \alpha \in [0, 1], \quad (3.47a)$$

*then  $\underline{\mathbf{Y}}(s, \alpha)$  is stable for all gain values up to  $\alpha = 1$ .*

*Proof.* If (3.47a) is satisfied,  $\underline{\mathbf{Y}}$  cannot become singular for any allowable values of  $\omega$  and  $\alpha$ , so no eigenmodes can cross into the RHP.  $\square$

### Replacing Rotational Functions with DQR-Transformation Matrices

At this point, though, we acknowledge the central modeling difference between AC and DC microgrid networks.

- In DC microgrids, component dynamics can be modeled with scalar transfer functions  $Y(s) \in \mathbb{C}^{1 \times 1}$ . To ensure the positive realness of the associated FRF  $Y(s = j\omega)$  across frequencies, the simple scalar rotational function  $\mathcal{D}(\omega, \alpha) = e^{j\phi(\omega, \alpha)}$  of (3.20) can be applied, such that  $\text{Re}\{Y(s = j\omega) \cdot e^{j\phi(\omega, \alpha)}\} > 0$ .
- In AC microgrids, component dynamics must be modeled with  $2 \times 2$  matrix transfer functions  $\mathcal{Y}(s) \in \mathbb{C}^{2 \times 2}$ . To ensure the positive definiteness of the associated FRFs, a scalar rotational function will not suffice, so we instead leverage the (parameterized) DQR-transformation matrices from Definition 4, such that  $\underline{\mathbf{M}}(\omega, \alpha)\mathcal{Y}(\omega, \alpha)\underline{\mathbf{G}}(\omega, \alpha) \succ 0$ .

We now offer an extension of Lemma 8, where  $\underline{\mathbf{Y}}(s, \alpha)$  is scaled by nonsingular transformation matrices  $\underline{\mathbf{M}} \in \mathbb{C}^{2n \times 2n}$  and  $\underline{\mathbf{G}} \in \mathbb{C}^{2n \times 2n}$ .

**Lemma 9.** Assume  $\underline{\mathbf{Y}} \equiv \underline{\mathbf{Y}}(s, \alpha)$  is stable for  $\alpha = 0$ . Set  $s = j\omega$ . If there exist nonsingular transformation matrices  $\underline{\mathbf{M}} \equiv \underline{\mathbf{M}}(\omega, \alpha)$  and  $\underline{\Gamma} \equiv \underline{\Gamma}(\omega, \alpha)$  which satisfy

$$(\underline{\mathbf{M}}\underline{\mathbf{Y}}\underline{\Gamma}) + (\underline{\mathbf{M}}\underline{\mathbf{Y}}\underline{\Gamma})^\dagger \succ 0, \quad \forall \omega \geq 0, \quad \forall \alpha \in [0, 1], \quad (3.48)$$

then  $\underline{\mathbf{Y}}(s, \alpha)$  is stable for all gain values up to  $\alpha = 1$ .

*Proof.* Suppose that  $\underline{\mathbf{Y}}(\omega, \alpha)$  is singular for some allowable values of  $\omega$  and  $\alpha$ . Then  $\underline{\mathbf{M}}\underline{\mathbf{Y}}\underline{\Gamma}$  is also singular for any (nonsingular) choices of  $\underline{\mathbf{M}}$  and  $\underline{\Gamma}$ , so (3.48) cannot be strictly positive definite. Therefore, if (3.48) is satisfied,  $\underline{\mathbf{Y}}$  cannot become singular, and no eigenvalues can cross into the RHP.  $\square$

We now offer a decentralized version of Lemma 9 which is entirely analogous to Theorem 4 in the DC case. This theorem, which represents the main contribution of this section, considers the full set  $\mathcal{C}$  of components (lines, loads, and sources  $\mathcal{Y}_k \equiv \mathcal{Y}_k(\omega, \alpha)$ ) which are used to construct the parameterized version of  $\underline{\mathbf{Y}}(s)$  in (3.46) (i.e.  $\underline{\mathbf{Y}}(s, \alpha)$ ). In the proof, we assume  $\underline{\mathbf{M}}$  and  $\underline{\Gamma}$  take the following block diagonal structure, where each block  $\mathbf{M}, \Gamma \in \mathbb{C}^{2 \times 2}$ :

$$\underline{\mathbf{M}} = \begin{bmatrix} \mathbf{M} & & \\ & \ddots & \\ & & \mathbf{M} \end{bmatrix}, \quad \underline{\Gamma} = \begin{bmatrix} \Gamma & & \\ & \ddots & \\ & & \Gamma \end{bmatrix}. \quad (3.49)$$

**Theorem 5.** Assume  $\underline{\mathbf{Y}} \equiv \underline{\mathbf{Y}}(s, \alpha)$  is stable for  $\alpha = 0$ . Set  $s = j\omega$ . If there exist parameterized DQR-transformation matrices  $\mathbf{M} \equiv \mathbf{M}(\omega, \alpha)$  and  $\Gamma \equiv \Gamma(\omega, \alpha)$  which satisfy

$$\det\{\mathbf{M}(\omega, \alpha)\} \neq 0, \quad \forall \omega \geq 0, \quad \forall \alpha \in [0, 1] \quad (3.50a)$$

$$\det\{\Gamma(\omega, \alpha)\} \neq 0, \quad \forall \omega \geq 0, \quad \forall \alpha \in [0, 1] \quad (3.50b)$$

$$(\mathbf{M}\mathcal{Y}_k\Gamma) + (\mathbf{M}\mathcal{Y}_k\Gamma)^\dagger \succ 0, \quad \forall \omega \geq 0, \quad \forall \alpha \in [0, 1], \quad \forall k \in \mathcal{C}, \quad (3.50c)$$

then  $\underline{\mathbf{Y}}(s, \alpha)$  is stable for all gain values up to  $\alpha = 1$ .

*Proof.* We follow the same logic as in the proof of Theorem 4. If  $\underline{\mathbf{Y}}(s, \alpha)$  is driven unstable, then there must be some point  $\omega^*$ ,  $\alpha^*$  where  $\underline{\mathbf{Y}}(\omega, \alpha)$  becomes singular. At this point, the matrix  $\underline{\mathbf{M}}\underline{\mathbf{Y}}\underline{\Gamma}$  must also be singular. Assume, though, that (3.50)

holds. Decomposing the system matrix via (3.46) and applying (3.49) yields

$$\underline{\mathbf{M}}\underline{\mathbf{Y}}\underline{\Gamma} = \underline{\mathbf{M}}\underline{\mathbf{Y}}_L\underline{\Gamma} + \underline{\mathbf{M}}\underline{\mathbf{Y}}_S\underline{\Gamma}. \quad (3.51)$$

If there is no vector  $\mathbf{v}^* \neq \mathbf{0}$  such that  $(\mathbf{v}^*)^\dagger \underline{\mathbf{M}}\underline{\mathbf{Y}}\underline{\Gamma} \mathbf{v}^* = 0$ , then  $\underline{\mathbf{Y}}$  never becomes singular, and no eigenmode may cross into the right half plane.

As a direct consequence of (3.50c),

$$0 = \min_{\mathbf{v} \neq \mathbf{0}} \{ \mathbf{v}^\dagger (\underline{\mathbf{M}}\underline{\mathbf{Y}}_S\underline{\Gamma}) \mathbf{v} \} \quad (3.52)$$

$$0 = \min_{\mathbf{v} \neq \mathbf{0}} \{ \mathbf{v}^\dagger (\underline{\mathbf{M}}\underline{\mathbf{Y}}_L\underline{\Gamma}) \mathbf{v} \}. \quad (3.53)$$

since  $\underline{\mathbf{Y}}_S$  is a block diagonal matrix, and  $\underline{\mathbf{Y}}_L$  is a graph Laplacian. Since these matrices cannot share any null vectors, though,  $0 > \min_{\mathbf{v} \neq \mathbf{0}} \{ \mathbf{v}^\dagger (\underline{\mathbf{M}}(\underline{\mathbf{Y}}_S + \underline{\mathbf{Y}}_L)\underline{\Gamma}) \mathbf{v} \}$ , and  $\underline{\mathbf{Y}}$  can never be driven singular. Thus, no eigenmode can cross into the unstable RHP.  $\square$

As described in the previous section, the rotational functions  $\mathcal{D}(\omega, \alpha) = e^{j\phi(\omega, \alpha)}$  used to certify stability of DC microgrids can be determined by visual inspection of properly parameterized phase portrait plots, such as in Fig. 3-7. In the AC microgrid case, where transformation matrices are instead required, such visual inspection methods are not necessary applicable (due to the high-dimensional nature of the problem of the problem). In the following subsection, we provide one such rotational matrix which can be used to certify the stability of a particular class of AC microgrid systems.

### 3.3.2 Test Results: Droop-Controlled Microgrid

We are now in the position to construct fully decentralized stability certificates that are valid for inverter-based microgrids of arbitrary size. We assume this system contains two components: droop controlled inverters, and RL lines/loads. To analyze this system, we first parameterize the droop controller from (3.15) via

$$\mathcal{Y}_i(\omega, \alpha) = \begin{bmatrix} R_c + j\omega L_c & -X_c - \frac{\alpha \cdot k_q}{1 + \tau j\omega} \\ X_c + \frac{\alpha \cdot k_p}{j\omega - \tau \omega^2} & R_c + j\omega L_c \end{bmatrix}^{-1}, \quad (3.54)$$

where we have simply multiplied both  $k_p$  and  $k_q$  coefficients by  $\alpha$ , so that  $\alpha = 0$  corresponds to a definitely stable system. As the base case, we use inverter coupling resistance and reactance parameters of  $R_c = 0.01$  pu and  $X_c = 0.015$  pu, respectively (per unit values of impedances in inverter-based microgrids are always small [184]).

The inverter frequency droop coefficient is  $k_p = 1.3 \cdot 10^{-3}$  pu (0.13%), and the voltage droop coefficient is  $k_q = 7.5 \cdot 10^{-3}$  pu (0.75%). Network line reactance and resistance values are chosen to be the same as the corresponding inverter coupling inductance and resistance values. The corresponding line admittance  $\mathcal{Y}_{jk}$  is given by (3.10).

In our previous works on the topic [182], we have identified that  $\mathbf{M} = \mathbb{1}$ ,  $\mathbf{\Gamma} = \mathbb{1}$  can certify stability at high frequencies, and  $\mathbf{M} = \bar{T}_4$ ,  $\mathbf{\Gamma} = \mathbb{1}$  (where  $\bar{T}_4$  is a basis matrix associated with (2.179)) can certify stability at low frequencies. In order to unite the stability guarantees in these separate frequency regions, we propose to parameterize the transformation matrix  $\mathbf{M}$  with a sigmoid function  $\sigma_p(\omega)$  via

$$\mathbf{M}(\omega, \alpha) = \begin{bmatrix} \sigma_p(\omega) & \sigma_p(\omega) - 1 \\ 1 - \sigma_p(\omega) & \sigma_p(\omega) \end{bmatrix} \quad (3.55)$$

$$\sigma_p(\omega) = \frac{1}{1 + e^{-\beta_t(\omega - \omega_t)}}, \quad (3.56)$$

where  $\beta_t > 0$  controls the steepness of the sigmoid transition and  $\omega_t > 0$  controls the location of the sigmoid transition. This matrix  $\mathbf{M}(\omega, \alpha)$  has three key properties:

$$\lim_{\omega \rightarrow 0} \mathbf{M}(\omega, \alpha) \approx \begin{bmatrix} 0 & -1 \\ 1 & 0 \end{bmatrix} \quad (3.57a)$$

$$\lim_{\omega \rightarrow \infty} \mathbf{M}(\omega, \alpha) = \begin{bmatrix} 1 & 0 \\ 0 & 1 \end{bmatrix} \quad (3.57b)$$

$$\det \{\mathbf{M}(\omega, \alpha)\} = \sigma_p(\omega)^2 - (\sigma_p(\omega) - 1)(1 - \sigma_p(\omega)) \quad (3.57c)$$

$$= 1 + 2\sigma_p(\omega)(\sigma_p(\omega) - 1) \quad (3.57d)$$

$$\neq 0 \quad (3.57e)$$

Due to its nonsingularity, it represents a suitable transformation for satisfying condition (3.50). Before testing this matrix, we first showcase results associated with the naive choice of  $\mathbf{M} = \mathbf{\Gamma} = \mathbb{1}$ . These results are shown in Fig. (3-12), where we plot the eigenvalues of  $(\mathbf{M}\mathcal{Y}_k\mathbf{\Gamma}) + (\mathbf{M}\mathcal{Y}_k\mathbf{\Gamma})^\dagger$  from (3.50c). As can be seen in this figure, for large values of  $\alpha$  and low values of frequency, one of the inverter eigenvalues “dips” negative into the red region, so (3.50) is not satisfied. Therefore, decentralized stability certification is not achieved.

In the second test, we keep  $\mathbf{\Gamma} = \mathbb{1}$ , but we set  $\mathbf{M}$  equal to (3.55). These results are shown in Fig. 3-13, where we see that, across all considered gain and frequency values, no eigenvalues become negative. Accordingly, our choice of transformation

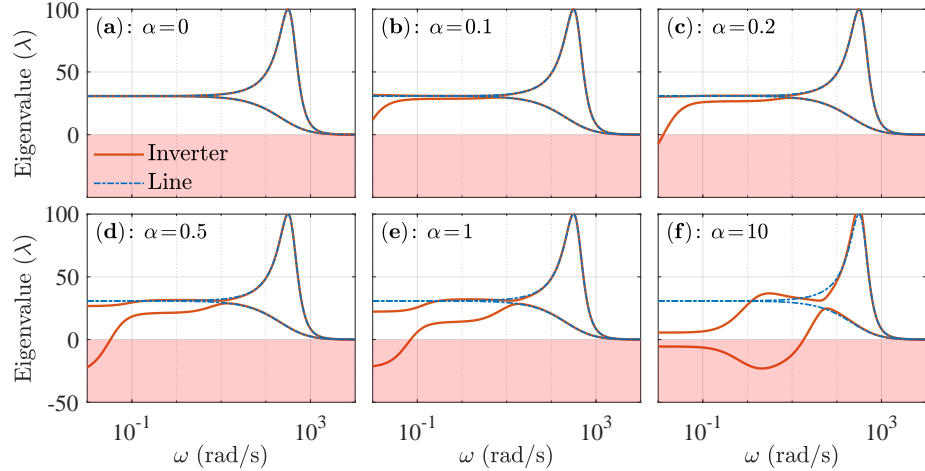


Figure 3-12: Plotted are the eigenvalues associated with the matrix  $(\mathbf{M}\mathcal{Y}_k\boldsymbol{\Gamma}) + (\mathbf{M}\mathcal{Y}_k\boldsymbol{\Gamma})^\dagger$ , for both inverter and line admittances, across a continuum of frequency and gain values. In this trivial case,  $\mathbf{M} = \boldsymbol{\Gamma} = \mathbb{1}$ . Since inverter eigenvalues dip into the negative (i.e. lower red shaded) region, (3.50) cannot be satisfied.

matrices satisfies (3.50), and so decentralized stability certificates can be generated. That is, an arbitrary number of the considered devices can be interconnected in an arbitrary manner, and the resulting network will be guaranteed small signal stable. Of course, the resulting stability certificate is only valid for devices whose parameters match the ones tested in this subsection and for gain values which are less than or equal to  $\alpha = 10$ . Testing a broader range of parameter values and devices can be achieved by simply plotting their corresponding eigenvalue curves in Fig. 3-13 and ensuring that no eigenvalues dip negative.

### 3.3.3 Connecting AC Microgrid Decentralized Stability Certificates to Forced Oscillation Source Location

Before concluding this chapter, we offer brief remarks on the connection between the proposed AC microgrid stability standards and the problem of locating forced oscillations in transmission networks. If (3.50) can be satisfied, such that parameterized matrices  $\mathbf{M}(\omega, \alpha)$  and  $\boldsymbol{\Gamma}(\omega, \alpha)$  can simultaneously rotate all microgrid elements positive definite, then (2.126) implies there is some quadratic quantity which is everywhere dissipated in the microgrid network. This furthermore implies that there exists a time domain integral which could trace the “flow” of this quadratic quantity (using only terminal device measurements). Therefore, there would exist an energy-based procedure which could locate the sources of forced oscillations with complete accu-

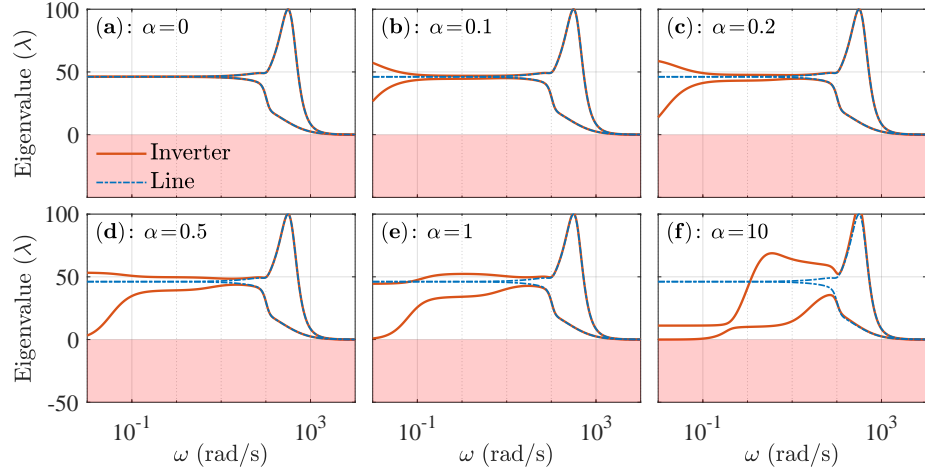


Figure 3-13: Plotted are the eigenvalues associated with the matrix  $(\mathbf{M}\mathcal{Y}_k\Gamma) + (\mathbf{M}\mathcal{Y}_k\Gamma)^\dagger$ , for both inverter and line admittances, across a continuum of frequency and gain values. In this non-trivial case,  $\Gamma = \mathbb{1}$ , but  $\mathbf{M}$  is set to (3.55). Since no eigenvalues dip into the negative (i.e. lower red shaded) region, (3.50) is satisfied.

racy (i.e. the quadratic flow would always lead back to the source of the oscillation). While locating the sources of forced oscillations is not necessarily the goal of (3.50) and the associated theorem, it is interesting to note the mathematical underpinnings which connect energy-based forced oscillation source location procedures (i.e. the DEF method) and procedures which can produce decentralized stability certificates for microgrid networks.



# Chapter 4

## Vector Fitting Approaches for Real-Time Predictive Modeling of Low Frequency Power System Dynamics

This chapter is broken into three sections. In the first section, we provide the mathematical background which will be necessary for solving the problems considered in this chapter. In the second section, we derive the Real-Time Vector Fitting (RTVF) scheme and test its application on two types of simulated systems: synthetic test systems and high order closed loop generator systems. In the third section, we propose the stochastic-RTVF (sRTVF) formulation, which is suitable for observing dynamics which are corrupted by unobservable stochastic inputs (i.e. stochastically-obscured dynamics).

### 4.1 Mathematical Background

#### 4.1.1 Overview of the Time Domain Vector Fitting Algorithm

We consider a possibly nonlinear dynamic system  $\mathcal{S}$  with input and output signals denoted as  $\mathbf{u}(t) \in \mathbb{R}^P$  and  $\mathbf{y}(t) \in \mathbb{R}^P$ , respectively. For later use, we denote with  $\mathbf{x}(t) \in \mathbb{R}^{\bar{N}}$  some unknown system state vector, where  $\bar{N}$  represents the true (physical) order of the system dynamics. We assume no information on the internal system representation; instead, we assume a measurement tool is available that returns  $K$

samples of time-domain input-output vectors

$$\mathbf{u}(t_k), \mathbf{y}(t_k) \quad k = 1, \dots, K \quad (4.1)$$

acquired at sampling rate  $F_s$ . Without loss of generality, we set  $t_1 = 0$  throughout this thesis. All derivations will hold true for  $t_1 \neq 0$ , provided the time variable is redefined as  $t \leftarrow t - t_1$ . When the underlying system  $\mathcal{S}$  is Linear and Time-Invariant (LTI), Laplace-domain input and output signals are related by

$$\mathbf{Y}(s) = \check{\mathbf{H}}(s)\mathbf{U}(s). \quad (4.2)$$

An estimate  $\mathbf{H}(s)$  of the true transfer function  $\check{\mathbf{H}}(s)$  can be determined from the samples (4.1) through one of the several available data-driven model order reduction methods. In particular, the TDVF scheme [73, 71, 72] considered in this work assumes that the system is initially at rest, and the *initial conditions* vanish identically as

$$\mathbf{u}(0) \equiv \mathbf{0}, \quad \mathbf{y}(0) \equiv \mathbf{0}, \quad \mathbf{x}(0) \equiv \mathbf{0}. \quad (4.3)$$

This setting guarantees that only the zero-state response contribution is present in the output samples. The basic TDVF scheme assumes availability of

- time series of each output  $y_{ij}(t)$  at port  $i$  excited by a single input  $u_j(t)$  placed at port  $j$  and acting alone, with  $u_{k \neq j} = 0$ ; this requirement imposes a restriction on the training sequences that can be used for model extraction;
- some initial estimate of the dominant system poles  $\{q_n, n = 1, \dots, N\}$ . Usually, such poles are initialized as random real or complex conjugate pairs with  $\text{Re}\{q_n\} < 0$  and  $|q_n| < \Omega$ , where  $\Omega$  is the modeling bandwidth of interest [73, 76].

Based on the training data, TDVF constructs the approximation

$$d_0 \cdot y_{ij}(t) + \sum_{n=1}^N d_n \cdot y_{ij}^{(n)}(t) \approx c_{ij}^{(0)} \cdot u_j(t) + \sum_{n=1}^N c_{ij}^{(n)} \cdot u_j^{(n)}(t) \quad (4.4)$$

for  $t = t_k$  with  $k = 1, \dots, K$ , where  $c_{ij}^{(n)}$  and  $d_n$  are unknown coefficients to be determined via a linear least squares solution. In (4.4), superscript  $(n)$  denotes the result obtained by the single-pole filter (i.e. convolution) via

$$z^{(n)}(t) = \int_0^t e^{q_n(t-\tau)} z(\tau) d\tau \quad (4.5)$$

on any arbitrary signal  $z(t)$  with  $z(0) = 0$ . The associated linear least-squares problem is solved for the coefficients  $c_{ij}^{(n)}$  and  $d_n$ :

$$\min_{d_n, c_{ij}^{(n)}} \sum_{k=1}^K \left| d_0 \cdot y_{ij}(t_k) - c_{ij}^{(0)} \cdot u_j(t_k) + \sum_{n=1}^N \left( d_n \cdot y_{ij}^{(n)}(t_k) - c_{ij}^{(n)} \cdot u_j^{(n)}(t_k) \right) \right|^2. \quad (4.6)$$

The time domain approximation (4.4) corresponds to the frequency-domain relation

$$Y_{ij}(s) \approx H_{ij}(s) U_j(s) \approx \frac{c_{ij}^{(0)} + \sum_{n=1}^N \frac{c_{ij}^{(n)}}{s - q_n}}{d_0 + \sum_{n=1}^N \frac{d_n}{s - q_n}} \cdot U_j(s) \quad (4.7)$$

which provides an element-wise rational approximation  $H_{ij}(s) \approx \check{H}_{ij}(s)$  written in barycentric form. The initial poles  $q_n$  in (4.7) cancel out, and the actual poles of  $H_{ij}(s)$  correspond to the zeros  $z_n$  of the denominator

$$D(s) = d_0 + \sum_{n=1}^N \frac{d_n}{s - q_n}. \quad (4.8)$$

Problem (4.4) is solved iteratively, by using these zeros as starting poles for the next iteration via  $q_n \leftarrow z_n$ . Iterations stop when the poles and/or the least-squares residual (fitting error) stabilize [73, 108], or alternatively when a maximum number of iterations  $\nu_{\max}$  is reached. A good proxy for pole convergence is provided by the norm of the vector  $\mathbf{d} = [d_1, \dots, d_N]^\top$ , which collects all denominator coefficients excluding  $d_0$ . When such coefficients approach zero, the denominator function  $D(s)$  approaches a constant value, implying that the poles and the zeros of  $D(s)$  are nearly coincident. Under this condition, the poles become invariant through iterations and convergence is attained. Therefore, the iterations can be stopped when

$$\sqrt{\sum_{i=1}^N d_i^2} \leq \epsilon \quad (4.9)$$

where  $\epsilon$  is a desired tolerance. Alternatively, a maximum number of algorithm iterations  $\nu_{\max}$  can be set. Pseudocode for the basic TDVF scheme, which constructs the approximate rational transfer matrix  $\mathbf{H}(s)$ , is reported in Algorithm 5. Furthermore, Fig. 4-1 depicts the TDVF pole converge procedure graphically, where convergence is achieved when (4.9) is satisfied.

---

**Algorithm 5** The TDVF algorithm

---

**Input:** Time samples  $\mathbf{u}(t_k)$ ,  $\mathbf{y}(t_k)$ , sampling frequency  $F_s$ , starting poles  $\{q_1, \dots, q_N\}$ , maximum iteration number  $\nu_{\max}$

**Output:** Estimated transfer function  $\mathbf{H}(s)$

```

1: for  $j = 1 \dots P$  do
2:   for  $\nu = 1, \dots, \nu_{\max}$  do
3:     Compute the filtered signals  $\tilde{u}_j^{(n)}, \tilde{y}_{ij}^{(n)}$  using (4.5)
4:     Build and solve the least squares problem (4.6)
5:     Compute the zeros  $z_n$  of denominator  $D(s)$  in (4.7)
6:     Set  $q_n \leftarrow z_n$ 
    end
7:   Solve (4.6) by constraining  $d_0 = 1$  and  $d_n = 0$ 
  end
8: return:  $\mathbf{H}(s)$ , where  $H_{ij}(s)$  is the numerator of (4.7)

```

---

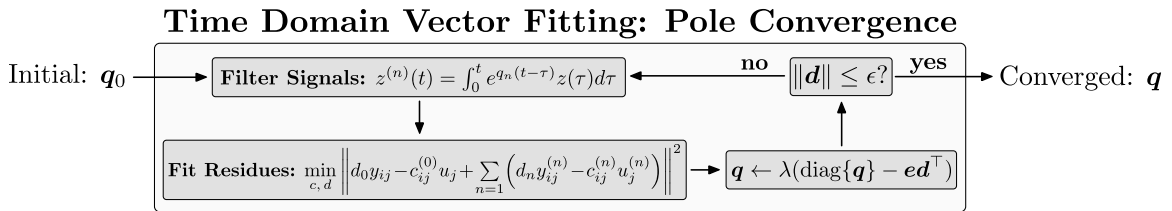


Figure 4-1: Shown is the pole convergence procedure associated with TDVF. In this figure,  $\mathbf{q} = [q_1, \dots, q_N]^T$  is the vector of poles from (4.8),  $\mathbf{d} = [d_1, \dots, d_N]^T$  is the vector of denominator coefficients from the numerator of (4.8),  $\mathbf{e} = [1, \dots, 1]^T$  is a vector of 1's, and  $\lambda\{\cdot\}$  is the eigenvalue operator.

### 4.1.2 The Overdetermined Modified Yule–Walker Method

In this subsection, we outline the Overdetermined Modified Yule–Walker (OMYW) method for a SISO discrete time system [174]. This method was successfully applied to a power system inference problem in the highly cited paper [189]. Although we do not make exact use of the OMYW method, we leverage its key innovation when deriving the stochastic-RTVF methodology later in this thesis.

To begin, we assume a discrete-time linear system is excited by unobservable, stochastic input sequence  $u[n]$ , which is pure AWGN. The output sequence is given by  $y[n]$ . The so-called Autoregressive-Moving Average (ARMA) model relates these sequences via

$$y[n] + a_1y[n-1] + \cdots + a_Ny[n-N] = b_0u[n] + b_1u[n-1] + \cdots + b_Mu[n-M], \quad (4.10)$$

where the autoregressive sequence is of order  $N$ , and the moving average sequence is of order  $M$ . We now define the auto-correlation function (ACF)

$$r(k) = E\{y[n]y[n-k]\}$$

where  $E\{\cdot\}$  is the expected value operator. We now multiply the ARMA sequence through by  $y[n-k]$  and take the expected value:

$$r(k) + \sum_{i=1}^N a_i r(k-i) = \sum_{j=0}^M b_j E\{y[n-k]u[n-j]\}. \quad (4.11)$$

The OMYW method makes the following key observation: for any  $k > M$ , the RHS must be equal to 0, since the output must be uncorrelated with future noise inputs:

$$r(k) = - \sum_{i=1}^N a_i r(k-i), \quad \forall k > M. \quad (4.12)$$

For  $k = M+1, M+2, \dots, M+P$ , (4.12) can be rewritten as the linear system  $\mathbf{r} = -\mathbf{R}\mathbf{a}$ , where the Toeplitz autocorrelation matrix  $\mathbf{R} \in \mathbb{R}^{P \times N}$  takes the form

$$\mathbf{R} = \begin{bmatrix} r(M) & r(M-1) & \cdots & r(M-N+1) \\ r(M+1) & r(M) & \cdots & r(M-N+2) \\ \vdots & \vdots & \ddots & \vdots \\ r(M+P-1) & r(M+P-2) & \cdots & r(M-N+P) \end{bmatrix}. \quad (4.13)$$

As a final step, we approximate the true ACF via

$$r(k) \approx \frac{1}{H-k} \sum_{n=k}^H y[n]y[n-k], \quad (4.14)$$

where  $y[H]$  is the final element in the sequence. The entries of  $\mathbf{R}$  are approximated similarly. Assuming  $P > N$ , the associated linear system may be solved using over-determined least squares:

$$\mathbf{a} = -(\mathbf{R}^T \mathbf{R})^{-1} \mathbf{R}^T \mathbf{r}. \quad (4.15)$$

If  $P = N$ , then (4.13) is square and the system is exactly determined. In [143], the authors assume  $P = N$  and  $M = 0$ , where the assumption  $P = N$  is a question of data section and model order, and the assumption of  $M = 0$  assumes the system can be approximated as purely auto-regressive, with no moving average component. Once the vector  $\mathbf{a}$  has been solved for, the “poles” of the system can be inferred [189].

## 4.2 Handling Initial Conditions in Vector Fitting for Real Time Modeling of Power System Dynamics

In this section, we derive the Real-Time Vector Fitting procedure.

### 4.2.1 A New Problem Setting for TDVF

Let us now consider system  $\mathcal{S}$  operating in real time, with input and output measured signals (4.1) collected during system operation. Since data recording may start at an arbitrary time instant when system is not at rest, the output samples  $\mathbf{y}(t)$  may include contributions from both the zero-input and the zero-state response, implying that all initial conditions cannot be considered as vanishing as in (4.3). Moreover, all input channels are expected to be active concurrently. Therefore, the basic TDVF assumptions do not hold and need a generalization.

From now on, we assume a mildly nonlinear systems  $\mathcal{S}$ , whose dynamics can be

approximated [25] by splitting inputs, outputs and states as

$$\begin{aligned}\mathbf{u}(t) &= \mathbf{U}_0 + \tilde{\mathbf{u}}(t), \\ \mathbf{y}(t) &= \mathbf{Y}_0 + \tilde{\mathbf{y}}(t), \\ \mathbf{x}(t) &= \mathbf{X}_0 + \tilde{\mathbf{x}}(t),\end{aligned}\tag{4.16}$$

where

$$\mathbf{U}_0 = \mathbf{u}(0), \quad \mathbf{X}_0 = \mathbf{x}(0), \quad \mathbf{Y}_0 = \mathbf{y}(0)\tag{4.17}$$

are regarded as *non-necessarily* vanishing initial conditions. The evolution of the *small-signal* components  $\tilde{\mathbf{u}}(t)$ ,  $\tilde{\mathbf{y}}(t)$ ,  $\tilde{\mathbf{x}}(t)$  can be accurately related by an LTI operator with transfer function  $\check{\mathbf{H}}(s)$ . Our main objective is to devise a numerical scheme that, based on the samples (4.1), returns an estimate  $\mathbf{H}(s) \approx \check{\mathbf{H}}(s)$  of the small-signal transfer function. This objective is attained by exploiting two generalizations of the basic TDVF scheme:

1. We remove the requirements of pure zero-state conditions by allowing for the presence of nonvanishing initial conditions (4.17). This is addressed in 4.2.2.
2. We allow for all input components  $u_j$  acting concurrently in the training time series, as in common system operation conditions. This is addressed in 4.2.3.

### 4.2.2 Handling Initial Conditions

In this section, we formulate a generalized identification problem that provides an estimate  $\mathbf{H}(s)$  of the small-signal transfer function, assuming non-vanishing initial conditions. Although initial conditions  $\mathbf{U}_0$ ,  $\mathbf{Y}_0$  are known from the training data, no information on the initial state  $\mathbf{X}_0$  is available. Thus, a direct decomposition of  $\mathbf{y}(t)$  into its zero-state and zero-input contributions is generally not possible. This section provides theoretical justification for the proposed RTVF formulation.

In order to characterize the role of the unknown initial state, we first consider a generic LTI system in state-space form:

$$\begin{aligned}\dot{\mathbf{x}}(t) &= \mathbf{A}\mathbf{x}(t) + \mathbf{B}\mathbf{u}(t), \\ \mathbf{y}(t) &= \mathbf{C}\mathbf{x}(t) + \mathbf{D}\mathbf{u}(t),\end{aligned}\tag{4.18}$$

with the only restriction that  $\mathbf{A}$  should be nonsingular. Inserting the signal decom-

position (4.16) into (4.18) leads to

$$\dot{\tilde{\mathbf{x}}}(t) = \dot{\tilde{\mathbf{x}}}(t) = \mathbf{A}(\mathbf{X}_0 + \tilde{\mathbf{x}}(t)) + \mathbf{B}(\mathbf{U}_0 + \tilde{\mathbf{u}}(t)) \quad (4.19)$$

$$\tilde{\mathbf{y}}(t) + \mathbf{Y}_0 = \mathbf{C}(\mathbf{X}_0 + \tilde{\mathbf{x}}(t)) + \mathbf{D}(\mathbf{U}_0 + \tilde{\mathbf{u}}(t)). \quad (4.20)$$

The output (4.20) can be equivalently rewritten by splitting the constant and the time-varying small-signal components as

$$\mathbf{Y}_0 = \mathbf{C}\mathbf{X}_0 + \mathbf{D}\mathbf{U}_0, \quad (4.21)$$

$$\tilde{\mathbf{y}}(t) = \mathbf{C}\tilde{\mathbf{x}}(t) + \mathbf{D}\tilde{\mathbf{u}}(t), \quad \forall t \geq 0. \quad (4.22)$$

Two scenarios are possible:

1. The system is at constant steady-state<sup>1</sup> for  $t = 0$  (equivalently,  $\forall t \leq 0$ ). Under this assumption, all small-signal components vanish for  $t \leq 0$ . Therefore, (4.19) reduces to

$$\mathbf{A}\mathbf{X}_0 + \mathbf{B}\mathbf{U}_0 = \mathbf{0} \rightarrow \mathbf{X}_0 = -\mathbf{A}^{-1}\mathbf{B}\mathbf{U}_0 \quad (4.23)$$

and provides the initial state condition  $\mathbf{X}_0$ . Since  $\mathbf{A}$  is nonsingular, the system has no poles at the origin and supports constant steady-state operation. Combining (4.19) with (4.23), for  $t > 0$ , the small-signal components fulfill the standard dynamic equation

$$\dot{\tilde{\mathbf{x}}}(t) = \mathbf{A}\tilde{\mathbf{x}}(t) + \mathbf{B}\tilde{\mathbf{u}}(t). \quad (4.24)$$

Combining (4.22) and (4.24) provides the small-signal transfer function  $\check{\mathbf{H}}(s)$  in terms of the state-space matrices:

$$\check{\mathbf{H}}(s) = \mathbf{C}(s\mathbb{1} - \mathbf{A})^{-1}\mathbf{B} + \mathbf{D} = \frac{\check{\mathbf{N}}(s)}{\check{D}(s)} \quad (4.25)$$

with  $\check{D}(s) = |s\mathbb{1} - \mathbf{A}|$ . Identification of a rational model for  $\check{\mathbf{H}}(s)$  can be performed by subtracting the initial conditions  $\mathbf{U}_0$ ,  $\mathbf{Y}_0$  from the input and output signals and then applying a zero-state identification scheme, such as basic TDVF, to small-signal components  $\tilde{\mathbf{u}}(t)$ ,  $\tilde{\mathbf{y}}(t)$ .

2. The second scenario is relevant for our application, and it corresponds to the

---

<sup>1</sup>This scenario is common in electronic circuit simulation, where a constant bias is applied first and all initial conditions are found; transient analysis is performed next, starting from the computed initial conditions.

case where the system is *not* operating under constant steady-state conditions for  $t < 0$ . In this setting, (4.23) does not hold and

$$\mathbf{X}_0 \neq -\mathbf{A}^{-1}\mathbf{B}\mathbf{U}_0. \quad (4.26)$$

Therefore, even if the initial conditions  $\mathbf{U}_0$ ,  $\mathbf{Y}_0$  are removed from the input and output signals, the corresponding small-signal output  $\tilde{\mathbf{y}}(t)$  still includes a contribution from the initial state. This contribution is analyzed next.

### Characterization of residual zero-input contributions

Assuming that  $\mathbf{U}_0$  and  $\mathbf{X}_0$  are known, system evolution in terms of small-signal state components is obtained by integrating the dynamic equation (4.19) for  $t > 0$ . For clarity, we perform this integration step-by-step:

$$\dot{\tilde{\mathbf{x}}}(t) = \mathbf{A}(\mathbf{X}_0 + \tilde{\mathbf{x}}(t)) + \mathbf{B}(\mathbf{U}_0 + \tilde{\mathbf{u}}(t)) \quad (4.27)$$

$$e^{-\mathbf{A}t} (\dot{\tilde{\mathbf{x}}}(t) - \mathbf{A}\tilde{\mathbf{x}}(t)) = e^{-\mathbf{A}t} (\mathbf{B}\tilde{\mathbf{u}}(t) + \mathbf{A}\mathbf{X}_0 + \mathbf{B}\mathbf{U}_0) \quad (4.28)$$

$$\int_0^t e^{-\mathbf{A}\tau} (\dot{\tilde{\mathbf{x}}}(\tau) - \mathbf{A}\tilde{\mathbf{x}}(\tau)) d\tau = \int_0^t e^{-\mathbf{A}\tau} (\mathbf{B}\tilde{\mathbf{u}}(\tau) + \mathbf{A}\mathbf{X}_0 + \mathbf{B}\mathbf{U}_0) d\tau \quad (4.29)$$

$$e^{-\mathbf{A}\tau} \tilde{\mathbf{x}}(\tau)|_0^t = \int_0^t e^{-\mathbf{A}\tau} (\mathbf{B}\tilde{\mathbf{u}}(\tau) + \mathbf{A}\mathbf{X}_0 + \mathbf{B}\mathbf{U}_0) d\tau \quad (4.30)$$

$$\tilde{\mathbf{x}}(t) = \int_0^t e^{\mathbf{A}(t-\tau)} (\mathbf{B}\tilde{\mathbf{u}}(\tau) + \mathbf{A}\mathbf{X}_0 + \mathbf{B}\mathbf{U}_0) d\tau \quad (4.31)$$

Analytically integrating the constant RHS terms in (4.31) allows us to write

$$\tilde{\mathbf{x}}(t) = \int_0^t e^{\mathbf{A}(t-\tau)} \mathbf{B}\tilde{\mathbf{u}}(\tau) d\tau + [e^{\mathbf{A}t} - \mathbb{1}] \underbrace{(\mathbf{X}_0 + \mathbf{A}^{-1}\mathbf{B}\mathbf{U}_0)}_{\mathbf{T}_0}, \quad (4.32)$$

where the contribution of the initial state condition is explicit. Note that, in case of steady-state operation for  $t < 0$ , the second term in (4.32) vanishes since  $\mathbf{T}_0 = \mathbf{0}$ , and the corresponding solution reduces to the solution of the small-signal system (4.24). The term  $\mathbf{T}_0$  can thus be considered as the difference between the actual initial state  $\mathbf{X}_0$  and the constant state that would be obtained if the system were operating under steady-state conditions excited by the constant input  $\mathbf{U}_0$ .

Taking the Laplace transform of (4.32) yields

$$\widetilde{\mathbf{X}}(s) = (s\mathbb{1} - \mathbf{A})^{-1} \mathbf{B} \widetilde{\mathbf{U}}(s) + [(s\mathbb{1} - \mathbf{A})^{-1} - s^{-1}\mathbb{1}] \mathbf{T}_0. \quad (4.33)$$

Inserting (4.33) into the output equation (4.22) leads to

$$\tilde{\mathbf{Y}}(s) = \mathbf{C}\tilde{\mathbf{X}}(s) + \mathbf{D}\tilde{\mathbf{U}}(s) = \check{\mathbf{H}}(s)\tilde{\mathbf{U}}(s) + \mathbf{\Gamma}_0(s), \quad (4.34)$$

where  $\check{\mathbf{H}}(s)$  is given by (4.25). Additionally,

$$\mathbf{\Gamma}_0(s) = (\mathbf{C}(s\mathbb{1} - \mathbf{A})^{-1} - s^{-1}\mathbf{C})\mathbf{T}_0 = \frac{\check{\mathbf{G}}(s)}{s \cdot \check{D}(s)}, \quad (4.35)$$

where  $\check{\mathbf{G}}(s)$  is an unknown polynomial vector. Relation (4.34) is therefore equivalent to

$$\tilde{\mathbf{Y}}(s) = \frac{\check{\mathbf{N}}(s)}{\check{D}(s)}\tilde{\mathbf{U}}(s) + \frac{\check{\mathbf{G}}(s)}{s \cdot \check{D}(s)}. \quad (4.36)$$

The two terms in (4.36) share the same denominator  $\check{D}(s)$  up to a pole at  $s = 0$ , which represents the constant contribution of the non-vanishing initial conditions. This observation is the key enabling factor for building a self-consistent vector fitting scheme to estimate model  $\mathbf{H}(s) \approx \check{\mathbf{H}}(s)$ , as it properly takes into account the presence of the additional term  $\mathbf{\Gamma}_0(s)$  in (4.34).

### 4.2.3 The Real-Time Vector Fitting scheme

In this section, we propose our Real-Time Vector Fitting (RTVF) scheme. In particular, our key idea and the proposed generalizations follow:

1. **The key idea** of our method consists of adding to the standard rational transfer function expression an extra term that shares the same denominator  $D(s)$  plus a pole at  $s = 0$ , representing the constant contribution of the non-vanishing initial conditions.

$$\tilde{\mathbf{Y}}(s) \approx \frac{\mathbf{N}(s)}{D(s)}\tilde{\mathbf{U}}(s) + \frac{\mathbf{G}(s)}{s \cdot D(s)}. \quad (4.37)$$

2. Since polynomials  $\mathbf{N}(s)$  and  $D(s)$  are typically expanded in a standard barycentric form as in (4.7) using an initial pole set  $q_n$ , we propose the use of a similar expansion for the components of the unknown vector  $\mathbf{G}(s)$ :

$$G_i(s) = b_i^{(0)} + \sum_{n=1}^N \frac{b_i^{(n)}}{s - q_n} \quad \forall i = 1, \dots, P. \quad (4.38)$$

3. We further propose to account for multiple inputs potentially exciting the sys-

tem simultaneously by applying linear superposition and expressing each output component  $\tilde{Y}_i(s)$  in terms of all input components  $\tilde{U}_j(s)$ .

The above considerations lead us to parameterize and formulate the fitting condition (4.37) as

$$\tilde{Y}_i(s) \approx \sum_{j=1}^P \frac{c_{ij}^{(0)} + \sum_{n=1}^N \frac{c_{ij}^{(n)}}{s - q_n}}{d_0 + \sum_{n=1}^N \frac{d_n}{s - q_n}} \tilde{U}_j(s) + \frac{b_i^{(0)} + \sum_{n=1}^N \frac{b_i^{(n)}}{s - q_n}}{s \cdot \left( d_0 + \sum_{n=1}^N \frac{d_n}{s - q_n} \right)}, \quad \forall i = 1, \dots, P. \quad (4.39)$$

In (4.39), the coefficients  $c_{ij}^{(n)}$  represent the elements in the numerator  $\mathbf{N}(s)$  of the small-signal model transfer function  $\mathbf{H}(s)$  expressed in barycentric form. The coefficients  $d_n$  of the denominator are common to all transfer matrix entries, so that a common pole set is enforced for the model. Finally, the coefficients  $b_i^{(n)}$  provide a parameterization of the zero-input response in barycentric form, as written in (4.37).

Multiplying both sides by the common denominator and taking the inverse Laplace transform leads to the following time-domain fitting condition for  $t \geq 0$ :

$$d_0 \cdot \tilde{y}_i(t) + \sum_{n=1}^N d_n \cdot \tilde{y}_i^{(n)}(t) \approx \sum_{j=1}^P \left[ c_{ij}^{(0)} \cdot \tilde{u}_j(t) + \sum_{n=1}^N c_{ij}^{(n)} \cdot \tilde{u}_j^{(n)}(t) \right] + b_i^{(0)} \cdot \Theta(t) + \sum_{n=1}^N b_i^{(n)} \Theta^{(n)}(t), \quad \forall i = 1, \dots, P, \quad (4.40)$$

where  $\Theta(t)$  is the Heaviside unit step function, filtered input  $\tilde{u}_j^{(n)}(t)$  and output  $\tilde{y}_i^{(n)}(t)$  signals are obtained as in (4.5), and the filtered step function signals are

$$\Theta^{(n)}(t) = \int_0^t e^{q_n(t-\tau)} \Theta(\tau) d\tau. \quad (4.41)$$

#### 4.2.4 Implementation

In this section, we provide a compact and efficient formulation of the least squares formulation at the heart of the RTVF routine. Writing (4.40) for  $t = t_k$ , with  $k = 1, \dots, K$ , leads to the following RTVF condition in matrix form:

$$\boldsymbol{\phi}_i \cdot \mathbf{d} + \sum_{j=1}^P \boldsymbol{\psi}_j \cdot \mathbf{c}_{ij} + \boldsymbol{\beta} \cdot \mathbf{b}_i \approx \mathbf{0} \quad \forall i = 1, 2, \dots, P, \quad (4.42)$$

where the vectors collecting the unknown coefficients are

$$\mathbf{d} = \begin{bmatrix} d_0 \\ \vdots \\ d_N \end{bmatrix}, \mathbf{c}_{ij} = \begin{bmatrix} c_{ij}^{(0)} \\ \vdots \\ c_{ij}^{(N)} \end{bmatrix}, \mathbf{b}_i = \begin{bmatrix} b_i^{(0)} \\ \vdots \\ b_i^{(N)} \end{bmatrix}, \quad (4.43)$$

and where the regressor matrices collecting the filtered signal time samples (according to (4.5)) are defined as

$$\boldsymbol{\phi}_i = - \begin{bmatrix} \tilde{y}_i(t_1) & \tilde{y}_i^{(1)}(t_1) & \dots & \tilde{y}_i^{(N)}(t_1) \\ \vdots & \vdots & \ddots & \vdots \\ \tilde{y}_i(t_K) & \tilde{y}_i^{(1)}(t_K) & \dots & \tilde{y}_i^{(N)}(t_K) \end{bmatrix} \quad (4.44)$$

$$\boldsymbol{\psi}_j = \begin{bmatrix} \tilde{u}_j(t_1) & \tilde{u}_j^{(1)}(t_1) & \dots & \tilde{u}_j^{(N)}(t_1) \\ \vdots & \vdots & \ddots & \vdots \\ \tilde{u}_j(t_K) & \tilde{u}_j^{(1)}(t_K) & \dots & \tilde{u}_j^{(N)}(t_K) \end{bmatrix} \quad (4.45)$$

$$\boldsymbol{\beta} = \begin{bmatrix} 1 & \Theta^{(1)}(t_1) & \dots & \Theta^{(N)}(t_1) \\ \vdots & \vdots & \ddots & \vdots \\ 1 & \Theta^{(1)}(t_K) & \dots & \Theta^{(N)}(t_K) \end{bmatrix}. \quad (4.46)$$

Further, by defining

$$\Delta = [\boldsymbol{\psi}_1 \ \dots \ \boldsymbol{\psi}_P \ \boldsymbol{\beta}], \ \mathbf{a}_i = [\mathbf{c}_{i1}^T \ \dots \ \mathbf{c}_{iP}^T \ \mathbf{b}_i^T]^T \quad (4.47)$$

and collecting all components, (4.42) reveals the bordered-block-diagonal structure of the RTVF least squares system:

$$\begin{bmatrix} \Delta & \mathbf{0} & \dots & \mathbf{0} & \boldsymbol{\phi}_1 \\ \mathbf{0} & \Delta & \dots & \mathbf{0} & \boldsymbol{\phi}_2 \\ \vdots & \vdots & \ddots & \vdots & \vdots \\ \mathbf{0} & \mathbf{0} & \dots & \Delta & \boldsymbol{\phi}_P \end{bmatrix} \begin{bmatrix} \mathbf{a}_1 \\ \mathbf{a}_2 \\ \vdots \\ \mathbf{a}_P \\ \mathbf{d} \end{bmatrix} \approx \mathbf{0}. \quad (4.48)$$

Standard techniques can be employed to avoid the all-zero trivial solution, as explained in [75, 73].

As in standard TDVF, once the set of unknown coefficients is found by solving (4.48), the zeros  $z_n$  of the denominator  $D(s)$  are computed and used as initial poles for the next iteration. The process is repeated until convergence. Pseudocode

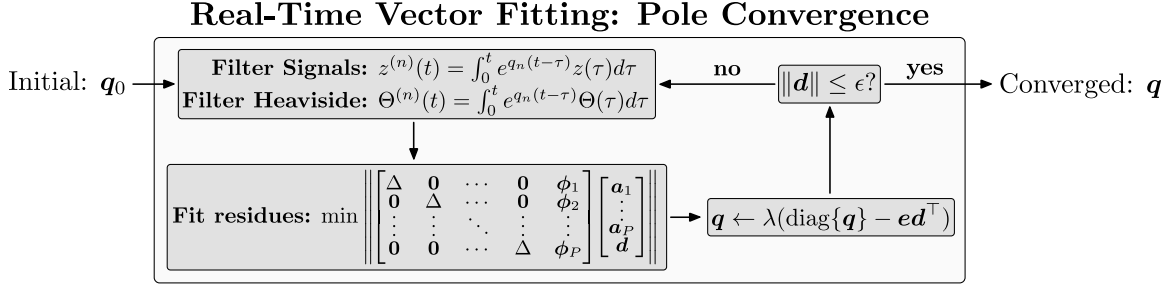


Figure 4-2: Shown is the pole convergence procedure associated with RTVF. In this figure,  $\mathbf{q} = [q_1, \dots, q_N]^T$  is the vector of poles which become increasingly refined as the procedure iterates.

for RTVF is provided in Algorithm 6. The final steps (lines 8–10) estimate the residues of a rational approximation based on the fixed poles obtained from the pole relocation process (lines 1–7). In line 10, the vector  $\tilde{\mathbf{y}}_i$  collects all time samples of the  $i$ -th small-signal output component. Furthermore, Fig. 4-2 graphically portrays the iteration scheme.

---

**Algorithm 6** The RTVF algorithm

---

**Input:** Time samples  $\mathbf{u}(t_k)$ ,  $\mathbf{y}(t_k)$ , sampling frequency  $F_s$ , starting poles  $\{q_1, \dots, q_N\}$ , maximum iteration number  $\nu_{\max}$

**Output:** Estimated transfer function  $\mathbf{H}(s)$

- 1: Compute  $\tilde{\mathbf{u}}(t_k) \leftarrow \mathbf{u}(t_k) - \mathbf{u}(t_1)$ ,  $\tilde{\mathbf{y}}(t_k) \leftarrow \mathbf{y}(t_k) - \mathbf{y}(t_1)$
  - 2: **for**  $\nu = 1, \dots, \nu_{\max}$  **do**
  - 3:   Compute filtered signals  $\tilde{y}_i^{(n)}(t_k)$ ,  $\tilde{u}_i^{(n)}(t_k)$ ,  $\Theta^{(n)}(t_k)$
  - 4:   Build and solve the least squares problem (4.48)
  - 5:   Compute the zeros  $z_n$  of denominator  $D(s)$  in (4.8)
  - 6:   Set  $q_n \leftarrow z_n$
  - 7: **end**
  - 8: Set  $D(s) = 1$
  - 9: Compute filtered signals  $\tilde{u}_i^{(n)}(t_k)$ ,  $\Theta^{(n)}(t_k)$
  - 10: Build matrix  $\Delta$  and solve  $\Delta \mathbf{a}_i \approx \tilde{\mathbf{y}}_i$  for  $i = 1, \dots, P$
  - 11: **return:**  $\mathbf{H}(s) = \mathbf{N}(s)$ , where  $N_{ij}(s)$  is numerator of (4.7)
- 

#### 4.2.5 Numerical Results

##### Consistency

We tested the RTVF consistency by running a systematic experimental campaign over a set of synthetic randomly generated LTI reference systems, with the objective of checking whether RTVF could provide accurate estimates of all system poles. All modeled systems shared the same dynamic order of  $N = 10$ , but had different sizes,

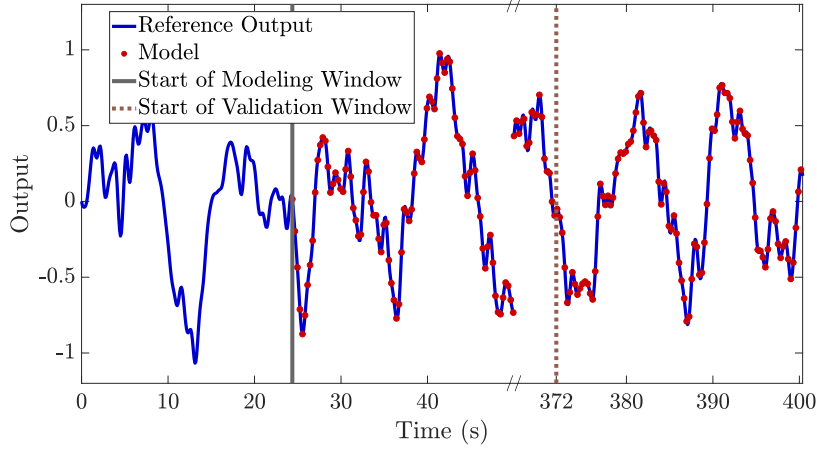


Figure 4-3: Time domain modeling results for a synthetic test case with  $P = 2$ . The modeling window starts after 24 s, the validation window starts at 372 s.

with  $P$  ranging from 2 to 30. The set of input-output data were generated as colored noise which showed a flat power spectrum up to angular frequency  $\omega_{\max}$ , where the fastest pole of the reference system appeared. The sampling frequency was fixed to  $F_s = 10 \omega_{\max}/2\pi$ , and the total number of collected samples was  $K = 5000$  in all cases. The modeling window started at sample  $k = 250$ .

Three metrics were used to assess performance of RTVF:

- the consistency of the pole estimates, as measured by the Hausdorff distance<sup>2</sup>  $d_H(\mathcal{P}, \mathcal{Q})$  between the set of exact poles  $\mathcal{P} = \{p_1, \dots, p_N\}$  of the true system and the set of numerically computed poles  $\mathcal{Q} = \{q_1, \dots, q_N\}$ ;
- the worst-case time domain output error, computed as

$$E_\infty = \max_{i=1, \dots, P} \|\mathbf{y}_i - \check{\mathbf{y}}_i\|_\infty, \quad (4.50)$$

- and the RMS-normalized maximum error, computed as

$$E_\infty^{\text{RMS}} = \max_{i=1, \dots, P} \frac{\|\mathbf{y}_i - \check{\mathbf{y}}_i\|_\infty}{\|\check{\mathbf{y}}_i\|_2}. \quad (4.51)$$

The experiments showed that RTVF recovered the system poles almost exactly, with a set distance  $d_H(\mathcal{P}, \mathcal{Q}) \leq 10^{-10}$  for all 29 test cases. Similar results were ob-

---

<sup>2</sup>The *Hausdorff distance* between two sets  $\mathcal{P}$  and  $\mathcal{Q}$  is defined as

$$d_H(\mathcal{P}, \mathcal{Q}) = \max\{\sup_{p \in \mathcal{P}} \inf_{q \in \mathcal{Q}} \|p - q\|, \sup_{q \in \mathcal{Q}} \inf_{p \in \mathcal{P}} \|p - q\|\}. \quad (4.49)$$

tained from the output errors: both  $E_\infty$  and  $E_\infty^{\text{RMS}}$  were less than  $10^{-11}$ . As Fig. 4-3 shows, there is no practical difference between the model and the output data samples. In this idealized setting, we conclude that the performance of RTVF is excellent across all investigated metrics.

To further test the consistency of RTVF, we simulated the presence of measurement noise on the input and output signals (for the case where  $P = 2$ ,  $N = 10$ ). Signal corruption was performed by adding a vector of zero-mean Gaussian random variables  $\mathbf{x}_n$  to any input or output small-signal vector  $\tilde{\mathbf{x}}$  as

$$\tilde{\mathbf{x}}_N = \tilde{\mathbf{x}} + \mathbf{x}_n, \quad (4.52)$$

with a prescribed signal to noise ratio

$$\alpha = \text{SNR} = 20 \log \frac{\text{RMS}\{\tilde{\mathbf{x}}\}}{\text{RMS}\{\mathbf{x}_n\}}. \quad (4.53)$$

In our experiments, we considered increasing levels of SNR, ranging from 10 to 100, with resolution steps of 2. For each level of SNR, we modeled  $R = 50$  different synthetic systems, and we computed the average *Signal to Error Ratio* (SER) both in time and frequency domain, which is defined as follows. Let  $\mathbf{z}$  be a vector collecting the samples of either a reference time-domain output signal or a target frequency-domain transfer matrix element, and  $\mathbf{z}_M$  the corresponding response of one of the  $R$  models. Then for this signal the SER is defined as

$$\text{SER} = 20 \log \frac{\text{RMS}\{\mathbf{z}\}}{\text{RMS}\{\mathbf{z} - \mathbf{z}_M\}}. \quad (4.54)$$

For any fixed SNR level, we computed the time-domain TD-SER by averaging the performance induced by (4.54) over the  $R$  models and the two output signals. The frequency-domain FD-SER was computed in the same way, by averaging over the transfer matrix elements. These two metrics are shown in the top panel of Fig. 4-4.

The meaning of the SER being above or below the black line threshold is that RTVF is either rejecting or amplifying the presence of the noise on the data, respectively. Since the TD-SER is always above the plane bisector (solid black line), RTVF is able to partially reject the presence of measurements noise in the training data. This noise rejection property is expected, since the basis functions involved in the estimation procedure effectively filter the noisy input and output signals via (4.5). On the other hand, FD-SER follows the bisector almost exactly, confirming also a

good frequency-domain accuracy.

The noise-corrupted training input signals for a representative test case for SNR = 16 are depicted in the middle panel of Fig. 4-4, whereas the corresponding extracted model is validated against the reference time-domain output in the bottom panel. Even with this significant amount of noise, the time-domain prediction capabilities of the model are excellent.

## IEEE 39-Bus System Results

In order to test the performance of RTVF in a simulated power system setting, we collected data from time domain simulations performed on the IEEE 39-Bus New England system. This system includes 10 generators and 19 ZIP loads; the associated load, network, and generator models and numerical parameters were taken directly from [87]. The exact modeling of this network, though, is given in Appendix B.1. Accordingly, each generator was modeled as a 6<sup>th</sup> order synchronous machine with 3<sup>rd</sup> order automatic voltage regulators and power system stabilizers; additionally, each generator was outfitted with a 3<sup>rd</sup> order turbine governor (Type I) [129]. Each generator system, with its three controllers, had a total of 15 dynamical states. The interaction between the generator, its controllers, and the network is shown in Fig. 4-5. All time domain simulations were performed using MATLAB’s DAE solver ode23t by setting relative and absolute error tolerances to  $10^{-7}$  and  $10^{-8}$ , respectively.

**Load Perturbations:** In order to mimic ambient load fluctuations, we applied an Ornstein-Uhlenbeck (OU) process [128] to the active and reactive power demands at each load. The dynamics of these processes are given by  $\tau \dot{u}_p = -u_p + \eta_p$  and  $\tau \dot{u}_q = -u_q + \eta_q$ , where  $\eta_p, \eta_q$  are zero-mean Gaussian variables, and the “load reversal” time constant  $\tau$  was set to 50s. We further applied a low-pass filter (LPF), with a cutoff frequency of  $\sim 9\text{Hz}$ , to the OU variables such that  $\hat{u} = \text{LPF}\{u\}$ . This filtering operation was applied because dynamics above this frequency range become inconsistent with the quasi-stationary phasor approximation used in modeling the network’s dynamics. Therefore, high frequency load behavior is effectively neglected. Finally, these filtered OU variables were parameterized with time variable  $t$  using a cubic spline interpolation and applied to the individual ZIP loads via

$$P(t, V) = P_0(1 + \beta \cdot \hat{u}_p(t)) (a_Z \bar{V}^2 + a_I \bar{V}^1 + a_P \bar{V}^0) \quad (4.55)$$

$$Q(t, V) = Q_0(1 + \beta \cdot \hat{u}_q(t)) (b_Z \bar{V}^2 + b_I \bar{V}^1 + b_P \bar{V}^0), \quad (4.56)$$

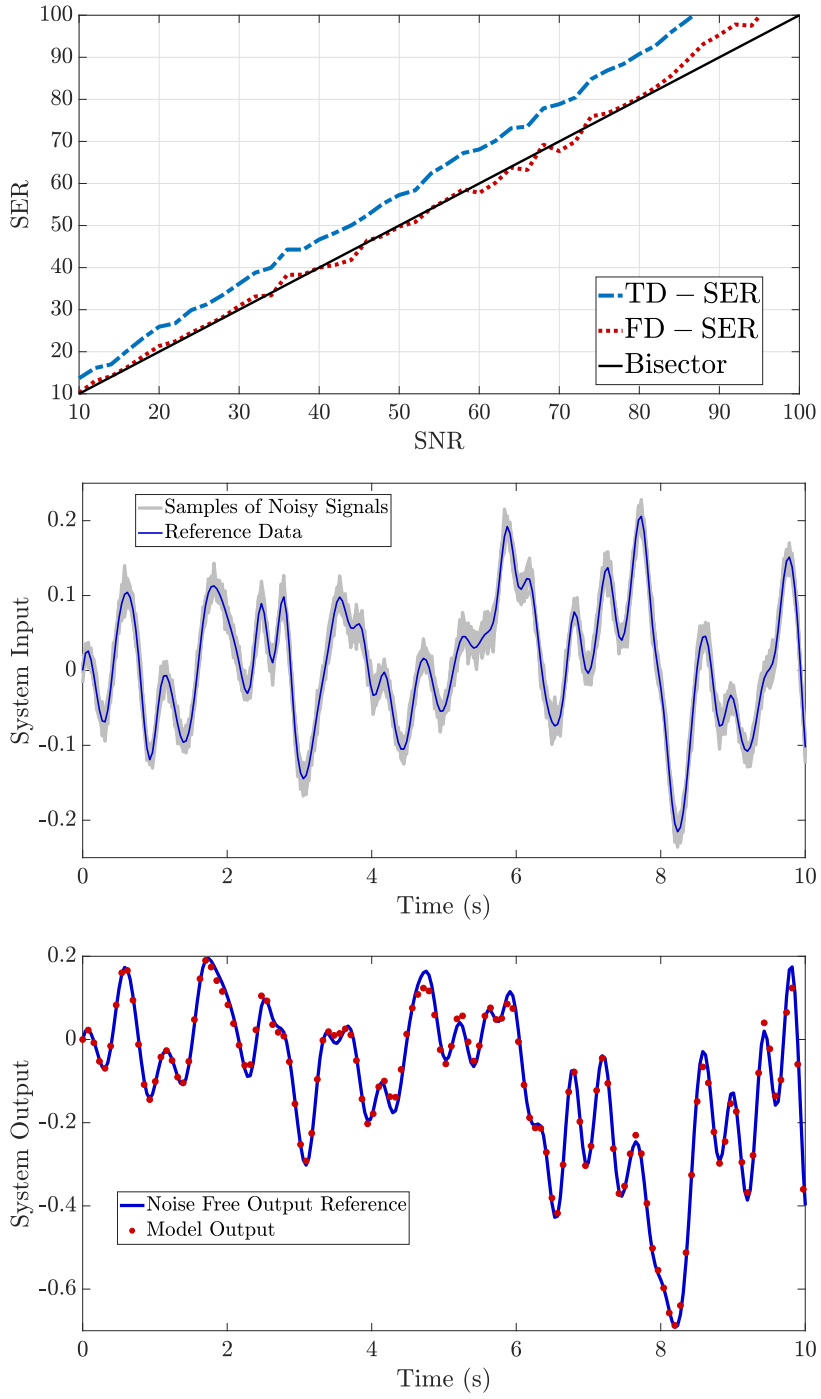


Figure 4-4: Top panel: the trend of TD – SER and FD – SER against the SNR. Middle panel: corrupting one training input signal (solid line) with SNR=16 (a cloud of  $R = 50$  different realizations are depicted in a grey shade). Bottom panel: response of a time domain model extracted from one noisy data realization (SNR=16) compared to the reference noise-free signal.

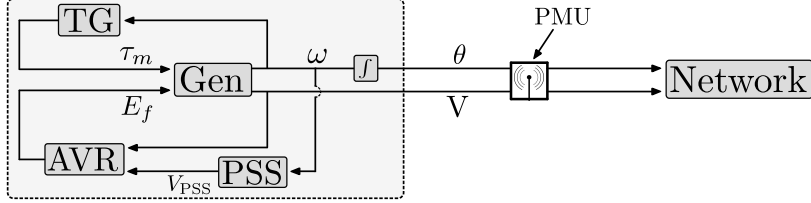


Figure 4-5: Shown is the interaction between the generator, its three controllers, and the network. The PMU collects data at the generator's point of connection.

where  $\bar{V} \equiv V/V_0$ . As a final step, scalar variable  $\beta$  in (4.55)-(4.56) was experimentally tuned to a numerical value of  $\beta = 50$ ; this tuning generated load perturbations whose corresponding network voltage perturbations approximately matched those of real PMU data (in terms of signal strength).

We then applied RTVF to data measured at the machine-network interface in order to model the generator's closed-loop dynamics. For modeling purposes, we treated voltage magnitude  $V(t)$  and voltage phase  $\theta(t)$  signals as inputs, and we treated current magnitude  $I(t)$  and current phase  $\phi(t)$  signals as outputs. The RTVF algorithm sought to generate a MIMO model with  $P = 2$  and various reduced orders  $N$ .

In order to validate the quality of the model generated in the absence of measurement noise, we refer to the time and frequency domain references provided by the exact machine equations. The results are provided in Fig. 4-6. The results show the model accuracy is excellent in both the time and frequency domains, even though the reduced model order (in this case  $N = 9$ ) is less than the machine's true model order ( $\bar{N} = 15$ ).

---

### Algorithm 7 Measurement Noise Application

---

**Input:** Voltage & current signals  $V(t)$ ,  $I(t)$ ,  $\theta(t)$ ,  $\phi(t)$ ; desired SNR

**Output:** Noisy voltage & current signals  $V_n(t)$ ,  $I_n(t)$ ,  $\theta_n(t)$ ,  $\phi_n(t)$

- 1:  $\sigma_{Vn} \leftarrow \text{RMS}\{V(t) - E\{V(t)\}\} \cdot 10^{-\text{SNR}/20}$
- 2:  $\sigma_{In} \leftarrow \text{RMS}\{I(t) - E\{I(t)\}\} \cdot 10^{-\text{SNR}/20}$
- 3:  $V_n(t) \leftarrow V(t) + \sigma_{Vn} \cdot \eta(t)$
- 4:  $I_n(t) \leftarrow I(t) + \sigma_{In} \cdot \eta(t)$
- 5:  $\theta_n(t) \leftarrow \theta(t) + \sigma_{Vn} \cdot \eta(t)/E\{V(t)\}$
- 6:  $\phi_n(t) \leftarrow \phi(t) + \sigma_{In} \cdot \eta(t)/E\{I(t)\}$

**Return:**  $V_n(t)$ ,  $I_n(t)$ ,  $\theta_n(t)$ ,  $\phi_n(t)$

---

**Measurement Noise:** In order to further gauge the practical effectiveness of RTVF, we applied measurement noise to the voltage and current signals measured by the

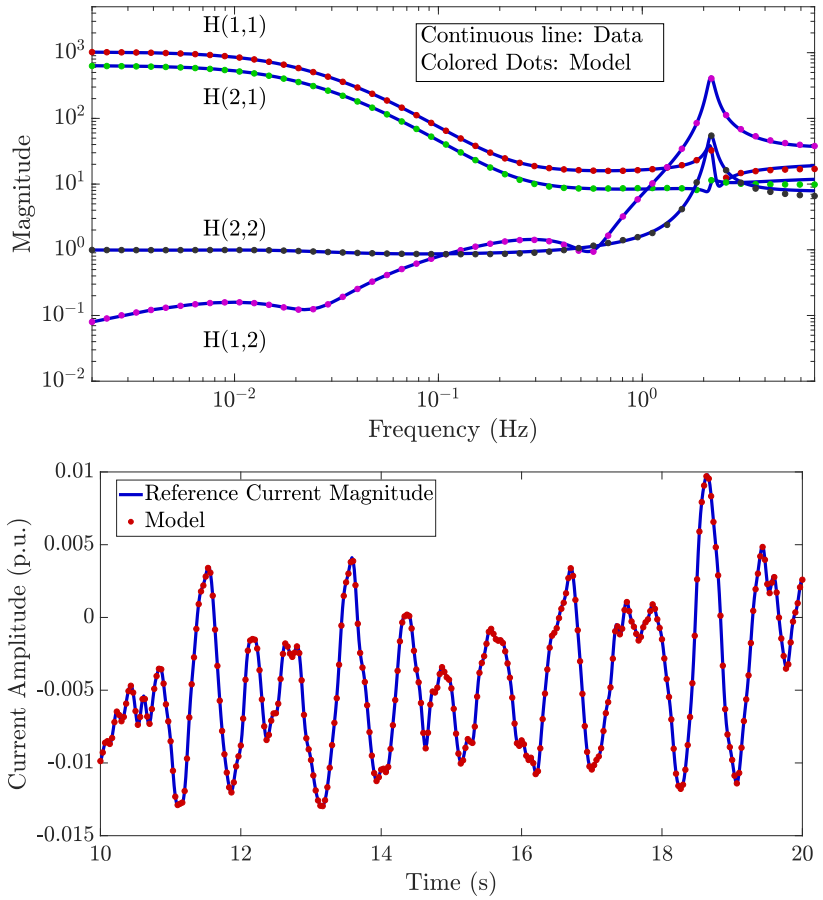


Figure 4-6: Noise-free generator model extraction. Top panel: frequency domain validation of the generator model (order  $N = 9$ ) against exact machine equations. Bottom panel: the time domain validation of the model against the current magnitude reference output.

PMU. To apply this noise, we utilized the procedure outlined in Algorithm 7, where  $\eta(t)$  represents an AWG noise vector. In this algorithm, an SNR is first specified in terms of magnitude (V, I) signals<sup>3</sup>, and the proper amount of noise is then added. Next, noise with an appropriate standard deviation is applied to the phase signals ( $\theta, \phi$ ), such that the total vector error (TVE) in the complex plane would be a circular cloud. In other words, an “equivalent” amount of noise is applied to both the magnitude and phase data, relative to the specified SNR value.

Top and middle panels of Fig. 4-7 report the frequency- and time-domain fitting performance of a RTVF model of order  $N = 7$  obtained for  $\text{SNR} = 32\text{dB}$ . The corresponding noise-corrupted voltage magnitude signals are depicted in the bottom panel. Compared to the performance in the noise-free setting (Fig. 4-6), these results show that the frequency-domain model accuracy is still quite acceptable, and that the accuracy in the time domain seems to be not affected by the presence of noise. Therefore, we conclude that the time prediction capabilities of RTVF models extracted from noisy signals are potentially adequate for power system applications.

### 4.3 The stochastic-RTVF Scheme

In this section, we pose an extension of the RTVF procedure which is suitable for performing real-time predictive modeling of stochastically forced dynamical systems. This new procedure is termed stochastic-RTVF (i.e. sRTVF), and brief test results are presented at the end of the section to showcase its feasibility.

To derive the sRTVF procedure, we consider the practical problem of using vector fitting to identify the dynamics of a system whose output behavior is a function of two components: (i) observable inputs, and (ii) unobservable stochastic inputs. For example, consider the closed loop generator system in Fig. 4-8. Internally, there exists some unobservable, stochastic noise process  $n(t, \xi)$  which is “corrupting” the observed (i.e. measured) dynamics at the terminal of the machine. A blind application of RTVF, with inputs  $V(t), \theta(t)$  and outputs  $I(t), \phi(t)$ , will identify not only the dynamics of the machine, but also the effects of the noise. This is problematic, since most predictive modeling strategies generally seek to identify physical, deterministic dynamics and are unconcerned with the behavior and effects of such noise. This sort of situation is a commonly acknowledged roadblock when it comes to real-time modeling of aggregate load dynamics (e.g. due to random internal switching behavior).

---

<sup>3</sup>Because phase angles drift aggressively, faithfully defining their “signal strength” for noise application purposes is not a straightforward procedure.

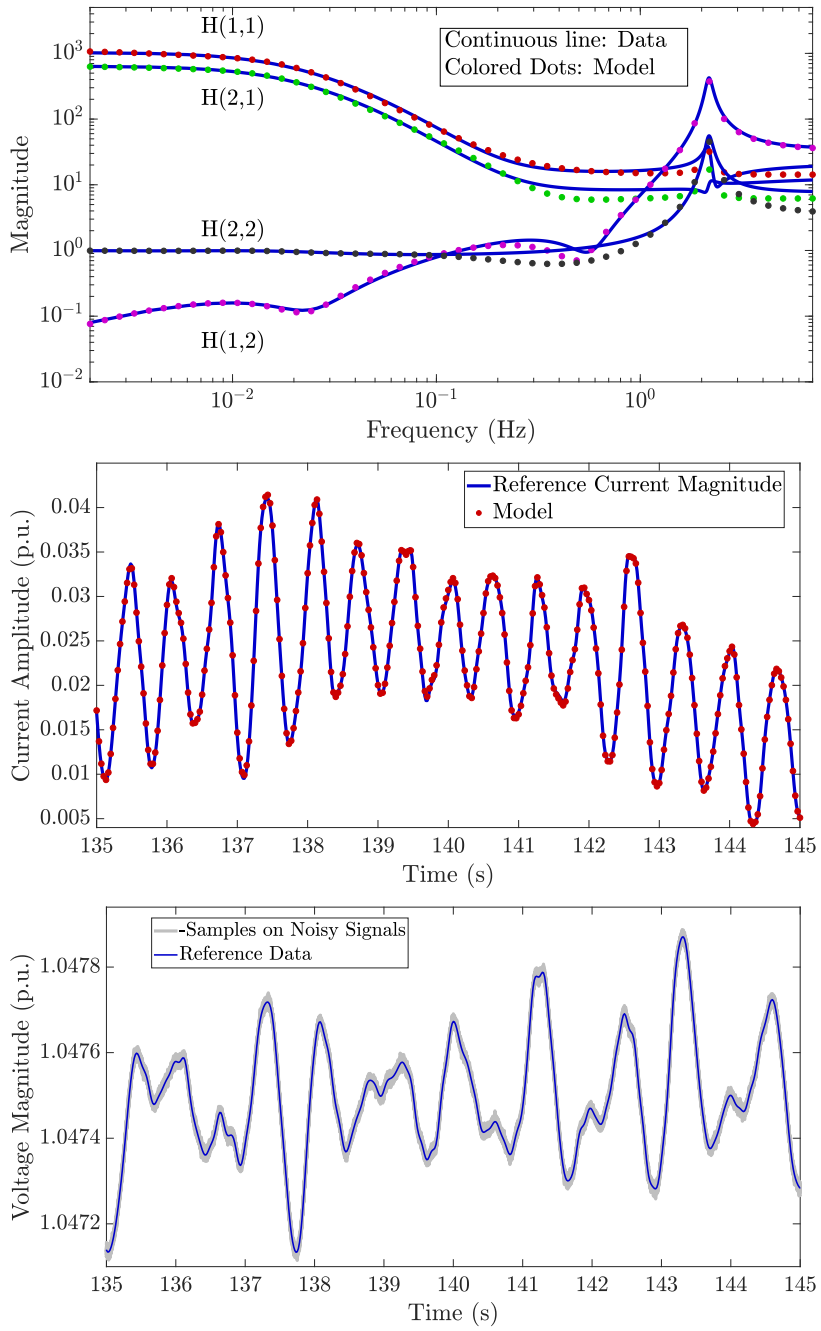


Figure 4-7: Generator model training from noisy data ( $\text{SNR} = 32$ ). Top panel: frequency responses. Middle panel: small signal current magnitude. Bottom panel: noise-corrupted input training signals (samples from a cloud of  $R = 100$  different realizations depicted with a shade of grey).

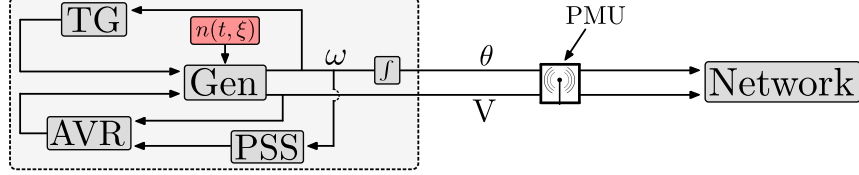


Figure 4-8: Generator System with Observable Stochastic Input

#### 4.3.1 Stochastic Process Characterization

As with any stochastic formulation, we derive the sRTVF under a series of modeling assumptions about the nature of the underlying stochasticity [174]. In doing so, we consider a Wise Sense Stationary (WSS) stochastic processes  $n(t, \xi)$ , where  $E_t\{n(t, \xi)\} = 0$ . That is, the expected value of the process at any given time has 0 mean. If this is a white noise process, then the associated autocorrelation function (ACF)  $R_{n,n}(\tau)$  takes the familiar form

$$R_{n,n}(\tau) = E\{n(t + \tau, \xi)n(t, \xi)\} = \sigma^2 \delta_{t,t+\tau}. \quad (4.57)$$

In other words,  $R_{n,n}(\tau \neq 0) = 0$ . If  $n(t, \xi)$  is used to represent the unobservable stochastic input which we are considering, the restriction that it is fully white is overly restrictive in most practical applications. Therefore, we offer the following definition which effectively relaxes the pure “white” noise assumption.

**Definition 12.** A WSS stochastic process  $n(t, \xi)$  is referred to as a **Relaxed White Noise Process (RWNP)** if, for some sufficiently short time period  $\gamma_t$ , the autocorrelation function satisfies

$$R_{n,n}(\tau) = 0, \quad \forall \tau \geq \gamma_t. \quad (4.58)$$

Therefore, a RWNP may have slight correlation at high frequencies, but is at all lower frequencies uncorrelated. For example, a pure white noise process  $n_p(t, \xi)$  is technically a RWNP with  $\gamma_t = \epsilon \approx 0$ . As another example, assume  $n_f(t, \xi)$  is the result of white noise being passed through a low-pass filter with an *exact* cutoff frequency of  $f_s$  Hz; it is therefore a “colored” noise process. Accordingly,  $n_f(t, \xi)$  is a RWNP with  $\gamma_t = 1/f_s$ . That is,  $R_{n,n}(\tau) = 0$ ,  $\tau \geq 1/f_s$ . Intuitively, low frequency trends (below  $f_s$ ) are still uncorrelated in time.

Finally, we note that if some RWNP  $n(t, \xi)$  satisfies  $E\{n(t + \tau, \xi)n(t, \xi)\} = 0$ ,  $\tau \geq \gamma_t$ , then passing  $n(t, \xi)$  through a causal linear filter  $h(t)$  will not affect this null expectation. That is,  $E\{n(t + \tau, \xi)n_f(t, \xi)\} = 0$ ,  $\tau \geq \gamma_t$ , where  $n_f(t, \xi) = \int_{-\infty}^{\infty} h(\tau)n(t - \tau, \xi)d\tau$ .

$\tau, \xi)$  d $\tau$  for some causal impulse response function  $h(t)$ . The associated proof comes from a direct application of the causality principle.

### 4.3.2 Formulating the sRTVF Procedure

In this subsection, we offer an explicit, step-by-step formulation of the sRTVF formulation. We accordingly consider a system whose linear (or linearized) dynamics may be stated by

$$\begin{aligned}\dot{\mathbf{x}}(t) &= \mathbf{A}\mathbf{x}(t) + \mathbf{B}\mathbf{u}(t) + \mathbf{B}_n\mathbf{n}(t) \\ \mathbf{y}(t) &= \mathbf{C}\mathbf{x}(t) + \mathbf{D}\mathbf{u}(t) + \mathbf{D}_n\mathbf{n}(t),\end{aligned}\tag{4.59}$$

which is both LTI and fully analogous to (4.18). In (4.59), though,  $\mathbf{n}(t)$  is some stochastic and unobservable noise process vector. Specifically, we assume<sup>4</sup> each independent vector entry to be a RWNP with some associated  $\gamma_t$ . As with the RTVF formulation, we decompose all signals into the small-signal and initial condition components:

$$\begin{aligned}\mathbf{u}(t) &= \mathbf{U}_0 + \tilde{\mathbf{u}}(t), \\ \mathbf{n}(t) &= \mathbf{N}_0 + \tilde{\mathbf{n}}(t), \\ \mathbf{y}(t) &= \mathbf{Y}_0 + \tilde{\mathbf{y}}(t), \\ \mathbf{x}(t) &= \mathbf{X}_0 + \tilde{\mathbf{x}}(t).\end{aligned}\tag{4.60}$$

We plug these into the dynamic equations:

$$\dot{\tilde{\mathbf{x}}}(t) = \mathbf{A}(\mathbf{X}_0 + \tilde{\mathbf{x}}(t)) + \mathbf{B}(\mathbf{U}_0 + \tilde{\mathbf{u}}(t)) + \mathbf{B}_n(\mathbf{N}_0 + \tilde{\mathbf{n}}(t))\tag{4.61}$$

$$\mathbf{Y}_0 + \tilde{\mathbf{y}}(t) = \mathbf{C}(\mathbf{X}_0 + \tilde{\mathbf{x}}(t)) + \mathbf{D}(\mathbf{U}_0 + \tilde{\mathbf{u}}(t)) + \mathbf{D}_n(\mathbf{N}_0 + \tilde{\mathbf{n}}(t)).\tag{4.62}$$

At the output, we have constant bias term  $\mathbf{Y}_0 = \mathbf{C}\mathbf{X}_0 + \mathbf{D}\mathbf{U}_0 + \mathbf{D}_n\mathbf{N}_0$ , which we neglect. The small-signal output form is given by

$$\tilde{\mathbf{y}}(t) = \mathbf{C}\tilde{\mathbf{x}}(t) + \mathbf{D}\tilde{\mathbf{u}}(t) + \mathbf{D}_n\tilde{\mathbf{n}}(t),\tag{4.63}$$

where again,  $\tilde{\mathbf{n}}(t)$  is unobservable. As with the RTVF formulation, we assume the presence of non-vanishing ICs, such that  $\mathbf{A}\mathbf{X}_0 + \mathbf{B}\mathbf{U}_0 + \mathbf{B}_n\mathbf{N}_0 \neq \mathbf{0}$ . By collecting the constant terms from (4.61), we follow the exact steps (4.27)-(4.32) from the previous

---

<sup>4</sup>This assumption is motivated by some physical property of the underlying noise process.

section to compute the state response

$$\tilde{\mathbf{x}}(t) = \int_0^t e^{\mathbf{A}(t-\tau)} [\mathbf{B}\tilde{\mathbf{u}}(\tau) + \mathbf{B}_n\tilde{\mathbf{n}}(\tau)] d\tau + [e^{\mathbf{A}t} - \mathbb{1}] \underbrace{(\mathbf{X}_0 + \mathbf{A}^{-1}\mathbf{B}\mathbf{U}_0 + \mathbf{A}^{-1}\mathbf{B}_n\mathbf{N}_0)}_{\mathbf{F}_0}, \quad (4.64)$$

where  $\mathbf{F}_0 \neq \mathbf{0}$ , since the initial conditions are non-vanishing. Taking the Laplace transform of (4.64) and (4.63), we have state and output response expressions:

$$\widetilde{\mathbf{X}}(s) = (s\mathbb{1} - \mathbf{A})^{-1}[\mathbf{B}\widetilde{\mathbf{U}}(s) + \mathbf{B}_n\widetilde{\mathbf{N}}(s)] + [(s\mathbb{1} - \mathbf{A})^{-1} - s^{-1}\mathbb{1}] \mathbf{F}_0 \quad (4.65)$$

$$\begin{aligned} \widetilde{\mathbf{Y}}(s) &= [\mathbf{C}(s\mathbb{1} - \mathbf{A})^{-1}\mathbf{B} + \mathbf{D}] \widetilde{\mathbf{U}}(s) + [\mathbf{C}(s\mathbb{1} - \mathbf{A})^{-1}\mathbf{B}_n + \mathbf{D}_n] \widetilde{\mathbf{N}}(s) \\ &\quad + \mathbf{C}[(s\mathbb{1} - \mathbf{A})^{-1} - s^{-1}\mathbb{1}] \mathbf{F}_0. \end{aligned} \quad (4.66)$$

For clarity, we write  $(s\mathbb{1} - \mathbf{A})^{-1}$  as the canonical ratio of an adjoint and a determinant:

$$(s\mathbb{1} - \mathbf{A})^{-1} = \frac{\text{adj}(s\mathbb{1} - \mathbf{A})}{\det(s\mathbb{1} - \mathbf{A})} \equiv \frac{\mathcal{A}(s)}{\mathcal{D}(s)}. \quad (4.67)$$

Plugging (4.67) into (4.66), we have

$$\begin{aligned} \widetilde{\mathbf{Y}}(s) &= \left[ \frac{\mathbf{C}\mathcal{A}(s)\mathbf{B} + \mathcal{D}(s)\mathbf{D}}{\mathcal{D}(s)} \right] \widetilde{\mathbf{U}}(s) + \left[ \frac{\mathbf{C}\mathcal{A}(s)\mathbf{B}_n + \mathcal{D}(s)\mathbf{D}_n}{\mathcal{D}(s)} \right] \widetilde{\mathbf{N}}(s) \\ &\quad + \left[ \frac{\mathbf{C}(\mathcal{A}(s)s - \mathcal{D}(s)\mathbb{1}) \mathbf{F}_0}{s \cdot \mathcal{D}(s)} \right] \end{aligned} \quad (4.68)$$

$$= \left[ \frac{\mathbf{N}(s)}{\mathcal{D}(s)} \right] \widetilde{\mathbf{U}}(s) + \left[ \frac{\mathbf{N}_n(s)}{\mathcal{D}(s)} \right] \widetilde{\mathbf{N}}(s) + \left[ \frac{\mathbf{H}(s)}{s \cdot \mathcal{D}(s)} \right] \quad (4.69)$$

The key observation here, as with RTVF, is that (i) the input transfer function, (ii) the noise transfer function, and (iii) the element associated with the non-vanishing ICs all share a common set of poles (plus an extra  $s = 0$  pole in the final instance). We now apply the common vector fitting “trick”, i.e. introduce a set of basis poles, and perform a partial fraction expansion of the formulation. In doing so, we assume there are  $P$  observable inputs and  $P$  outputs, but there are  $Q$  unobservable stochastic

inputs, where in theory,  $0 \leq Q \leq \infty$ . We express the  $i^{\text{th}}$  observable output  $\tilde{\mathbf{Y}}_i(s)$  via

$$\begin{aligned} \tilde{\mathbf{Y}}_i(s) = \sum_{j=1}^P & \left[ \frac{c_{ij}^{(0)} + \sum_{n=1}^N \frac{c_{ij}^{(n)}}{s - q_n} \tilde{\mathbf{U}}_j(s)}{d_0 + \sum_{n=1}^N \frac{d_n}{s - q_n}} \right] + \sum_{j=1}^Q & \left[ \frac{h_{ij}^{(0)} + \sum_{n=1}^N \frac{h_{ij}^{(n)}}{s - q_n} \tilde{\mathbf{N}}_j(s)}{d_0 + \sum_{n=1}^N \frac{d_n}{s - q_n}} \right] \\ & + \left[ \frac{b_i^{(0)} + \sum_{n=1}^N \frac{b_i^{(n)}}{s - q_n}}{s \cdot \left( d_0 + \sum_{n=1}^N \frac{d_n}{s - q_n} \right)} \right]. \end{aligned} \quad (4.70)$$

Multiplying through by the common basis poles yields

$$\begin{aligned} \tilde{\mathbf{Y}}_i(s) \left( d_0 + \sum_{n=1}^N \frac{d_n}{s - q_n} \right) = & \sum_{j=1}^P \left[ \left( c_{ij}^{(0)} + \sum_{n=1}^N \frac{c_{ij}^{(n)}}{s - q_n} \right) \tilde{\mathbf{U}}_j(s) \right] \\ & + \sum_{j=1}^Q \left[ \left( h_{ij}^{(0)} + \sum_{n=1}^N \frac{h_{ij}^{(n)}}{s - q_n} \right) \tilde{\mathbf{N}}_j(s) \right] + \frac{1}{s} \left[ b_i^{(0)} + \sum_{n=1}^N \frac{b_i^{(n)}}{s - q_n} \right]. \end{aligned} \quad (4.71)$$

Finally, we take an inverse Laplace transform:

$$\begin{aligned} d_0 \cdot \tilde{y}_i(t) + \sum_{n=1}^N d_n \cdot \tilde{y}_i^{(n)}(t) = & \sum_{j=1}^P \left[ c_{ij}^{(0)} \cdot \tilde{u}_j(t) + \sum_{n=1}^N c_{ij}^{(n)} \cdot \tilde{u}_j^{(n)}(t) \right] \\ & + \sum_{j=1}^Q \left[ h_{ij}^{(0)} \cdot \tilde{n}_j(t) + \sum_{n=1}^N h_{ij}^{(n)} \cdot \tilde{n}_j^{(n)}(t) \right] + \left[ b_i^{(0)} \cdot \Theta(t) + \sum_{n=1}^N b_i^{(n)} \Theta^{(n)}(t) \right], \end{aligned} \quad (4.72)$$

where signal  $z^{(n)}$  is the result of a filtering procedure from (4.5),  $\Theta(t)$  is the Heaviside unit step function, and  $\Theta^n(t)$  is the filtered step function from (4.41). By noting that  $z^{(0)}(t) = z(t)$ , we may state the time domain expression (4.72) more succinctly:

$$\sum_{n=0}^N d_n \tilde{y}_i^{(n)}(t) = \sum_{j=1}^P \left[ \sum_{n=0}^N c_{ij}^{(n)} \tilde{u}_j^{(n)}(t) \right] + \sum_{j=1}^Q \left[ \sum_{n=0}^N h_{ij}^{(n)} \tilde{n}_j^{(n)}(t) \right] + \left[ \sum_{n=0}^N b_i^{(n)} \Theta^{(n)}(t) \right], \quad (4.73)$$

where  $i \in \{1, \dots, P\}$ . Using the previous section's notation, (4.73) may be stated as:

$$\phi_i \mathbf{d} + \sum_{j=1}^P \psi_j \mathbf{c}_{ij} + \sum_{j=1}^Q \chi_j \mathbf{h}_{ij} + \boldsymbol{\beta} \mathbf{b} \approx \mathbf{0}, \quad i \in \{1, \dots, P\}. \quad (4.74)$$

In (4.74), we leverage four data matrices:  $\phi_i$ ,  $\psi_j$  and  $\beta$  from (4.44)-(4.46); and

$$\chi_j = \begin{bmatrix} \tilde{n}_j(t_1) & \tilde{n}_j^{(1)}(t_1) & \cdots & \tilde{n}_j^{(N)}(t_1) \\ \vdots & \vdots & \ddots & \vdots \\ \tilde{n}_j(t_K) & \tilde{n}_j^{(1)}(t_K) & \cdots & \tilde{n}_j^{(N)}(t_K) \end{bmatrix}. \quad (4.75)$$

Expression (4.74) also uses four coefficient vectors:

$$\mathbf{d} = \begin{bmatrix} d_0 \\ \vdots \\ d_N \end{bmatrix}, \mathbf{c}_{ij} = \begin{bmatrix} c_{ij}^{(0)} \\ \vdots \\ c_{ij}^{(N)} \end{bmatrix}, \mathbf{h}_{ij} = \begin{bmatrix} h_{ij}^{(0)} \\ \vdots \\ h_{ij}^{(N)} \end{bmatrix}, \mathbf{b}_i = \begin{bmatrix} b_i^{(0)} \\ \vdots \\ b_i^{(N)} \end{bmatrix}. \quad (4.76)$$

We use the proposed notation, along with  $\Delta$  and  $\mathbf{a}$  from (4.47), to construct system

$$\begin{bmatrix} \Delta & \mathbf{0} & \cdots & \mathbf{0} & \phi_1 \\ \mathbf{0} & \Delta & \cdots & \mathbf{0} & \phi_2 \\ \vdots & \vdots & \ddots & \vdots & \vdots \\ \mathbf{0} & \mathbf{0} & \cdots & \Delta & \phi_P \end{bmatrix} \begin{bmatrix} \mathbf{a}_1 \\ \mathbf{a}_2 \\ \vdots \\ \mathbf{a}_P \\ \mathbf{d} \end{bmatrix} + \begin{bmatrix} \Lambda & \mathbf{0} & \cdots & \mathbf{0} \\ \mathbf{0} & \Lambda & \cdots & \mathbf{0} \\ \vdots & \vdots & \ddots & \vdots \\ \mathbf{0} & \mathbf{0} & \cdots & \Lambda \end{bmatrix} \begin{bmatrix} \mathbf{e}_1 \\ \mathbf{e}_2 \\ \vdots \\ \mathbf{e}_P \end{bmatrix} \approx \mathbf{0}, \quad (4.77)$$

where  $\Lambda = [\chi_1 \cdots \chi_Q]$  and  $\mathbf{e}_i = [\mathbf{h}_{i1}^T \cdots \mathbf{h}_{iQ}^T]^T$ ,  $i \in \{1, \dots, P\}$ . As a reminder,  $P$  denotes the number of observable inputs and  $Q$  denotes the number of unobservable stochastic inputs. We note that (4.77) is fully analogous to (4.48) from the RTVF formulation, except with the addition of noise terms (contained in  $\Lambda$ ).

At this point, we digress slightly and rewrite the data ‘‘matrices’’ as general functions of time. That is,

$$\phi_i(t) = - \begin{bmatrix} \tilde{y}_i(t) & \tilde{y}_i^{(1)}(t) & \cdots & \tilde{y}_i^{(N)}(t) \end{bmatrix} \quad (4.78)$$

$$\psi_j(t) = \begin{bmatrix} \tilde{u}_j(t) & \tilde{u}_j^{(1)}(t) & \cdots & \tilde{u}_j^{(N)}(t) \end{bmatrix} \quad (4.79)$$

$$\chi_j(t) = \begin{bmatrix} \tilde{n}_j(t) & \tilde{n}_j^{(1)}(t) & \cdots & \tilde{n}_j^{(N)}(t) \end{bmatrix} \quad (4.80)$$

$$\beta(t) = \begin{bmatrix} 1 & \Theta^{(1)}(t) & \cdots & \Theta^{(N)}(t) \end{bmatrix} \quad (4.81)$$

We do the same for the “big” data matrices:

$$\boldsymbol{\Delta}(t) = \begin{bmatrix} \boldsymbol{\psi}_1(t) & \cdots & \boldsymbol{\psi}_P(t) & \boldsymbol{\beta}(t) \end{bmatrix} \quad (4.82)$$

$$\boldsymbol{\Lambda}(t) = \begin{bmatrix} \boldsymbol{\chi}_1(t) & \cdots & \boldsymbol{\chi}_Q(t) \end{bmatrix}. \quad (4.83)$$

We apply these changes to (4.77), which is now, effectively, transformed into an underdetermined system of equations (for any single time realization  $t = t_0$ ):

$$\begin{bmatrix} \boldsymbol{\Delta}(t) & \mathbf{0} & \cdots & \mathbf{0} & \boldsymbol{\phi}_1(t) \\ \mathbf{0} & \boldsymbol{\Delta}(t) & \cdots & \mathbf{0} & \boldsymbol{\phi}_2(t) \\ \vdots & \vdots & \ddots & \vdots & \vdots \\ \mathbf{0} & \mathbf{0} & \cdots & \boldsymbol{\Delta}(t) & \boldsymbol{\phi}_P(t) \end{bmatrix} \begin{bmatrix} \mathbf{a}_1 \\ \mathbf{a}_2 \\ \vdots \\ \mathbf{a}_P \\ \mathbf{d} \end{bmatrix} + \begin{bmatrix} \boldsymbol{\Lambda}(t) & \mathbf{0} & \cdots & \mathbf{0} \\ \mathbf{0} & \boldsymbol{\Lambda}(t) & \cdots & \mathbf{0} \\ \vdots & \vdots & \ddots & \vdots \\ \mathbf{0} & \mathbf{0} & \cdots & \boldsymbol{\Lambda}(t) \end{bmatrix} \begin{bmatrix} \mathbf{e}_1 \\ \mathbf{e}_2 \\ \vdots \\ \mathbf{e}_P \end{bmatrix} \approx \mathbf{0}. \quad (4.84)$$

We define a column vector of output functions similarly:

$$\mathbf{y}(t) = [ y_1(t) \ y_2(t) \ \cdots \ y_P(t) ]^T. \quad (4.85)$$

Next, we shift this sequence backwards in time by some  $\delta t$ , and multiply through using a Hadamard product, and take the expected value of each row:

$$\begin{aligned} \mathbb{E} \left\{ \mathbf{y}(t - \delta t) \odot \left( \begin{bmatrix} \boldsymbol{\Delta}(t) & \mathbf{0} & \cdots & \mathbf{0} & \boldsymbol{\phi}_1(t) \\ \mathbf{0} & \boldsymbol{\Delta}(t) & \cdots & \mathbf{0} & \boldsymbol{\phi}_2(t) \\ \vdots & \vdots & \ddots & \vdots & \vdots \\ \mathbf{0} & \mathbf{0} & \cdots & \boldsymbol{\Delta}(t) & \boldsymbol{\phi}_P(t) \end{bmatrix} \begin{bmatrix} \mathbf{a}_1 \\ \mathbf{a}_2 \\ \vdots \\ \mathbf{a}_P \\ \mathbf{d} \end{bmatrix} \right. \right. \\ \left. \left. + \begin{bmatrix} \boldsymbol{\Lambda}(t) & \mathbf{0} & \cdots & \mathbf{0} \\ \mathbf{0} & \boldsymbol{\Lambda}(t) & \cdots & \mathbf{0} \\ \vdots & \vdots & \ddots & \vdots \\ \mathbf{0} & \mathbf{0} & \cdots & \boldsymbol{\Lambda}(t) \end{bmatrix} \begin{bmatrix} \mathbf{e}_1 \\ \mathbf{e}_2 \\ \vdots \\ \mathbf{e}_P \end{bmatrix} \right) \right\} \approx \mathbf{0}. \quad (4.86) \end{aligned}$$

This simply multiplies the  $i^{\text{th}}$  function  $y_i(t - \delta t)$  through the  $i^{\text{th}}$  row of (4.84) and takes the expected value. For example, in the first row,  $\mathbb{E}\{y_1(t - \delta t) \cdot \boldsymbol{\Delta}(t)\}$ ,  $\mathbb{E}\{y_1(t - \delta t) \cdot \boldsymbol{\phi}_1(t)\}$ , etc. The correlation between the shifted output  $y_i$  and (i) the filtered input and Heaviside signals of  $\boldsymbol{\Delta}$ , (ii) the filtered output of  $\boldsymbol{\phi}$ , and (iii) the filtered

noise of  $\Lambda$  are given by

$$\mathbf{R}_{\Delta,y_i}(\delta t) = \text{E} \{y_i(t - \delta t)\Delta(t)\} \quad (4.87)$$

$$\mathbf{R}_{\phi_i,y_i}(\delta t) = \text{E} \{y_i(t - \delta t)\phi_i(t)\} \quad (4.88)$$

$$\mathbf{R}_{\Lambda,y_i}(\delta t) = \text{E} \{y_i(t - \delta t)\Lambda(t)\}. \quad (4.89)$$

When computing the correlation between the output and the filtered noise  $\Lambda$  in (4.89), we seek to invoke a causality principle: future values of noise cannot be correlated with past values of the output. Since the noise process of  $\Lambda$  has been filtered, though, present values of filtered noise are a function of past values of noise.

In order to cancel out this correlation term, we must shift the output sufficiently far backwards in time. For example, in the Yule-Walker method, the discrete time ARMA model of (4.10) writes the output  $y[n]$  as a sum of stochastic inputs  $u[n]$  shifted backwards in time by up to  $M$  steps (up to  $u[n-M]$ ). Therefore, when simplifying the correlation relation from (4.11) to (4.12), the correlating output sequence is shifted backwards to  $y[n-k]$ ,  $k > M$ .

In the continuous time relation of (4.84), the system is assumed stable, and so all filtering effects exponentially decay as  $t \rightarrow \infty$ . Therefore, in the limit, the correlation between the filtered noise sequence and the shifted output  $\mathbf{R}_{\Lambda,y_i}(\delta t) = \text{E} \{y_i(t - \delta t)\Lambda(t)\}$  will decay to  $\mathbf{0}$ :

$$\lim_{\delta t \rightarrow \infty} \mathbf{R}_{\Lambda,y_i}(\delta t) = \mathbf{0}. \quad (4.90)$$

Practically speaking, though, the effects of the noise will decay much sooner than  $\delta t = \infty$ . If the slowest pole in the system has a time constant of  $\tau_s$ , then the noise effects will decay to less than 1% of their initially contributing influence after just  $5\tau_s$ . Therefore, we enforce the following approximating heuristic:

$$\mathbf{R}_{\Lambda,y_i}(\delta t) \approx \mathbf{0}, \quad \delta t \geq \eta\tau_s, \quad (4.91)$$

where time constant  $\tau_s$  is associated with the slowest pole, and  $\eta$  controls the amount

of noise decay which is desired. Due to (4.91), relation (4.86) simplifies to

$$\begin{bmatrix} \mathbf{R}_{\Delta,y_1}(\delta t) & \mathbf{0} & \cdots & \mathbf{0} & \mathbf{R}_{\phi_1,y_1}(\delta t) \\ \mathbf{0} & \mathbf{R}_{\Delta,y_2}(\delta t) & \cdots & \mathbf{0} & \mathbf{R}_{\phi_2,y_2}(\delta t) \\ \vdots & \vdots & \ddots & \vdots & \vdots \\ \mathbf{0} & \mathbf{0} & \cdots & \mathbf{R}_{\Delta,y_P}(\delta t) & \mathbf{R}_{\phi_P,y_P}(\delta t) \end{bmatrix} \begin{bmatrix} \mathbf{a}_1 \\ \mathbf{a}_2 \\ \vdots \\ \mathbf{a}_P \\ \mathbf{d} \end{bmatrix} \approx \mathbf{0}, \quad \delta t \geq \eta\tau_s. \quad (4.92)$$

Assuming the correlation time shift is larger than  $\eta\tau_s$ , the noise terms vanish entirely. What is truly useful is that the expectation operator kills off *all* of the noise terms. In formulating this procedure, we assumed there were  $Q$  of these noise injections, where  $0 \leq Q \leq \infty$ . Thus, we make no assumption about how many noise terms there are, or how they enter into the state space model. We simply assume their present values are uncorrelated with previous values of the output.

As written, we note that (4.92) evaluated for a single value of  $\delta t$  is severely under-determined. Thus, we need to evaluate the expression for many values of  $\delta t \geq \eta\tau_s$ . In order to make the formulation similar to the canonical RTVF formulation, we define tall, skinny vectors  $\hat{\mathbf{R}}_{\Delta,y_i}$  and  $\hat{\mathbf{R}}_{\phi_i,y_i}$  which are simply the evaluation of the auto/cross-correlation functions for a variety of time shifts:

$$\hat{\mathbf{R}}_{\Delta,y_i} = \begin{bmatrix} \mathbf{R}_{\Delta,y_i}(\delta t = \eta\tau_s + \gamma) \\ \mathbf{R}_{\Delta,y_i}(\delta t = \eta\tau_s + 2\gamma) \\ \vdots \\ \mathbf{R}_{\Delta,y_i}(\delta t = \eta\tau_s + \mathcal{K}\gamma) \end{bmatrix}, \quad \hat{\mathbf{R}}_{\phi_i,y_i} = \begin{bmatrix} \mathbf{R}_{\phi_i,y_i}(\delta t = \eta\tau_s + \gamma) \\ \mathbf{R}_{\phi_i,y_i}(\delta t = \eta\tau_s + 2\gamma) \\ \vdots \\ \mathbf{R}_{\phi_i,y_i}(\delta t = \eta\tau_s + \mathcal{K}\gamma) \end{bmatrix}. \quad (4.93)$$

We note that constant  $\mathcal{K}$ , seen in the bottom rows of (4.93), serves a similar function to the value  $K$  in RTVF from (4.44)-(4.46), as they both quantify the number of data points used in constructing the data matrices. While  $K$  specifies the number of data points pulled from the filtered signals,  $\mathcal{K}$  specifies the number of times we evaluate the correlation function for different time shifts  $\gamma$ . Inserting (4.93) into (4.92) yields

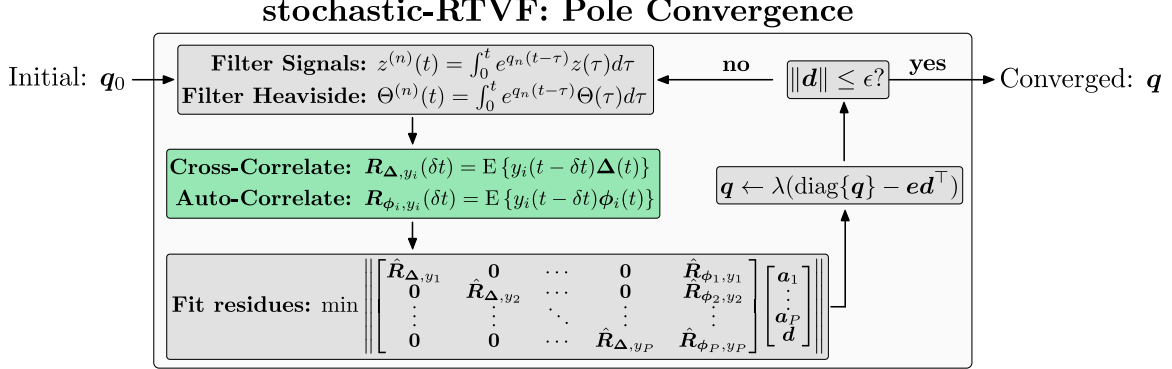


Figure 4-9: Shown is the pole convergence procedure associated with sRTVF. In this figure,  $\mathbf{q} = [q_1, \dots, q_N]^T$  is the vector of poles which becomes increasingly refined as the procedure iterates. The green box performs the cross- and auto-correlation calculations from (4.87)-(4.88).

the following linear system:

$$\begin{bmatrix} \hat{\mathbf{R}}_{\Delta,y_1} & 0 & \cdots & 0 & \hat{\mathbf{R}}_{\phi_1,y_1} \\ 0 & \hat{\mathbf{R}}_{\Delta,y_2} & \cdots & 0 & \hat{\mathbf{R}}_{\phi_2,y_2} \\ \vdots & \vdots & \ddots & \vdots & \vdots \\ 0 & 0 & \cdots & \hat{\mathbf{R}}_{\Delta,y_P} & \hat{\mathbf{R}}_{\phi_P,y_P} \end{bmatrix} \begin{bmatrix} a_1 \\ a_2 \\ \vdots \\ a_P \\ d \end{bmatrix} = 0_v, \quad (4.94)$$

which can be solved via conventional overdetermined least squares methods.

### Computing the Final Residues

Once the sRTVF algorithm has converged, the final step is to compute the model residues (i.e. zeros). At convergences,  $\mathcal{D}(s) = 1$ , so there is no filtering needed of the output signals. Therefore  $\Delta\mathbf{a}_i + \boldsymbol{\phi}_i\mathbf{d} + \boldsymbol{\Lambda}\mathbf{e}_1 \approx \mathbf{0}$  simplifies down to  $\Delta\mathbf{a}_i + y_i(t) + \boldsymbol{\Lambda}\mathbf{e}_1 \approx \mathbf{0}$ . To eliminate the noise terms, we once again apply the correlation trick, i.e.  $E\{y_i(t - \delta t) \cdot (\Delta\mathbf{a}_i + y_i(t) + \boldsymbol{\Lambda}\mathbf{e}_1)\} \approx \mathbf{0}$ . Distributing out the expected value operator yields

$$E\{y_i(t - \delta t) \cdot \Delta\mathbf{a}_i\} + E\{y_i(t - \delta t) \cdot y_i(t)\} + \cancel{E\{y_i(t - \delta t) \cdot \boldsymbol{\Lambda}\mathbf{e}_1\}} \approx \mathbf{0}, \delta t \geq \eta\tau_s. \quad (4.95)$$

Therefore, the final linear system which needs to be solved is  $\hat{\mathbf{R}}_{\Delta,y_i}\mathbf{a}_i = -\hat{\mathbf{R}}_{y_i,y_i}$ . Fig. 4-9 graphically portrays the iterative scheme associated with the sRTVF procedure.

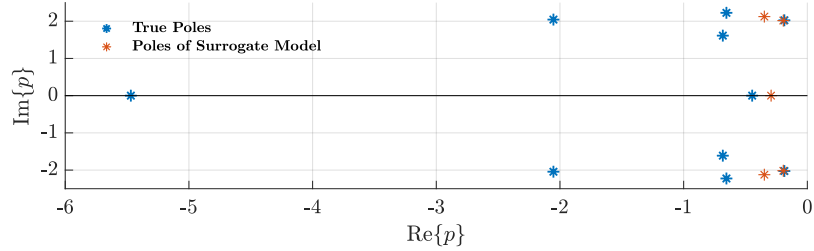


Figure 4-10: Shown are the true poles  $p$  of the 10<sup>th</sup> order synthetic system. Also shown are the surrogate poles identified by the sRTVF procedure.

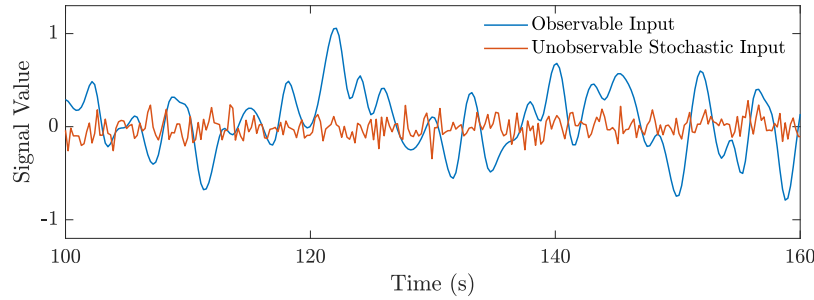


Figure 4-11: Shown are both of the inputs concurrently applied to the synthetic system. Only the observable blue curve is used by the vector fitting algorithm.

### 4.3.3 Illustrative Test Results

In order to showcase the feasibility of the sRTVF approach, we present an illustrative test result on a synthetic, 10<sup>th</sup> order linear system with one observable input, one unobservable stochastic input, and one observable output. Therefore, from a physical point of view, this is a MISO system, but from a modeling perspective, this is a SISO system (since one of the inputs is unobservable and not incorporated). The true, physical poles of this system are plotted in Fig. 4-10.

In running the sRTVF procedure, we sought to identify an  $N = 5^{\text{th}}$  order surrogate model of the system dynamics. After simulating with the observable and unobservable input signals shown in Fig. 4-11, the sRTVF procedure was applied with  $\mathcal{K} = 500$  evaluations of the correlations functions (see (4.93)). The time shift correlation parameter  $\gamma$  from (4.93) was simply set equal to the inverse of the sampling frequency. The surrogate poles identified by sRTVF are shown in Fig. 4-10. The poles with the lowest damping ratio (i.e. closest to the  $j\omega$  axis) are identified almost exactly. While the fitting is not perfect, the resulting surrogate model shows excellent time domain predictive modeling capabilities, as showcased by Fig. 4-12.

Finally, Fig. 4-13 compares the magnitude response of the true FRF with that of the identified surrogate model. At low frequencies (i.e. below 1 Hz), the surrogate

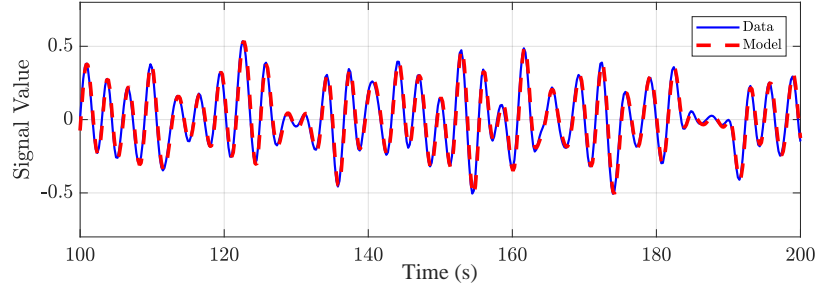


Figure 4-12: The blue curve represents the data measured at the output terminal of the system. The dashed red curve was generated by feeding the measured input data into the identified sRTVF model and simulating forward in time. Clearly, there is a high degree of agreement between the measured output and the predicted output data.

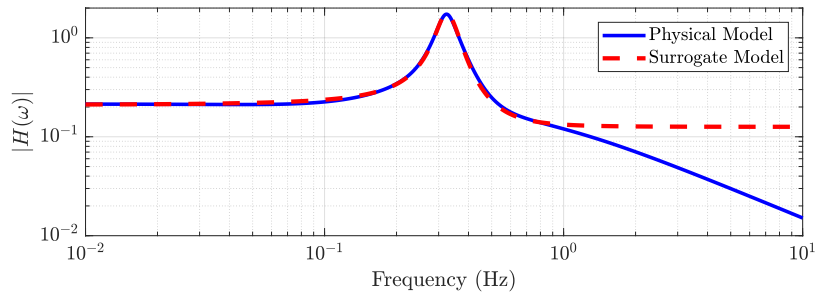


Figure 4-13: Shown is a comparison between the true 10<sup>th</sup> order FRF and the surrogate 5<sup>th</sup> order FRF, as identified by the sRTVF procedure.

model shows a high degree of accuracy.

# Chapter 5

## Accelerating Probabilistic Steady State Operational Analysis of Electrical Distribution Networks

In this chapter, we speed up the probabilistic analysis of steady state power flow models in distribution grids. In the first section, we provide the mathematical background which will be necessary for solving the problems considered in this chapter. The second section of this chapter will address the probabilistic power flow problem, while the third section will address the probabilistic state estimation problem.

### 5.1 Mathematical Background

This section will offer power flow and state estimation methodologies suitable for single phase networks. Later in this chapter, these methodologies will be extended to include three-phase networks.

**Remark 4.** *Throughout this thesis, the notation  $\mathbf{A}^{-1}\mathbf{b}$  (where  $\mathbf{A}$  is an invertible matrix and  $\mathbf{b}$  is a suitably sized vector) should always be interpreted as a “linear system solve” of system  $\mathbf{Ax} = \mathbf{b}$  for some vector  $\mathbf{x}$  (as opposed to performing the computation of matrix inverse  $\mathbf{A}^{-1}$ , followed by a matrix-vector product).*

#### 5.1.1 Standard Network Model Statement

In defining a suitable network for the power flow and state estimation problems, we assume there is one unique bus which represents the distribution network substation

(i.e. point of common coupling). When defining the model for a single-phase network, researchers often denote its graph  $G(\mathcal{V}, \bar{\mathcal{E}})$ , with edge set  $\bar{\mathcal{E}}$ ,  $|\bar{\mathcal{E}}| = m$ , vertex set  $\mathcal{V}$ ,  $|\mathcal{V}| = n$ , and signed nodal incidence matrix  $\bar{E} \in \mathbb{R}^{m \times n}$ .

**Remark 5.** For notational clarity, when defining variables which *include* the substation node, an overline will be used. For instance,  $\bar{E}$  contains all network nodes, including the substation.

The nodal admittance (“Y-bus”) matrix takes the form

$$\bar{Y}_b = \bar{E}^T Y_l \bar{E} + \bar{Y}_s, \quad (5.1)$$

where  $Y_l \in \mathbb{C}^{m \times m}$  and  $\bar{Y}_s \in \mathbb{C}^{n \times n}$  are the diagonal line and shunt admittance matrices, respectively. In this network, we define  $\bar{\mathbf{V}} e^{j\bar{\boldsymbol{\theta}}} \in \mathbb{C}^n$  and  $\bar{\mathbf{I}} e^{j\bar{\boldsymbol{\phi}}} \in \mathbb{C}^n$  as the nodal voltage and nodal current injection phasor vectors, respectively, where  $\bar{\mathbf{V}}, \bar{\boldsymbol{\theta}}, \bar{\mathbf{I}}, \bar{\boldsymbol{\phi}} \in \mathbb{R}^n$ . These vectors satisfy  $\bar{\mathbf{I}} e^{j\bar{\boldsymbol{\phi}}} = \bar{Y}_b \bar{\mathbf{V}} e^{j\bar{\boldsymbol{\theta}}}$ .

### 5.1.2 The Power Flow Problem

In this network, the *deterministic* power flow problem seeks to determine the nodal voltage phasors which satisfy a set of nonlinear power flow equations. In polar form, the active and reactive power flow equations [69] at node  $i$  are written as

$$P_i = V_i \sum_{k \in \mathcal{V}} V_k (G_{ik} \cos(\theta_{ik}) + B_{ik} \sin(\theta_{ik})) \quad (5.2a)$$

$$Q_i = V_i \sum_{k \in \mathcal{V}} V_k (G_{ik} \sin(\theta_{ik}) - B_{ik} \cos(\theta_{ik})), \quad (5.2b)$$

where  $B_{ik} = \text{Im}\{\bar{Y}_b^{(ik)}\}$  and  $G_{ik} = \text{Re}\{\bar{Y}_b^{(ik)}\}$  are susceptance and conductance values, respectively. Nonlinear system (5.2) may be extended to include a full network of nodes by writing the nodal power flow equations as

$$\bar{\mathbf{S}}(\bar{\mathbf{x}}) = \begin{bmatrix} \text{Re}\{\text{diag}(\bar{\mathbf{V}} e^{j\bar{\boldsymbol{\theta}}})(\bar{Y}_b \bar{\mathbf{V}} e^{j\bar{\boldsymbol{\theta}}})^*\} \\ \text{Im}\{\text{diag}(\bar{\mathbf{V}} e^{j\bar{\boldsymbol{\theta}}})(\bar{Y}_b \bar{\mathbf{V}} e^{j\bar{\boldsymbol{\theta}}})^*\} \end{bmatrix}, \quad (5.3)$$

writing the vector of voltage magnitude and phase angle variables as

$$\bar{\mathbf{x}} = [\bar{\mathbf{V}}^T, \bar{\boldsymbol{\theta}}^T]^T \in \mathbb{R}^{2n}, \quad (5.4)$$

and writing the vector of nodal power injections as

$$\bar{\mathbf{s}} = [\bar{\mathbf{P}}^T, \bar{\mathbf{Q}}^T]^T \in \mathbb{R}^{2n}. \quad (5.5)$$

The resulting system may be compactly written as

$$\bar{\mathbf{s}} = \bar{\mathbf{S}}(\bar{\mathbf{x}}). \quad (5.6)$$

**Definition 13.** A *power flow solution* is any vector  $\bar{\mathbf{x}}$  satisfying

$$\{\bar{\mathbf{x}} \in \mathbb{R}^{2n} \mid \|\bar{\mathbf{S}}(\bar{\mathbf{x}}) - \bar{\mathbf{s}}\| < \epsilon\}. \quad (5.7)$$

In practice, a power flow solver attempts to minimize residual function  $\bar{\mathbf{g}}(\bar{\mathbf{x}}) \equiv \bar{\mathbf{S}}(\bar{\mathbf{x}}) - \bar{\mathbf{s}}$ , which codifies the mismatch between the specified and the predicted nodal power injections. Since power injection is only specified at a subset of nodes (i.e. not the substation), the residual to be minimized reduces to

$$\mathbf{g}(\mathbf{x}) \equiv \mathbf{S}(\mathbf{x}) - \mathbf{s}. \quad (5.8)$$

We note that  $\mathbf{x} = [\mathbf{V}^T, \boldsymbol{\theta}^T]^T$  is equivalent to  $\bar{\mathbf{x}}$ , but with the feeder voltage (magnitude and phase) deleted. Similarly,  $\mathbf{S}(\cdot)$  and  $\mathbf{s}$  correspond to the power flow functions and injections, respectively, at all buses in the network *except* the feeder bus.

In the *probabilistic* power flow problem, there is uncertainty in the value of the loads in  $\mathbf{s}$ ; this uncertainty is parameterized by some distribution vector  $\boldsymbol{\xi} \in \mathbb{R}^t$  via  $\mathbf{s}(\boldsymbol{\xi})$ , where generally  $t \ll 2n$ , depending on the number of uncertain loads. The PPF solver thus seeks to map the input distribution on the power injections to an output distribution on power flow solutions (i.e. voltage profiles) by solving  $\mathbf{S}(\mathbf{x}) - \mathbf{s}(\boldsymbol{\xi}) = \mathbf{0}$ , as in [167].

### 5.1.3 Standard Numerical Solution Technique for Power Flow

A power flow solver seeks to minimize the residual (5.8) of the nonlinear power flow equations. This system represents an equal number of equations and unknowns. Newton-Raphson iterations are most commonly used to solve this system:

$$\begin{aligned} \text{Solve: } \mathbf{J}(\mathbf{x}^{(i)})\Delta\mathbf{x}^{(i)} &= -\mathbf{g}(\mathbf{x}^{(i)}), \\ \mathbf{x}^{(i+1)} &\leftarrow \mathbf{x}^{(i)} + \Delta\mathbf{x}^{(i)}, \end{aligned} \quad (5.9)$$

where  $\mathbf{J}(\mathbf{x}^{(i)})$  is the *reduced* power flow Jacobian (RPFJ) matrix, which is typically constructed using the summation of explicit partial derivative terms [69]. In [23], however, Bolognani and D'orfler propose a novel Jacobian structure:

$$\mathbf{J}(\mathbf{x}^{(i)}) = (\langle \text{diag}(\mathbf{I}e^{-j\phi}) \rangle + \langle \text{diag}(\mathbf{V}e^{j\theta}) \rangle N \langle Y_b \rangle) R(\mathbf{V}e^{j\theta}). \quad (5.10)$$

The terms  $R(\cdot)$ ,  $N$ , and  $\langle \cdot \rangle$  are given in [23] and contextually demonstrated in (5.11):

$$\langle \text{diag}(\mathbf{I}e^{-j\phi}) \rangle = \begin{bmatrix} \text{Re}\{\text{diag}(\mathbf{I}e^{-j\phi})\} & \text{Im}\{\text{diag}(\mathbf{I}e^{-j\phi})\} \\ -\text{Im}\{\text{diag}(\mathbf{I}e^{-j\phi})\} & \text{Re}\{\text{diag}(\mathbf{I}e^{-j\phi})\} \end{bmatrix} \quad (5.11a)$$

$$\langle \text{diag}(\mathbf{V}e^{j\theta}) \rangle = \begin{bmatrix} \text{Re}\{\text{diag}(\mathbf{V}e^{j\theta})\} & -\text{Im}\{\text{diag}(\mathbf{V}e^{j\theta})\} \\ \text{Im}\{\text{diag}(\mathbf{V}e^{j\theta})\} & \text{Re}\{\text{diag}(\mathbf{V}e^{j\theta})\} \end{bmatrix} \quad (5.11b)$$

$$N \langle Y_b \rangle = \begin{bmatrix} E^T Y_l^g E & -E^T Y_l^b E - Y_s^b \\ -E^T Y_l^b E - Y_s^b & -E^T Y_l^g E \end{bmatrix} \quad (5.11c)$$

$$R(\mathbf{V}e^{j\theta}) = \begin{bmatrix} \text{diag}(\cos(\theta)) & -\text{Im}\{\text{diag}(\mathbf{V}e^{j\theta})\} \\ \text{diag}(\sin(\theta)) & \text{Re}\{\text{diag}(\mathbf{V}e^{j\theta})\} \end{bmatrix}, \quad (5.11d)$$

where  $\mathbf{V}e^{j\theta}$ ,  $\mathbf{I}e^{-j\phi}$  are appropriately reduced voltage, current vectors. The diagonal matrices  $Y_s^b = \text{Im}\{Y_s\}$ ,  $Y_l^g = \text{Re}\{Y_l\}$ , and  $Y_l^b = \text{Im}\{Y_l\}$  come from the “reduced” Y-bus matrix:

$$Y_b = E^T Y_l E + Y_s. \quad (5.12)$$

Matrix  $E$  comes from eliminating the root node column  $c_1$  of the full incidence matrix:  $\bar{E} = [c_1 \ E]$ .

#### 5.1.4 Additional State Estimation Equations

When solving the state estimation equations, we will consider three types of measurements: power injections, power line flows, and voltage magnitudes. The nodal active and reactive power injection functions are given by (5.3), although in this subsection, we assume the slack bus voltage is given, and we will write the reduced power injection equations as a function of the reduced voltage vector:  $\mathbf{S}(\mathbf{x})$ .

Next, we define the power line flow<sup>1</sup> function  $\mathbf{F}(\mathbf{x})$ . On each line, there are two

---

<sup>1</sup>The power injection equations (5.2) and (5.3) historically called the “power flow” or “load flow” equations, even though they solve for power injections. In the state estimation problem, we consider

potential flow functions: from the “sending” end to the “receiving” end, and vice versa. Without loss of generality, we assume measurement flow devices are only located on the sending end of the lines. We thus define flow function

$$\mathbf{F}(\mathbf{x}) = \begin{bmatrix} \text{Re}\{\text{diag}(\bar{E}_1 \bar{\mathbf{V}} e^{j\bar{\theta}})(Y_l \bar{E} \bar{\mathbf{V}} e^{j\bar{\theta}})^*\} \\ \text{Im}\{\text{diag}(\bar{E}_1 \bar{\mathbf{V}} e^{j\bar{\theta}})(Y_l \bar{E} \bar{\mathbf{V}} e^{j\bar{\theta}})^*\} \end{bmatrix}, \quad (5.13)$$

where matrix  $\bar{E}_1 = (|\bar{E}| + \bar{E})/2$  selects sending end voltages. For completion, we also define the voltage magnitude function  $\mathbf{M}(\mathbf{x})$ , which simply selects voltage magnitude coordinates:

$$\mathbf{M}(\mathbf{x}) = \mathbf{V}. \quad (5.14)$$

As written,  $\mathbf{S}(\mathbf{x})$ ,  $\mathbf{F}(\mathbf{x})$ ,  $\mathbf{M}(\mathbf{x})$  return *all* (non-reduced) network injections, flows, and voltage magnitudes. At the physical locations where these quantities are not measured, the corresponding equations from these functions will be eventually removed.

### 5.1.5 Power System State Estimation

In the state estimation problem, we seek to construct the unknown state vector  $\mathbf{x}$  from a set of noisy (or incomplete) measurements in order to minimize a residual cost function. In this paper, we assume there are three types of measurements: voltage magnitudes, power flows, and power injections.

1.  $\mathbf{M}$ ,  $|\mathbf{M}| = \mathbf{m}$ , is the set of voltage *magnitudes* which are measured. The associated magnitude residual function is  $\mathbf{m}_i(\mathbf{x})$ , and  $\check{\mathbf{m}}_i = \check{\mathbf{V}}_i$  is the  $i^{\text{th}}$  magnitude measurement.
2.  $\mathbf{F}$ ,  $|\mathbf{F}| = \mathbf{f}$ , is the set of active and reactive power line *flows* that are measured. The flow residual function is  $\mathbf{f}_i(\mathbf{x})$  and  $\check{\mathbf{f}}_i$  is the  $i^{\text{th}}$  power flow measurement.
3.  $\mathbf{S}$ ,  $|\mathbf{S}| = \mathbf{s}$ , is the set of active and reactive power *injections* that are measured. The associated residual function is  $\mathbf{s}_i(\mathbf{x})$ , and  $\check{\mathbf{s}}_i$  is the  $i^{\text{th}}$  injection measurement.

---

true “flow” measurements. To differentiate between the two, the power flow equations will be typically referred to as power injections equations, while the flow equations (i.e. (5.13)) will *always* be referred to as “power line flow” equations.

Each residual function takes the form of a predictive function of the state  $\mathbf{x}$  minus a measurement:

$$\mathbf{m}_i(\mathbf{x}) = \mathbf{M}_i(\mathbf{x}) - \check{\mathbf{m}}_i, \quad i \in \mathbb{M} \quad (5.15a)$$

$$\mathbf{f}_i(\mathbf{x}) = \mathbf{F}_i(\mathbf{x}) - \check{\mathbf{f}}_i, \quad i \in \mathbb{F} \quad (5.15b)$$

$$\mathbf{s}_i(\mathbf{x}) = \mathbf{S}_i(\mathbf{x}) - \check{\mathbf{s}}_i, \quad i \in \mathbb{S}. \quad (5.15c)$$

We concatenate these residual functions (5.15) into vector  $\mathbf{r}(\mathbf{x})$ :

$$\mathbf{r}(\mathbf{x}) = [\mathbf{m}(\mathbf{x})^T, \mathbf{f}(\mathbf{x})^T, \mathbf{s}(\mathbf{x})^T]^T. \quad (5.16)$$

The typical state estimator seeks to minimize the unconstrained function  $K(\mathbf{x})$  over the field  $\mathbf{x}$ :

$$\min_{\mathbf{x}} K(\mathbf{x}) = \min_{\mathbf{x}} \frac{1}{2} \mathbf{r}(\mathbf{x})^T \boldsymbol{\Sigma}^{-1} \mathbf{r}(\mathbf{x}), \quad (5.17)$$

where  $\boldsymbol{\Sigma}$  is the diagonal covariance matrix associated with the concatenated measurement vector  $\check{\mathbf{r}} = [\check{\mathbf{m}}^T, \check{\mathbf{f}}^T, \check{\mathbf{g}}^T]^T$ .

**Definition 14.** *Vector  $\check{\mathbf{r}}$  is referred to as a **measurement profile**.*

**Assumption 2.** *The substation voltage is known and therefore not included as an unknown variable in the state estimator.*

Due to measurement redundancy, the DSSE residual equations (5.16) are typically cast as an *overdetermined* set of nonlinear equations [169], i.e., the associated DSSE problem (5.17) has a unique, generally nonzero solution. This paper targets the situation proposed in [110], where the DSSE problem is technically overdetermined, but a subset of the pseudo-measurements are extremely uncertain (with uniform distribution). Thus, our proposed APSE will sample from this uncertain measurement space and produce rapid DSSE system solves.

**Assumption 3.** *The DSSE equations (5.16) are overdetermined, and (5.17) has a unique minimizer, but a subset of the measurements are highly uncertain with uniform distribution.*

Defining  $p \equiv n - 1$ , which is the number of unknown *complex* voltages, Assumptions 2 and 3 necessitate  $\mathbb{m} + \mathbb{f} + \mathbb{s} > 2p$ .

### 5.1.6 Numerical State Estimation Solution Techniques

In solving the state estimation problem (5.17), the first order optimality condition of  $\partial K(\mathbf{x})/\partial \mathbf{x}_i = 0, \forall \mathbf{x}$  must be satisfied. Employing Gauss-Newton, we linearize  $\mathbf{r}(\mathbf{x}_0 + \Delta\mathbf{x}) \approx \mathbf{r}(\mathbf{x}_0) + \mathbf{J}_r \Delta\mathbf{x}$ , where  $\mathbf{x} = \mathbf{x}_0 + \Delta\mathbf{x}$  and  $\mathbf{J}_r = \frac{\partial \mathbf{r}(\mathbf{x})}{\partial \mathbf{x}} = [\mathbf{J}_m^T, \mathbf{J}_f^T, \mathbf{J}_s^T]^T$ . Approximating,

$$K(\mathbf{x}) \approx \frac{1}{2} (\mathbf{r}_0 + \mathbf{J}_r \Delta\mathbf{x})^T \Sigma^{-1} (\mathbf{r}_0 + \mathbf{J}_r \Delta\mathbf{x}) \equiv \tilde{K}(\Delta\mathbf{x}). \quad (5.18)$$

Optimality condition  $\partial \tilde{K}(\Delta\mathbf{x})/\partial \Delta\mathbf{x} = 0$  is satisfied by

$$\mathbf{G}(\mathbf{x}_0) \Delta\mathbf{x} = -\mathbf{J}_r^T \Sigma^{-1} \mathbf{r}(\mathbf{x}_0). \quad (5.19)$$

where  $\mathbf{G}(\mathbf{x}_0) = \mathbf{J}_r^T \Sigma^{-1} \mathbf{J}_r$ . The associated iterative state estimation solution scheme becomes

$$\mathbf{x}^{(k+1)} = \mathbf{x}^{(k)} - \mathbf{G}(\mathbf{x}^{(k)})^{-1} \mathbf{J}_r^T \Sigma^{-1} \mathbf{r}(\mathbf{x}^{(k)}). \quad (5.20)$$

#### Alternative Solution via QR Factorization

In many applications, the “gain” matrix  $\mathbf{G}(\mathbf{x})$  can be poorly conditioned, so it is desirable to avoid solving the associated linear system in (5.20) directly. As an alternative, we consider the over-determined and weighted linear system of equations

$$\Sigma^{-\frac{1}{2}} \mathbf{J}_r \Delta\mathbf{x} = -\Sigma^{-\frac{1}{2}} \mathbf{r}(\mathbf{x}_0). \quad (5.21)$$

Factoring  $\Sigma^{-\frac{1}{2}} J_r$  into the product of an orthogonal matrix  $\mathcal{Q}$  and upper right triangular matrix  $\mathcal{R}$ , i.e.  $\mathcal{Q}\mathcal{R} = \Sigma^{-\frac{1}{2}} J_r$ , the iterative scheme (5.20) updates to

$$\mathbf{x}^{(k+1)} = \mathbf{x}^{(k)} - \mathcal{R}^{-1} (\mathcal{Q}^T \Sigma^{-\frac{1}{2}} \mathbf{r}(\mathbf{x}^{(k)})). \quad (5.22)$$

In the absence of poorly conditioned numerics, (5.20) and (5.22) take the same step and should converge to the same solution.

**Definition 15.** We define the standard iterative algorithm (5.22) as the Gauss-Newton via QR (**GNvQR**) solution technique.

### 5.1.7 Neumann Series Expansion of a Perturbed Matrix

In this thesis, we make use of the following standard result. Consider linear system

$$(\mathbf{A} + \epsilon \mathbf{D})\mathbf{x} = \mathbf{b} \quad (5.23)$$

where  $\mathbf{A}$  is a constant matrix,  $\epsilon \mathbf{D}$  is a *changing* perturbation matrix with some small scalar  $\epsilon$ , and  $\mathbf{b}$  is a *changing* right hand side. The  $k^{\text{th}}$  Neumann series expansion of the matrix  $(\mathbf{A} + \epsilon \mathbf{D})^{-1}$  can be used to approximate the solution  $\mathbf{x}$ :

$$\mathbf{x} \approx \sum_{i=0}^k (-1)^i (\mathbf{A}^{-1} \epsilon \mathbf{D})^i \mathbf{A}^{-1} \mathbf{b} + \mathcal{O}(\epsilon^{k+1}). \quad (5.24)$$

The series (5.24) converges when  $\epsilon < 1/\rho(\mathbf{A}^{-1} \mathbf{D})$  [55], where  $\rho(\cdot)$  is the spectral radius operator. To efficiently compute (5.24), one can first decompose  $\mathbf{A}$  into its LU factors. Then, each instance of  $\mathbf{A}^{-1}$  can be implemented with efficient system solves by using the LU factors in standard forward-elimination and back-substitution routines. After initializing  $\mathbf{z}^{(0)} = \mathbf{x}^{(0)}$  by solving  $\mathbf{L}\mathbf{U}\mathbf{x}^{(0)} = \mathbf{b}$ , one can then iterate until the desired accuracy is reached:

$$\begin{aligned} \text{Solve: } \mathbf{L}\mathbf{U}\mathbf{z}^{(i+1)} &= \epsilon \mathbf{D}\mathbf{z}^{(i)} \\ \mathbf{x}^{(i+1)} &\leftarrow \mathbf{x}^{(i)} + (-1)^i \mathbf{z}^{(i+1)}. \end{aligned} \quad (5.25)$$

**Remark 6.** The complexity of a single iteration is  $\mathcal{O}(n^2)$  when  $\mathbf{A}$  and  $\mathbf{D}$  are dense, and it is  $\mathcal{O}(n)$  when they are sparse.

### 5.1.8 Projection Based Model Order Reduction

A standard way to further speed up the solution of system (5.23) involves looking for a solution  $\hat{\mathbf{x}} \in \mathbb{R}^q$  in a low dimensional subspace. One may represent the solution

$$\mathbf{x} \approx \mathbb{V}\hat{\mathbf{x}} \quad (5.26)$$

as a linear combination of columns of an orthonormal projection operator  $\mathbb{V} \in \mathbb{R}^{n \times q}$ ,  $q \ll n$ . The approximate solution can be obtained by efficiently solving the reduced system

generated by a standard Galerkin testing [206]:

$$(\hat{\mathbf{A}} + \epsilon \hat{\mathbf{D}}) \hat{\mathbf{x}} = \hat{\mathbf{b}}, \quad (5.27)$$

where  $\hat{\mathbf{A}} = \mathbb{V}^T \mathbf{A} \mathbb{V} \in \mathbb{R}^{q \times q}$ ,  $\hat{\mathbf{D}} = \mathbb{V}^T \mathbf{D} \mathbb{V} \in \mathbb{R}^{q \times q}$  and  $\hat{\mathbf{b}} = \mathbb{V}^T \mathbf{b} \in \mathbb{R}^q$ . The literature on projection based model order reduction provides many options for constructing operator  $\mathbb{V}$ . Later in this paper, we will modify and make use of some of the techniques (here combined and summarized in Algorithm 8) and theoretical results in [42] and in [54] for dynamic update of parameterized reduced order models.

---

**Algorithm 8** Model Order Reduction with Dynamic Update

---

- 1:  $\mathbf{x} \leftarrow$  Solve full order system (5.23), e.g. with Neumann (5.25)
  - 2:  $\mathbb{V} \leftarrow \mathbf{x}/\|\mathbf{x}\|$ ,  $\hat{\mathbf{A}} \leftarrow \mathbb{V}^T \mathbf{A} \mathbb{V}$
  - 3: **for** each new  $\mathbf{D}$  and/or  $\mathbf{b}$  **do**
  - 4:    $\hat{\mathbf{D}} \leftarrow \mathbb{V}^T \mathbf{D} \mathbb{V}$ ,  $\hat{\mathbf{b}} \leftarrow \mathbb{V}^T \mathbf{b}$
  - 5:    $\hat{\mathbf{x}} \leftarrow$  Solve Reduced System (5.27)
  - 6:   **if**  $\|(\mathbf{A} + \epsilon \mathbf{D}) \mathbb{V} \hat{\mathbf{x}} - \mathbf{b}\| >$  tolerance **then**
  - 7:      $\mathbf{x} \leftarrow$  Solve full order system (5.23)
  - 8:      $\mathbf{v} \leftarrow \mathbf{x} - \mathbb{V} \mathbb{V}^T \mathbf{x}$                $\triangleright$  remove projection into  $\mathbb{V}$
  - 9:      $\mathbb{V} \leftarrow [\mathbb{V} \ \mathbf{v}/\|\mathbf{v}\|]$                $\triangleright$  extend subspace
  - 10:     $\hat{\mathbf{A}} \leftarrow \begin{bmatrix} \hat{\mathbf{A}} & \mathbb{V}^T \mathbf{A} \mathbf{v} \\ \mathbf{v}^T \mathbf{A} \mathbb{V} & \mathbf{v}^T \mathbf{A} \mathbf{v} \end{bmatrix}$   $\triangleright$  update reduced model
- 

## 5.2 Accelerated Probabilistic Power Flow via Model Order Reduction and Neumann Expansion

### 5.2.1 Computationally Efficient Power Flow Solution via Neumann Series Expansion

The primary computational bottleneck in the power flow problem is solving (5.9). In this subsection, we show how to solve system (5.9) efficiently in  $\mathcal{O}(n)$  operations via Neumann series expansion iterations (5.25). Effectively, this is accomplished by putting Jacobian (5.10) into framework (5.23). We further propose practical convergence criteria. Finally, we outline the power flow algorithm and offer an extension to three-phase systems.

## Neumann Series Expansion Applied to Power Flow

We rewrite linear system (5.9) as two sub-systems:

$$(\langle \text{diag}(\tilde{\mathbf{I}}^*) \rangle + \langle \text{diag}(\tilde{\mathbf{V}}) \rangle N \langle E^T Y_l E + Y_s \rangle) \mathbf{y} = \mathbf{b} \quad (5.28)$$

$$R(\tilde{\mathbf{V}}) \Delta \mathbf{x} = \mathbf{y}, \quad (5.29)$$

where, for convenience,  $\mathbf{b} = -\mathbf{g}(\mathbf{x})$ ,  $\tilde{\mathbf{V}} = \mathbf{V} e^{j\theta}$ ,  $\tilde{\mathbf{I}} = \mathbf{I} e^{j\phi}$ .

**Remark 7.** System (5.29) can be solved in  $\mathcal{O}(n)$ .

Considering (5.28), we multiply both sides by  $\langle \text{diag}(\tilde{\mathbf{V}}) \rangle^{-1}$  to yield

$$\left( \underbrace{N \langle E^T Y_l E + Y_s \rangle}_{\mathcal{L}\mathcal{U}} + \underbrace{\langle \text{diag}(\tilde{\mathbf{V}}) \rangle^{-1} \langle \text{diag}(\tilde{\mathbf{I}}^*) \rangle}_{\mathcal{D}} \right) \mathbf{y} = \underbrace{\langle \text{diag}(\tilde{\mathbf{V}}) \rangle^{-1} \mathbf{b}}_{\mathbf{b}}. \quad (5.30)$$

**Remark 8.** Matrix  $N \langle E^T Y_l E + Y_s \rangle$  will always be symmetric in a per-unitized network. Therefore, we perform an  $LDL^T$  decomposition, and assign  $\mathcal{L} = L$  and  $\mathcal{U} = DL^T$ . There might also be orthogonal permutation matrix  $\mathcal{P}$ , such that

$$\mathcal{P}^T (N \langle E^T Y_l E + Y_s \rangle) \mathcal{P} = \mathcal{L}\mathcal{U}. \quad (5.31)$$

**Remark 9.** Both  $\mathcal{D}$  and  $\mathbf{b}$  in (5.30) can be computed in  $\mathcal{O}(n)$ .

In summary, in  $\mathcal{O}(n)$  operations, we can express (5.9) as

$$(\mathcal{L}\mathcal{U} + \mathcal{D}) \mathbf{y} = \mathbf{b}, \quad (5.32)$$

via (5.30), where  $\mathcal{L}$ ,  $\mathcal{U}$  are lower and upper triangular matrices respectively. Since the  $\mathcal{L}\mathcal{U}$  factors are functions of network admittance parameters and topology, their values are constant at each iteration. When considering the most efficient way to solve (5.32), we note that matrix  $\mathcal{D}$  is composed of load currents scaled by nodal voltages. In a *distribution network*, these are typically very small compared to the  $\mathcal{L}\mathcal{U}$  matrix elements. We therefore consider  $\mathcal{D}$  as a perturbation of matrix  $\mathcal{L}\mathcal{U}$ , and we apply the Neumann series iteration (5.25).

## Practical Neumann Series Convergence Criteria

To justify this Neumann series application, the following theorem presents practical convergence condition (5.33). This theorem deals with complex, rather than real, coordinates. Accordingly, we define  $\mathcal{D}_c = \text{diag}(\tilde{\mathbf{V}})^{-1} \text{diag}(\tilde{\mathbf{I}}^*)$  and  $\mathcal{L}_c \mathcal{U}_c = E^T Y_l E$ .

**Theorem 6.** Matrix inverse  $(\mathcal{L}_c \mathcal{U}_c + \mathcal{D}_c)^{-1}$  can be approximated by a Neumann series iteration, as in (5.25), if

$$\rho(E^T Y_l E) > \max\{|\tilde{\mathbf{I}}|\}. \quad (5.33)$$

*Proof.* For  $(\mathcal{D}_c + \mathcal{L}_c \mathcal{U}_c)^{-1}$  to be approximated by a Neumann series, then  $\rho((\mathcal{L}_c \mathcal{U}_c)^{-1} \mathcal{D}_c) < 1$  must hold. Expanding,

$$\rho((\mathcal{L}_c \mathcal{U}_c)^{-1} \mathcal{D}_c) = \rho((E^T Y_l E)^{-1} \text{diag}(\tilde{\mathbf{V}})^{-1} \text{diag}(\tilde{\mathbf{I}}^*)) \quad (5.34a)$$

$$\leq \rho((E^T Y_l E)^{-1}) \rho(\text{diag}(\tilde{\mathbf{I}}^*)) \quad (5.34b)$$

$$= \frac{\max\{|\tilde{\mathbf{I}}|\}}{\rho(E^T Y_l E)}, \quad (5.34c)$$

where  $\rho(\text{diag}(\tilde{\mathbf{V}})^{-1}) \approx 1$  is assumed due to per-unitization.  $\square$

If the largest load current magnitude is safely below  $\rho(E^T Y_l E)$ , then the Neumann series will converge. Since load currents are typically less than 1 p.u. and network admittance values are typically much larger, this condition is usually satisfied by a large margin. For example, in the IEEE 123-bus network [161],  $\|\mathcal{L}\mathcal{U}\|/\|\mathcal{D}\| \approx 4 \times 10^4$ .

## Solving Power Flow via Neumann Expansion

The full power flow procedure, outlined in Algorithm 9, iterates until Newton converges according to some tolerance on the residual injection at each bus. This solver is termed the Neumann Series Based Power Flow (**NSBPF**) solver. At several points, this power flow solver calls Algorithm 10, which solves the pre-factored network admittance matrix using forward-elimination and backward-substitution.

## Extension to Unbalanced Three-Phase Networks

The numerical routine proposed in Algorithm 9 can be readily extended to an unbalanced, three-phase network. In these networks, each element must be described by

$$\begin{bmatrix} \tilde{\mathbf{l}}_{ij} \\ \tilde{\mathbf{l}}_{ji} \end{bmatrix} = \begin{bmatrix} \mathbf{Y}_{ii} & \mathbf{Y}_{ji} \\ \mathbf{Y}_{ij} & \mathbf{Y}_{jj} \end{bmatrix} \begin{bmatrix} \tilde{\mathbf{V}}_i \\ \tilde{\mathbf{V}}_j \end{bmatrix}, \quad (5.35)$$

where the stated admittance matrix is  $6 \times 6$  and  $\tilde{\mathbf{l}}_{ij}, \tilde{\mathbf{V}}_i \in \mathbb{C}^{3 \times 1}$ . This formulation assumes properly grounded neutral phases which are eliminated via Kron reduction. If one or more of the phases do not exist (i.e. “disjoint” phase extensions), then the corresponding columns of the admittance matrix (5.35) are removed. The three

---

**Algorithm 9** Neumann Series Based Power Flow (NSBPF)

---

**Require:** Matrix factors  $\mathcal{L}, \mathcal{U}, \mathcal{P}$  from (5.31); specified power injections  $\mathbf{s}$ ; initial voltage guess  $\mathbf{x}_0$ ; reduced power flow function  $\mathbf{S}(\cdot)$

**Ensure:** Solution  $\mathbf{x}$  satisfies  $\mathbf{S}(\mathbf{x}) \approx \mathbf{s}$

```
1: function  $\mathbf{x} \leftarrow \text{NSBPF}(\mathcal{L}, \mathcal{U}, \mathcal{P}, \mathbf{S}, \mathbf{x}_0)$ 
2:    $k \leftarrow 0$ 
3:    $\mathbf{b} \leftarrow \mathbf{s} - \mathbf{S}(\mathbf{x}_k)$ 
4:   while  $\|\mathbf{b}\|_\infty > \text{tolerance } \epsilon_N$  do
5:     Construct  $\langle \text{diag}(\tilde{\mathbf{V}}) \rangle$  and  $\langle \text{diag}(\tilde{\mathbf{I}}^*) \rangle$  from  $\mathbf{x}_k$ 
6:      $\mathbf{b} \leftarrow \text{Solve: } \langle \text{diag}(\tilde{\mathbf{V}}) \rangle \mathbf{b} = \mathbf{b}$ 
7:      $\mathcal{D} \leftarrow \text{Solve: } \langle \text{diag}(\tilde{\mathbf{V}}) \rangle \mathcal{D} = \langle \text{diag}(\tilde{\mathbf{I}}^*) \rangle$ 
8:      $i \leftarrow 0$ 
9:      $\mathbf{y}^{(0)} = \mathbf{z} \leftarrow \text{FEBS}(\mathcal{L}, \mathcal{U}, \mathcal{P}, \mathbf{b})$ 
10:    for desired number of NS iterations do
11:       $i \leftarrow i + 1$ 
12:       $\mathbf{z} \leftarrow \text{FEBS}(\mathcal{L}, \mathcal{U}, \mathcal{P}, \mathcal{D}\mathbf{z})$ 
13:       $\mathbf{y}^{(i+1)} \leftarrow \mathbf{y}^{(i)} + (-1)^i \mathbf{z}$ 
14:    end
15:     $\Delta\mathbf{x}_k \leftarrow \text{Solve: } R(\tilde{\mathbf{V}})\Delta\mathbf{x}_k = \mathbf{y}$ 
16:     $\mathbf{x}_{k+1} \leftarrow \mathbf{x}_k - \Delta\mathbf{x}_k$ 
17:     $\mathbf{b} \leftarrow \mathbf{s} - \mathbf{S}(\mathbf{x}_k)$ 
18:     $k \leftarrow k + 1$ 
end
19: return  $\mathbf{x}$ 
```

---

---

**Algorithm 10** Forward-Elimination Back-Substitution (FEBS)

---

**Require:** Matrix factors  $\mathcal{L}, \mathcal{U}, \mathcal{P}$ ; RHS vector  $\mathbf{b}$

**Ensure:** Returned  $\mathbf{x}$  satisfies  $\mathcal{P}\mathcal{L}\mathcal{U}\mathcal{P}^T\mathbf{x} = \mathbf{b}$

```
1: function  $\mathbf{x} \leftarrow \text{FEBS}(\mathcal{L}, \mathcal{U}, \mathcal{P}, \mathbf{b})$ 
2:    $\mathbf{z} \leftarrow \text{solve } (\mathcal{L}\mathbf{z} = \mathcal{P}^T\mathbf{b}) \text{ with Forward-Elimination}$ 
3:    $\mathbf{y} \leftarrow \text{solve } (\mathcal{U}\mathbf{y} = \mathbf{z}) \text{ with Back-Substitution}$ 
4:    $\mathbf{x} \leftarrow \mathcal{P}\mathbf{y}$ 
5: return  $\mathbf{x}$ 
```

---

phase nodal admittance matrix associated with the full network is constructed by properly placing and summing the individual primitive admittance matrices. This nodal admittance matrix, including shunts, is written as  $\mathbf{Y}_b$ . For more details on formulating the three-phase admittance matrix, see [52]. Using this matrix, the three-phase reduced power flow Jacobian can be directly constructed as

$$\mathbf{J} = (\langle \text{diag}(\tilde{\mathbf{I}}^*) \rangle + \langle \text{diag}(\tilde{\mathbf{V}}) \rangle \mathbf{N} \langle \mathbf{Y}_b \rangle) R(\tilde{\mathbf{V}}). \quad (5.36)$$

Any undefined terms can be inferred from (5.10), with the guiding assumption that both current and voltage vectors are concatenated  $n$ -phase vectors, where  $n = 1, 2, 3$  depending on the nature of the disjoint phase extensions.

**Remark 10.** *The admittance  $\mathbf{N} \langle \mathbf{Y}_b \rangle$  from (5.36) will necessarily be symmetric. Accordingly, the LDL decomposition proposed in Remark 8 will be a valid factorization for this matrix.*

Other three-phase structures can be constructed analogously. Using these updated expressions, the solution to the three-phase power flow can proceed as outlined in Alg. 9.

### 5.2.2 Reduced Order Modeling of the Nonlinear Power Flow for Probabilistic Power Flow

In this subsection, we first motivate the low-rank nature of power flow solutions in the PPF problem. Next, we leverage a projection subspace in order to perform model order reduction on the full power flow problem, and we show how Newton iterations can be used to solve the associated over-determined nonlinear system. Finally, we combine our proposed model order reduction method with our Neumann series based power flow algorithm in order to quickly solve for PPF solutions.

#### Model Order Reduction of the Power Flow Problem

A PPF solver considers the probable loading levels of a distribution network over some probabilistic horizon. The corresponding set of operating points is inherently low-rank. Anchored by tightly regulated feeder voltages, the network voltage profile  $\mathbf{x} \in \mathbb{R}^n$  typically lives in a fairly low-dimensional subspace characterized by  $\mathbb{V} \in \mathbb{R}^{n \times q}$  from (5.26). When  $\mathbb{V}$  is populated with a sufficient number of appropriately chosen

dominant basis vectors, the low order vector  $\hat{\mathbf{x}}$  can represent the full order state with a high degree of accuracy.

To exploit the usefulness of subspace  $\mathbb{V}$  beyond the Galerkin projection of (5.27), we note that the power flow equations become quadratic when written in Cartesian coordinates  $V_r = \text{Re}\{Ve^{j\theta}\}$ ,  $V_i = \text{Im}\{Ve^{j\theta}\}$ . We can therefore express the reduced residual function (5.8) as an *exact* second order Taylor series expansion. Writing the reduced voltage vector in Cartesian coordinates as  $\mathbf{x}_c$ ,

$$\mathbf{g}(\delta\mathbf{x}_c) = \mathbf{S}(\mathbf{x}_{c0}) + \mathbf{J}_{c0}\delta\mathbf{x}_c + \frac{1}{2}\mathbf{H}_c(\delta\mathbf{x}_c \otimes \delta\mathbf{x}_c) - \mathbf{s}, \quad (5.37)$$

where  $\delta\mathbf{x}_c = \mathbf{x}_c - \mathbf{x}_{c0}$  is a perturbation from some nominal operating point  $\mathbf{x}_{c0}$ , and  $\mathbf{J}_{c0} \equiv \mathbf{J}_c(\mathbf{x}_{c0})$  and  $\mathbf{H}_c$  are Jacobian and Hessian matrices, respectively. The expansion of the Cartesian coordinate power flow equations has a Jacobian which is equal to (5.10), but with the elimination of the polar-to-Cartesian conversion matrix  $R(\cdot)$ :

$$\mathbf{J}_c = (\langle \text{diag}(\tilde{\mathbf{I}}_r - j\tilde{\mathbf{I}}_i) \rangle + \langle \text{diag}(\tilde{\mathbf{V}}_r + j\tilde{\mathbf{V}}_i) \rangle N \langle Y_b \rangle). \quad (5.38)$$

Notably, (5.38) is a *linear* function of Cartesian voltage coordinates, so the Hessian  $\mathbf{H}_c \in \mathbb{R}^{n \times n^2}$  is constant. With  $i^{\text{th}}$  unit vector  $\mathbf{e}_i$ ,

$$\mathbf{H}_c = \left[ \begin{array}{cccccc} \frac{d\mathbf{J}_c}{d\tilde{\mathbf{V}}_{r,1}} & \dots & \frac{d\mathbf{J}_c}{d\tilde{\mathbf{V}}_{r,n}} & \frac{d\mathbf{J}_c}{d\tilde{\mathbf{V}}_{i,1}} & \dots & \frac{d\mathbf{J}_c}{d\tilde{\mathbf{V}}_{i,n}} \end{array} \right] \quad (5.39)$$

$$\frac{d\mathbf{J}_c}{d\tilde{\mathbf{V}}_{r,i}} = \langle \text{diag}(Y_b^* \mathbf{e}_i) \rangle + \langle \text{diag}(\mathbf{e}_i) \rangle N \langle Y_b \rangle \quad (5.40)$$

$$\frac{d\mathbf{J}_c}{d\tilde{\mathbf{V}}_{i,i}} = \langle \text{diag}(-jY_b^* \mathbf{e}_i) \rangle + \langle \text{diag}(j\mathbf{e}_i) \rangle N \langle Y_b \rangle. \quad (5.41)$$

Leveraging  $\mathbf{x}_c \approx \mathbb{V}\hat{\mathbf{x}}_c$ , as in (5.26), we note that  $\mathbb{V}\hat{\mathbf{x}}_c = \mathbb{V}\hat{\mathbf{x}}_{c0} + \mathbb{V}\delta\hat{\mathbf{x}}_c$ . Substituting  $\mathbb{V}\delta\hat{\mathbf{x}}_c \approx \delta\mathbf{x}_c$  into (5.37),

$$\mathbf{g}(\mathbb{V}\delta\hat{\mathbf{x}}_c) = \mathbf{S}_0 + \mathbf{J}_{c0}\mathbb{V}\delta\hat{\mathbf{x}}_c + \frac{1}{2}\mathbf{H}_c(\mathbb{V} \otimes \mathbb{V})(\delta\hat{\mathbf{x}}_c \otimes \delta\hat{\mathbf{x}}_c) - \mathbf{s}, \quad (5.42)$$

where  $\mathbf{S}_0 = \mathbf{S}(\mathbf{x}_0)$  and Kronecker products in (5.42) have been separated [48]. Minimizing residual  $\mathbf{g}(\mathbb{V}\delta\hat{\mathbf{x}}_c)$  in a least squares sense represents the minimization of an overdetermined nonlinear system. The Newton-like algorithm for minimizing the least squares problem  $\|\mathbf{g}(\mathbb{V}\delta\hat{\mathbf{x}}_c)\|_2^2$  can be derived by keeping the constant + linear terms of the expansion (5.42) and then solving for iterative values of  $\delta\hat{\mathbf{x}}_c$  via Moore-Penrose:

$$\delta\hat{\mathbf{x}}_c^{(i+1)} = \delta\hat{\mathbf{x}}_c^{(i)} - [(\mathbf{J}_{c0}\mathbb{V})^T \mathbf{J}_{c0}\mathbb{V}]^{-1}(\mathbf{J}_c\mathbb{V})^T \mathbf{g}(\mathbb{V}\delta\hat{\mathbf{x}}_c^{(i)}). \quad (5.43)$$

In solving (5.43), we notice that whenever  $\mathbf{g}(\mathbb{V}\delta\hat{\mathbf{x}}_c^{(i)})$  is evaluated, it is left multiplied by  $(\mathbf{J}_{c0}\mathbb{V})^T$ . We therefore define  $\hat{\mathbf{J}} = \mathbf{J}_{c0}\mathbb{V}$  and then multiply (5.42) through by  $\hat{\mathbf{J}}^T$ :

$$\hat{\mathbf{g}}(\delta\hat{\mathbf{x}}_c) = \hat{\mathbf{S}}_0 + \hat{\mathbf{G}}\delta\hat{\mathbf{x}}_c + \frac{1}{2}\hat{\mathbf{H}}(\delta\hat{\mathbf{x}}_c \otimes \delta\hat{\mathbf{x}}_c) - \hat{\mathbf{s}} \quad (5.44)$$

where  $\hat{\mathbf{g}} = \hat{\mathbf{J}}^T\mathbf{g}$ ,  $\hat{\mathbf{S}}_0 = \hat{\mathbf{J}}^T\mathbf{S}_0$ ,  $\hat{\mathbf{G}} = \hat{\mathbf{J}}^T\hat{\mathbf{J}}$ ,  $\hat{\mathbf{H}} = \hat{\mathbf{J}}^T\mathbf{H}_c(\mathbb{V} \otimes \mathbb{V})$ , and  $\hat{\mathbf{s}} = \hat{\mathbf{J}}^T\mathbf{s}$ . Importantly, (5.44) is a *square* system, i.e., it has  $q$  equations and  $q$  variables in  $\delta\hat{\mathbf{x}}_c$ . Applying a Newton-like (i.e. neglecting Hessian contributions) method to (5.44) yields the iterative routine

$$\delta\hat{\mathbf{x}}_c^{(i+1)} = \delta\hat{\mathbf{x}}_c^{(i)} - \hat{\mathbf{G}}^{-1}\hat{\mathbf{g}}(\delta\hat{\mathbf{x}}_c^{(i)}), \quad (5.45)$$

where, again,  $\hat{\mathbf{G}}$  is the result of a modified Galerkin projection:  $\hat{\mathbf{G}} = (\mathbf{J}_{c0}\mathbb{V})^T\mathbf{J}_{c0}\mathbb{V}$ . Notably,  $\hat{\mathbf{J}}$ ,  $\hat{\mathbf{G}}$ , and  $\hat{\mathbf{H}}$  are *constant* matrices and do not need to be updated at each step  $\delta\hat{\mathbf{x}}_c^{(i)}$ .

**Remark 11.** Because (5.44) is a determined system, the residual  $\hat{\mathbf{g}}$  can be driven to  $\mathbf{0}$ . This residual, though, is merely a **projection** of the true residual  $\mathbf{g}$  of (5.37) into the low-rank space  $(\mathbf{J}_c\mathbb{V})^T$ . Therefore,  $\hat{\mathbf{g}} = \mathbf{0}$  does not imply  $\mathbf{g} = \mathbf{0}$ .

Once converged,  $\delta\hat{\mathbf{x}}_c^{(i)}$  will be equal to the reduced state deviation which is the least squares minimizer of (5.42). Notably, the reduced residual  $\hat{\mathbf{g}}(\delta\hat{\mathbf{x}}_c^{(i)})$  and the steps of (5.45) can both be computed very quickly, since the reduced system is extremely small ( $q \times q$ ). A key property of this low-dimensional system is that (5.45) reliably converges even though  $\hat{\mathbf{G}}$  is not updated between iterations; as will be shown, it is only updated when the basis  $V$  dynamically expands. The procedure associated with the ROM system solve (5.45) is given in Algorithm 11 and is termed the Reduced Model Solver (**RMS**).

---

**Algorithm 11** Reduced Model Solver (RMS)

---

```

1: function  $[\delta\hat{\mathbf{x}}_c, \mathbf{x}] \leftarrow \text{RMS}(\mathbb{V}, \hat{\mathbf{S}}_0, \hat{\mathbf{G}}, \hat{\mathbf{H}}, \hat{\mathbf{x}}_{c0}, \delta\hat{\mathbf{x}}_c^{(1)}, \hat{\mathbf{s}})$ 
2:    $\hat{\mathbf{g}} \leftarrow \hat{\mathbf{S}}_0 + \hat{\mathbf{G}}\delta\hat{\mathbf{x}}_c^{(1)} + \frac{1}{2}\hat{\mathbf{H}}(\delta\hat{\mathbf{x}}_c^{(1)} \otimes \delta\hat{\mathbf{x}}_c^{(1)}) - \hat{\mathbf{s}}$ 
3:    $i \leftarrow 1$ 
4:   while  $\|\hat{\mathbf{g}}\|_\infty > \text{tolerance } \hat{\epsilon}_N$  do
5:      $\delta\hat{\mathbf{x}}_c^{(i+1)} \leftarrow \delta\hat{\mathbf{x}}_c^{(i)} - \hat{\mathbf{G}}^{-1}\hat{\mathbf{g}}(\delta\hat{\mathbf{x}}_c^{(i)})$ 
6:      $i \leftarrow i + 1$ 
7:    $\hat{\mathbf{g}} \leftarrow \hat{\mathbf{S}}_0 + \hat{\mathbf{G}}\delta\hat{\mathbf{x}}_c^{(i)} + \frac{1}{2}\hat{\mathbf{H}}(\delta\hat{\mathbf{x}}_c^{(i)} \otimes \delta\hat{\mathbf{x}}_c^{(i)}) - \hat{\mathbf{s}}$ 
end
8:   return  $\delta\hat{\mathbf{x}}_c \leftarrow \delta\hat{\mathbf{x}}_c^{(i)}, \mathbf{x} \leftarrow \text{Cartesian-to-Polar}\{\mathbb{V}(\delta\hat{\mathbf{x}}_c + \hat{\mathbf{x}}_{c0})\}$ 

```

---

Failure of convergence of Alg. 11 has not been witnessed by the authors. Such potential failure, though, would always be detected by the APPF algorithm, as shown in Fig. 5-1, in which case the full order model will be used to solve the system.

## Dynamic Subspace Expansion

The quality of the RMS solution is a function of how effectively the subspace  $\mathbb{V}$  has been “filled out”. In order to expand  $\mathbb{V}$ , we assume we have an emerging sequence of valid power flow solutions in Cartesian coordinates. We then leverage the dynamic subspace expansion technique characterized by line 9 in Algorithm 8. In this way, the basis  $\mathbb{V}$  is *dynamically* constructed as an outer loop PPF solver runs. Such dynamic updating is computationally cheap, and it ensures that  $\mathbb{V}$  only contains subspace vectors which are useful for solving a particular PPF problem. Indeed,  $\mathbb{V}$  growing too large will slow the iterative scheme (5.45) down considerably. As  $\mathbb{V}$  grows in size, though, the quality of the RMS results will improve. The expansion procedure is outlined in Algorithm 12, which also includes updates of  $\hat{\mathbf{J}}$ ,  $\hat{\mathbf{G}}$ ,  $\hat{\mathbf{H}}$ ,  $\delta\hat{\mathbf{x}}_c$  and  $\hat{\mathbf{S}}_0$ . Notably, the “sort( $\cdot$ )” function ensures that  $\hat{\mathbf{H}}$  is properly ordered, so it correctly interacts with Kronecker product  $\delta\hat{\mathbf{x}}_c \otimes \delta\hat{\mathbf{x}}_c$  in (5.44). For computational expediency, we also note that this algorithm tracks  $\mathbf{H}_K$ , which is effectively the latest update of  $\mathbf{H}_c(\mathbb{V} \otimes \mathbb{V})$ . The full expansion procedure is termed the Dynamic Subspace Expansion (**DSE**). As the subspace  $\mathbb{V}$  grows in size,

- the operation  $\mathbb{V} \otimes \mathbb{V}$  becomes exponentially more time intensive (even if previously computed terms are saved),
- but  $\mathbb{V} \leftarrow [\mathbb{V} \; \mathbf{x}]$  adds marginally less important basis terms.

Accordingly, the first elements of  $\delta\hat{\mathbf{x}}_c$  tend to be orders of magnitude larger than the final elements. Since  $\mathbb{V} \otimes \mathbb{V}$  is *only* used in constructing  $\hat{\mathbf{H}}$ , which in-turn is used to compute the quadratic terms in the residual function  $\hat{\mathbf{g}}$  from (5.44), we can curtail the growth of  $\hat{\mathbf{H}}$  by choosing to only keep the expansions associated with first  $(n_q)^2$  quadratic terms of  $\delta\hat{\mathbf{x}}_c \otimes \delta\hat{\mathbf{x}}_c$ . This can be done without reasonably compromising the quality of (5.44), and it is implemented in line 9 of Alg. 12. The test results section provides further discussion.

## Combining NSBPF, RMS, and DSE for Accelerated PPF

We now propose one coherent routine which incorporates the NSBPF, the RMS, and the DSE. On the surface, this solver behaves like other sampling-based PPF solves:

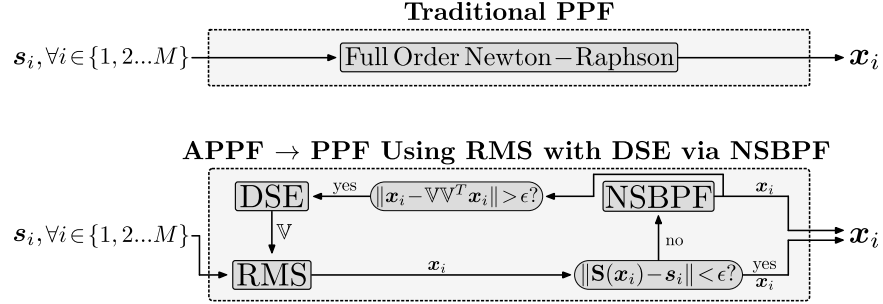


Figure 5-1: Contrasted are the traditional sampling-based Probabilistic Power Flow (PPF) (top panel), and the Accelerated Probabilistic Power Flow (APPF). In the APPF, a reduced modeler first attempts to solve power flow. If it fails, the full-order Neumann series solver is used. If the resulting solution isn't in the basis  $\mathbb{V}$ , it is dynamically added, and the reduced model is updated.

it loops over various sampled load profiles and solves power flow for each one. Such architecture can be seen in the top panel of Fig. 5-1, where a traditional Newton-Raphson solver (i.e. (5.9)) is used. Our routine, shown in the bottom panel of Fig. 5-1, first attempts to solve power flow using the RMS. If the resulting residual is too large, then the inadequate solution is passed to the NSBPF routine so it can find an adequate one. The resulting solution is then passed to the DSE, and the subspace  $\mathbb{V}$  is potentially updated. Further details are given in Algorithm 13, which is termed the Accelerated Probabilistic Power Flow (**APPF**).

### 5.2.3 Test Results

In this section, we present test results which were collected on the IEEE 8500-node test feeder. To construct this test case, we used OpenDSS [51] to carefully export the admittance matrix, nominal loading values, transformer tap ratios, transformer configurations ( $\Delta : Y$ ,  $Y : Y$ , split-phase) and base voltage levels of this network to MATLAB. We then per-unitized the network with a base power of 100kW and base voltages of 66.5kV, 7.2kV and 120V on the appropriate buses. In our tests, all tap ratios and switch configurations were assumed fixed. Additionally, the nominal three-phase feeder voltage was assumed static across all trials. With this per-unitization, the largest nominal load current was 0.51 pu, meaning (5.34c) was satisfied by many orders of magnitude.

In testing this network, we chose a subset  $\mathcal{S}$ ,  $|\mathcal{S}| = 25$ , of the largest loads in the 8500-node network and assumed an extremely high degree of input variability. Accordingly, we sampled from IID Gaussian distributions, such that the sampled active

---

**Algorithm 12** Dynamic Subspace Expansion (DSE)

---

```

1: function  $[\mathbb{V}, \hat{\mathbf{J}}, \hat{\mathbf{G}}, \hat{\mathbf{H}}, \mathbf{H}_K, \delta\hat{\mathbf{x}}_c, \hat{\mathbf{S}}_0] \leftarrow \text{DSE}(\mathbb{V}, \hat{\mathbf{J}}, \hat{\mathbf{G}}, \hat{\mathbf{H}}, \mathbf{H}_K, \delta\hat{\mathbf{x}}_c, \hat{\mathbf{S}}_0, \mathbf{S}_0, \mathbf{x}, \mathbf{J}_{c0}, \mathbf{H}_c)$ 
2:    $\mathbf{x}_c \leftarrow \text{Polar to Cartesian}\{\mathbf{x}\}$ 
3:    $\mathbf{v} \leftarrow \mathbf{x}_c - \mathbb{V}\mathbb{V}^T\mathbf{x}_c$ 
4:   if  $\|\mathbf{v}\| > \text{tolerance } \epsilon_B$  then
5:      $\delta\hat{\mathbf{x}}_c \leftarrow [\delta\hat{\mathbf{x}}_c^T \|\mathbf{v}\|]^T$ 
6:      $\mathbf{v} \leftarrow \mathbf{v}/\|\mathbf{v}\|$ 
7:      $\mathbf{v}_J \leftarrow \mathbf{J}_{c0}\mathbf{v}$ 
8:      $\hat{\mathbf{G}} \leftarrow \begin{bmatrix} \hat{\mathbf{G}} & \hat{\mathbf{J}}\mathbf{v}_J \\ \mathbf{v}_J^T \hat{\mathbf{J}} & \mathbf{v}_J^T \mathbf{v}_J \end{bmatrix}$ 
9:     if  $\text{size}\{\delta\hat{\mathbf{x}}_c\} \leq n_q$  then
10:       $\mathbb{V}_k \leftarrow \text{sort}\{\mathbf{v} \otimes \mathbb{V}, \mathbf{v} \otimes \mathbf{v}\}$ 
11:       $\mathbf{K} \leftarrow \mathbf{H}_c \mathbb{V}_k$ 
12:       $\hat{\mathbf{H}} \leftarrow \text{sort} \begin{bmatrix} \hat{\mathbf{H}} & \hat{\mathbf{J}}^T \mathbf{K} \\ \mathbf{v}_J^T \mathbf{H}_K & \mathbf{v}_J^T \mathbf{K} \end{bmatrix}$ 
13:       $\mathbf{H}_K \leftarrow \text{sort}[\mathbf{H}_K \mathbf{H}_c \mathbb{V}_k]$ 
14:    end
15:     $\hat{\mathbf{S}}_0 \leftarrow [\hat{\mathbf{S}}_0^T \mathbf{v}_J^T \mathbf{S}_0]^T$ 
16:     $\hat{\mathbf{J}} \leftarrow [\hat{\mathbf{J}} \mathbf{v}_J]$ 
17:     $\mathbb{V} \leftarrow [\mathbb{V} \mathbf{v}]$ 
end
18: return  $\mathbb{V}, \hat{\mathbf{J}}, \hat{\mathbf{G}}, \hat{\mathbf{H}}, \mathbf{H}_K, \delta\hat{\mathbf{x}}_c, \hat{\mathbf{S}}_0$ 

```

---

and reactive power were generated via  $\{P, Q\}_i^{(s)} = \{P, Q\}_i(1 + \mathcal{N}(\sigma, 0))$ ,  $i \in \mathcal{S}$ . In each case, the loads in  $\mathcal{S}$  were assumed to have distributed energy resource capabilities (i.e. rooftop PV, battery charging/discharging capabilities, etc.). Accordingly, the standard deviation in was set to  $\sigma = 1$ , meaning the loads could potentially switch sign and become sources in some sampling instances. Since samples were drawn randomly, this sampling routine is called Simple Random Sampling (SRS) [77]. The sampling procedure was performed 1000 times for each load, the largest of which vary between -110kW and +60kW of active power, for example (see Fig. 5-2). The remainder of the loads were left fixed to one half their nominal values. Next, we documented the speed-up of the APPF relative to the traditional PPF solver (see top panel of Fig. 5-1) in the context of SRS. All simulations were performed using MATLAB R2017b on a Dell XPS laptop, equipped with an Intel i5 CPU @ 2.30GHz and 8 GB of RAM.

## Traditional PPF

First, we applied the traditional PPF solver from Fig. 5-1. The Newton stopping criteria on the power injection residual was set to  $\epsilon_N = 10^{-4}$ , i.e.  $\|\mathbf{S}(\mathbf{x}_i) - \mathbf{s}_i\|_\infty < 10^{-4}$ . Physically, this corresponds to conservation of power being satisfied below 10 Watts at each node in the network. Looping over the 1000 loading configurations,

---

**Algorithm 13** Accelerated Probabilistic Power Flow (APPF): PPF Using RMS with DSE via NSBPF

---

**Require:** Matrix factors  $\mathcal{L}, \mathcal{U}, \mathcal{P}$  from (5.31); initial voltage solution  $\mathbf{x}_0$  of nominal power injection  $\mathbf{S}_0$ ; nominal reduced power flow function  $\mathbf{S}(\cdot)$ ; reduced power flow Hessian  $\mathbf{H}_c$  and Jacobian  $\mathbf{J}_{c0}$  evaluated at  $\mathbf{x}_0$ , specified power injection profiles  $\mathbf{s}_i$  for each  $i = 1, 2, \dots, M$

**Ensure:** Each solution  $\mathbf{x}_i$  satisfies  $\mathbf{S}(\mathbf{x}_i) \approx \mathbf{s}_i$

```

1: function  $[\mathbf{x}_1, \mathbf{x}_2, \dots, \mathbf{x}_M] \leftarrow \text{APPF } (\mathcal{L}, \mathcal{U}, \mathcal{P}, \mathbf{s}, \mathbf{x}_0, \mathbf{S}_0, \mathbf{J}_{c0}, \mathbf{H}_c)$ 
2:    $\mathbf{x}_{c0} \leftarrow \text{Polar-to-Cartesian}\{\mathbf{x}_0\}$ 
3:    $\hat{\mathbf{x}}_{c0} \leftarrow \|\mathbf{x}_{c0}\|$ 
4:    $\delta\hat{\mathbf{x}}_c \leftarrow 0$ 
5:    $\mathbb{V} \leftarrow \mathbf{x}_{c0}/\|\mathbf{x}_{c0}\|$ 
6:    $\hat{\mathbf{J}} \leftarrow \mathbf{J}_{c0}\mathbb{V}$ 
7:    $\hat{\mathbf{S}}_0 \leftarrow \hat{\mathbf{J}}^T \mathbf{S}_0$ 
8:    $\hat{\mathbf{G}} \leftarrow \hat{\mathbf{J}}^T \hat{\mathbf{J}}$ 
9:    $\mathbf{H}_K \leftarrow \mathbf{H}_c(\mathbb{V} \otimes \mathbb{V})$ 
10:   $\hat{\mathbf{H}} \leftarrow \hat{\mathbf{J}}^T \mathbf{H}_K$ 
11:   $i \leftarrow 1$ 
12:  while  $i \leq M$  do
13:     $\hat{\mathbf{s}}_i \leftarrow \hat{\mathbf{J}}^T \mathbf{s}_i$ 
14:     $[\delta\hat{\mathbf{x}}_c, \mathbf{x}_i] \leftarrow \text{RMS}(\mathbb{V}, \hat{\mathbf{S}}_0, \hat{\mathbf{G}}, \hat{\mathbf{H}}, \hat{\mathbf{x}}_{c0}, \delta\hat{\mathbf{x}}_c, \hat{\mathbf{s}}_i)$ 
15:    if  $\|\mathbf{S}(\mathbf{x}_i) - \mathbf{s}_i\|_\infty > \text{tolerance } \epsilon_N$  then
16:       $\mathbf{x}_i \leftarrow \text{NSBPF}(\mathcal{L}, \mathcal{U}, \mathcal{P}, \mathbf{s}_i, \mathbf{x}_i)$ 
17:       $[\mathbb{V}, \hat{\mathbf{J}}, \hat{\mathbf{G}}, \hat{\mathbf{H}}, \mathbf{H}_K, \delta\hat{\mathbf{x}}_c, \hat{\mathbf{S}}_0] \leftarrow \text{DSE}(\mathbb{V}, \hat{\mathbf{J}}, \hat{\mathbf{G}}, \hat{\mathbf{H}}, \mathbf{H}_K, \delta\hat{\mathbf{x}}_c, \hat{\mathbf{S}}_0, \mathbf{x}_i, \mathbf{J}_{c0}, \mathbf{H}_c)$ 
18:    end
19:     $i \leftarrow i + 1$ 
end
20:  return  $\mathbf{x}_1, \mathbf{x}_2, \dots, \mathbf{x}_M$ 

```

---

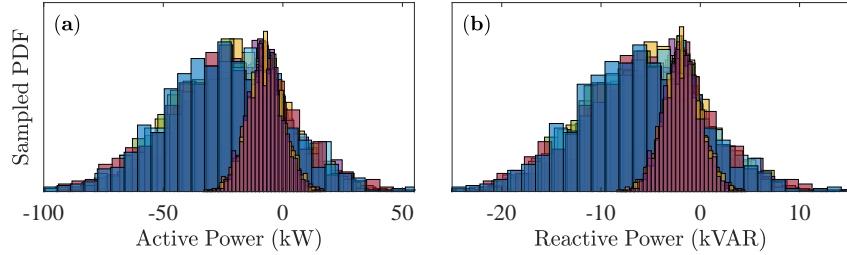


Figure 5-2: Sampled active and reactive power input distributions (panels **(a)** and **(b)**, respectively) for the 25 largest loads in the 8500-node network.

Newton required between 2 and 3 steps to converge for all load configurations except for the first one, as shown in panel **(a)** of Fig. 5-5. Ultimately, the full simulation required **~190 seconds** to run, meaning each power flow lasted about 0.19 seconds. Sample results from the simulation are shown in Fig. 5-3. These plots show voltage and current distributions in the network, and they represent some of the ways that characterizing the probabilistic output from a PPF routine can be useful. The results generated by the traditional PPF routine, for all practical purposes are *identical* to the results generated by the APPF routine in the following subsection, i.e. the data shown in Fig. 5-3 could be generated by either process.

## APPF

In order to run the APPF, three additional tolerances were needed: the RMS convergence tolerance  $\hat{\epsilon}_N$  from Alg. 11, which was set to  $\hat{\epsilon}_N = 10^{-5}$ , the expansion curtailment constant  $n_q$  from Alg. 12, which was set to  $n_q = 37$ , and the basis expansion tolerance  $\epsilon_B$  from Alg. 12. The choice of  $\epsilon_B$  was particularly important: if set too large, the basis would never fill up and the RMS would perform poorly, but if set too small, the basis would fill up endlessly and slow the RMS down considerably. In testing the 8500-node network, we found  $\epsilon_B = 10^{-4}$  to be an effective compromise.

With these tolerances set, the APPF simulation required **~20 seconds** to run. Relative to the traditional PPF, the APPF ran almost **10x faster**. The supermajority of this time, though, was spent construing matrix  $\hat{\mathbf{H}} = \hat{\mathbf{J}}^T \mathbf{H}_c (\mathbb{V} \otimes \mathbb{V})$ , which occurred as subspace  $\mathbb{V}$  was being intermittently constructed during the first 60 or so load profile iterations. Once  $\mathbb{V}$  was sufficiently filled out, the RMS could solve the power flow problem without any help from the NSBPF (and without any more basis expansions). The final 940 load profiles were solved in 2.90 seconds. Relative to the final 940 solves of the traditional PPF, the APPF ran **~61x faster**. The full timing breakdown is graphically portrayed in Fig. 5-4.

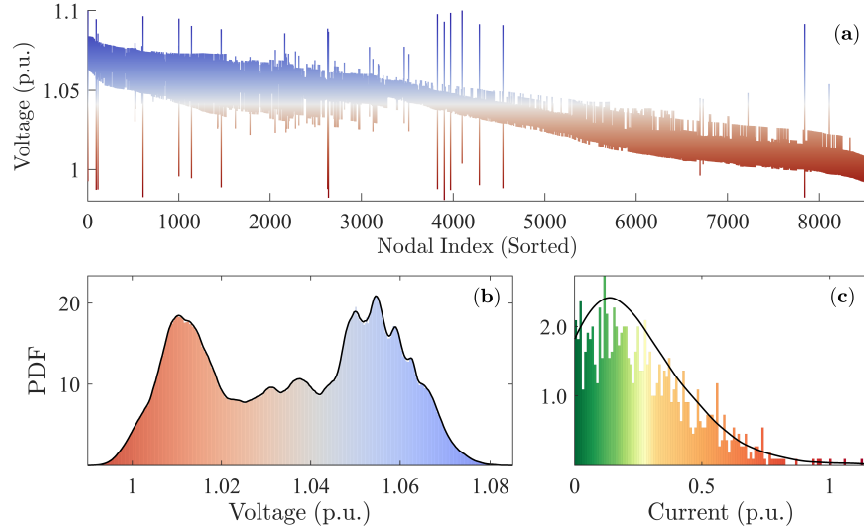


Figure 5-3: PPF results from the 8500-node network. Panel (a) shows the range of output voltages across 1000 trials for each node (sorted for clarity.) Panel (b) shows a histogram of all  $1000 \times 8531$  voltage magnitude points across all nodes, with an approximated black PDF curve plotted on top. Panel (c) shows a histogram of the current magnitudes flowing on the line connecting nodes 5724 and 8410; an approximated black PDF curve is plotted on top.

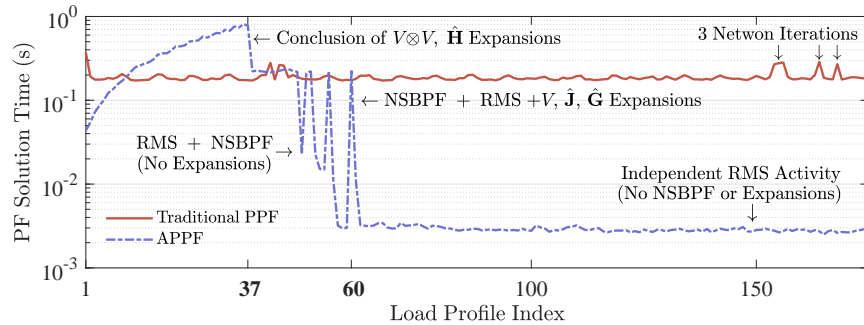


Figure 5-4: Shown is timing analysis for the traditional Newton-based PPF solver versus the APPF solver over the first 175 load profiles. Notably, the traditional PPF solver has a fairly constant solve speed, usually requiring two Newton iterations (although the locations of three iterations are marked in the upper right). At load profile  $n_q = 37$ , the APPF stopped building  $\mathbf{H}_c$ , which was becoming very time intensive. Between load profiles 38 and 60, the NSBPF and RMS worked together to continue building out the basis  $\mathbb{V}$  and solving the system. After load profile 60, the RMS quickly solved the system on its own without the NSBPF, and no more basis expansion was needed.

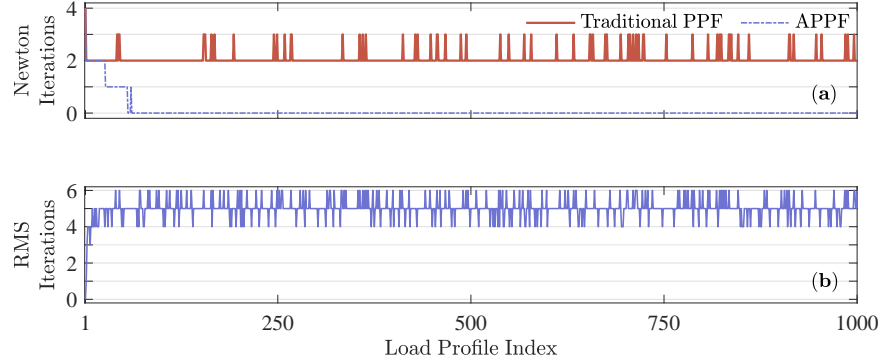


Figure 5-5: Panel (a) shows the number of Newton iterations performed by traditional PPF for each new load profile vs. the number of Newton iterations taken by the NSBPF solver in the APPF. Panel (b) shows the number of iterations taken by the RMS inside the APPF.

It is also instructive to consider how many Newton iterations the traditional PPF and the APPF solvers were required to perform on the full nonlinear system. This is shown in panel (a) of Fig. 5-5. As the APPF runs and  $\mathbb{V}$  fills up, the number of required Newton iterations by NSBPF solver in Alg. 9 drops from 4, to 3, to 2, to 1, to 0. When the APPF does take a Newton step, though, it is much faster than the traditional PPF Newton step, due to the Neumann expansion. On average:

- Traditional PPF Newton step time (mean): **0.11 seconds**
- APPF Newton step time via NSBPF (mean): **0.02 seconds**

Panel (b) of Fig. 5-5 shows the number of iterations, usually 5 or 6, taken by the RMS as the load profiles are processed. This relatively large number of iterations is due to the recycling of approximate reduced Jacobian  $\hat{\mathbf{G}}$ . If  $\hat{\mathbf{G}}$  was exactly computed at each step, fewer iterations would be necessary. Such updating, though, is far more expensive than adding additional iterations, so we tolerate the high iteration count in Fig. 5-5.

As the APPF solver ran, the basis  $\mathbb{V}$  dynamically expanded to include 52 orthonormal columns, giving it an ultimate dimension of  $(2 \cdot 8531) \times 52$ . As  $\mathbb{V}$  expanded, the RMS became increasingly effective at solving the power flow problem without any help from the NSBPF. This is shown very clearly by Fig. 5-6, which shows how the RMS output residual decreases as the solver cycles through the load profiles. It is interesting to note the salient “residual cliff” in panel (a), quite clearly located at load profile 27. To further explore its significance, we stacked the voltage solution vectors  $\mathbf{x}_i$  (found by traditional PPF) inside data matrix  $\mathbf{W} = [\mathbf{x}_1, \mathbf{x}_2, \dots, \mathbf{x}_{1000}]$ .

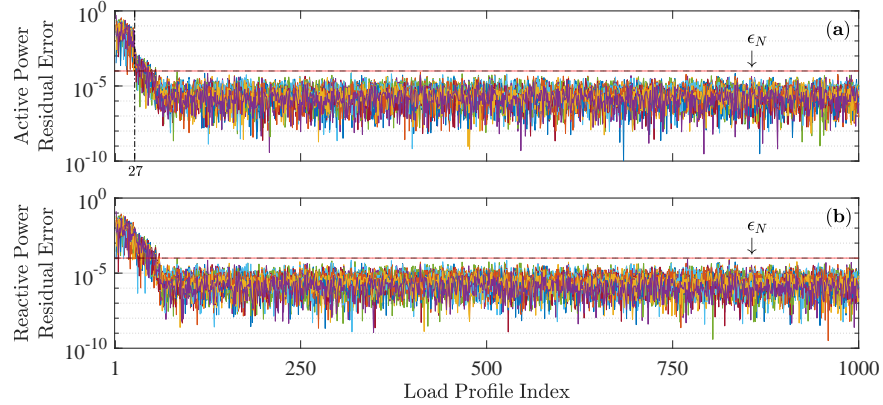


Figure 5-6: Residual active and reactive power (panels (a) and (b), respectively) at the 25 perturbed load buses in the 8500-node network *after* the RMS has converged. As  $\mathbb{V}$  expands, the RMS is able to consistently drive the residual at each of these buses below the stopping criteria  $\epsilon_N$ .

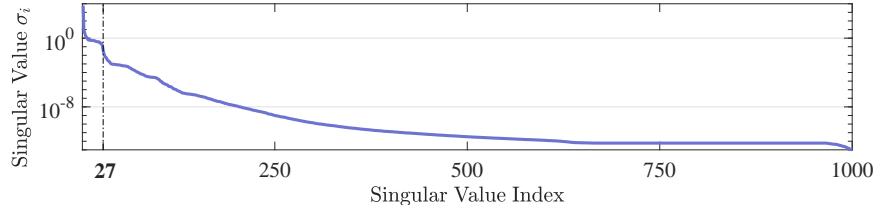


Figure 5-7: Plot of the singular values  $\sigma$  of matrix  $\mathbf{W} = [\mathbf{x}_1, \mathbf{x}_2, \dots, \mathbf{x}_{1000}]$ .

We then took the SVD of  $\mathbf{W}$ , i.e.  $\boldsymbol{\sigma} = \text{svd}\{\mathbf{W}\}$ . The results are shown in Fig. 5-7, which clearly shows a steep drop-off after the 27<sup>th</sup> largest singular value. This provides a nice qualitative explanation for the residual cliff in Fig. 5-6: the first 27 columns of subspace  $\mathbb{V}$  capture the most important features of the voltage profile, where “important” is quantified by the magnitude of a corresponding singular value.

## 5.3 Accelerated Probabilistic State Estimation in Distribution Grids via Model Order Reduction

### 5.3.1 Model Order Reduction of the State Estimation Problem

In this section, we apply the model order reduction scheme proposed the previous section to the probabilistic state estimation problem.

## An Exact Expansion of the State Estimation Equations

We seek to express the residuals (5.15) as exact second order expansions. This can be achieved for (5.15b)-(5.15c) by simply moving to Cartesian voltage coordinates, where the power flow and injection functions become quadratic. We write reduced voltage vector  $\mathbf{x}$  in Cartesian coordinates as

$$\mathbf{x}_c = [\mathbf{V}_r^T, \mathbf{V}_i^T]^T, \quad (5.46)$$

where  $\mathbf{V}_r = \text{Re}\{\tilde{\mathbf{V}}\}$  and  $\mathbf{V}_i = \text{Im}\{\tilde{\mathbf{V}}\}$ . In Cartesian coordinates, the second order expansion of the voltage magnitude residual function (5.15a), will not be exact, since the expansion of  $(V_r^2 + V_i^2)^{\frac{1}{2}}$  has infinite terms. Therefore, we choose to update (5.15a) by taking the difference of the squares:

$$\tilde{\mathbf{m}}_i(\mathbf{x}_c) = \mathbf{M}_i(\mathbf{x})^2 - \check{\mathbf{m}}_i^2 \quad (5.47a)$$

$$= (V_{r,i}^2 + V_{i,i}^2) - \check{V}_i^2, \quad i \in \mathbb{M}. \quad (5.47b)$$

The effects of this minor change can be compensated for by altering the associated weights in covariance matrix  $\Sigma$ .

To form the expansions of (5.15b)-(5.15c) and (5.47), we consider some nominal system state, characterized by  $\mathbf{x}_{c0}$ , and some deviation from this nominal value, characterized by  $\delta\mathbf{x}_c = \mathbf{x}_c - \mathbf{x}_{c0}$ . We write the residual expansions as exact functions of this perturbation, valid  $\forall\delta\mathbf{x}_c$ :

$$\tilde{\mathbf{m}}(\delta\mathbf{x}_c) = \mathbf{M}_{c0}^2 + \mathbf{J}_{\tilde{\mathbf{m}},c0}\delta\mathbf{x}_c + \frac{1}{2}\mathbf{H}_{\tilde{\mathbf{m}},c}(\delta\mathbf{x}_c \otimes \delta\mathbf{x}_c) - \check{\mathbf{m}}^2 \quad (5.48)$$

$$\mathbf{f}(\delta\mathbf{x}_c) = \mathbf{F}_{c0} + \mathbf{J}_{\mathbf{f},c0}\delta\mathbf{x}_c + \frac{1}{2}\mathbf{H}_{\mathbf{f},c}(\delta\mathbf{x}_c \otimes \delta\mathbf{x}_c) - \check{\mathbf{f}} \quad (5.49)$$

$$\mathbf{s}(\delta\mathbf{x}_c) = \mathbf{S}_{c0} + \mathbf{J}_{\mathbf{s},c0}\delta\mathbf{x}_c + \frac{1}{2}\mathbf{H}_{\mathbf{s},c}(\delta\mathbf{x}_c \otimes \delta\mathbf{x}_c) - \check{\mathbf{s}}, \quad (5.50)$$

where  $\otimes$  is the Kronecker product, and  $\mathbf{M}_{c0} \equiv \mathbf{M}(\mathbf{x}_{c0})$ ,  $\mathbf{J}_{\tilde{\mathbf{m}},c0} \equiv \mathbf{J}_{\tilde{\mathbf{m}},c}(\mathbf{x}_{c0})$ , etc. Next, we derive the Jacobian  $\mathbf{J}$  and Hessian  $\mathbf{H}$  terms.

We first consider the Jacobian terms in (5.48)-(5.50). Noting that  $\mathbb{Z}_{\{r,i\}} \in \mathbb{R}^{m \times p}$ , the Jacobian associated with (5.47b) is simply

$$J_{\tilde{\mathbf{m}},c} = 2[\mathbb{Z}_r \ \mathbb{Z}_i], \quad \mathbb{Z}_{\{r,i\}i,j} = \begin{cases} \mathbf{V}_{\{r,i\}i}, & j = \mathbb{M}_i \\ 0, & \text{otherwise,} \end{cases} \quad (5.51)$$

where  $\mathbb{M}_i$  refers to the  $i^{\text{th}}$  element of set  $\mathbb{M}$ . The flow and injection Jacobians are first

given in the more familiar polar coordinates:

$$\mathbf{J}_s = (\langle \text{diag}(\mathbf{I}e^{-j\phi}) \rangle + \langle \text{diag}(\mathbf{V}e^{j\theta}) \rangle N \langle Y_b \rangle) R(\mathbf{V}e^{j\theta}) \quad (5.52)$$

$$\mathbf{J}_f = (\langle \text{diag}(\hat{\mathbf{I}}_l e^{-j\hat{\phi}_l}) \hat{E}_1 \rangle + \langle \text{diag}(\hat{E}_1 \mathbf{V}e^{j\theta}) \rangle \hat{N}_l \langle \hat{Y}_l \hat{E} \rangle) R(\mathbf{V}e^{j\theta}). \quad (5.53)$$

The terms  $R(\cdot)$ ,  $N$ , and  $\langle \cdot \rangle$  from (5.52) are explicitly given in [23] and are not re-stated here. Vector  $\mathbf{I}e^{j\phi}$  is the calculated current injections at all non-slack nodes, and vector  $\hat{\mathbf{I}}_l e^{j\hat{\phi}_l}$  is the calculated current flows on all lines with flow measurement devices. The other hatted terms in (5.53) are equal to their non-hatted counterparts, but with the set of non-measured lines removed. The form of the flow Jacobian (5.53) is novel and ultimately represents the derivative of the flow functions (5.15b) on lines where flow measurements exist. In Cartesian coordinates, the injection and flow Jacobians (5.52)-(5.53) simplify down to

$$\mathbf{J}_{s,c} = (\langle \text{diag}(\mathbf{I}_r - j\mathbf{I}_i) \rangle + \langle \text{diag}(\mathbf{V}_r + j\mathbf{V}_i) \rangle N \langle Y_b \rangle) \quad (5.54)$$

$$\mathbf{J}_{f,c} = (\langle \text{diag}(\hat{\mathbf{I}}_{l,r} - j\hat{\mathbf{I}}_{l,i}) \hat{E}_1 \rangle + \langle \text{diag}(\hat{E}_1 (\mathbf{V}_r + j\mathbf{V}_i)) \rangle \hat{N}_l \langle \hat{Y}_l \hat{E} \rangle). \quad (5.55)$$

We observe that Jacobians (5.51), (5.54), (5.55) are *linear* functions of Cartesian voltage, so their associated Hessians  $\mathbf{H}_{\tilde{\mathbf{m}},c}$ ,  $\mathbf{H}_{f,c}$  and  $\mathbf{H}_{s,c}$  are constant. While not derived explicitly, these matrices can be found by taking the derivative of Jacobians (5.51), (5.54), and (5.55) with respect to state vector  $\mathbf{x}_c$  (5.46). In the sequel,  $\mathbf{V}_{r,i}$ , for example, refers to the  $i^{\text{th}}$  element of the vector  $\mathbf{V}_r$  which, by definition, excludes the slack voltage. First, we define the voltage magnitude residual Hessian:

$$\mathbf{H}_{\tilde{\mathbf{m}},c} = \left[ \begin{array}{ccc|ccc} \frac{d\mathbf{J}_{\tilde{\mathbf{m}},c}}{d\mathbf{V}_{r,1}} & \dots & \frac{d\mathbf{J}_{\tilde{\mathbf{m}},c}}{d\mathbf{V}_{r,p}} & \frac{d\mathbf{J}_{\tilde{\mathbf{m}},c}}{d\mathbf{V}_{i,1}} & \dots & \frac{d\mathbf{J}_{\tilde{\mathbf{m}},c}}{d\mathbf{V}_{i,p}} \end{array} \right] \quad (5.56)$$

$$\begin{aligned} \frac{d\mathbf{J}_{\tilde{\mathbf{m}},c}}{d\mathbf{V}_{r,i}} &= 2 [\mathbb{M} \ 0] \\ \frac{d\mathbf{J}_{\tilde{\mathbf{m}},c}}{d\mathbf{V}_{i,i}} &= 2 [0 \ \mathbb{M}] \end{aligned} \quad \mathbb{M}_{j,k} = \begin{cases} 1, & \mathbb{M}_j = i, k = i \\ 0, & \text{otherwise,} \end{cases} \quad (5.57)$$

where  $\mathfrak{m} = |\mathbb{M}|$ ,  $p = n - 1$ ,  $i \in [1, \dots, p]$ ,  $j \in [1, \dots, \mathfrak{m}]$  and  $k \in [1, \dots, p]$ . Next, we define the power flow residual Hessian:

$$\mathbf{H}_{f,c} = \left[ \begin{array}{ccc|ccc} \frac{d\mathbf{J}_{f,c}}{d\mathbf{V}_{r,1}} & \dots & \frac{d\mathbf{J}_{f,c}}{d\mathbf{V}_{r,p}} & \frac{d\mathbf{J}_{f,c}}{d\mathbf{V}_{i,1}} & \dots & \frac{d\mathbf{J}_{f,c}}{d\mathbf{V}_{i,p}} \end{array} \right] \quad (5.58)$$

$$\frac{d\mathbf{J}_{f,c}}{d\mathbf{V}_{r,i}} = \langle \text{diag}(\hat{Y}_l^* \hat{E} \mathbf{e}_i) \hat{E}_1 \rangle + \langle \text{diag}(\hat{E}_1 \mathbf{e}_i) \rangle \hat{N}_l \langle \hat{Y}_l \hat{E} \rangle \quad (5.59)$$

$$\frac{d\mathbf{J}_{f,c}}{d\mathbf{V}_{i,i}} = \langle \text{diag}(-j\hat{Y}_l^* \hat{E} \mathbf{e}_i) \hat{E}_1 \rangle + \langle \text{diag}(j\hat{E}_1 \mathbf{e}_i) \rangle \hat{N}_l \langle \hat{Y}_l \hat{E} \rangle, \quad (5.60)$$

where  $i \in [1, \dots, p]$ , and  $\mathbf{e}_i \in \mathbb{R}^p$  is the standard unit vector. Finally, we define the

power injection residual Hessian:

$$\mathbf{H}_{\mathbf{s},c} = \left[ \begin{array}{ccc|ccc} \frac{d\mathbf{J}_{\mathbf{s},c}}{d\mathbf{V}_{r,1}} & \dots & \frac{d\mathbf{J}_{\mathbf{s},c}}{d\mathbf{V}_{r,p}} & \frac{d\mathbf{J}_{\mathbf{s},c}}{d\mathbf{V}_{i,1}} & \dots & \frac{d\mathbf{J}_{\mathbf{s},c}}{d\mathbf{V}_{i,p}} \end{array} \right] \quad (5.61)$$

$$\frac{d\mathbf{J}_{\mathbf{s},c}}{d\mathbf{V}_{r,i}} = \langle \text{diag}(Y_b^* \mathbf{e}_i) \rangle + \langle \text{diag}(\mathbf{e}_i) \rangle N \langle Y_b \rangle \quad (5.62)$$

$$\frac{d\mathbf{J}_{\mathbf{s},c}}{d\mathbf{V}_{i,i}} = \langle \text{diag}(-jY_b^* \mathbf{e}_i) \rangle + \langle \text{diag}(j\mathbf{e}_i) \rangle N \langle Y_b \rangle. \quad (5.63)$$

Concatenating the function, constant, Jacobian, and Hessian terms of (5.48)-(5.50), and then multiplying through by weighting matrix  $\Sigma^{-\frac{1}{2}}$ , we get

$$\mathbf{r}(\delta\mathbf{x}_c) = \mathbf{R}_{c0} + \mathbf{J}_{c0}\delta\mathbf{x}_c + \frac{1}{2}\mathbf{H}_c(\delta\mathbf{x}_c \otimes \delta\mathbf{x}_c) - \check{\mathbf{r}}_\sigma. \quad (5.64)$$

In (5.64),  $\mathbf{R}_{c0} = \Sigma^{-\frac{1}{2}}[\mathbf{M}_{c0}^{2T}, \mathbf{F}_{c0}^T, \mathbf{S}_{c0}^T]^T$ , and  $\check{\mathbf{r}}_\sigma = \Sigma^{-\frac{1}{2}}[\check{\mathbf{m}}^T, \check{\mathbf{f}}^T, \check{\mathbf{s}}^T]^T$  for example. We note that (5.64) contains measurement profile  $\check{\mathbf{r}}$ ; this will be updated (i.e. perturbed) on each sequential state estimation solve.

## Reduced Order Modeling

We again hypothesize the existence of some subspace  $\mathbb{V} \in \mathbb{R}^{2p \times q}$ ,  $q \ll 2p$ , whose column space can accurately approximate the solution of a state estimation problem:

$$\mathbf{x}_c \approx \mathbb{V}\hat{\mathbf{x}}_c, \quad (5.65)$$

where  $\hat{\mathbf{x}}_c \in \mathbb{R}^q$  is a very low-dimensional vector. Due to linearity,  $\mathbb{V}\hat{\mathbf{x}}_c = \mathbb{V}\hat{\mathbf{x}}_{c0} + \mathbb{V}\delta\hat{\mathbf{x}}_c$ . We now substitute  $\mathbb{V}\delta\hat{\mathbf{x}}_c \approx \delta\mathbf{x}_c$  into residual function (5.64):

$$\mathbf{r}(\delta\hat{\mathbf{x}}_c) = \mathbf{R}_{c0} + \mathbf{J}_{c0}\mathbb{V}\delta\hat{\mathbf{x}}_c + \frac{1}{2}\mathbf{H}_c(\mathbb{V} \otimes \mathbb{V})(\delta\hat{\mathbf{x}}_c \otimes \delta\hat{\mathbf{x}}_c) - \check{\mathbf{r}}_\sigma. \quad (5.66)$$

**Remark 12.** While the state estimation equations of (5.16) are overdetermined due to measurement redundancy, system (5.64) is overdetermined to a much higher degree since we have reduced input dimensionality from  $\mathbf{x} \in \mathbb{R}^{2p}$  to  $\delta\hat{\mathbf{x}}_c \in \mathbb{R}^q$ ,  $q \ll 2p$ .

To further reduce (5.64), we implement the previously proposed projection, where we multiply (5.64) through by  $\hat{\mathbf{J}} \equiv (\mathbf{J}_{c0}\mathbb{V})^T$ :

$$\hat{\mathbf{r}}(\delta\hat{\mathbf{x}}_c) = \hat{\mathbf{R}}_{c0} + \hat{\mathbf{G}}_{c0}\delta\hat{\mathbf{x}}_c + \frac{1}{2}\hat{\mathbf{H}}_c(\delta\hat{\mathbf{x}}_c \otimes \delta\hat{\mathbf{x}}_c) - \hat{\check{\mathbf{r}}}_\sigma, \quad (5.67)$$

whose variable definitions may be inferred. Since (5.67) now has the same number of equations and unknowns, the reduced residual vector  $\hat{\mathbf{r}}(\delta\hat{\mathbf{x}}_c)$  can be driven to zero.

The approximated Newton-like iterative solution for (5.67) is given by

$$\delta\hat{\mathbf{x}}_c^{(i+1)} = \delta\hat{\mathbf{x}}_c^{(i)} - \hat{\mathbf{G}}_{c0}^{-1}\hat{\mathbf{r}}(\delta\hat{\mathbf{x}}_c^{(i)}). \quad (5.68)$$

System (5.68) is extremely low dimensional compared to analogous system (5.20), and it can therefore be iterated very rapidly. When  $\hat{\mathbf{r}} \rightarrow \mathbf{0}$  and (5.68) converges, the low-dimensional solution is converted back to the full order state vector:  $\mathbf{x}_c \leftarrow \mathbf{x}_{c0} + \mathbb{V}\delta\hat{\mathbf{x}}_c$ . As the state estimator solves new measurement profiles, the Jacobian  $\mathbf{J}_{c0}$  is continuously recycled, but  $\hat{\mathbf{R}}_{c0} = (\mathbf{J}_{c0}\mathbb{V})^T\mathbf{R}_{c0}$ ,  $\hat{\mathbf{G}}_{c0} = (\mathbf{J}_{c0}\mathbb{V})^T(\mathbf{J}_{c0}\mathbb{V})$ , and  $\hat{\mathbf{H}}_c = (\mathbf{J}_{c0}\mathbb{V})^T\mathbf{H}_c(\mathbb{V}\otimes\mathbb{V})$  are continuously updated as basis  $\mathbb{V}$  dynamically expands.

**Definition 16.** We define the iterative algorithm (5.68) as the Reduced Model State Estimator (**RMSE**).

### Dynamic Subspace Expansion

In order to dynamically construct the orthonormalized subspace  $\mathbb{V}$ , we leverage the dynamic subspace expansion approach proposed in [54]. Our version of this procedure takes sequential *state estimation* solutions  $\mathbf{x}_c$  and projects them onto the subspace:  $\mathbf{v} = \mathbf{x}_c - \mathbb{V}\mathbb{V}^T\mathbf{x}_c$ . If  $\|\mathbf{v}\| > \epsilon$ , then  $\mathbb{V}$  is updated:

$$\mathbb{V} = [\mathbb{V} \ \mathbf{v}/\|\mathbf{v}\|]. \quad (5.69)$$

When  $\mathbb{V}$  is updated, the values of  $\hat{\mathbf{R}}_{c0}$ ,  $\hat{\mathbf{G}}_{c0}$ , and  $\hat{\mathbf{H}}_c$  are also updated. Vector  $\hat{\mathbf{r}}_\sigma$  is also updated, but this changes for each new measurement profile, regardless. For an efficient update scheme, please refer to the DSE algorithm presented in the previous section (i.e. Algorithm 12).

**Definition 17.** We define the update procedure (5.69) and the associated updates of  $\hat{\mathbf{R}}_{c0}$ ,  $\hat{\mathbf{G}}_{c0}$ , and  $\hat{\mathbf{H}}_c$  as the Dynamic Subspace Expansion (**DSE**) routine.

### Accelerated Probabilistic State Estimation

We now describe the full APSE procedure, which is depicted in Fig. 5-8. For each new measurement profile input  $\check{\mathbf{r}}_i$ , the RMSE of (5.68) attempts to solve the state estimation problem. If the solution does not meet the convergence criteria of the full order state estimator, then the Gauss-Newton via QR factorization algorithm of (5.22) is used to solve the system. Finally, if the GNvQR solution does not have a sufficiently

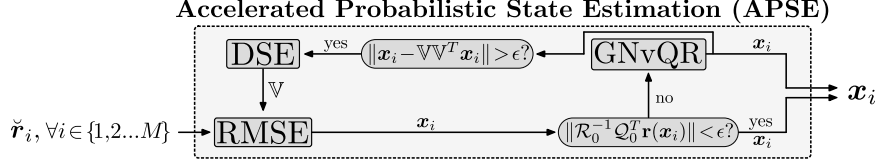


Figure 5-8: In the APSE algorithm, sampled measurement profiles are passed to the RMSE. If the results are of sufficient accuracy, the solver moves on to the next measurement profile. Otherwise, GNvQR solves the system. The resulting solution is then conditionally used to update basis  $\mathbb{V}$ .

large component is the basis, then  $\mathbb{V}$  is updated and passed back the RMSE. As basis  $\mathbb{V}$  expands, the RMSE returns solutions which are of higher and higher accuracy. For more detailed steps, Algorithm 14 provides procedural pseudocode.

Testing the quality of the RMSE solution on the full order model is a nontrivial operation. Since an optimal state estimation solution generally yields a non-zero residual, decreasing step size is often used as convergence criteria. To test if our RMSE solution meets this step size-based convergence criteria, we pre-factor a scaled Jacobian via  $\mathcal{Q}_0 \mathcal{R}_0 = \Sigma^{-\frac{1}{2}} \mathbf{J}_{c0}$ , where, for speed,  $\mathcal{Q}_0$  and  $\mathcal{R}_0$  are continually recycled. If

$$\|\mathcal{R}_0^{-1} \mathcal{Q}_0^T \mathbf{r}(\mathbf{x}_i)\|_\infty < \epsilon \quad (5.70)$$

is satisfied, then the RMSE solution is accepted. This test is shown on bottom right of Fig. 5-8 and line 12 of Algorithm 14.

### 5.3.2 Numerical Test Results

In this section, we present test results collected from the unbalanced, three-phase IEEE 8500-node distribution network. A detailed overview of this system is provided in the previous section. To engender a realistic amount of measurement redundancy, we assume complex power flow measurements are collected on 300 medium-voltage lines throughout the network, and voltage magnitude measurements are collected at 300 medium-voltage nodes throughout the network. At the majority of the approximately 2,500 low-voltage loads, we assume the availability of real-time smart-meter data in the form of complex power injection measurements.

Next, we identify two regions in the network which contain substantial load measurement uncertainty<sup>2</sup>. These regions are termed Uncertainty Regions (URs), and

---

<sup>2</sup>Such uncertainty could be caused by localized inclement weather effects, localized signal loss, or

---

**Algorithm 14** Accelerated Probabilistic State Estimator (APSE)

---

**Require:** Initial voltage solution  $\mathbf{x}_{c0}$  of measurement profile  $\check{\mathbf{r}}_0$ , weighted  $\mathbf{R}_{c0}$  and weighted Jacobian  $\mathbf{J}_{c0}$  evaluated at  $\mathbf{x}_{c0}$ , weighted Hessian  $\mathbf{H}_c$ , measurement profiles  $\check{\mathbf{r}}_i$  for  $i = 1, 2, \dots, M$

```

1: function  $[\mathbf{x}_1, \mathbf{x}_2, \dots, \mathbf{x}_M] \leftarrow \text{APSE}(\check{\mathbf{r}}, \mathbf{x}_{c0}, \mathbf{R}_{c0}, \mathbf{J}_{c0}, \mathbf{H}_c, J_{\mathbf{r}}(\cdot), \Sigma)$ 
2:    $\hat{\mathbf{x}}_{c0} \leftarrow \|\mathbf{x}_{c0}\|$ 
3:    $\mathbb{V} \leftarrow \mathbf{x}_{c0}/\hat{\mathbf{x}}_{c0}$ 
4:    $\hat{\mathbf{R}}_{c0} \leftarrow (\mathbf{J}_{c0}\mathbb{V})^T \mathbf{R}_{c0}$ 
5:    $\hat{\mathbf{G}}_{c0} \leftarrow (\mathbf{J}_{c0}\mathbb{V})^T (\mathbf{J}_{c0}\mathbb{V})$ 
6:    $\hat{\mathbf{H}}_c \leftarrow (\mathbf{J}_{c0}\mathbb{V})^T \mathbf{H}_c (\mathbb{V} \otimes \mathbb{V})$ 
7:    $i \leftarrow 1$ 
8:   while  $i \leq M$  do
9:      $\hat{\check{\mathbf{r}}}_i \leftarrow (\mathbf{J}_{c0}\mathbb{V})^T \Sigma^{-\frac{1}{2}} \check{\mathbf{r}}_i$ 
10:     $\delta\hat{\mathbf{x}}_c \leftarrow \text{Solve RMSE of (5.68) to convergence}$ 
11:     $\mathbf{x}_i \leftarrow \text{Cartesian-to-Polar}\{\mathbf{x}_{c0} + \mathbb{V}\delta\hat{\mathbf{x}}_c\}$ 
12:    if  $\|\mathcal{R}_0^{-1}\mathcal{Q}_0^T \mathbf{r}(\mathbf{x}_i)\|_\infty > \text{tolerance } \epsilon_N$  then
13:       $\mathbf{x}_i \leftarrow \text{Solve GNvQR of (5.22) to convergence}$ 
14:       $\mathbf{x}_{c,i} \leftarrow \text{Polar-to-Cartesian}\{\mathbf{x}_i\}$ 
15:      Update  $\mathbb{V}, \hat{\mathbf{R}}_{c0}, \hat{\mathbf{G}}_{c0}, \hat{\mathbf{H}}_c$  via (5.69) and DSE routine
16:    end
16:     $i \leftarrow i + 1$ 
end
17: return  $\mathbf{x}_1, \mathbf{x}_2, \dots, \mathbf{x}_M$ 

```

---

both of them are geographically identified in Fig. 5-9. As in [110], we assume the load uncertainty in these URs is uniformly distributed. The upper and lower bounds of these uniform distributions are chosen as  $\pm 50\%$  of the historical usage mean. Next, we sample from each of these load distributions 1000 times, and we then solve 1000 instantiations of the state estimation problem (5.17).

For comparison purposes, we first solve each of the resulting state estimation problems using the traditional GNvQR algorithm (5.22). Sample voltage and current results are shown in Fig. 5-10. Timing results are shown in Fig. 5-11. The average solve time of the GNvQR algorithm for each measurement profile was **0.33 seconds**, yielding a total solve time of 332 seconds.

Next, we solved the sequential state estimation problems using the APSE procedure. The timing results in Fig. 5-10 show that once the subspace  $\mathbb{V}$  had been completed (i.e it was filled out enough to solve all future measurement profiles), the APSE algorithm was approximately **4.5 times faster** than the traditional GNvQR solver. Furthermore, we include the solve times of the RMSE algorithm itself (which is internal to the APSE – see Fig. 5-8). The RMSE is *an order of magnitude faster* than the APSE. This is because the main bottleneck of the APSE is not the reduced even a lack of measurement devices in some region.

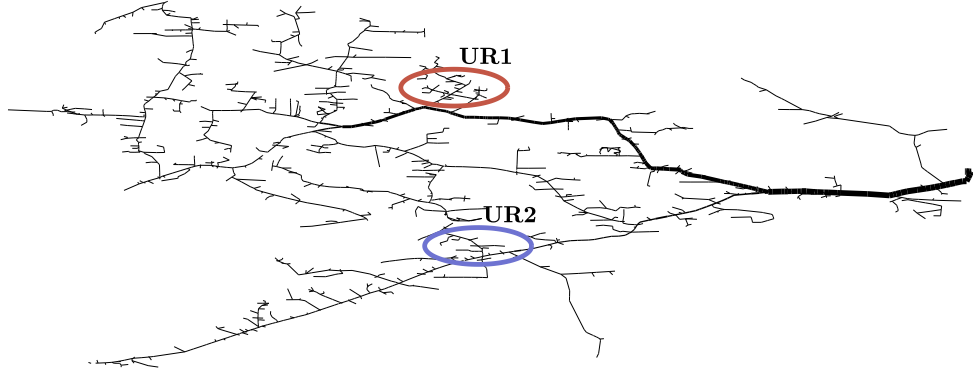


Figure 5-9: Map of the 8500-node network (LV distribution load buses not shown). The two measurement Uncertainty Regions (URs) are identified. In each of these URs, we identify 30 loads whose measurements are highly uncertain.

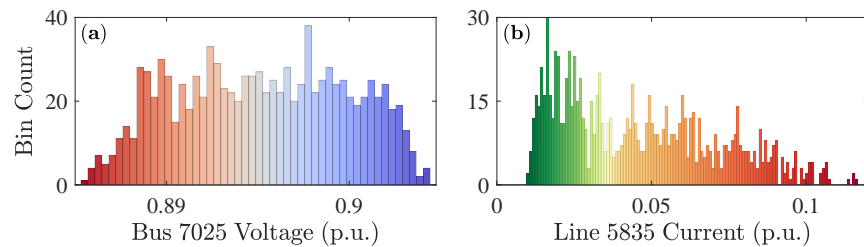


Figure 5-10: Shown are voltage magnitude (panel (a)) and current magnitude (panel (b)) histograms resulting from the 1000 solves of the 8500-node network.

model solves, but instead the testing of the reduced model solution on the full order model via (5.70). Future work will focus on developing a reduced model solution testing procedure which is faster than (5.70).

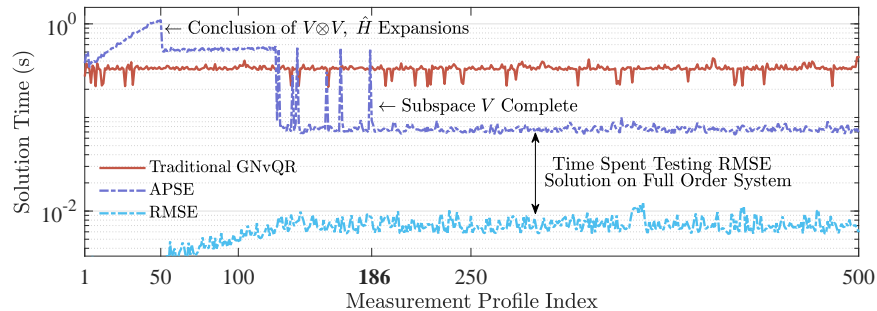


Figure 5-11: Timing analysis of the full order solver (GNvQR), the APSE, and the RMSE. After measurement profile 186, the APSE is 4.5 times faster than the GNvQR procedure. The amount of time spent testing the RMSE solution via (5.70) dominates the APSE and is shown by the double-arrow. The expansion of  $\hat{\mathbf{H}}$  concludes after measurement profile 50.

# Chapter 6

## Conclusions and Future Work

In this chapter, we offer concluding remarks associated with each of the problems considered in this thesis. Following these remarks, we offer a series of proposed future work extensions associated with each project.

### 6.1 Concluding Remarks

Through extensive investigations, we have confirmed the central premise of the thesis, as stated in Section 1.1. That is, we conclude that the inverse problem tools of inference, estimation, and prediction can be used to characterize useful<sup>1</sup> power system models. While each of the addressed problems are united under the same application (i.e. data-driven control of power systems), the modeling and solution methodologies varied widely. Before recounting the specific contributions and results from each chapter, we first offer a single descriptive paragraph which ties all four modeling and solution methodologies together in a single cohesive manner.

Locating the sources of forced oscillations in power systems can be simplified by considering an equivalent problem in the frequency domain, where FO sources show up like analogous current injections. Since the associated equivalent circuit obeys the corresponding laws of steady-state linear circuit theory, including Tellegen’s theorem, various forms of quadratic power are conserved in the network, and the system can be naturally analyzed from an (incremental) energy perspective. On a smaller scale, microgrid networks can be described identically, minus the forcing function, with all of their linearized dynamics encoded in a perturbative

---

<sup>1</sup>The term “useful” is defined relative to the application (i.e. data-driven control from Fig. 1-1) and the ultimate goal of the application (i.e. power system stability).

admittance matrix model. By analyzing the frequency response associated with this model’s constituent components, quadratic energy functions (i.e. DQR-transformation matrices) can be identified which guarantee the transformed system will remain DQR, and therefore, small-signal stable under any interconnection of the considered devices. In both problems (FOs and microgrids), though, a suitable linearized model is required to perform such analysis. To this end, vector fitting approaches, such as the proposed RTVF procedure, can leverage measured terminal input/output data to construct a MIMO surrogate model of such underlying linearized dynamics. Despite its predictive capabilities, such a model will naturally be a surrogate of (typically) reduced order, only capturing the effects which are sufficiently salient in the observed data. The sheer size of power systems naturally invites such reduced order modeling techniques. Model order reduction can be applied not only to the system dynamics, but also to the steady state network models, whose solutions typically operate in low-dimensional subspaces over short operational periods due to natural loading correlation and engineered network structuring. Accordingly, a reduced order surrogate model of the network’s power flow equations can be constructed via projection-based model order reduction techniques. Once completed, this densely structured ROM can be used to solve the network equations, relative to some practical degree of accuracy, orders of magnitude faster than the full order model can.

### 6.1.1 Forced Oscillations

In Chapter 2, we proposed an equivalent circuit transformation of a time domain power system model. This equivalent circuit is constructed by linearizing and carefully transforming the power system model into the frequency domain, and thus constructing the FRF associated with individual network elements. In order to perform source identification, we showed that FO sources show up like current sources in this equivalent circuit. By comparing a generator’s measured and predicted current spectrums around the forcing frequency, and then comparing the results to a calculated noise floor, we developed a simple decentralized procedure for locating the source of the current injection (i.e. FO) exciting the circuit. Initially, our methodology assumed the operator has access to the high fidelity generator models and their associated parameters.

In the second part of this chapter, we developed a Bayesian framework for locating the sources of FOs in the presence of generator model parameter uncertainty and strong measurement noise effects. By incorporating generator model parameter priors and a carefully constructed likelihood function, we formulated a Maximum A Poste-

riori optimization problem which could be solved in a decentralized manner. In each of the provided test cases, the optimizer was able to reconstruct the generator parameters with a sufficiently high degree of accuracy to ultimately allow for the origins of the FOs to be exactly located. Additionally, the method showed good performance in the context of a system experiencing multiple concurrent FOs. Although applied exclusively to generators, the methodology could be extended to other dynamic elements of the power system, such as dynamic loads or FACTS devices, which may also represent FO sources. And while Algorithm 1 was designed for the purpose of locating FO sources, it also presents a potentially useful method for performing independent parameter estimation, with direct applications to dynamic model verification and load modeling.

In the third part of this chapter, we interpreted the popular DEF method from the viewpoint of either (i) a dissipative system with a particular quadratic supply rate in the time domain, or (ii) a transformed system which became positive real in the frequency domain. After defining the associated DQR-transformation matrices, we were able to use eigenvalue analysis to algebraically classify various component models from power systems as either DQR or non-DQR. Next, we utilized the proposed equivalent circuit transformation to build up a full “perturbative” system model; this perturbative model provides a useful framework for understanding how FOs linearly propagate in a electrical power systems. Using Tellegen’s theorem, we leveraged this perturbative propagation framework to further motivate and analyze the DEF method at a system level; this is the first system-level investigation of the DEF method, to the authors’ knowledge. We proved that the DEF’s shortcomings in a classical power system cannot be avoided by simply selecting a new DQR-transformation (quadratic energy function). We further developed necessary (and by extension, sufficient) conditions for the failure of the DEF method. When power system operators have access to an analytical system model, they may use our proposed framework to analytically predict apriori if the DEF method might fail ( $\lambda_1 \geq 0, \lambda_2 \leq 0$ ), will fail ( $\lambda_1, \lambda_2 \leq 0$ ), or will succeed ( $\lambda_1, \lambda_2 \geq 0$ ). This may be especially useful in small, microgrid networks where system architecture is known more fully and line loss ratios are much higher. One obvious drawback to the proposed approach for the apriori testing of DEF performance is the need for an analytical system model. Load models, especially, may be highly uncertain from the perspective of a system operator. Several of the theorems in this section assumed a lossy classical power system model, but the underlying frameworks for building the perturbative network model and testing the DEF method are actually quite general and can be used to interpret a variety of

linear propagation phenomena.

### 6.1.2 Microgrid Stability Certificates

In Chapter 3, we developed fully decentralized small-signal stability criteria for microgrid networks. If satisfied, this criteria can allow for the plug-and-play operability of the considered microgrid elements. The proposed decentralized conditions allow us to step beyond the traditional DQR approach (which utilizes a standard quadratic energy function) and utilize different certificates in different regions of frequency domain. We believe that these results will have practical impact, such as by fostering the development of ready-to-use standards for microgrid loads and sources, that can be directly used by industry.

In the first part of the chapter, we considered DC microgrids, and we developed a procedure which simply analyzes the phase response of properly parameterized microgrid elements. If the phase responses satisfy (or, can be *engineered* to satisfy) certain criteria across some region of the frequency domain, then there exists an energy function which can certify the small-signal stability of the considered elements, under an arbitrary interconnection, in that particular region of the frequency spectrum. We then tested the proposed methods on a simulated low voltage DC microgrid network with buck-converter interfaced loads.

In the second part of the chapter, we considered AC microgrids, where the simple phase condition developed in the first part is systematically replaced by parameterized transformation matrices. Once identified, these transformation matrices can be used to certify the plug-and-play stability of various AC microgrid elements across relevant bands of the frequency spectrum. In the test results section, we identified once such matrix which was parameterized using sigmoid functions and could certify the plug-and-play stability of a droop-controlled inverter-based AC microgrid model (for the given parameter values).

### 6.1.3 Predictive Modeling via Vector Fitting

In Chapter 4, we proposed a new procedure, termed Real-Time Vector Fitting (RTVF), which performs real-time predictive modeling of linearized dynamics. While the RTVF algorithm can be applied across a broad range of dynamical engineering systems, it was specifically developed to perform real-time predictive modeling of generator dynamics in the presence of ambient perturbations. Accordingly, RTVF explicitly accounts for the presence of initial state decay in the generator's observed

outputs. Also, RTVF can be applied in the face of concurrently active input signals, since this is a practical constraint for any three-phase power system component modeled using a quasi-stationary phasor approximation at its terminals. The simulated test results, collected from synthetic test systems and high order nonlinear generator models, show-cased RTVF’s ability to perform online predictive modeling with a high degree of accuracy. In order to model power system components which have some degree of inherent stochasticity, we proposed an extension of the RTVF protocol, termed stochastic-RTVF (sRTVF). Using correlation functions, sRTVF attempts to eliminate unobservable noisy inputs which stochastically interfere with deterministic predictive modeling methods (such as the canonically posed RTVF).

Given the widescale deployment of PMUs and the newly mandated MOD-33 modeling/validation ordinances, RTVF provides power system operators with a valuable tool. This tool, for example, can build real-time models of generator systems whose physical prior models are completely unknown. It can also validate or enhance prior models which are supposedly well known. Additionally, since controller parameters (e.g. droop gains) are often changed at the local level without system operator awareness, RTVF can be used to infer the true value of these parameters in real-time. Such capability allows system operators to maintain small-signal stability and ensure that generators are properly adhering to market regulations. To enhance practical effectiveness, future extensions could couple RTVF with advanced measurement noise filtering mechanisms. Also, physically-aware regularization techniques could be developed to allow system operators to more effectively “track” a system’s shifting dynamics as operating equilibriums evolve over time.

#### 6.1.4 Distribution System Power Flow and State Estimation

In Chapter 5, we showed how to speed up “any” sampling-based PPF solver by 1) leveraging the low-rank nature of distribution network voltage profiles and generating a surrogate ROM, and 2) exploiting the “small” nature of distribution network loads and applying a custom Neumann series-based method. Our resulting APPF algorithm, which combines both contributions, was tested on the 8500-node network, speeding up state of the art PPF methods by up to 60 times.

Next, we applied the same ROM methodology to the problem of probabilistic state estimation in distribution systems. The resulting algorithm, termed the Accelerated Probabilistic State Estimator (APSE), was found to be approximately 4.5 times faster than a traditional full order Gauss-Newton-based state estimator in the 8500-node

network. The super majority of the APSE run-time, though, was spent testing the quality of the resulting solution on the full order system. Without this test, the APSE is over 50 times faster than the full order estimator.

Coupling the APPF and APSE algorithms with advanced uncertainty quantification and collocation sampling tools will be a highly useful and readily applicable next step for this work. Dramatically speeding up power flow and state estimation solve times in massive distribution networks, though, has a plethora of potential uses, even beyond short-term probabilistic modeling. For example, the methods can be applied when solving the network equations associated with any ensemble of power injection profiles. This ensemble could be associated with some long-term planning horizon for either determining optimal control policies or making asset utilization and investment decisions. Additionally, due to its small size and dense structure, the ROM itself could (i) contain practically useful information about the network and (ii) be used as a surrogate in all sorts of real-time model predictive control (MPC) applications which are inherently time constrained.

## 6.2 Future Work Extensions

We now present three potential extensions to the work presented in this thesis. The first extension proposes the use of machine learning for identifying more suitable energy functions for oscillation tracing and microgrid stability analysis. The second proposes embedding a Volterra series into the vector fitting formulation to capture nonlinear (or at least weakly nonlinear) effects. Finally, the third extension proposes an observability framework for distribution grid estimation and control.

### 6.2.1 Identifying Effective Energy Functions: From Semidefinite Programming to Neural Networks

In Chapters 2 and 3, we relied heavily on, so-called, DQR-transformation matrices  $\mathbf{M}(s)$  and  $\boldsymbol{\Gamma}(s)$ . For example, in Chapter 2, we identified the DQR-transformation matrices implicitly associated with the DEF method, and in Chapter 3, we sought to identify parameterized versions of these matrices (i.e.  $\mathbf{M}(s, \alpha)$ ,  $\boldsymbol{\Gamma}(s, \alpha)$ ) that could generate decentralized small-signal stability certificates.

## A Semidefinite Programming Approach

In order to both (i) improve upon existing energy-based methods for performing FO source identification, and (ii) identify matrices which render a larger class of microgrid components DQR, semidefinite programming approaches can be naturally formulated. While the following methodology could be applied to either problem (i) or (ii), we use FO tracing (rather than microgrid stability) as the guiding example.

Consider a linearized power system  $\Sigma_l$  composed of many linearized sub-systems  $\Sigma_{l,i}$  (i.e. lines, loads, generators with controllers). Each of these subsystems are characterized by two primary features: parameter values ( $\mathbf{p}$ ) and equilibrium point ( $\kappa$ ). We then build the frequency response function  $\mathcal{Y}_i(\omega, \mathbf{p}, \kappa)$  for each of these elements, which is a function of frequency, parameter values, and linearization (equilibrium) point  $\kappa$ . Our task, then, is to find a set of common transformation matrices  $\mathbf{M}(\omega)$  and  $\mathbf{\Gamma}(\omega)$  which render all elements of the network positive real, across all potential parameter values and equilibrium points. Mathematically, this can be stated as a feasibility problem: can we find common matrices  $\mathbf{M}(\omega)$  and  $\mathbf{\Gamma}(\omega)$  which simultaneously make all system elements positive real?

$$\begin{aligned} & \min_{\mathbf{M}, \mathbf{\Gamma}} \{ \cdot \} \\ \text{s.t. } & \mathbf{M}(\omega) \mathcal{Y}_i(\omega, \mathbf{p}, \kappa) \mathbf{\Gamma}(\omega) + (\mathbf{M}(\omega) \mathcal{Y}_i(\omega, \mathbf{p}, \kappa) \mathbf{\Gamma}(\omega))^{\dagger} \succ 0, \forall_i, \forall \omega > 0, \forall \mathbf{p} \in \mathcal{P}, \forall \kappa \in \mathcal{K} \\ & \det\{\mathbf{M}(\omega)\} \neq 0, \forall \omega > 0 \\ & \det\{\mathbf{\Gamma}(\omega)\} \neq 0, \forall \omega > 0, \end{aligned} \tag{6.1}$$

where  $\mathcal{P}$  is the plausible set of model parameters and  $\mathcal{K}$  is the plausible set of equilibrium points. If we can find these matrices, then per (2.126), there will be an associated time domain integral which “outperforms” the DEF method. As posed (6.1), is totally intractable and, per Theorem 2, certainly infeasible. Therefore, we can transform (6.1) into a relaxed minimization which just penalizes the constraint for not being met exactly. One such relaxation might penalize the cost function whenever both eigenvalues are not positive:

$$\begin{aligned} & \max_{\mathbf{M}, \mathbf{\Gamma}} \sum_{i, \omega, \kappa, \mathbf{p}} \det\{\mathbf{A}_i(\omega, \mathbf{p}, \kappa)\} \cdot \text{trace}\{\mathbf{A}_i(\omega, \mathbf{p}, \kappa)\} \\ \text{s.t. } & \mathbf{A}_i(\omega, \mathbf{p}, \kappa) = \mathbf{M}(\omega) \mathcal{Y}_i(\omega, \mathbf{p}, \kappa) \mathbf{\Gamma}(\omega) + (\mathbf{M}(\omega) \mathcal{Y}_i(\omega, \mathbf{p}, \kappa) \mathbf{\Gamma}(\omega))^{\dagger} \\ & \det\{\mathbf{M}(\omega)\} \neq 0, \forall \omega > 0 \\ & \det\{\mathbf{\Gamma}(\omega)\} \neq 0, \forall \omega > 0. \end{aligned} \tag{6.2}$$

Such an optimization approach may still be computationally infeasible, given its sheer size, and the resulting matrices may not be able to render “enough” system components DQR.

### A Neural Network Approach

Alternatively, we can choose to search for any energy function which is not constrained to a quadratic functional form. In this case, concepts such as positive realness and DQR are no longer relevant, because the supply rate is no longer quadratic in nature. Instead, we can look for some sort of generic non-singular energy functional which always decays. To state this mathematically, we define the dynamical transition function  $\Phi_i$  which maps the inputs from sub-system  $\Sigma_i$  to its outputs (through time domain integration somehow):  $\mathbf{y} = \Phi_i(\mathbf{u}, \mathbf{p}, \kappa)$ . Using massive amount of training data, we can seek to use a neural network which effectively identifies a function  $f(\cdot)$  which satisfies

$$\begin{aligned} & \min_{f(\cdot)} \{\cdot\} \\ \text{s.t. } & f(\mathbf{u}, \mathbf{y}) > 0, \forall i, \forall \mathbf{u}, \forall \mathbf{p}, \forall \kappa \\ & \mathbf{y} = \Phi_i(\mathbf{u}, \mathbf{p}, \kappa). \end{aligned}$$

Other constraints are probably needed, and the function may need a more specific form. The main idea, though, is this: if all elements of the network dissipate the “energy” defined in function  $f(\cdot)$ , then the source must supply this “energy”.

#### 6.2.2 Predictive Modeling of Weakly Nonlinear Systems: Embedding a Volterra Series inside Vector Fitting

Despite its versatility, efficiency, and predictive modeling capabilities, vector fitting approaches are highly sensitive to, and greatly impacted by, the effects of nonlinear residuals in the data. Accordingly, the VF approaches presented in this thesis are only suitable when the underlying dynamics are highly linear (i.e. weakly, weakly nonlinear). In order to overcome this limitation, future work can focus on embedding a so-called Volterra series [63] inside of a time domain-based vector fitting formulation. Volterra series are most applicable for describing weakly nonlinear systems, and they are commonly used to capture the distortion effects associated with transistor amplification.

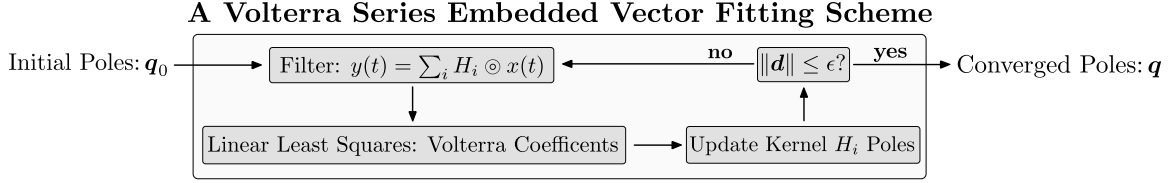


Figure 6-1: A depiction of a vector fitting procedure which has been embedded with a Volterra series representation of the underlying dynamical system.

TDVF, RTVF, and sRTVF all leverage a classical result of linear system theory:

$$y(t) = \int_0^t h(t - \tau)x(\tau)d\tau. \quad (6.3)$$

That is, the output  $y(t)$  of a linear system can be computed by convolving the input  $x(t)$  with the system dynamics  $h(t)$  (as codified by the impulse response). When the system dynamics are not linear, though, a Volterra series may be instead employed:

$$\begin{aligned} y(t) = h_0 + \int_0^t h_1(\tau)x(t - \tau)d\tau + \int_0^t h_2(\tau_1, \tau_2)x(t - \tau_1)x(t - \tau_2)d\tau_1 d\tau_2 \\ + \int_0^t h_3(\tau_1, \tau_2, \tau_3)x(t - \tau_1)x(t - \tau_2)x(t - \tau_3)d\tau_1 d\tau_2 d\tau_3 + \dots \end{aligned} \quad (6.4)$$

where  $h_i$  are known as Volterra kernels. For convenience, we choose to write (6.4) via  $y(t) = \sum_i H_i \odot x(t)$ . To formulate a vector fitting-type problem, we recognize (6.4) as a sort of filtering procedure associated with some set of basis poles. Once this filtering has occurred, the standard vector fitting procedure may commence, as depicted by Fig. 6-1. In this procedure, once the “filtering” stage as been completed, the (generalized) residual coefficients can be solved for in a linear least squares sense<sup>2</sup>. Next, the basis poles of the Volterra kernels can be updated using these new residual coefficients. Finally, a convergence criteria can be tested.

Regarding this proposed procedure, there are two primary open research questions. First, how can the Volterra series representation be embedded with basis poles, as we do in standard vector fitting? (See, for example, the  $s - q_n$  terms in (4.7)). Second, once the residual coefficients have been computed, how do we update the basis-embedded-kernels, as portrayed in the lower right block of Fig. 6-1? Once these technical questions have been addressed, the procedure could be ready for testing.

---

<sup>2</sup>In order to effectively shrink the dimensionality of the problem, slight  $l_2$  norm regularization can be added which penalizes the size of the coefficients associated with the most nonlinear components of the model. This may help “steer” the solution towards a more linear one, if desired.

As one final note, we recall that the stochastic-RTVF scheme is built around the fundamental principle of causality. Since any physical system, be it hyper-nonlinear or purely linear, obeys causality, we note that a stochastic variation of the Volterra embedded procedure from Fig. 6-1 may be realized. This could allow for the real-time predictive modeling of nonlinear systems which suffer from unobservable stochastic variations. Such an algorithm could be very powerful and extremely useful.

### 6.2.3 Representing the Estimation, Control and Performance of Distribution Grids as a Cascade of Nonlinear Maps

In this subsection, we consider how the interaction between estimation, control, and performance maps can lead to a smaller, more targeted reduced order model of a distribution network. We begin by considering the operational paradigm portrayed by Fig. 6-2. In this figure, state estimation yields some data set  $\mathbf{x}$ . Next, this data set is used to make some set of control decisions  $\mathbf{w}$ . Finally, the control decisions have an impact on the network, and this is quantified by some performance metric  $\mathbf{m}$ , which somehow quantifies the performance of the network in practically meaningful ways. An important observation, though, is that some data which is “observed” through the state estimation routine may not be used or needed by the controller. Furthermore, we note that some control decisions may have no impact on the performance of the network. Practical quantification of such impact, though, must be performed in a high dimensional space, since the interaction between certain control decisions could amplify or negate each other<sup>3</sup>. In the end, the performance metric  $\mathbf{m}$  is key, and observable data and control decisions which do not affect the system performance are effectively irrelevant. The functions in Fig. 6-2 inspire the following interactions:

$$\mathbf{m} = \mathbf{f}(\mathbf{x}, \mathbf{p}, \mathbf{w}) \tag{6.5a}$$

$$= \mathbf{f}(\mathbf{x}, \mathbf{p}, \mathbf{h}(\mathbf{x}, \mathbf{p})) \tag{6.5b}$$

$$= \mathbf{f}(\mathbf{g}^{-1}(\mathbf{y}), \mathbf{p}, \mathbf{h}(\mathbf{g}^{-1}(\mathbf{y}), \mathbf{p})). \tag{6.5c}$$

With this observation in mind, we may consider Fig. 6-3, which shows the explicit overlap between estimation, control, and performance. The star in the middle represents the region of state space which can be estimated, is used by the controller,

---

<sup>3</sup>Consider, for example, a difference amplifier in the field of circuits:  $y = K(x_1 - x_2)$ . While output  $y$  is sensitive to both  $\Delta x_1$  and  $\Delta x_2$ , it is not sensitive to  $\Delta x_1 = \Delta x_2$ .

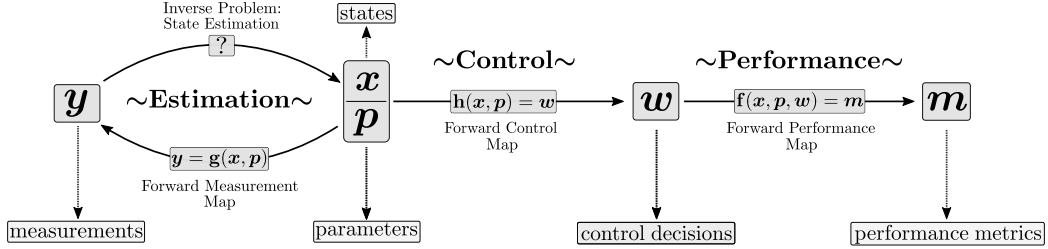


Figure 6-2: Interaction between estimation, control, and performance processes in a distribution network.

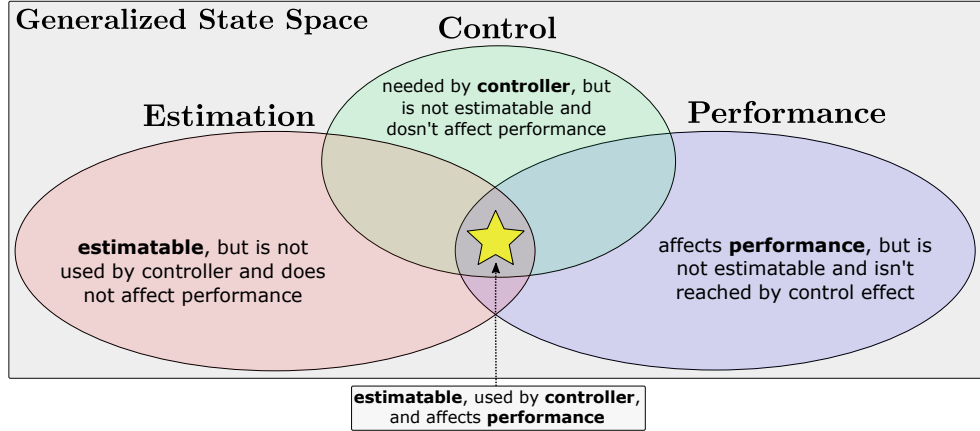


Figure 6-3: Overlap between what can be observed through state estimation, what is needed for control, and what affects system performance. This diagram is overlaid on a “generalized” state space, since the state space region might refer to more than just the canonical nodal voltage “state” vector  $\mathbf{x} = [\mathbf{V}^T, \boldsymbol{\theta}^T]^T$ . We note that in a practical system, some regions of overlap between these circles may be null.

and eventually has effect on the system performance metric. From the perspective of state estimation/reconstruction by a ROM, this is the most important region of the diagram, since the results will be both used by a controller and have effect on the system performance.

In order to speed up the power flow and state estimation problems, we leveraged a ROM of the power flow and state estimation equations. When building up this ROM, we ensured that it would be able to accurately reconstruct the full state of the network (i.e. accurate complex voltages at every node in the network). From a practical perspective though, we can seek to construct a reduced order model whose output preserves the relationship between performance  $\mathbf{m}$  and measurements (or forecasts)  $\mathbf{y}$  from (6.5c). Thus, future work should characterize (6.5c) and implement a more targeted reduced order modeling strategy in order to eliminate aspects of the ROM which produce information which has no effect on system performance.



# Appendix A

## Forced Oscillation Modeling Tools

### A.1 Modeling Phase Shifting Transformers

We consider the complications associated with a two port element whose current flow is not a linear function of terminal voltage differentials. To do so, we return to a *standard* steady state (rather than perturbative) power system model, and we consider a transmission line with complex admittance  $\tilde{y}_{ij} \in \mathbb{C}^1$ . If  $\tilde{V}_i, \tilde{V}_j \in \mathbb{C}^1$  are the phasor voltages associated with buses  $i$  and  $j$ , then the standard two port model associated with a tap changing transformer may be stated as

$$\begin{bmatrix} \tilde{I}_{ij} \\ \tilde{I}_{ji} \end{bmatrix} = \begin{bmatrix} \frac{\tilde{y}_{ij}}{c^2} & -\frac{\tilde{y}_{ij}}{c} \\ -\frac{\tilde{y}_{ij}}{c} & \tilde{y}_{ij} \end{bmatrix} \begin{bmatrix} \tilde{V}_i \\ \tilde{V}_j \end{bmatrix}, \quad (\text{A.1})$$

where  $c$  is the tap ratio and  $\tilde{I}_{ij}, \tilde{I}_{ji} \in \mathbb{C}^1$  are the current flows. Considering the top equation, the flow  $\tilde{I}_{ij}$  may be written as

$$\tilde{I}_{ij} = \frac{\tilde{y}_{ij}}{c^2} \tilde{V}_i - \frac{\tilde{y}_{ij}}{c} \tilde{V}_j \quad (\text{A.2a})$$

$$= \frac{\tilde{y}_{ij}}{c} \left( \tilde{V}_i - \tilde{V}_j \right) + \tilde{V}_i \tilde{y}_{ij} \left( \frac{1-c}{c^2} \right). \quad (\text{A.2b})$$

From (A.2b), we may thus interpret  $\tilde{y}_{ij}/c$  as the series impedance between the lines, and we may interpret  $\tilde{V}_i \tilde{y}_{ij}(1-c)/c^2$  as a *shunt* current injection at bus  $i$  caused by the tap changer. A similar shunt injection will exist at bus  $j$ . In this way, any two port element whose current flow isn't directly proportional to  $\tilde{V}_i - \tilde{V}_j$  (phase shifting transformer, HVDC line, etc.) can be expressed as the sum of a linear flow term and a shunt injection term. Once these relations are appropriately converted into the perturbative system model, matrices (2.160) and (2.162) can be updated accordingly.

## A.2 Polar to Cartesian Transformation Matrices

An inherent problem exists when attempting to compute (2.199) in a realistic power system. Because the system has natural integration effects, the phase angles of the system constantly drift; this can be seen in the (simulated or real) time series data of any system with stochastic loads. Because generator admittance can be a function of steady state rotor angle  $\delta$ , such as in (2.135), the underlying admittance will be constantly changing as system phase angle drifts. Due to the infusion of such nonlinear effects, FFT analysis of rectangular (or Cartesian) coordinate variables will yield outputs which are incompatible with the perturbative model proposed in Section 2.4.2: the underlying admittances will be constantly changing as system phase angle drifts. Polar coordinate formulations, however, do not have this same drawback. As a workaround, we may introduce the concept of *effective* rectangular perturbation. To do so, we first introduce matrices  $T_1$  and  $T_{1,i}$  which linearize standard phasors  $V_r + jV_i = Ve^{j\theta}$  and  $I_r + jI_i = Ie^{j\phi}$ , respectively [39, eq. (10)]:

$$\begin{bmatrix} \Delta V_r \\ \Delta V_i \end{bmatrix} = \underbrace{\begin{bmatrix} \cos(\theta) & -V \sin(\theta) \\ \sin(\theta) & V \cos(\theta) \end{bmatrix}}_{T_1} \begin{bmatrix} \Delta V \\ \Delta \theta \end{bmatrix} \quad (\text{A.3})$$

$$\begin{bmatrix} \Delta I_r \\ \Delta I_i \end{bmatrix} = \underbrace{\begin{bmatrix} \cos(\phi) & -I \sin(\phi) \\ \sin(\phi) & I \cos(\phi) \end{bmatrix}}_{T_{1,i}} \begin{bmatrix} \Delta I \\ \Delta \phi \end{bmatrix}. \quad (\text{A.4})$$

We now assume we have some admittance  $\mathcal{Y}_g$  which relates polar voltage and current perturbations via  $\tilde{\mathbf{I}}_p = \mathcal{Y}_g \tilde{\mathbf{V}}_p$ . This relationship will not be affected by system phase angle drift. We thus transform the expression via

$$T_{1,i} \tilde{\mathbf{I}}_p = T_{1,i} \mathcal{Y}_g T_1^{-1} T_1 \tilde{\mathbf{V}}_p \quad (\text{A.5a})$$

$$\tilde{\mathbf{I}}_e = (T_{1,i} \mathcal{Y}_g T_1^{-1}) \tilde{\mathbf{V}}_e, \quad (\text{A.5b})$$

where  $\theta$  and  $\phi$  from (A.3)-(A.4) are chosen as their respective instantaneous values at  $t=0$  in the PMU data (any reference angle may be used so long as it is consistent across all transformations). Vectors  $\tilde{\mathbf{I}}_e$  and  $\tilde{\mathbf{V}}_e$  represent the effective rectangular perturbation vectors. Thus, (A.5b) is a fully consistent equation and may be used to update the  $P^*$  flow equation in (2.199).

## A.3 Positive Realness: Admittance and Impedance

Rather than dealing with the admittance  $\mathcal{Y}$  from  $\tilde{\mathbf{I}} = \mathcal{Y} \tilde{\mathbf{V}}$ , it may be convenient to deal with impedance  $\mathcal{Z} = \mathcal{Y}^{-1}$  instead. We define  $\mathbf{N}_{\mathcal{Y}} = \mathbf{M}\mathcal{Y} + (\mathbf{M}\mathcal{Y})^\dagger$  and  $\mathbf{N}_{\mathcal{Z}} = \mathbf{M}\mathcal{Z} + (\mathbf{M}\mathcal{Z})^\dagger$ .

**Theorem 7.** *If  $\mathbf{N}_{\mathcal{Y}}$  is (non)DQR,  $\mathbf{N}_{\mathcal{Z}}$  is (non)DQR.*

*Proof.* Starting with  $\tilde{\mathbf{I}} = \mathcal{Y}\tilde{\mathbf{V}}$ , we multiply through by  $\tilde{\mathbf{V}}^\dagger \mathbf{M}$ :

$$\operatorname{Re}\{\tilde{\mathbf{V}}^\dagger \mathbf{M} \tilde{\mathbf{I}}\} = \operatorname{Re}\{\tilde{\mathbf{V}}^\dagger \mathbf{M} \mathcal{Y} \tilde{\mathbf{V}}\}. \quad (\text{A.6})$$

Similarly, starting with  $\mathcal{Z}\tilde{\mathbf{I}} = \tilde{\mathbf{V}}$ , we multiply through by  $\tilde{\mathbf{I}}^\dagger \mathbf{M}$ :

$$\operatorname{Re}\{\tilde{\mathbf{I}}^\dagger \mathbf{M} \mathcal{Z} \tilde{\mathbf{I}}\} = \operatorname{Re}\{\tilde{\mathbf{I}}^\dagger \mathbf{M} \tilde{\mathbf{V}}\}. \quad (\text{A.7})$$

Since  $\operatorname{Re}\{\tilde{\mathbf{V}}^\dagger \mathbf{M} \tilde{\mathbf{I}}\} = \alpha \in \mathbb{R}$ , then

$$(\alpha)^\dagger = \operatorname{Re}\{\tilde{\mathbf{V}}^\dagger \mathbf{M} \tilde{\mathbf{I}}\}^\dagger \quad (\text{A.8a})$$

$$= \operatorname{Re}\{\tilde{\mathbf{I}}^\dagger \mathbf{M} \tilde{\mathbf{V}}\} \quad (\text{A.8b})$$

since  $\mathbf{M} = \mathbf{M}^\dagger$ . Because  $\operatorname{Re}\{\tilde{\mathbf{I}}^\dagger \mathbf{M} \mathcal{Z} \tilde{\mathbf{I}}\} = \operatorname{Re}\{\tilde{\mathbf{V}}^\dagger \mathbf{M} \mathcal{Y} \tilde{\mathbf{V}}\}$ ,

$$\tilde{\mathbf{I}}^\dagger (\mathbf{M} \mathcal{Z} + (\mathbf{M} \mathcal{Z})^\dagger) \tilde{\mathbf{I}} = \tilde{\mathbf{V}}^\dagger (\mathbf{M} \mathcal{Y} + (\mathbf{M} \mathcal{Y})^\dagger) \tilde{\mathbf{V}}. \quad (\text{A.9})$$

Thus,  $\mathbf{N}_Y$  and  $\mathbf{N}_Z$  share the same dissipativity classification.  $\square$

## A.4 DEF: A Power-Voltage Formulation

The original DEF integral, as given in [35], may be stated as

$$W_{\text{DE}} = \int \operatorname{Im}\{I^* dV\} \quad (\text{A.10a})$$

$$= \int \operatorname{Im}\left\{\left(\frac{P+jQ}{V e^{j\theta}}\right) dV e^{j\theta}\right\} \quad (\text{A.10b})$$

where  $dV e^{j\theta} = (\dot{V} + j\dot{\theta}V)e^{j\theta} dt$ . We thus restate  $W_{\text{DE}}$  as

$$W_{\text{DE}} = \int \operatorname{Im}\left\{\frac{1}{V}(P + jQ)(\dot{V} + j\dot{\theta}V)dt\right\} \quad (\text{A.11a})$$

$$= \int (P\dot{\theta} + Q\dot{V}/V)dt. \quad (\text{A.11b})$$

Other publications commonly state the term  $(Q\dot{V}/V)dt$  as  $Qd \ln(V)$ . Assuming small perturbations of (A.10), we may write  $d \ln(V) \approx dV/V_0 = (\dot{V}/V_0)dt$ . We have

$$W_{\text{DE}} \approx \int (P\dot{\theta} + Q\dot{V}/V_0)dt. \quad (\text{A.12})$$

We now suppose there is some FRF  $\mathcal{H}$  which relates output oscillations  $\tilde{P}$  and  $\tilde{Q}$  with input oscillations  $\tilde{V}$  and  $\tilde{\theta}$  via

$$\begin{bmatrix} \tilde{P} \\ \tilde{Q} \end{bmatrix} = \mathcal{H} \begin{bmatrix} \tilde{\theta} \\ \tilde{V} \end{bmatrix}. \quad (\text{A.13})$$

We define a new dissipativity transformation matrix

$$\mathbf{K} = \begin{bmatrix} j & 0 \\ 0 & \frac{j}{V_0} \end{bmatrix}. \quad (\text{A.14})$$

We use  $\mathbf{K}$  to write  $\tilde{\mathbf{S}} = \mathcal{H}(\mathbf{K}^{-1}\mathbf{K})\tilde{\mathbf{V}}_p$ . The dissipativity of the underlying system may be tested via the following relation, where  $\tilde{\mathbf{S}}$  and  $\tilde{\mathbf{V}}_p$  are from (A.13) as previously defined in (2.202):

$$\text{Re}\{(\mathbf{K}\tilde{\mathbf{V}}_p)^\dagger \tilde{\mathbf{S}}\} = \text{Re}\{\tilde{\mathbf{V}}_p^\dagger (\mathbf{K}^\dagger \mathcal{H}) \tilde{\mathbf{V}}_p\}. \quad (\text{A.15})$$

By the proof logic presented in [40], the following conditions are equivalent after a sufficient number of perturbation cycles:

$$\mathbf{K}^\dagger \mathcal{H} + (\mathbf{K}^\dagger \mathcal{H})^\dagger \succeq 0 \Leftrightarrow \text{Re}\{\tilde{\mathbf{V}}_p^\dagger \mathbf{K}^\dagger \tilde{\mathbf{S}}\} \geq 0 \quad (\text{A.16a})$$

$$\Leftrightarrow W_{\text{DE}} \geq 0. \quad (\text{A.16b})$$

If instead of  $\mathcal{H}$ , the dynamics of the system were described by the admittance  $\mathcal{Y}$ , (A.17) follows directly from (A.16b):

$$\mathbf{K}\mathcal{H} + (\mathbf{K}\mathcal{H})^\dagger \succeq 0 \Leftrightarrow \mathbf{M}\mathcal{Y} + (\mathbf{M}\mathcal{Y})^\dagger \succeq 0. \quad (\text{A.17})$$

## A.5 Basis Matrices of the Classical Generator

In a linear SISO system, admittance may be computed as the simple ratio of complex inputs and complex outputs. This cannot be done in a MIMO system. Assuming complex input ( $\tilde{\mathbf{u}}_v$ ) and output ( $\tilde{\mathbf{y}}$ ) vectors for the system in (2.59) are given, a generalized admittance  $\mathcal{Y} \in \mathbb{C}^{2 \times 2}$  cannot be directly inferred since (2.59) represents four real linear equations while  $\mathcal{Y}$  is specified with 8 coefficients ( $a_i, b_i, i \in \{1, 2, 3, 4\}$ ):

$$\begin{bmatrix} \mathcal{Y}_1 & \mathcal{Y}_2 \\ \mathcal{Y}_3 & \mathcal{Y}_4 \end{bmatrix} = \sum_{i=1}^4 (a_i + jb_i) \bar{T}_i. \quad (\text{A.18})$$

The system is thus underdetermined (by a factor of two). For a classical generator, though, this is not the case. This is an important observation, because the dynamics of a system experiencing a FO are dominated by the electromechanical response of synchronous generators.

**Proposition 1.** *The admittance  $\mathcal{Y}_g$  of a classical generator can be uniquely specified as the weighted sum of six basis matrices with only **four** real coefficients.*

*Proof.* It may be observed that  $\mathcal{Y}_g$  in (2.135) contains no complex combination of basis matrix  $\bar{T}_1$ . Therefore,  $\mathcal{Y}_g$  may be written using six basis matrix coefficients  $a_i, b_i, i \in \{2, 3, 4\}$  via  $\mathcal{Y}_g = \sum_{i=2 \dots 4} (a_i + jb_i)\bar{T}_i$ . We further observe that for  $(a_2 + jb_2)\bar{T}_2$  and  $(a_3 + jb_3)\bar{T}_3$ , the ratios of  $a_2/b_2$  and  $a_3/b_3$  must be equal, so  $a_2 = b_2a_3/b_3$ . This eliminates one coefficient. Finally, we write  $\gamma = \gamma_r + j\gamma_i$  and observe that  $b_2 = \gamma_i \sin(\delta) \cos(\delta)$  while  $b_3 + b_4 = \gamma_i \sin^2(\delta)$  and  $b_3 - b_4 = -\gamma_i \cos^2(\delta)$ . Solving this system yields  $b_4 = +\sqrt{b_2^2 + b_3^2}$  (assuming damping  $D$  is positive). Therefore,  $\mathcal{Y}_g$  may be specified with just four coefficients:  $a_3, a_4, b_2$ , and  $b_3$ .  $\square$

**Corollary 9.** *From Proposition 1, classical generator admittance  $\mathcal{Y}_g$  can be specified with only four parameters. Thus, the inference problem  $\min_{\mathcal{Y}_g} \{\hat{\mathbf{y}} - \mathcal{Y}_g \tilde{\mathbf{u}}_v\}$  represents 4 equations and 4 unknowns and is thus a “determined” problem. Accordingly, the admittance of a classical generator can be fully inferred from terminal data.*

## A.6 The Effects of Resistive Energy Injections from Transmission Networks

Given that *any* admittance matrix  $\mathcal{Y}$  may be written as the complex sum of the four weighted basis matrices, we introduce the following useful definition:

**Definition 18.** *We assume some admittance  $\mathcal{Y}$  may be written as  $\mathcal{Y} = \sum_{i=1}^4 (a_i + jb_i)\bar{T}_i$ . Using matrices  $\mathbf{M}$  and  $\Gamma$  from Corollary 3, where  $\Gamma = (j\beta\bar{T}_4)\mathbf{M}^\dagger$ , we define  $P^* = \text{Re}\{\mathbf{u}^\dagger (\mathbf{M}\mathcal{Y}\Gamma) \mathbf{u}\}$  as the **dissipating power** for input vector  $\mathbf{u}$ . We further define two other types of quadratic power: **resistive power**  $P_r^*$  and **damping power**  $P_d^*$ , where  $P^* = P_r^* + P_d^*$ , and*

- $P_r^* = \text{Re}\{\mathbf{u}^\dagger (\mathbf{M}(a_1\bar{T}_1)\Gamma) \mathbf{u}\}$
- $P_d^* = \text{Re}\{\mathbf{u}^\dagger (\mathbf{M}(jb_2\bar{T}_2 + jb_3\bar{T}_3 + jb_4\bar{T}_4)\Gamma) \mathbf{u}\}.$

We show that the sign of the injected resistive energy associated with a transmission network can be negated if all system voltages are complex conjugated.

**Theorem 8.** *Consider a lossy transmission network (just the network). For any transformed voltage vector  $\mathbf{U}_b$  which yields quadratic energy  $\text{Re}\{\mathbf{U}_b^\dagger (\underline{\mathbf{M}}(E_a^\dagger \mathcal{Y}_L E_a)\underline{\Gamma}) \mathbf{U}_b\} = P_r^*$ , there exists conjugated vector  $\mathbf{U}_b^*$  which yields an equal and opposite quadratic energy  $\text{Re}\{\mathbf{U}_b^{*\dagger} (\underline{\mathbf{M}}(E_a^\dagger \mathcal{Y}_L E_a)\underline{\Gamma}) \mathbf{U}_b^*\} = -P_r^*$ , where  $\underline{\mathbf{M}}$  and  $\underline{\Gamma}$ , with submatrices  $\mathbf{M}$  and  $\Gamma$ , yield from Corollary 3.*

*Proof.* We split the transmission line matrix into its conductive and susceptive parts:  $\mathcal{Y}_L = \mathcal{Y}_{\bar{G}} + \mathcal{Y}_{\bar{B}}$ , where  $\mathcal{Y}_{\bar{G},i} = G_i\bar{T}_1$  and  $\mathcal{Y}_{\bar{B},i} = B_i\bar{T}_4$ . We also define block matrices  $\mathbf{M} = j\bar{T}_4\Gamma$  and  $\Gamma = \bar{T}_1$  from  $\underline{\mathbf{M}}$  and  $\underline{\Gamma}$ . Therefore,  $\underline{\mathbf{M}}(E_a^\dagger \mathcal{Y}_L E_a)\underline{\Gamma} = \underline{\mathbf{M}}(E_a^\dagger (\mathcal{Y}_{\bar{G}} + \mathcal{Y}_{\bar{B}}) E_a)$ . The Hermitian part (termed  $\mathbf{H}$ ) is

$$\mathbf{H} = \underline{\mathbf{M}} E_a^\dagger \left( \frac{\mathcal{Y}_G + \mathcal{Y}_{Bx}}{2} \right) E_a + E_a^\dagger \left( \frac{\mathcal{Y}_G - \mathcal{Y}_{Bx}}{2} \right) E_a \underline{\mathbf{M}}^\dagger \quad (\text{A.19a})$$

$$= \underline{\mathbf{M}} (E_a^\dagger \frac{\mathcal{Y}_G}{2} E_a) + (E_a^\dagger \frac{\mathcal{Y}_G}{2} E_a) \underline{\mathbf{M}} \quad (\text{A.19b})$$

$$= \underline{\mathbf{M}} (E_a^\dagger \mathcal{Y}_G E_a) \quad (\text{A.19c})$$

where the matrices of (A.19b) commute since the product of Hermitian matrices is also Hermitian. We define  $\bar{G}_{ij} \equiv jG_{ij}\bar{T}_4$ , where  $G_{ij}$  is the scalar line conductance connecting buses  $i$  and  $j$ , and  $\mathbf{u}_i \subset \mathbf{U}_b$  is the voltage element of  $\mathbf{U}_b$  associated with bus  $i$ . From (A.19c), the quadratic power is

$$P_r^* = \sum_{i=1}^n \mathbf{u}_i^\dagger \left( \sum_{j \neq i} \bar{G}_{ij} \right) \mathbf{u}_i - \sum_{j \neq i} \sum_{i \neq j}^n \mathbf{u}_i^\dagger \bar{T}_4 \bar{G}_{ij} \mathbf{u}_j \quad (\text{A.20a})$$

$$= \sum_{i,j \in \mathcal{E}} (\mathbf{u}_i^\dagger \bar{G}_{ij} \mathbf{u}_i + \mathbf{u}_j^\dagger \bar{G}_{ij} \mathbf{u}_j - \mathbf{u}_i^\dagger \bar{G}_{ij} \mathbf{u}_j - \mathbf{u}_j^\dagger \bar{G}_{ij} \mathbf{u}_i) \quad (\text{A.20b})$$

$$= \sum_{i,j \in \mathcal{E}} (\mathbf{u}_i - \mathbf{u}_j)^\dagger \bar{G}_{ij} \underbrace{(\mathbf{u}_i - \mathbf{u}_j)}_{\mathbf{u}_{ij}}. \quad (\text{A.20c})$$

The quadratic quantity  $\mathbf{x}^\dagger \bar{G}_{ij} \mathbf{x} = \epsilon$  may be negated by conjugating the input (proof trivial):  $\mathbf{x}^{*\dagger} \bar{G}_{ij} \mathbf{x}^* = -\epsilon$ . By taking  $\mathbf{U}_b^*$  as an input to  $\text{Re}\{\underline{\mathbf{M}}\mathbf{U}_b^{*\dagger} (E_a^\dagger \mathcal{Y}_G E_a) \mathbf{U}_b^*\}$ , by (A.20c) we thus have  $\sum_{i,j \in \mathcal{E}} \mathbf{u}_{ij}^{*\dagger} \bar{G}_{ij} \mathbf{u}_{ij}^* = -P_r^*$ .  $\square$

We note that  $\mathbf{U}_b$  cannot be chosen arbitrarily; it must represent a valid solution to the linear system of (2.170a). Since  $\mathbf{U}_b$  is not itself a degree of freedom but rather a response to some current injection, statements about the mathematical characteristics of  $\mathbf{M}\mathcal{Y}_N\Gamma + (\mathbf{M}\mathcal{Y}_N\Gamma)^\dagger$  are difficult to prove using energy-based arguments.

We now characterize how the eigenvalues change as resistance is added to  $\Sigma_c$ .

**Theorem 9.** *Consider  $\mathbf{N}_c$  from  $\Sigma_c$ . No amount of additional resistance to lines or loads can cause the eigenvalues of  $\mathbf{N}_c$  to both become negative: if  $\det(\mathbf{N}_c) \geq 0$  then  $\text{trace}(\mathbf{N}_c) \geq 0$ .*

*Proof.* Consider some altered version of  $\Sigma_c$  where all resistance has been removed from the system. In this situation,  $\lambda_1, \lambda_2 \geq 0$  according to Theorem 3.

Consider some secondary altered version of  $\Sigma_c$  where generators have no damping (making them “lossless”). In this situation, matrix  $\mathcal{Y}_N$  will be purely real ( $\mathcal{Y}_N \in \mathbb{R}^{2 \times 2}$ ) via (2.171). Therefore, assuming lossy lines,  $\lambda_1 = -\lambda_2 \neq 0$ .

All real systems exist between these two alternatives. We now consider a system with nominal resistance and some value  $\alpha$  which parameterizes the amount of damping in the system generators ( $\alpha = 0$  corresponds to no damping). When  $\alpha = 0$ ,  $\lambda_1 = -\lambda_2 \neq 0$ . As  $\alpha \rightarrow \infty$ , then  $\lambda_1, \lambda_2 \rightarrow \mathbb{R}^+$ . In between these extremes, if for some value of  $\alpha > 0$ , there is  $\lambda_1, \lambda_2 \in \mathbb{R}^-$ , then it would imply that the addition of positive damping causes the system to lose the ability to dissipate the quadratic energy which the generator damping consumes. This is a contradiction, so at least one eigenvalue must always remain positive for all levels of damping and resistance.  $\square$

**Remark 13.** *Since the DWE  $\mathcal{Y}_N$  is the admittance of the network “seen” by the source, the negative DWE  $-\mathcal{Y}_N$  is the admittance “seen” by the network behind the source bus. By Theorem 9, the eigenvalues of  $\mathbf{N}_c = \frac{1}{2}(\mathbf{M}\mathcal{Y}_N\Gamma) + \frac{1}{2}(\mathbf{M}\mathcal{Y}_N\Gamma)^\dagger$  can never be simultaneously negative. Stated differently, the eigenvalues of  $-\mathbf{N}_c$  can never be simultaneously positive. For this reason, the admittance seen by the network behind the FO source can never be truly DQR.*

# Appendix B

## Simulation Modeling Notes

### B.1 Modeling AC Power System Dynamics

The mathematical model which can be used to describe the dynamics of an AC power system is commonly given by the DAE set

$$\dot{\mathbf{x}} = \mathbf{f}(\mathbf{x}, \mathbf{z}, \mathbf{u}) \quad (\text{B.1a})$$

$$\mathbf{0} = \mathbf{g}(\mathbf{x}, \mathbf{z}, \mathbf{u}) \quad (\text{B.1b})$$

$$\mathbf{y} = \mathbf{h}(\mathbf{x}, \mathbf{z}, \mathbf{u}), \quad (\text{B.1c})$$

where  $\mathbf{x}$  is a vector of state variables,  $\mathbf{z}$  is a vector of algebraic variables (usually including nodal voltage magnitude  $V$  and phase  $\theta$  variables),  $\mathbf{u}$  is a vector of inputs (i.e. control signals, system changes, stochastic load perturbations, etc.), and  $\mathbf{y}$  is a vector of desired outputs. The following subsections describe the component models.

#### Algebraic Power Flow Equations

At each node in the system, the power flow equations must remain balanced for all time. The power flow (i.e. injection) equations are stated by

$$P_i = V_i \sum_{k \in \mathcal{K}} V_k (G_{ik} \cos(\theta_{ik}) + B_{ik} \sin(\theta_{ik})) \quad (\text{B.2})$$

$$Q_i = V_i \sum_{k \in \mathcal{K}} V_k (G_{ik} \sin(\theta_{ik}) - B_{ik} \cos(\theta_{ik})), \quad (\text{B.3})$$

where  $\mathcal{K}$  is the set of all nodes, and  $G_{ik}$ ,  $B_{ik}$  are corresponding elements from the nodal admittance matrix.

## Synchronous Generator Equations

Power system models typically contain both 4<sup>th</sup> and 6<sup>th</sup> order machines, depending on configuration. The 4<sup>th</sup> order generator model is stated as follows [129]:

$$\dot{\delta} = \omega \quad (\text{B.4})$$

$$\frac{2H}{\omega_0} \dot{\omega} = \tau_m - \tau_e - D\omega \quad (\text{B.5})$$

$$T'_{d0} \dot{e}'_q = E_f - (x_d - x'_d)i_d - e'_q \quad (\text{B.6})$$

$$T'_{q0} \dot{e}'_d = (x_q - x'_q)i_q - e'_d \quad (\text{B.7})$$

where  $\omega = 0$  at equilibrium. The electrical torque in the airgap,  $\tau_e$ , commonly takes the form

$$\tau_e = \phi_d i_q - \phi_q i_d. \quad (\text{B.8})$$

The generator currents and voltages are related by

$$\begin{bmatrix} e_d \\ e_q \end{bmatrix} = \begin{bmatrix} e'_d \\ e'_q \end{bmatrix} - \begin{bmatrix} r_a & -x'_q \\ x'_d & r_a \end{bmatrix} \begin{bmatrix} i_d \\ i_q \end{bmatrix} \quad (\text{B.9})$$

and the flux variables are given by

$$\phi_d = e'_q - x'_d i_d \quad (\text{B.10})$$

$$\phi_q = -e'_d - x'_q i_q \quad (\text{B.11})$$

or, alternatively,  $\phi_d = r_a i_q + e_q$  and  $\phi_q = -r_a i_d - e_d$ . The electrical power at the terminals of the machine are

$$P_e = e_d i_d + e_q i_q \quad (\text{B.12})$$

$$Q_e = e_q i_d - e_d i_q \quad (\text{B.13})$$

We note that the electrical power at the terminal of the generator is equal to the airgap torque minus the power losses across the stator resistance:

$$e_d i_d + e_q i_q = (\phi_d i_q - \phi_q i_d) - r_a (i_q^2 + i_d^2). \quad (\text{B.14})$$

Since stator dynamics have been neglected,  $\dot{\phi}_d = \dot{\phi}_q = 0$ , and the electrical torque in the airgap is assumed equal to the electrical power in the airgap.

The 6<sup>th</sup> order generator model is stated as follows [129]:

$$\dot{\delta} = \omega \quad (\text{B.15})$$

$$\frac{2H}{\omega_0} \dot{\omega} = \tau_m - \tau_e - D\omega \quad (\text{B.16})$$

$$T'_{do} \dot{e}'_q = E_f - (x_d - x'_d - \gamma_d) i_d - e'_q \quad (\text{B.17})$$

$$T'_{qo} \dot{e}'_d = (x_q - x'_q - \gamma_q) i_q - e'_d \quad (\text{B.18})$$

$$T''_{do} \dot{e}''_q = e'_q - e''_q - (x'_d - x''_d + \gamma_d) i_d \quad (\text{B.19})$$

$$T''_{qo} \dot{e}''_d = e'_d - e''_d + (x'_q - x''_q + \gamma_q) i_q, \quad (\text{B.20})$$

where

$$\gamma_q = T''_{qo} x''_q \frac{x_q - x'_q}{T'_{qo} x'_q} \quad (\text{B.21})$$

$$\gamma_d = T''_{do} x''_d \frac{x_d - x'_d}{T'_{do} x'_d}. \quad (\text{B.22})$$

The voltages and currents are related via

$$\begin{bmatrix} v_d \\ v_q \end{bmatrix} = \begin{bmatrix} e''_d \\ e''_q \end{bmatrix} - \begin{bmatrix} r_a & -x''_q \\ x''_d & r_a \end{bmatrix} \begin{bmatrix} i_d \\ i_q \end{bmatrix}. \quad (\text{B.23})$$

Again, electrical power at the terminals of the machine are

$$P_e = e_d i_d + e_q i_q \quad (\text{B.24})$$

$$Q_e = e_q i_d - e_d i_q. \quad (\text{B.25})$$

The electrical torque in the airgap (again approximated by the electrical power in the airgap) is given via

$$\tau_e = \phi_d i_q - \phi_q i_d \quad (\text{B.26})$$

$$= e_d i_d + e_q i_q + r_a (i_q^2 + i_d^2), \quad (\text{B.27})$$

where

$$\phi_d = e''_q - x''_d i_d \quad (\text{B.28})$$

$$\phi_q = -e''_d - x''_q i_q. \quad (\text{B.29})$$

In both generator cases,  $e_d = V \sin(\delta - \theta)$  and  $e_q = V \cos(\delta - \theta)$ . The interaction between the generator model and its various controllers is shown in Fig. B-1.

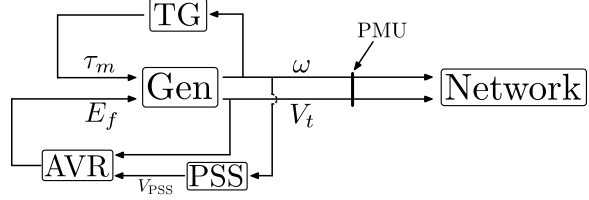


Figure B-1: Generator interacting with its controllers and the network. The (6<sup>th</sup> order) generator + controller system has a total of 15 differential states, with time constants varying from 0.01s to 50s.

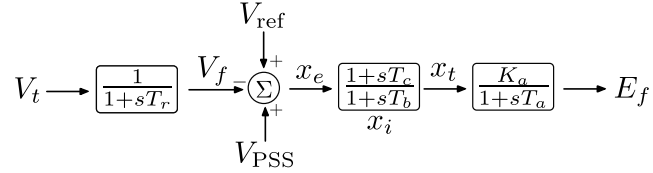


Figure B-2: Automatic Voltage Regulator

### Generator Automatic Voltage Regulator (AVR) Equations

The AVR regulates the terminal voltage of the generator. The relevant differential equations are given by

$$T_r \dot{V}_f = V_t - V_f \quad (\text{B.30})$$

$$T_a \dot{E}_f = K_a x_t - E_f \quad (\text{B.31})$$

$$\dot{x}_i = x_e - x_t \quad (\text{B.32})$$

and the algebraic equations are stated as

$$x_e = V_{\text{ref}} + V_{\text{PSS}} - V_f \quad (\text{B.33})$$

$$T_b x_t = T_c x_e + x_i. \quad (\text{B.34})$$

The transfer function is given below.

### Generator Power System Stabilizer (PSS) Equations

The power system stabilizer damps out unstable frequency modes. The relevant differential equations are given by

$$T_w \dot{x}_w = V_w \quad (\text{B.35})$$

$$\dot{x}_p = V_w - V_p \quad (\text{B.36})$$

$$\dot{x}_q = V_p - V_{\text{pss}}, \quad (\text{B.37})$$

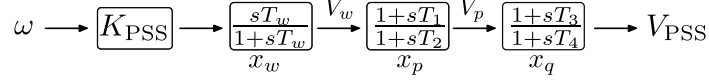


Figure B-3: Power System Stabilizer

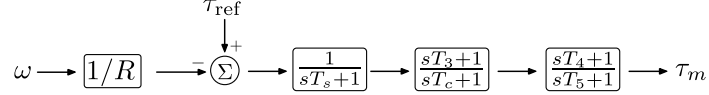


Figure B-4: Turbine Governor

and the algebraic equations are stated as

$$V_w = \omega K_{\text{PSS}} - x_w \quad (\text{B.38})$$

$$T_2 V_p = T_1 V_w + x_p \quad (\text{B.39})$$

$$T_4 V_{\text{PSS}} = T_3 V_p + x_q. \quad (\text{B.40})$$

The transfer function is given below.

### Generator Turbine Governor (TG) Equations

The turbine governor regulates generator power output as a function of terminal frequency. The differential equations are given by

$$T_s \dot{x}_1 = \tau_{\text{ref}} - \frac{1}{R} \omega - x_1 \quad (\text{B.41})$$

$$T_c \dot{x}_2 = \left(1 - \frac{T_3}{T_c}\right) x_1 - x_2 \quad (\text{B.42})$$

$$T_5 \dot{x}_3 = \left(1 - \frac{T_4}{T_5}\right) \left(x_2 + \frac{T_3}{T_c} x_1\right) - x_3 \quad (\text{B.43})$$

and the only algebraic is given by

$$\tau_m = x_3 + \frac{T_4}{T_5} \left(x_2 + \frac{T_3}{T_c} x_1\right). \quad (\text{B.44})$$

The transfer function is given below.

### Algebraic “ZIP” Load Equations

The instantaneous active and reactive power consumed by the loads in the network are often modeled as functions of the nodal voltage magnitude  $V$  relative to its nominal

voltage  $V_0$ :

$$P = P_0(1 + u_p) \left( K_Z \left( \frac{V}{V_0} \right)^2 + K_I \left( \frac{V}{V_0} \right)^1 + K_P \left( \frac{V}{V_0} \right)^0 \right) \quad (\text{B.45})$$

$$Q = Q_0(1 + u_q) \left( K_Z \left( \frac{V}{V_0} \right)^2 + K_I \left( \frac{V}{V_0} \right)^1 + K_P \left( \frac{V}{V_0} \right)^0 \right). \quad (\text{B.46})$$

The variables  $u_p$  and  $u_q$  can codify the stochastic variation of the loads via an Ornstein-Uhlenbeck random process [66]:

$$\tau \dot{u}_p = -u_p + \eta_i \quad (\text{B.47})$$

$$\tau \dot{u}_q = -u_q + \eta_i, \quad (\text{B.48})$$

where  $\eta_i$  are IID Gaussian random variables.

### Linearization Analysis

Often times, it is helpful to linearize the power system DAE model (B.1) in order to directly relate input and output perturbations. We perform this linearization by first computing Jacobians

$$\Delta \dot{\mathbf{x}} = [\mathbf{f}_x] \Delta \mathbf{x} + [\mathbf{f}_y] \Delta \mathbf{z} + [\mathbf{f}_u] \Delta \mathbf{u} \quad (\text{B.49})$$

$$\mathbf{0} = [\mathbf{g}_x] \Delta \mathbf{x} + [\mathbf{g}_y] \Delta \mathbf{z} + [\mathbf{g}_u] \Delta \mathbf{u} \quad (\text{B.50})$$

$$\Delta \mathbf{y} = [\mathbf{h}_x] \Delta \mathbf{x} + [\mathbf{h}_y] \Delta \mathbf{z} + [\mathbf{h}_u] \Delta \mathbf{u}. \quad (\text{B.51})$$

Next, we eliminate the algebraic variable perturbations via Kron reduction:

$$\Delta \mathbf{z} = -[\mathbf{g}_y]^{-1} ([\mathbf{g}_x] \Delta \mathbf{x} + [\mathbf{g}_u] \Delta \mathbf{u}). \quad (\text{B.52})$$

Substituting, we have

$$\Delta \dot{\mathbf{x}} = \underbrace{[\mathbf{f}_x - \mathbf{f}_y \mathbf{g}_y^{-1} \mathbf{g}_x]}_{\mathbf{A}} \Delta \mathbf{x} + \underbrace{[\mathbf{f}_u - \mathbf{f}_y \mathbf{g}_y^{-1} \mathbf{g}_u]}_{\mathbf{B}} \Delta \mathbf{u} \quad (\text{B.53})$$

$$\Delta \mathbf{y} = \underbrace{[\mathbf{h}_x - \mathbf{h}_y \mathbf{g}_y^{-1} \mathbf{g}_x]}_{\mathbf{C}} \Delta \mathbf{x} + \underbrace{[\mathbf{h}_u - \mathbf{h}_y \mathbf{g}_y^{-1} \mathbf{g}_u]}_{\mathbf{D}} \Delta \mathbf{u}. \quad (\text{B.54})$$

In the Laplace domain, the linearized input and output perturbations are thus related by  $\tilde{\mathbf{y}}(s) = (\mathbf{C}(s\mathbb{1} - \mathbf{A})^{-1}\mathbf{B} + \mathbf{D})\tilde{\mathbf{u}}(s)$ .

## B.2 Initialization and Modeling of DC Microgrid Dynamics in the Time Domain

### Initialization

To initialize the DC microgrid network in Fig. 3-6, for example, we assume steady state ( $\omega = 0$ ) operation. We then order the network such that buses 1 through  $n_s$  are source buses while buses  $n_s + 1$  through  $n$  are load buses. We define  $Y_l$  as the diagonal matrix of line admittances, where each diagonal element is  $1/r_{ij}$ , and we define  $Y_s$  as the diagonal matrix of shunt (i.e. load) admittances, where each diagonal element is  $D^2/R$  (i.e. the *negative* of incremental resistance (3.40)). We further define the real matrix

$$Y_b = E^T Y_l E + Y_s \quad (\text{B.55})$$

as the nodal admittance matrix. Next, we define  $\mathbf{V}_s$  as the vector of *known* source voltages,  $\mathbf{V}_l$  as the vector of *unknown* load voltages, and  $\mathbf{I}_s$  as the vector of *unknown* current injections at the sources. Partitioning (B.55), we therefore have

$$\left[ \begin{array}{c|c} Y_{b1} & Y_{b2} \\ \hline Y_{b3} & Y_{b4} \end{array} \right] \left[ \begin{array}{c} \mathbf{V}_s \\ \mathbf{V}_l \end{array} \right] = \left[ \begin{array}{c} \mathbf{I}_s \\ \mathbf{0} \end{array} \right]. \quad (\text{B.56})$$

By re-arranging the bottom set of equations from (B.56), the unknown steady state voltages may be computed as

$$\mathbf{V}_l = -Y_{b4}^{-1} Y_{b3} \mathbf{V}_s. \quad (\text{B.57})$$

### Time Domain Simulation

In order to simulate the small-signal dynamics of the network in Fig. 3-6, we first initialized the system via (B.57). Using the calculated equilibrium, we defined the differential algebraic equation (DAE) set

$$\dot{\mathbf{x}} = \mathbf{A}\mathbf{x} + \mathbf{B}\mathbf{u} \quad (\text{B.58})$$

$$\mathbf{0} = E^T \mathbf{x}_l + \mathbf{x}_s, \quad (\text{B.59})$$

where  $\mathbf{A}$  encodes the dynamics of the buck converters, filter capacitors, and network lines, and  $\mathbf{B}$  processes the inputs from the voltage sources  $\mathbf{u}$ . To enforce conservation of currents, (B.59) ensures the sum of line currents  $\mathbf{x}_l$  and shunt currents  $\mathbf{x}_s$  are equal to 0 at each node.



# Appendix C

## Dynamic Phasor Modeling

In the modeling and analysis of AC power systems, phasors are ubiquitous. While invaluable in steady state analysis, an extension of the phasor concept, known as the dynamic phasor, is very useful in the dynamic modeling of electromechanical machines, inverters, and microgrid networks. To motivate the dynamic phasor, we consider two three-phase voltage and current (injection or line flow) vectors:

$$\mathbf{v}(t) = \begin{bmatrix} v_a(t) \\ v_b(t) \\ v_c(t) \end{bmatrix}, \quad \mathbf{i}(t) = \begin{bmatrix} i_a(t) \\ i_b(t) \\ i_c(t) \end{bmatrix}, \quad (\text{C.1})$$

where each signal is assumed to be operate “around” equilibrium frequency  $\omega_0$ . In order to construct a dynamic phasor representation of (C.1), there are a variety of alternatives, such as the amplitude-invariant Clarke transform [80]. In this thesis, we use the standard (amplitude-invariant) Park Transform [137]:

$$\mathbf{T}_p(t) = \frac{2}{3} \begin{bmatrix} \cos(\omega_0 t) & \cos(\omega_0 t - \frac{2\pi}{3}) & \cos(\omega_0 t + \frac{2\pi}{3}) \\ -\sin(\omega_0 t) & -\sin(\omega_0 t - \frac{2\pi}{3}) & -\sin(\omega_0 t + \frac{2\pi}{3}) \\ \frac{1}{2} & \frac{1}{2} & \frac{1}{2} \end{bmatrix}, \quad (\text{C.2})$$

such that

$$\begin{bmatrix} V_d(t) \\ V_q(t) \\ V_0(t) \end{bmatrix} = \mathbf{T}_p(t)\mathbf{v}(t), \quad \begin{bmatrix} I_d(t) \\ I_q(t) \\ I_0(t) \end{bmatrix} = \mathbf{T}_p(t)\mathbf{i}(t), \quad (\text{C.3})$$

where the “zero” sequence term is 0 under balanced operation. We also note that in quasi-stationary steady state, the real-valued  $d$  and  $q$  axis signals are constant, i.e.  $\dot{V}_d(t) = \dot{V}_q(t) = 0$ , etc. We use these signals to define dynamic phasors:

$$\begin{aligned} \tilde{V}_{dq}(t) &= V_d(t) + jV_q(t) \\ \tilde{I}_{dq}(t) &= I_d(t) + jI_q(t). \end{aligned}$$

We now make the important distinction between so-called symmetrical (also referred to as isotropic, or rotational-invariant) and non-symmetric systems [80]. As the name implies, symmetrical systems present balanced three-phase impedances to the grid. Such systems include balanced RLC components, transformers, induction machines, and round-rotor synchronous machines. Asymmetric systems include unbalanced RLC components, and salient pole synchronous machines [80]. In these cases, the impedance seen by the  $d$  and  $q$  axis voltages is a function of the reference frame. When dealing with symmetrical components, it is convenient to use dynamic phasors to define voltage and current signals which rotate in the complex plane:

$$\tilde{V}(t) = \tilde{V}_{dq}(t)e^{j\omega_0 t} \quad (\text{C.4})$$

$$\tilde{I}(t) = \tilde{I}_{dq}(t)e^{j\omega_0 t} \quad (\text{C.5})$$

These signals can conveniently be used to analyze the impedance presented by a symmetrical RL line connecting buses  $j$  and  $k$ :

$$L \frac{d}{dt} \tilde{I}_{jk}(t) = \tilde{V}_j(t) - \tilde{V}_k(t) - R \tilde{I}_{jk}(t) \quad (\text{C.6})$$

Substituting in (C.4)-(C.5),

$$L \left( \frac{d}{dt} \tilde{I}_{dq,jk}(t) \right) e^{j\omega_0 t} = \tilde{V}_{dq,j}(t)e^{j\omega_0 t} - \tilde{V}_{dq,k}(t)e^{j\omega_0 t} - R \tilde{I}_{dq,jk}(t)e^{j\omega_0 t} - L j \omega_0 \tilde{I}_{dq,jk}(t)e^{j\omega_0 t},$$

which can be simplified by (i) multiplying through by  $e^{-j\omega_0 t}$ , (ii) breaking the problem down into its real and imaginary parts, and (iii) dropping the “of time” notation:

$$L \frac{d}{dt} I_{d,jk} = V_{d,j} - V_{d,k} - R I_{d,jk} + L \omega_0 I_{q,jk} \quad (\text{C.7})$$

$$L \frac{d}{dt} I_{q,jk} = V_{q,j} - V_{q,k} - R I_{q,jk} - L \omega_0 I_{d,jk}. \quad (\text{C.8})$$

The associated transfer function relating inputs ( $d$  and  $q$  axis voltage differentials) and outputs ( $d$  and  $q$  axis current flows) is given by

$$\begin{bmatrix} I_{d,jk} \\ I_{q,jk} \end{bmatrix} = \begin{bmatrix} Ls + R & -L\omega_0 \\ L\omega_0 & Ls + R \end{bmatrix}^{-1} \begin{bmatrix} V_{d,j} - V_{d,k} \\ V_{q,j} - V_{q,k} \end{bmatrix}, \quad (\text{C.9})$$

where  $X_0 = L\omega_0$  is a common simplification. Since this system is truly linear, the admittance in (C.9) is capable of relating the full (rather than small signal) voltage and current signals. When dealing with nonlinear systems, it becomes helpful to define small signal perturbations  $v_d(t)$ ,  $v_q(t)$ ,  $i_d(t)$ ,  $i_q(t)$  which are deviations away

from equilibrium points  $V_{d,0}$ ,  $V_{q,0}$ ,  $I_{d,0}$ ,  $I_{q,0}$ :

$$V_d(t) = V_{d,0} + v_d(t) \quad (\text{C.10})$$

$$V_q(t) = V_{q,0} + v_q(t) \quad (\text{C.11})$$

$$I_d(t) = I_{d,0} + i_d(t) \quad (\text{C.12})$$

$$I_q(t) = I_{q,0} + i_q(t). \quad (\text{C.13})$$

The small signal admittance associated with an RL line is given by (C.9) exactly:

$$\begin{bmatrix} i_{d,jk} \\ i_{q,jk} \end{bmatrix} = \begin{bmatrix} Ls + R & -L\omega_0 \\ L\omega_0 & Ls + R \end{bmatrix}^{-1} \begin{bmatrix} v_{d,j} - v_{d,k} \\ v_{q,j} - v_{q,k} \end{bmatrix}. \quad (\text{C.14})$$



# Bibliography

- [1] *Dissipativity and Passivity*, pages 5–41. Springer London, London, 2007.
- [2] Ieee guide for synchronization, calibration, testing, and installation of phasor measurement units (pmus) for power system protection and control. *IEEE Std C37.242-2013*, pages 1–107, March 2013.
- [3] Reliability guideline: Forced oscillation monitoring and mitigation. Technical report, North American Electric Reliability Corporation, Sep 2017.
- [4] Ali Abur and Antonio Gomez Exposito. *Power system state estimation: theory and implementation*. CRC press, 2004.
- [5] S. Achanta, M. Danielson, P. Evans, et al. Time synchronization in the electric power system. *North American synchrophasor Initiative, Tech Report NASPI-2017-TR-001*, March 2017.
- [6] Energy Information Agency. How many smart meters are installed in the united states, and who has them?, 2018.
- [7] U. Agrawal et al. Locating the source of forced oscillations using pmu measurements and system model information. In *2017 IEEE Power Energy Society General Meeting*, pages 1–5, July 2017.
- [8] U. Agrawal, J. Follum, J. W. Pierre, and D. Duan. Electromechanical mode estimation in the presence of periodic forced oscillations. *IEEE Transactions on Power Systems*, 34(2):1579–1588, March 2019.
- [9] Shahrokh Akhlaghi, Sunny Raheem, and Ning Zhou. Model validation lessons learned through implementing nerc mod-033-1. 02 2020.
- [10] N Al-Ashwal, D Wilson, and M Parashar. Identifying sources of oscillations using wide area measurements. In *Proceedings of the CIGRE US National Committee 2014 grid of the future symposium, Houston*, volume 19, 2014.
- [11] R. N. Allan, B. Borkowska, and C. H. Grigg. Probabilistic analysis of power flows. *Proceedings of the Institution of Electrical Engineers*, 121(12):1551–1556, 1974.

- [12] M. Amini and M. Almassalkhi. Investigating delays in frequency-dependent load control. In *2016 IEEE Innovative Smart Grid Technologies - Asia (ISGT-Asia)*, pages 448–453, Nov 2016.
- [13] P.M. Anderson and A.A. Fouad. *POWER SYSTEM CONTROL AND STABILITY, 2ND ED.* IEEE Press power engineering series. Wiley India Pvt. Limited, 2008.
- [14] Sofía Avila-Becerril, Diego Silva-Martínez, and Gerardo Espinosa-Pérez. On the robustness of a passivity-based controller for microgrids. *IFAC-PapersOnLine*, 50(1):6648 – 6653, 2017. 20th IFAC World Congress.
- [15] E.S. Banuelos-Cabral, J.J. Nuno-Ayon, B. Gustavsen, J.A. Gutierrez-Robles, V.A. Galvan-Sanchez, J. Sotelo-Castanon, and J.L. Garcia-Sanchez. Spectral fitting approach to estimate electromechanical oscillation modes and mode shapes by using vector fitting. *Electric Power Systems Research*, 176:105958, 2019.
- [16] N. Barabanov, R. Ortega, R. Grino, and B. Polyak. On Existence and Stability of Equilibria of Linear Time-Invariant Systems With Constant Power Loads. *IEEE Transactions on Circuits and Systems I: Regular Papers*, 63(1):114–121, 2016.
- [17] E. Barklund, N. Pogaku, M. Prodanovic, C. Hernandez-Aramburo, and T. C. Green. Energy management in autonomous microgrid using stability-constrained droop control of inverters. *IEEE Transactions on Power Electronics*, 23(5):2346–2352, Sep. 2008.
- [18] Julia A Belk, Wardah Inam, David J Perreault, and Konstantin Turitsyn. Stability and control of ad hoc dc microgrids. In *Decision and Control (CDC), 2016 IEEE 55th Conference on*, pages 3271–3278. IEEE, 2016.
- [19] Peter Benner, Serkan Gugercin, and Karen Willcox. A survey of projection-based model reduction methods for parametric dynamical systems. *SIAM Review*, 57(4):483–531, 2015.
- [20] B. Bilgin, P. Magne, P. Malysz, Y. Yang, V. Pantelic, M. Preindl, A. Korobkine, W. Jiang, M. Lawford, and A. Emadi. Making the case for electrified transportation. *IEEE Transactions on Transportation Electrification*, 1(1):4–17, June 2015.
- [21] E. Boardman. Advanced applications in an advanced distribution management system: Essentials for implementation and integration. *IEEE Power and Energy Magazine*, 18(1):43–54, 2020.
- [22] Tetiana Bogodorova, Luigi Vanfretti, Vedran S Perić, and Konstantin Turitsyn. Identifying uncertainty distributions and confidence regions of power plant parameters. *IEEE Access*, 5:19213–19224, 2017.

- [23] S. Bolognani and F. Dörfler. Fast power system analysis via implicit linearization of the power flow manifold. In *2015 53rd Annual Allerton Conference on Communication, Control, and Computing (Allerton)*, pages 402–409, 2015.
- [24] B. Borkowska. Probabilistic load flow. *IEEE Transactions on Power Apparatus and Systems*, PAS-93(3):752–759, 1974.
- [25] T. Bradde, S. Grivet-Talocia, G. C. Calafiore, A. V. Proskurnikov, Z. Mahmood, and L. Daniel. Bounded input dissipativity of linearized circuit models. *IEEE Transactions on Circuits and Systems I: Regular Papers*, 67(6):2064–2077, June 2020.
- [26] R. Brayton and J. Moser. Some Results on the Stability of Nonlinear Networks Containing Negative Resistances. *IEEE Transactions on Circuit Theory*, 11(1):165–167, 1964.
- [27] M. Brown, M. Biswal, S. Brahma, S. J. Ranade, and H. Cao. Characterizing and quantifying noise in pmu data. In *2016 IEEE Power and Energy Society General Meeting (PESGM)*, pages 1–5, July 2016.
- [28] Steven L Brunton and J Nathan Kutz. *Data-driven science and engineering: Machine learning, dynamical systems, and control*. Cambridge University Press, 2019.
- [29] I. R. Cabrera, B. Wang, and K. Sun. A method to locate the source of forced oscillations based on linearized model and system measurements. In *2017 IEEE Power Energy Society General Meeting*, pages 1–5, July 2017.
- [30] Xiao Cai, Feiping Nie, and Heng Huang. Exact top-k feature selection via l<sub>2</sub>, 0-norm constraint. In *IJCAI*, volume 13, pages 1240–1246, 2013.
- [31] James Candy. *Model-Based Processing*. Wiley Online Library, 2019.
- [32] Kathleen Cavanagh, Julia A Belk, and Konstantin Turitsyn. Transient Stability Guarantees for Ad Hoc DC Microgrids. *IEEE Control Systems Letters*, 2(1):139–144, 2018.
- [33] J. Chai, Y. Liu, Y. Liu, N. Bhatt, A. D. Rosso, and E. Farantatos. Measurement-based system reduction using autoregressive model. In *2016 IEEE/PES Transmission and Distribution Conference and Exposition (T D)*, pages 1–5, May 2016.
- [34] A. Chakrabortty, J. H. Chow, and A. Salazar. A measurement-based framework for dynamic equivalencing of large power systems using wide-area phasor measurements. *IEEE Transactions on Smart Grid*, 2(1):68–81, March 2011.
- [35] L. Chen, Y. Min, and W. Hu. An energy-based method for location of power system oscillation source. *IEEE Transactions on Power Systems*, 28(2):828–836, May 2013.

- [36] Lei Chen, Fei Xu, Yong Min, Maohai Wang, and Wei Hu. Transient energy dissipation of resistances and its effect on power system damping. *International Journal of Electrical Power and Energy Systems*, 91:201 – 208, 2017.
- [37] C. S. Cheng and D. Shirmohammadi. A three-phase power flow method for real-time distribution system analysis. *IEEE Transactions on Power Systems*, 10(2):671–679, May 1995.
- [38] S. Chevalier, P. Vorobev, and K. Turitsyn. A bayesian approach to forced oscillation source location given uncertain generator parameters. *IEEE Transactions on Power Systems*, pages 1–1, 2018.
- [39] S. Chevalier, P. Vorobev, and K. Turitsyn. Using effective generator impedance for forced oscillation source location. *IEEE Transactions on Power Systems*, pages 1–1, 2018.
- [40] S. Chevalier, P. Vorobev, K. Turitsyn, B. Wang, and S. Maslennikov. Using passivity theory to interpret the dissipating energy flow method. In *2019 IEEE Power Energy Society General Meeting (PESGM)*, pages 1–5, 2019.
- [41] Chun-Lien Su. Probabilistic load-flow computation using point estimate method. *IEEE Transactions on Power Systems*, 20(4):1843–1851, 2005.
- [42] L. Daniel, C. S. Ong, S. C. Low, K. H. Lee, and J. White. A multiparameter moment matching model reduction approach for generating geometrically parameterized interconnect performance models. *IEEE Transactions on Computer Aided Design of Integrated Circuits and Systems*, 23(5):678–693, May 2004.
- [43] Claudio De Persis, Erik RA Weitenberg, and Florian Dörfler. A power consensus algorithm for dc microgrids. *Automatica*, 89:364–375, 2018.
- [44] C. Delgado and J.A. Domínguez-Navarro. Point estimate method for probabilistic load flow of an unbalanced power distribution system with correlated wind and solar sources. *International Journal of Electrical Power & Energy Systems*, 61:267 – 278, 2014.
- [45] K. Diakos, Q. Wu, and A. H. Nielsen. Phasor measurement unit and phasor data concentrator test with real time digital simulator. In *2014 IEEE PES Asia-Pacific Power and Energy Engineering Conference (APPEEC)*, pages 1–5, Dec 2014.
- [46] L. Ding, A. Xue, F. Han, J. Li, M. Wang, T. Bi, and J. Wang. Dominant mode identification for low frequency oscillations of power systems based on prony algorithm. In *2010 5th International Conference on Critical Infrastructure (CRIS)*, pages 1–6, Sep. 2010.
- [47] Roel Dobbe, Werner van Westering, Stephan Liu, Daniel Arnold, Duncan Callaway, and Claire Tomlin. Forecasting-based state estimation for three-phase distribution systems with limited sensing, 2018.

- [48] Ning Dong and Jaijeet Roychowdhury. Piecewise polynomial nonlinear model reduction. In *Proceedings of the 40th Annual Design Automation Conference*, DAC '03, page 484–489, New York, NY, USA, 2003. Association for Computing Machinery.
- [49] L. Dosiek and J. W. Pierre. Estimating electromechanical modes and mode shapes using the multichannel armax model. *IEEE Transactions on Power Systems*, 28(2):1950–1959, 2013.
- [50] L. Dosiek, N. Zhou, J. W. Pierre, Z. Huang, and D. J. Trudnowski. Mode shape estimation algorithms under ambient conditions: A comparative review. *IEEE Transactions on Power Systems*, 28(2):779–787, May 2013.
- [51] R. C. Dugan and T. E. McDermott. An open source platform for collaborating on smart grid research. In *2011 IEEE Power and Energy Society General Meeting*, pages 1–7, 2011.
- [52] Roger C Dugan. Reference guide: The open distribution system simulator (opendss). *Electric Power Research Institute, Inc*, 7:29, 2012.
- [53] F. Dörfler, J. W. Simpson-Porco, and F. Bullo. Plug-and-play control and optimization in microgrids. In *53rd IEEE Conference on Decision and Control*, pages 211–216, Dec 2014.
- [54] T. El-Moselhy and L. Daniel. Variation-aware interconnect extraction using statistical moment preserving model order reduction. In *2010 Design, Automation Test in Europe Conference Exhibition (DATE 2010)*, pages 453–458, 2010.
- [55] T. El-Moselhy and L. Daniel. Variation-aware stochastic extraction with large parameter dimensionality: Review and comparison of state of the art intrusive and non-intrusive techniques. In *2011 12th International Symposium on Quality Electronic Design*, pages 1–10, 2011.
- [56] Ali Emadi, Mehrdad Ehsani, and John M Miller. *Vehicular electric power systems: land, sea, air, and space vehicles*. CRC press, 2003.
- [57] ERCOT. Ercot nodal operating guides. Technical report, ERCOT, Austin, TX, 2 2018.
- [58] Robert W Erickson and Dragan Maksimovic. *Fundamentals of power electronics*. Springer Science & Business Media, 2007.
- [59] M. Fan et al. Probabilistic power flow studies for transmission systems with photovoltaic generation using cumulants. *IEEE Transactions on Power Systems*, 27(4):2251–2261, 2012.
- [60] M. Farrokhabadi, C. A. Canizares, J. W. Simpson-Porco, E. Nasr, L. Fan, P. Mendoza-Araya, R. Tonkoski, U. Tamrakar, N. D. Hatziargyriou, D. Lagos,

R. W. Wies, M. Paolone, M. Liserre, L. Meegahapola, M. Kabalan, A. H. Hajimiragha, D. Peralta, M. Elizondo, K. P. Schneider, F. Tuffner, and J. T. Reilly. Microgrid stability definitions, analysis, and examples. *IEEE Transactions on Power Systems*, pages 1–1, 2019.

- [61] A. Feliachi. Identification of critical modes in power systems. *IEEE Transactions on Power Systems*, 5(3):783–788, Aug 1990.
- [62] Xiaogang Feng, Jinjun Liu, and Fred C Lee. Impedance specifications for stable dc distributed power systems. *IEEE Transactions on Power Electronics*, 17(2):157–162, 2002.
- [63] R. H. Flake. Volterra series representation of nonlinear systems. *Transactions of the American Institute of Electrical Engineers, Part II: Applications and Industry*, 81(6):330–335, 1963.
- [64] S. A. Foroutan and A. Srivastava. Generator model validation and calibration using synchrophasor data. In *2019 IEEE Industry Applications Society Annual Meeting*, pages 1–6, 2019.
- [65] Gene F Franklin, J David Powell, Abbas Emami-Naeini, and J David Powell. *Feedback control of dynamic systems*, volume 4. Prentice hall Upper Saddle River, 2002.
- [66] G. Ghanavati, P. D. H. Hines, and T. I. Lakoba. Identifying useful statistical indicators of proximity to instability in stochastic power systems. *IEEE Transactions on Power Systems*, 31(2):1360–1368, March 2016.
- [67] Mohammadreza Ghorbaniparvar. Survey on forced oscillations in power system. *Journal of Modern Power Systems and Clean Energy*, 5(5):671–682, Sep 2017.
- [68] J. Gleick. *Isaac Newton*. National bestseller. Vintage Books, 2004.
- [69] J.D. Glover, M.S. Sarma, and T. Overbye. *Power System Analysis & Design, SI Version*. Cengage Learning, 2012.
- [70] S. Grijalva and M. U. Tariq. Prosumer-based smart grid architecture enables a flat, sustainable electricity industry. In *ISGT 2011*, pages 1–6, Jan 2011.
- [71] S. Grivet-Talocia. Package macromodeling via time-domain vector fitting. *IEEE Microwave and Wireless Components Letters*, 13(11):472–474, November 2003.
- [72] S. Grivet-Talocia. The time-domain vector fitting algorithm for linear macro-modeling. *Int. Journal of Electronics and Communications (AEU)*, 58:293–295, 2004.
- [73] S. Grivet-Talocia and B. Gustavsen. *Passive Macromodeling: Theory and Applications*. John Wiley and Sons, New York, 2016 (published online on Dec 7, 2015).

- [74] G. Gruosso, R. S. Netto, L. Daniel, and P. Maffezzoni. Joined probabilistic load flow and sensitivity analysis of distribution networks based on polynomial chaos method. *IEEE Transactions on Power Systems*, 35(1):618–627, 2020.
- [75] B. Gustavsen. Improving the pole relocating properties of vector fitting. *Power Delivery, IEEE Transactions on*, 21(3):1587–1592, july 2006.
- [76] B. Gustavsen and A. Semlyen. Rational approximation of frequency domain responses by vector fitting. *Power Delivery, IEEE Transactions on*, 14(3):1052–1061, jul 1999.
- [77] M. Hajian, W. D. Rosehart, and H. Zareipour. Probabilistic power flow by monte carlo simulation with latin supercube sampling. *IEEE Transactions on Power Systems*, 28(2):1550–1559, 2013.
- [78] S. Han, N. Rong, T. Sun, and J. Zhang. An approach for estimating mode shape for participation of inter-area oscillation mode. In *2013 IEEE International Symposium on Circuits and Systems (ISCAS)*, pages 2968–2971, May 2013.
- [79] S. Han, Z. Xu, and C. Wu. Mode shape estimation and mode identification for inter-area oscillations utilizing correlation analysis techniques. In *2010 International Conference on Power System Technology*, pages 1–8, Oct 2010.
- [80] L. Harnefors. Modeling of three-phase dynamic systems using complex transfer functions and transfer matrices. *IEEE Transactions on Industrial Electronics*, 54(4):2239–2248, 2007.
- [81] Lennart Harnefors. Modeling of three-phase dynamic systems using complex transfer functions and transfer matrices. *IEEE Transactions on Industrial Electronics*, 54(4):2239–2248, 2007.
- [82] Lennart Harnefors, Massimo Bongiorno, and Stefan Lundberg. Stability analysis of converter-grid interaction using the converter input admittance. In *Power Electronics and Applications, 2007 European Conference on*, pages 1–10. IEEE, 2007.
- [83] N. Hatziargyriou, H. Asano, R. Iravani, and C. Marnay. Microgrids. *IEEE Power and Energy Magazine*, 5(4):78–94, July 2007.
- [84] J. F. Hauer, C. J. Demeure, and L. L. Scharf. Initial results in prony analysis of power system response signals. *IEEE Transactions on Power Systems*, 5(1):80–89, Feb 1990.
- [85] D. A. Haughton and G. T. Heydt. A linear state estimation formulation for smart distribution systems. *IEEE Transactions on Power Systems*, 28(2):1187–1195, May 2013.
- [86] IA Hiskens. Inverse problems in power systems. In *Bulk Power System Dynamics and Control V*, August 2001.

- [87] Ian Hiskens. Ieee pes task force on benchmark systems for stability controls. *Technical Report*, 2013.
- [88] "Ian Hiskens and Alexander Koeman". Power system parameter estimation. In *Australian Universities Power Engineering Conference*, June 1999.
- [89] R.A. Horn and C.R. Johnson. *Matrix Analysis*. Cambridge University Press, 1990.
- [90] J. Huang, Y. Xue, Z. Y. Dong, and K. P. Wong. An adaptive importance sampling method for probabilistic optimal power flow. In *2011 IEEE Power and Energy Society General Meeting*, pages 1–6, 2011.
- [91] Po-Hsu Huang. *Systematic control strategy for inverter-based microgrids*. PhD thesis, Massachusetts Institute of Technology, 2019.
- [92] T. Huang et al. Localization of forced oscillations in the power grid under resonance conditions. In *2018 52nd Annual Conference on Information Sciences and Systems (CISS)*, pages 1–5, March 2018.
- [93] Z. Huang, P. Du, D. Kosterev, and S. Yang. Generator dynamic model validation and parameter calibration using phasor measurements at the point of connection. *IEEE Transactions on Power Systems*, 28(2):1939–1949, 2013.
- [94] Wardah Inam, Julia A Belk, Konstantin Turitsyn, and David J Perreault. Stability, control, and power flow in ad hoc dc microgrids. In *Control and Modeling for Power Electronics (COMPEL), 2016 IEEE 17th Workshop on*, pages 1–8. IEEE, 2016.
- [95] S. H. Jakobsen and K. Uhlen. Vector fitting for estimation of turbine governing system parameters. In *2017 IEEE Manchester PowerTech*, pages 1–6, 2017.
- [96] D. Jeltsema and J. Scherpen. Multidomain modeling of nonlinear networks and systems. *IEEE Control Systems Magazine*, 29(4):28–59, 2009.
- [97] Philip B. Jones, Jonathan Levy, Jenifer Bosco, John Howat, and John W. Van Alst. The future of transportation electrification: Utility, industry and consumer perspectives. Technical report, 08/2018 2018.
- [98] Jackson John Justo, Francis Mwasilu, Ju Lee, and Jin-Woo Jung. Ac-microgrids versus dc-microgrids with distributed energy resources: A review. *Renewable and Sustainable Energy Reviews*, 24:387–405, 2013.
- [99] Jari Kaipio and Erkki Somersalo. *Statistical and computational inverse problems*, volume 160. Springer Science & Business Media, 2006.
- [100] H.K. Khalil. *Nonlinear Systems*. Pearson Education. Prentice Hall, 2002.

- [101] W. Kong, K. Ma, F. Li, and L. Sidebotham. Future distribution system architecture in the uk. In *2018 International Conference on Power System Technology (POWERCON)*, pages 516–521, Nov 2018.
- [102] D. N. Kosterev, C. W. Taylor, and W. A. Mittelstadt. Model validation for the august 10, 1996 wscc system outage. *IEEE Transactions on Power Systems*, 14(3):967–979, 1999.
- [103] B. Kroposki, B. Johnson, Y. Zhang, V. Gevorgian, P. Denholm, B. Hodge, and B. Hannegan. Achieving a 100% renewable grid: Operating electric power systems with extremely high levels of variable renewable energy. *IEEE Power and Energy Magazine*, 15(2):61–73, March 2017.
- [104] P. Kundur, J. Paserba, V. Ajjarapu, G. Andersson, A. Bose, C. Canizares, N. Hatziargyriou, D. Hill, A. Stankovic, C. Taylor, T. Van Cutsem, and V. Vitalal. Definition and classification of power system stability ieee/cigre joint task force on stability terms and definitions. *IEEE Transactions on Power Systems*, 19(3):1387–1401, Aug 2004.
- [105] Prabha Kundur et al. *Power system stability and control*, volume 7. McGraw-Hill New York, 1994.
- [106] V. B. Kurzin and V. S. Seleznev. Mechanism of emergence of intense vibrations of turbines on the sayano-shushensk hydro power plant. *Journal of Applied Mechanics and Technical Physics*, 51(4):590–597, Jul 2010.
- [107] Robert H Lasseter. Smart distribution: Coupled microgrids. *Proceedings of the IEEE*, 99(6):1074–1082, 2011.
- [108] S. Lefteriu and A. C. Antoulas. On the convergence of the vector-fitting algorithm. *Microwave Theory and Techniques, IEEE Transactions on*, 61(4):1435–1443, 2013.
- [109] Y. Li, R. Diao, et al. An innovative software tool suite for power plant model validation and parameter calibration using pmu measurements. In *2017 IEEE Power Energy Society General Meeting*, pages 1–5, 2017.
- [110] G. Lin, N. Zhou, T. Ferryman, and F. Tuffner. Uncertainty quantification in state estimation using the probabilistic collocation method. In *2011 IEEE/PES Power Systems Conference and Exposition*, pages 1–8, 2011.
- [111] H. Liu, L. Zhu, Z. Pan, F. Bai, Y. Liu, Y. Liu, M. Patel, E. Farantatos, and N. Bhatt. Armax-based transfer function model identification using wide-area measurement for adaptive and coordinated damping control. *IEEE Transactions on Smart Grid*, 8(3):1105–1115, May 2017.
- [112] J. Liu, J. Tang, F. Ponci, A. Monti, C. Muscas, and P. A. Pegoraro. Trade-offs in pmu deployment for state estimation in active distribution grids. *IEEE Transactions on Smart Grid*, 3(2):915–924, June 2012.

- [113] C. N. Lu, J. H. Teng, and W. . E. Liu. Distribution system state estimation. *IEEE Transactions on Power Systems*, 10(1):229–240, Feb 1995.
- [114] J. Ma, P. Zhang, H. j. Fu, B. Bo, and Z. y. Dong. Application of phasor measurement unit on locating disturbance source for low-frequency oscillation. *IEEE Transactions on Smart Grid*, 1(3):340–346, Dec 2010.
- [115] Jan Machowski, Zbigniew Lubosny, Janusz W Bialek, and James R Bumby. *Power system dynamics: stability and control*. John Wiley and Sons, 2020.
- [116] S. Maslennikov and E. Litvinov. Iso new england experience in locating the source of oscillations online. *IEEE Transactions on Power Systems*, pages 1–1, 2020.
- [117] S. Maslennikov, B. Wang, et al. A test cases library for methods locating the sources of sustained oscillations. In *2016 IEEE Power and Energy Society General Meeting (PESGM)*, pages 1–5, July 2016.
- [118] S. Maslennikov, B. Wang, and E. Litvinov. Locating the source of sustained oscillations by using pmu measurements. In *2017 IEEE Power Energy Society General Meeting*, pages 1–5, July 2017.
- [119] S. Maslennikov, B. Wang, Q. Zhang, a. Ma, a. Luo, a. Sun, and E. Litvinov. A test cases library for methods locating the sources of sustained oscillations. In *2016 IEEE Power and Energy Society General Meeting (PESGM)*, pages 1–5, July 2016.
- [120] Slava Maslennikov. personal correspondence, August 2019.
- [121] Slava Maslennikov and Eugene Litvinov. *Online Oscillations Management at ISO New England*, pages 257–283. Springer International Publishing, Cham, 2019.
- [122] Slava Maslennikov, Bin Wang, and Eugene Litvinov. Dissipating energy flow method for locating the source of sustained oscillations. *International Journal of Electrical Power and Energy Systems*, pages 55 – 62, 2017.
- [123] Slava Maslennikov, Bin Wang, and Eugene Litvinov. Dissipating energy flow method for locating the source of sustained oscillations. *International Journal of Electrical Power and Energy Systems*, pages 55 – 62, 2017.
- [124] J. L. Mathieu, S. Koch, and D. S. Callaway. State estimation and control of electric loads to manage real-time energy imbalance. *IEEE Transactions on Power Systems*, 28(1):430–440, Feb 2013.
- [125] Y. Meng, Z. Yu, D. Shi, D. Bian, and Z. Wang. Forced oscillation source location via multivariate time series classification. *ArXiv e-prints*, November 2017.

- [126] R.D. Middlebrook. Input filter considerations in design and application of switching regulators. *IEEE IAS Annual Meeting*, 1976.
- [127] F. Milano, F. Dörfler, G. Hug, D. J. Hill, and G. Verbič. Foundations and challenges of low-inertia systems (invited paper). In *2018 Power Systems Computation Conference (PSCC)*, pages 1–25, June 2018.
- [128] F. Milano and R. Zarate-Minano. A systematic method to model power systems as stochastic differential algebraic equations. *IEEE Transactions on Power Systems*, 28(4):4537–4544, 2013.
- [129] Federico Milano. *Power System Analysis Toolbox Reference Manual for PSAT version 2.1.8.*, 2.1.8 edition, 5 2013.
- [130] A. Minot, Y. M. Lu, and N. Li. A distributed gauss-newton method for power system state estimation. *IEEE Transactions on Power Systems*, 31(5):3804–3815, 2016.
- [131] K. Nagappan. Step-by-step formation of bus admittance matrix. *IEEE Transactions on Power Apparatus and Systems*, PAS-89(5):812–820, May 1970.
- [132] Isaac Newton. *The Principia: mathematical principles of natural philosophy*. Univ of California Press, 1999.
- [133] F. Ni, P. H. Nguyen, and J. F. G. Cobben. Basis-adaptive sparse polynomial chaos expansion for probabilistic power flow. *IEEE Transactions on Power Systems*, 32(1):694–704, 2017.
- [134] Iraklis P Nikolakakos, Hatem H Zeineldin, Mohamed Shawky El-Moursi, and Nikos D Hatzigergiou. Stability evaluation of interconnected multi-inverter microgrids through critical clusters. *IEEE Trans. Power Syst.*, 31(4):3060–3072, 2016.
- [135] James O'Brien, Tianying Wu, et al. Source location of forced oscillations using synchrophasor and scada data. In *HICSS*, 2017.
- [136] U.S. Department of Energy. Advanced metering infrastructure and customer systems. Technical report, sep 2016.
- [137] C. J. O'Rourke, M. M. Qasim, M. R. Overlin, and J. L. Kirtley. A geometric interpretation of reference frames and transformations: dq0, clarke, and park. *IEEE Transactions on Energy Conversion*, 34(4):2070–2083, 2019.
- [138] Trevor Park and George Casella. The bayesian lasso. *Journal of the American Statistical Association*, 103(482):681–686, 2008.
- [139] M. Pau, P. A. Pegoraro, and S. Sulis. Efficient branch-current-based distribution system state estimation including synchronized measurements. *IEEE Transactions on Instrumentation and Measurement*, 62(9):2419–2429, Sep. 2013.

- [140] N. Petra, C. G. Petra, Z. Zhang, E. M. Constantinescu, and M. Anitescu. A bayesian approach for parameter estimation with uncertainty for dynamic power systems. *IEEE Transactions on Power Systems*, 32(4):2735–2743, July 2017.
- [141] A. G. Phadke and J. S. Thorp. History and applications of phasor measurements. In *2006 IEEE PES Power Systems Conference and Exposition*, pages 331–335, Oct 2006.
- [142] B. J. Pierre, F. Wilches-Bernal, D. A. Schoenwald, R. T. Elliott, D. J. Trudnowski, R. H. Byrne, and J. C. Neely. Design of the pacific dc intertie wide area damping controller. *IEEE Transactions on Power Systems*, 34(5):3594–3604, 2019.
- [143] J. W. Pierre, D. J. Trudnowski, and M. K. Donnelly. Initial results in electromechanical mode identification from ambient data. *IEEE Transactions on Power Systems*, 12(3):1245–1251, Aug 1997.
- [144] John W. Pierre, Dan Trudnowski, Matthew Donnelly, Ning Zhou, Francis K. Tuffner, and Luke Dosiek. Overview of system identification for power systems from measured responses1. *IFAC Proceedings Volumes*, 45(16):989 – 1000, 2012. 16th IFAC Symposium on System Identification.
- [145] Estefanía Planas, Jon Andreu, José Ignacio Gárate, Iñigo Martínez de Alegría, and Edorta Ibarra. Ac and dc technology in microgrids: A review. *Renewable and Sustainable Energy Reviews*, 43:726–749, 2015.
- [146] Nagaraju Pogaku, Milan Prodanović, and Timothy C Green. Modeling, analysis and testing of autonomous operation of an inverter-based microgrid. *IEEE Trans. Power Electron.*, 22(2):613–625, 2007.
- [147] B. R. Pokhrel, N. Karthikeyan, B. Bak-Jensen, and J. R. Pillai. Effect of smart meter measurements data on distribution state estimation. In *2018 IEEE International Conference on Industrial Technology (ICIT)*, pages 1207–1212, Feb 2018.
- [148] A. Primadianto and C. Lu. A review on distribution system state estimation. *IEEE Transactions on Power Systems*, 32(5):3875–3883, Sep. 2017.
- [149] B Rajanarayan Prusty and Debashisha Jena. A critical review on probabilistic load flow studies in uncertainty constrained power systems with photovoltaic generation and a new approach. *Renewable and Sustainable Energy Reviews*, 69:1286 – 1302, 2017.
- [150] Ryan Quint. Applicable nerc reliability standards. 2016.
- [151] Amir M Rahimi and Ali Emadi. An analytical investigation of dc/dc power electronic converters with constant power loads in vehicular power systems. *IEEE Transactions on vehicular technology*, 58(6):2689–2702, 2009.

- [152] Z. Ren, W. Li, R. Billinton, and W. Yan. Probabilistic power flow analysis based on the stochastic response surface method. *IEEE Transactions on Power Systems*, 31(3):2307–2315, 2016.
- [153] Antonino Riccobono and Enrico Santi. Comprehensive review of stability criteria for dc distribution systems. In *Energy Conversion Congress and Exposition (ECCE), 2012 IEEE*, pages 3917–3925. IEEE, 2012.
- [154] Antonino Riccobono and Enrico Santi. Comprehensive review of stability criteria for dc power distribution systems. *IEEE Transactions on Industry Applications*, 50(5):3525–3535, 2014.
- [155] N. Rostamkolai, R. J. Piwko, and A. S. Matusik. Evaluation of the impact of a large cyclic load on the lilco power system using time simulation and frequency domain techniques. *IEEE Transactions on Power Systems*, 9(3):1411–1416, Aug 1994.
- [156] S. Sanchez, R. Ortega, G. Bergna, M. Molinas, and R. Grino. Conditions for existence of equilibrium points of systems with constant power loads. In *2013 IEEE 52nd Annual Conference on Decision and Control (CDC)*, pages 3641–3646. IEEE, 2013.
- [157] S. A. Nezam Sarmadi, V. Venkatasubramanian, and A. Salazar. Analysis of november 29, 2005 western american oscillation event. *IEEE Transactions on Power Systems*, 31(6):5210–5211, Nov 2016.
- [158] P.W. Sauer and M.A. Pai. *Power System Dynamics and Stability*. Stipes Publishing L.L.C., 2006.
- [159] L. Schenato, G. Barchi, D. Macii, R. Arghandeh, K. Poolla, and A. Von Meier. Bayesian linear state estimation using smart meters and pmus measurements in distribution grids. In *2014 IEEE International Conference on Smart Grid Communications (SmartGridComm)*, pages 572–577, Nov 2014.
- [160] Mark Schmidt, Glenn Fung, and Romer Rosales. Optimization methods for  $\ell_1$ -regularization. *University of British Columbia, Technical Report TR-2009*, 19, 2009.
- [161] K. P. Schneider, B. A. Mather, et al. Analytic considerations and design basis for the ieee distribution test feeders. *IEEE Transactions on Power Systems*, 33(3):3181–3188, 2018.
- [162] Ricardo Schumacher, Gustavo H.C. Oliveira, and Roman Kuiava. A novel time-domain linear ringdown method based on vector fitting for estimating electromechanical modes. *Electric Power Systems Research*, 160:300 – 307, 2018.
- [163] F. C. Schweppe. Power system static-state estimation, part iii: Implementation. *IEEE Transactions on Power Apparatus and Systems*, PAS-89(1):130–135, Jan 1970.

- [164] F. C. Schweppe and D. B. Rom. Power system static-state estimation, part ii: Approximate model. *IEEE Transactions on Power Apparatus and Systems*, PAS-89(1):125–130, Jan 1970.
- [165] F. C. Schweppe and J. Wildes. Power system static-state estimation, part i: Exact model. *IEEE Transactions on Power Apparatus and Systems*, PAS-89(1):120–125, Jan 1970.
- [166] A. Shafiu, N. Jenkins, and G. Strbac. Measurement location for state estimation of distribution networks with generation. *IEE Proceedings - Generation, Transmission and Distribution*, 152(2):240–246, March 2005.
- [167] H. Sheng and X. Wang. Probabilistic power flow calculation using non-intrusive low-rank approximation method. *IEEE Transactions on Power Systems*, 34(4):3014–3025, 2019.
- [168] J. W. Simpson-Porco, F. Dörfler, and F. Bullo. On Resistive Networks of Constant-Power Devices. *IEEE Transactions on Circuits and Systems II: Express Briefs*, 62(8):811–815, 2015.
- [169] R. Singh, B. C. Pal, and R. A. Jabr. Choice of estimator for distribution system state estimation. *IET Generation, Transmission Distribution*, 3(7):666–678, July 2009.
- [170] Suresh Singh, Aditya R Gautam, and Deepak Fulwani. Constant power loads and their effects in dc distributed power systems: A review. *Renewable and Sustainable Energy Reviews*, 72:407–421, 2017.
- [171] J.J.E. Slotine and W. Li. *Applied Nonlinear Control*. Prentice-Hall International Editions. Prentice-Hall, 1991.
- [172] M. Smith and D. Ton. Key connections: The u.s. department of energy’s microgrid initiative. *IEEE Power and Energy Magazine*, 11(4):22–27, July 2013.
- [173] Jennie C. Stephens, Elizabeth J. Wilson, and Tarla Rai Peterson. *Smart Grid (R)Evolution: Electric Power Struggles*. Cambridge University Press, 2015.
- [174] Petre Stoica, Randolph L Moses, et al. Spectral analysis of signals. 2005.
- [175] Scott D Sudhoff and Jonathan M Crider. Advancements in generalized imittance based stability analysis of dc power electronics based distribution systems. In *Electric Ship Technologies Symposium (ESTS), 2011 IEEE*, pages 207–212. IEEE, 2011.
- [176] Scott D Sudhoff, Steven F Glover, Peter T Lamm, Donald H Schmucker, and DE Delisle. Admittance space stability analysis of power electronic systems. *IEEE Transactions on Aerospace and Electronic Systems*, 36(3):965–973, 2000.

- [177] N. Tsolas, A. Arapostathis, and P. Varaiya. A structure preserving energy function for power system transient stability analysis. *IEEE Transactions on Circuits and Systems*, 32(10):1041–1049, October 1985.
- [178] M. Vaiman, R. Quint, et al. Using synchrophasors to improve bulk power system reliability in north america. In *2018 IEEE Power and Energy Society General Meeting (PESGM)*, pages 1–5, 2018.
- [179] Abraham Jan van der Schaft and AJ Van Der Schaft. *L<sub>2</sub>-gain and passivity techniques in nonlinear control*, volume 2. Springer, 2000.
- [180] L. Vanfretti, S. Bengtsson, V. S. Perić, and J. O. Gjerde. Effects of forced oscillations in power system damping estimation. In *2012 IEEE International Workshop on Applied Measurements for Power Systems (AMPS) Proceedings*, pages 1–6, Sept 2012.
- [181] A. von Meier, D. Culler, A. McEachern, and R. Arghandeh. Micro-synchrophasors for distribution systems. In *ISGT 2014*, pages 1–5, Feb 2014.
- [182] P. Vorobev, S. Chevalier, and K. Turitsyn. Decentralized stability rules for microgrids. In *2019 American Control Conference (ACC)*, pages 2596–2601, July 2019.
- [183] Petr Vorobev, Po-Hsu Huang, Mohamed Al Hosani, James L Kirtley, and Konstantin Turitsyn. A framework for development of universal rules for microgrids stability and control. In *Decision and Control (CDC), 2017 IEEE 56th Annual Conference on*, pages 5125–5130. IEEE, 2017.
- [184] Petr Vorobev, Po-Hsu Huang, Mohamed Al Hosani, James L Kirtley, and Konstantin Turitsyn. High-fidelity model order reduction for microgrids stability assessment. *IEEE Transactions on Power Systems*, 33(1):874–887, 2018.
- [185] Bin Wang and Kai SUN. Location methods of oscillation sources in power systems: a survey. *Journal of Modern Power Systems and Clean Energy*, 5(2):151–159, Mar 2017.
- [186] C. Wang, C. Li, G. Wu, G. Li, and Z. Du. Online identification of power system oscillation modes based on mode shape matching. In *2018 China International Conference on Electricity Distribution (CICED)*, pages 1576–1580, Sep. 2018.
- [187] Gang Wang, Georgios B. Giannakis, Jie Chen, and Jian Sun. Distribution system state estimation: an overview of recent developments. *Frontiers of Information Technology and Electronic Engineering*, 20(1):4–17, January 2019.
- [188] X. Wang and K. Turitsyn. Data-driven diagnostics of mechanism and source of sustained oscillations. *IEEE Transactions on Power Systems*, 31(5):4036–4046, Sept 2016.

- [189] R. W. Wies, J. W. Pierre, and D. J. Trudnowski. Use of arma block processing for estimating stationary low-frequency electromechanical modes of power systems. *IEEE Transactions on Power Systems*, 18(1):167–173, 2003.
- [190] F. Wilches-Bernal, B. J. Pierre, D. A. Schoenwald, R. T. Elliott, R. H. Byrne, J. C. Neely, and D. J. Trudnowski. Forced oscillations in the western interconnection with the pacific dc intertie wide area damping controller. In *2020 IEEE Power Energy Society Innovative Smart Grid Technologies Conference (ISGT)*, pages 1–5, 2020.
- [191] Carl M Wildrick, Fred C Lee, Bo H Cho, and Byungcho Choi. A method of defining the load impedance specification for a stable distributed power system. *IEEE Transactions on power Electronics*, 10(3):280–285, 1995.
- [192] Jan C. Willems. Dissipative dynamical systems part i: General theory. *Archive for Rational Mechanics and Analysis*, 45(5):321–351, Jan 1972.
- [193] Jan C. Willems. Dissipative dynamical systems part ii: Linear systems with quadratic supply rates. *Archive for Rational Mechanics and Analysis*, 45(5):352–393, Jan 1972.
- [194] H. Wu, Q. Duan, and J. Ma. Disturbance source self-diagnosis of the smart grid. In *2012 Spring Congress on Engineering and Technology*, pages 1–4, May 2012.
- [195] M. Wu and L. Xie. A feature-based diagnosis framework for power plant model validation. In *2018 Power Systems Computation Conference (PSCC)*, pages 1–7, 2018.
- [196] J. Wyatt, L. Chua, J. Gannett, I. Goknar, and D. Green. Energy concepts in the state-space theory of nonlinear n-ports: Part i-passivity. *IEEE Transactions on Circuits and Systems*, 28(1):48–61, 1981.
- [197] J. Wyatt, L. Chua, J. Gannett, I. Goknar, and D. Green. Energy concepts in the state-space theory of nonlinear n-ports: Part ii - losslessness. *IEEE Transactions on Circuits and Systems*, 29(7):417–430, 1982.
- [198] Ruichao Xie and D. Trudnowski. Distinguishing features of natural and forced oscillations. In *2015 IEEE Power Energy Society General Meeting*, pages 1–5, July 2015.
- [199] Wang Xuanyin, Li Xiaoxiao, and Li Fushang. Analysis on oscillation in electro-hydraulic regulating system of steam turbine and fault diagnosis based on psobp. *Expert Systems with Applications*, 37(5):3887 – 3892, 2010.
- [200] H. Ye, Y. Liu, P. Zhang, and Z. Du. Analysis and detection of forced oscillation in power system. *IEEE Transactions on Power Systems*, 32(2):1149–1160, March 2017.

- [201] H. Yu, C. Y. Chung, K. P. Wong, H. W. Lee, and J. H. Zhang. Probabilistic load flow evaluation with hybrid latin hypercube sampling and cholesky decomposition. *IEEE Transactions on Power Systems*, 24(2):661–667, 2009.
- [202] J. Yu, J. Yu, Y. Wang, Y. Cao, X. Lu, and D. Zhao. Passivity-based active stabilization for dc microgrid applications. *CSEE Journal of Power and Energy Systems*, 4(1):29–38, March 2018.
- [203] Pei Zhang and S. T. Lee. Probabilistic load flow computation using the method of combined cumulants and gram-charlier expansion. *IEEE Transactions on Power Systems*, 19(1):676–682, 2004.
- [204] X. Zhang, Y. Xue, S. You, Y. Liu, and Y. Liu. U.s. eastern interconnection (ei) model reductions using a measurement-based approach. In *2018 IEEE/PES Transmission and Distribution Conference and Exposition (T D)*, pages 1–5, April 2018.
- [205] X. Zhang, Y. Xue, S. You, Y. Liu, Z. Yuan, J. Chai, and Y. Liu. Measurement-based power system dynamic model reductions. In *2017 North American Power Symposium (NAPS)*, pages 1–6, Sep. 2017.
- [206] Z. Zhang, T. A. El-Moselhy, I. M. Elfadel, and L. Daniel. Stochastic testing method for transistor-level uncertainty quantification based on generalized polynomial chaos. *IEEE Transactions on Computer-Aided Design of Integrated Circuits and Systems*, 32(10):1533–1545, 2013.
- [207] J. Zhao and F. Dörfler. Distributed control and optimization in DC microgrids. *Automatica*, 61:18–26, November 2015.
- [208] Qing-Chang Zhong and George Weiss. Synchronverters: Inverters that mimic synchronous generators. *IEEE Transactions on Industrial Electronics*, 58(4):1259–1267, 2011.
- [209] N. Zhou and J. Dagle. Initial results in using a self-coherence method for detecting sustained oscillations. *IEEE Transactions on Power Systems*, 30(1):522–530, Jan 2015.
- [210] N. Zhou, Z. Huang, L. Dosiek, D. Trudnowski, and J. W. Pierre. Electromechanical mode shape estimation based on transfer function identification using pmu measurements. In *2009 IEEE Power Energy Society General Meeting*, pages 1–7, July 2009.